Probing Molecular Quantum Bits

Von der Fakultät Chemie der Universität Stuttgart zur Erlangung der Würde eines Doktors der Naturwissenschaften (Dr. rer. nat.) genehmigte Abhandlung

Vorgelegt von

Samuel Lenz
aus Böblingen

Hauptberichter:	Prof. Dr. Joris van Slageren
Mitberichter:	Prof. Dr. Jens Anders
Prüfungsvorsitzender:	Prof. Dr. Peer Fischer

Tag der mündlichen Prüfung: 8.12.2021

Institut für Physikalische Chemie der Universität Stuttgart
2021

Der experimentelle Teil dieser Arbeit wurde im Zeitraum vom 1. Januar 2016 bis 31. Juli 2019 am Institut für Physikalische Chemie der Universität Stuttgart in der Arbeitsgruppe van Slageren erarbeitet. Die schriftliche Ausarbeitung wurde im Zeitraum 1. August 2019 bis 1. Juli 2021 in Stuttgart verfasst.

Ich versichere, diese Arbeit selbstständig verfasst zu haben. Ich habe keine anderen als die angegebenen Quellen benutzt und alle wörtlich oder sinngemäß aus anderen Werken übernommene Aussagen als solche gekennzeichnet. Weder diese Arbeit noch wesentliche Teile daraus waren bisher Gegenstand eines anderen Prüfungsverfahrens. Das elektronische Exemplar stimmt mit allen eingereichten Exemplaren überein.

Samuel Lenz

Stuttgart, Juli 2021

Contents

Zusammenfassung

In dieser Arbeit werden Grundlagen erarbeitet, um molekulare Quantenbits (MQBs) über optische und elektrische Methoden auszulesen und steuern zu können sowie sie als Zwischenspeicher für Quanteninformationen von Photonen einzusetzen. Dies ist der nächste Schritt, damit MQBs mit ihren hervorragenden Eigenschaften auch in der Praxis zum Einsatz kommen können.

Ziel des ersten Teils der Arbeit ist ein optisch aktives MQB zu finden und dieses mittels Licht im sichtbaren/Nahinfrarot Bereich auszulesen. Umfangreiche spektroskopische Untersuchungen an dem Chrom(III)-Komplex $[Cr(ddpd)_2][BF_4]_3$ zeigen, dass sich der Komplex mit hervorragenden lumineszenten Eigenschaften sehr gut als MQB eignet. In der Tat weist dieser Komplex eine Kohärenzzeit $T_m = 8.4(1)$ µs auf und ist damit der Rekordhalter unter den Chrom(III) MQBs. Um diese Eigenschaft potentiell weiter zu verbessern wird auch eine deuterierte Variante des Komplexes untersucht. Dabei zeigt sich allerdings, dass das Reduzieren von Kernspins in der Umgebung des Komplexes einen deutlich positiveren Effekt auf die Kohärenzzeit hat, als zum Beispiel das Deuterieren des Komplexes selber. Der Zusammenhang zwischen den optischen und magnetischen Eigenschaften des MQBs wird mittels magnetischer Zirkulardichroismus Spektroskopie entschlüsselt, dazu wird ein theoretisches Modell für die Spin-Bahn Kopplung in diesen Komplex entwickelt. Ein wichtiges Ziel des ersten Kapitels ist das optische Auslesen des MQBs. Letztendlich wird dies weder über die Lumineszenz, noch dem MCD-Effekt des Komplexes erreicht. Messungen des optisch angeregten MQBs deuten darauf hin, das die beteiligten Spinrelaxationszeiten ungünstig für das optische Auslesen liegen. So bleibt ein hervorragendes MQB und mehrere Ansatzpunkte, welche Eigenschaften wichtig für das optische Auslesen eines MQBs sind.

Ziel des zweiten Kapitels ist die Weiterentwicklung eines gepulste Elektronenspinresonanz (ESR) Spektrometers bei 35 GHz um dünne Filme von MQBs auf einem Trägersubstrat messen zu können. Dabei soll das Spektrometer künftig eingesetzt werden um elektrisch angekoppelte MQBs zu charakterisieren und zu manipulieren. Dazu wird ein Fabry-Perot Resonator entwickelt, durch dessen Geometrie ein einfaches platzieren von großen und flachen Proben möglich ist. Seine Eigenschaften werden mittels eines Vektor Netzwerk Analysators (VNA) charakterisiert. Die verschiedenen, im Resona-

tor auftretenden Moden werden auf ihre Tauglichkeit für die gepulste ESR untersucht. Die am Besten geeignete Mode weist eine beladene Güte von $Q_{\mathrm{L}} = 1100$ auf und ist übergekoppelt. Durch die Überkopplung und die damit verbundene reduzierte beladene Güte wird sichergestellt, dass der Resonator eine Totzeit von nur 200 ns aufweist. Neben der elektrischen Charakterisierung wird auch die magnetische Feldkomponente der verschiedener Moden im Resonator untersucht. Dabei wird die Feldhomogenität mittels Rabi Nutationsmessungen bestimmt und mit Feldsimulationen verifiziert. Zu guter Letzt werden mehrere, dünne Filme mit dem Resonator in der gepulsten ESR gemessen. Messungen an einem 60 nm dünner Film von 20% Kupfer(II)phthalocyanin in Phthalocyanin sind problemlos möglich. Dabei wird gezeigt, dass sich die relevanten Qubit-Eigenschaften des Moleküls im Film nicht verschlechterten. Weiterhin wird die bevorzugte Orientierung der Moleküle im Bezug zur Substratfläche durch die Messungen bestimmt. Zum Schluss wird noch eine Serie dünner PMMA Filme gemessen, die das organische Radikal α,γ-Bisdiphenylen-β-phenylallyl (BDPA) beinhalten. Es ist möglich, Filme mit einer Schichtdicke von nur 10 nm zu messen. Letztendlich wird gezeigt, dass die Kohärenzzeit von BDPA im dünnen Film unabhängig von der Schichtdicke ist. Das ist wichtig, wenn MQBs später als dünner Filme auf elektrisch adressierbaren Chips eingesetzt werden sollen. Mit den Ergebnissen dieses Teils der Arbeit ist es nun möglich, dünnen Filme mit dem weiterentwickelten Spektrometer messen zu können ohne diese von ihrem Trägermaterial entfernen zu müssen. Das ist ein sehr gutes Ergebnis, da selbst bei den wenigen in der Literatur bekannten Untersuchungen die Filme nachträglich zerschnitten werden mussten, um genügend Probe in einem Probenröhrchen zu erhalten.

Das letzte Kapitel der Arbeit behandelt die starke Kopplung eines Spinensembles bestehend aus organischen Radikalen mit dem elektromagnetischen Feld im neu entwickelten Resonator. Ziel dieses Teils ist die Untersuchung, inwieweit MQBs als Quantenspeicher von Informationen einzelner Mikrowellenphotonen genutzt werden können. Das Erreichen der starken Kopplung wird durch eine große Probenmenge und der hohen Feldhomogenität im Resonator ermöglicht. Untersucht wird die Temperaturabhängigkeit der Spin-Feld-Wechselwirkung bei den Radikalen α,γ-Bisdiphenylen-β-phenylallyl (BDPA) und 2,2-Diphenyl-1-picrylhydrazyl (DPPH). Es kann selbst bei Raumtemperatur eine starke Kopplung erreicht werden. Außerdem wird der qualitative Zusammenhang zwischen der Magnetisierung der Radikale im thermischen Gleichgewicht und der Kopplungsstärke aufgedeckt. Ein klarer Zusammenhang zwischen Feldmode im Resonator und Kopplungsstärke wird hergestellt. Die Untersuchungen sind wichtig, da es prinzipiell möglich ist im Bereich der starken Kopplung Quanteninformationen von nur

einem Photon in diesem System zwischenzuspeichern. Dies wird im letzten Teil des dritten Kapitels noch weitergehend untersucht. Dabei wird gezeigt, dass die Phaseninformation von schwachen Mikrowellenpulsen mit einer Effizienz von $\eta = 2 \cdot 10^{-6}$ bei 7 K gespeichert und wieder ausgelesen werden kann. Ermöglicht wird das durch die inhomogene spektrale Verbreiterung der Spinresonanz in den Radikalen. Diese Untersuchungen zeigen eindrücklich das Potential von MQBs als Quantenspeicher. Die erreichte Effizienz ist dabei etwa zwei Größenordnungen kleiner als der aktuelle Stand der Technik, wobei dazu deutlich niedrigere Temperaturen im mK Bereich nötig waren. Eine theoretische Modellierung des Systems deutet darauf hin, dass durch eine Anpassung des Spinsystems eine deutliche Verbesserung der Effizienz um mehrere Größenordnungen zu erwarten ist. Damit wäre es möglich, mit sehr einfachen Mitteln einen Quantenspeicher für einzelne Photonen zu realisieren welches es nun im nächsten Schritt zu verifizieren gilt.

Summary

The results presented in this thesis lay the foundation for control and readout of molecular quantum bits (MQBs) via optical and electrical methods and to use them as a quantum memory for microwave photons. This is important for a future practical implementation of MQBs.

The first chapter of this thesis aims to find an optical active MQB and read out its state with visible/near-infrared light. Extensive spectroscopic studies on the chromium(III) complex $[Cr(ddpd)_2][BF_4]_3$ reveal that the highly luminescent complex is an excellent MQB with a long coherence time. In fact, the measured coherence time of $T_m = 8.4(1)$ µs is the longest one reported for a chromium(III) complex up to now. In the quest for enhancing this property even further, a deuterated variant of this MQB is studied as well. The studies demonstrate that the removal of protons in the environment of the MQB is much more beneficial to its coherence time compared to the cumbersome deuteration of the MQB itself. This is an important finding for future designs of MQBs. The connection between the optical and magnetic properties of the MQB is unraveled by the means of magnetic circular dichroism (MCD) spectroscopy in combination with a theoretical model developed for this complex. Although $[Cr(ddpd)_2][BF_4]_3$ is a very nice MQB with interesting optical properties, a successful attempt of reading out the spin state can not be presented. Neither utilizing its luminescent nor its MCD properties results in a clear measurement of the spin state. Further studies on the optically exited MQB lead to the conclusion that the spin relaxation rates involved in the optical process prevent the optical readout. This leaves an excellent MQB and several staring points which properties are important for an optical readout of a MQB.

The aim of the second chapter is the further development of an existing pulsed electron magnetic resonance (EPR) spectrometer operating at 35 GHz to measure thin films of MQBs. The spectrometer will be used in the future to characterize and control electrical coupled MQBs. Therefore, a Fabry-Pérot type resonator is developed which is especially designed for large flat samples, such as thin films on a substrate. It is thoroughly characterized by means of a vector network analyzer, including measuring the Q-factor and the coupling from the waveguide to the resonator. It turns out that for the mode with the best characteristics for EPR, the resonator is overcoupled with a total

$Q_{\mathrm{L}} = 1100$ leading to short dead time of about 200 ns. Beside the electrical characterization, the magnetic field components of several modes inside the resonator are investigated by an approach combining Rabi nutation measurements and field simulations. Using this resonator, pulsed EPR experiments are successfully carried out on an approximately 60 nm thin film of 20% copper (II) phthalocyanine in pure phthalocyanine. The measurements reveal that the qubit properties of the system do not degrade in the film compared to the corresponding bulk material. Furthermore, it is demonstrated how the preferred alignment of the molecules with respect to the substrate surface can be determined by pulsed EPR. Last but not least, a series of PMMA thin films containing the radical α,γ-Bisdiphenylene-β-phenylallyl (BDPA) are characterized by pulsed EPR utilizing the novel resonator. It is possible to measure a film with a thickness of only 10 nm. Furthermore, the relaxation times of the system do not change significantly in a thickness range of 10 nm to 100 nm compared to the bulk material. This demonstrates the high robustness of MQBs. By the means of the developed resonator, the spectrometer is now capable measuring thin films of MQBs without the need to post process the films like cutting or grinding. This is a very good result as in the few existing publications covering thin films, the film and/or substrate is cut in order to fit into an EPR tube.

In the last chapter, strong coupling of a spin ensemble and microwaves photons is realized utilizing the Fabry-Pérot resonator. The aim of this part is to use MQBs as a quantum memory for the information of single microwave photons. It is possible to achieve strong coupling due to homogeneous field distribution inside the resonator which can accommodate a large sample volume. The temperature dependence of α,γ-Bisdiphenylene-β-phenylallyl (BDPA) and 2,2-Diphenyl-1-picrylhydrazyl (DPPH) is investigated and it turns out that it is possible to maintain the strong coupling condition up to room temperature. Furthermore, the coupling strength is related to the magnetization of the sample in thermal equilibrium, which is affected by the exchange coupling occurring in the two systems. A clear connection between the resonator mode and the coupling strength is revealed. The investigations are very interesting as they demonstrate the possibility to store the quantum information of a single photon in such systems opening up a possible application in photon based quantum computing. This feature is explored in the last part of this chapter, where the storage of photonic excitations is further investigated. It is possible to store and retrieve the phase information from small excitation with an efficiency of $\eta = 2 \cdot 10^{-6}$ at 7 K. The presented efficiency is only two orders of magnitude smaller compared to the current state of the art where mK temperatures are needed in order to store any information at all. A theoretical de-

scription of the model leads to the conclusion that small modifications of the spin system would yield a efficiency several magnitudes larger compared to the presented one. Thus, the system seems to be capable to work as a very simple quantum memory for single photons which should be verified in a next step.

1. Introduction

Over the last three decades, informational technology has revolutionized our way of life. With the birth of the internet, global communication has been become much easier than before. Artificial intelligence have started to take over formerly human tasks. From molecular reactions [1] to the whole universe [2], we are now able to perform numerical simulations on every scale at a very high precision. All of that became possible by the invention of the computer which can perform simple mathematical operations at an unimaginable speed.

For example, consumer electronics like the gaming console Playstation 4 [3] can perform $4.2 \cdot 10^{12}$ floating point operations per second (FLOPS), i.e. the addition or multiplication of two 10-digit numbers. In contrast, the world record for mentally dividing ten 10-digit numbers by 5-digit numbers is 169 seconds [4] comparable with a rate of $6 \cdot 10^{-2}$ FLOPS. Thus, even if every human being on this world would be as fast as the world record holder, this would result in $4.6 \cdot 10^{8}$ FLOPS which means a simple Playstation 4 would still outperform us by a factor of 10000.

However, there are many mathematical problems a computer cannot solve in a reasonable time as they are too complex for the architecture of a classical computer. A prominent example is the prime decomposition of large numbers. Classical computers rely on bits, which are logical states with two possible values. To perform calculations, a computer performs logical operations on a set of bits. This leads to a very limited amount of basic operations a computer can perform.

To overcome this issue, quantum computers have been proposed. They rely on qu(antum)bits which are quantum systems featuring two states. In contrast to classical bits, a superposition of the two states can be prepared. Furthermore, quantum bits can be entangled which means while the state of the entangled bits is well defined, the single bits are not well defined anymore. This architecture leads to algorithms, which can solve problems like prime number decomposition [5], searches in large databases

[6] or solving linear equations [7] much faster than the classical computer. The reason for the speed up is that due to the available basic operations, the complexity of the corresponding algorithm shrinks. From the classical computer point of view, the quantum computer is able to perform several classical basic operations in parallel.

Theoretically, any quantum mechanical two level system can be used as a qubit because the underlying quantum mechanics is always the same. However, practical limitations may lead to a preference for a certain system. For example, qubits interact with their environment which leads to decoherence. This means, the state of the qubit may get lost during a calculation. Furthermore, a suitable physical interaction between qubits is necessary to entangle them. Obviously, manipulation and readout of qubit state must be possible. Last but not least, one or two qubits are not enough to perform any reasonable calculation. Thus, the physical system containing the qubits has to be scalable. The aforementioned considerations are summarized from the DiVincenco criteria [8] which a qubit system has to fulfill in order to be usable for quantum computing.

Many proposals for qubit systems exist, including superconducting circuits [9, 10], photons [11, 12], ultracold atoms [13, 14] and spins [15, 16]. This thesis focuses on the latter, more explicit on molecules with an residual electron spin which are called molecular qubits (MQBs) [17–19]. One of the many reasons speaking for MQBs are that they have very long coherence times, can be tuned by the means of chemical design, are easy to manipulate using microwave radiation and can be positioned relatively with atomic precision [20, 21].

However, there are some shortcomings as well. The most prominent technique for the manipulation of MQBs is pulsed electron paramagnetic resonance. Within this technique, ensembles of MQBs are manipulated by microwave pulses. In the end, it is only possible to detect the whole ensemble rather then the individual MQBs. Unfortunately, the latter is important for the scalability of the system. Furthermore, investigations on MQBs published in literature are mostly exclusively performed on bulk material like powder or solutions due to technical reasons. In any real world application, the MQBs have to be processed as, for example, thin film on a chip in order to interface the qubits for example electrically. Last but not least, high power microwave pulses are usually needed for manipulation and readout. This makes it on the first sight impossible to embed MQBs in a framework where single photons are used for the transfer of quantum information.

This thesis tackles the three mentioned problems in three individual chapters. The first chapter covers investigations on a photoactive chromium(III) complex. Within this chapter, the qubit properties of this compound are elaborated and the possibility of a spin state readout via optical methods is explored. In the second chapter, the development of a novel Fabry-Pérot resonator for pulsed EPR is presented. Using this resonator, investigations on thin films of MQBs are carried out and be discussed. The last chapter demonstrate that it is possible to strongly couple a spin ensemble to the electromagnetic field inside the novel resonator enabling qubit manipulation with single photons.

Preceding to this main part of the thesis, the next section covers the theoretical basics underlying this thesis.

2. Theoretical Background

Without the deep knowledge about how light interacts with matter, scientist would be blind to many aspects of nature. Exploiting this interaction in spectroscopy, chemists can study their compounds on a molecular level [22], physicists discover the composition of atoms [23] and biologists can have a look inside the living human body noninvasive in real time [24].

Thus, it is not a surprise that light-matter interaction is the core of this thesis in order to study qubits down to a quantum level. The chapter starts with the introduction of molecular qubits which are the matter investigated in this thesis. Recent developments and the first steps towards single spin readout are presented.

It follows a theoretical description of the interaction of the spin of MQBs with light. Here, the spins are treated on a quantum mechanical level while the light is described as a classical wave. This description forms the basis of electron paramagnetic resonance (EPR) which is the main method of investigation in this thesis.

The interaction of spins with light depends on the magnetic field of the electromagnetic radiation, thus it is relatively weak. To overcome this issue in EPR, a resonator (sometimes called cavity) is used. Because the design of a resonator for thin film samples is part of this thesis, some basics of resonators will be covered as well.

Last but not least, the description of spin-light interaction will be extended to a full quantum mechanical level, where we will see the emergence of polaritons which are pseudo particles being a mixture between light and matter. The latter is important in this thesis, as spin based polaritons are essentially qubits which can be manipulated on a single photon level.

2.1. Molecular quantum bits

2.1.1. Recent developments

As any other quantum system with defined states, the electron spin can be potentially used as a qubit as long the DiVincenzo criteria can be met [8]. Manipulation of spin based qubits by the means of pulsed EPR will be described in the next section. The important coherence time, e. g. the life time of a superposition state, corresponds to the phase memory time of the spin which will be introduced in the next Section as well.

The term molecular quantum bit (MQB) emerged from the molecular nanomagnet (MNM) community after researchers realized, that the electron spin in a MNM does not only has a potential as high density data storage but can be utilized as qubit as well [18, 25–27]. However, it turned out quickly that the coherence time in MNMs is limited due to the polynuclear nature leading to short spin-lattice relaxation times especially at higher temperatures which ultimately limits the coherence time [28]. In fact, the prominent MNM Cr_7Ni features a measurable coherence time only up to 10 K. It was already realized, that the exchange of protons with deuterons increases the coherence time as a bath of nuclear spins seemed to be the major contributor to decoherence in such systems as long the spin lattice relaxation can be neglect [18, 28, 29].

In order to make MQBs attractive, the research was focused on increasing the coherence time in order to met DiVincennzo's criterion for a reasonable long coherence time, e. g. much longer compared to the time needed for a qubit operation (about 10 ns for electron spin based qubits). The development led to a new generation of MQBs [17, 30] like the mononuclear copper(II) complex $[Cu(mnt)_2]^{2-}$. Due to the mononuclear nature, the spin lattice relaxation time was improved by several orders of magnitude which increased the upper limit of the quantum coherence time. Furthermore, deuteration of the counter ion $[PPh_4]^+$ led to a remarkable coherence time of 68 µs at 7 K which is over one order of magnitude larger compared to MNMs. In fact, even at room temperature the complex features a coherence time of 0.5 µs. Following this design principles, the coherence time in a MQB was increased even further in the virtually nuclear spin free complex $[V(C_8S_8)_3]^{2-}$ [31] to 675 µs.

Thus, it was impressively demonstrated that simple chemical design can massively improve the qubit properties of a MQB, one of the inherent advantage of MQBs compared to other electron spin based qubits.

2.1.2. Comparison of MQBs with solid state qubits

Beside MQBs, there are other hot qubit candidates based on the electron spin. As they are usually based on defects in semiconductor materials, they are called solid state qubits. Prominent examples are phosphorus donors in silicon (P@Si) and nitrogen vacancy centers in diamond (NVC). Both feature enormous long coherence times which can reach several milliseconds by using ^{29}Si [32] respectively ^{13}C enriched [33] host material. Figure 2.1 shows the coherence times of the mentioned solid state qubits compared to the MQBs introduced in the section before. However, a closer look on figure 2.1 reveals that the coherence time of P@Si quickly degrades over temperature compared to MQBs making them only usable at cryogenic temperatures. NVCs on the other hand, can reach millisecond coherence times up to room temperature. However, compared to MQBs NVCs only exist in the host material and can not be isolated. A molecule can exist on its own, especially a charge neutral complex. This leads to an inherent advantage over solid state qubits when it comes to scale up the system. MQBs are thus independent from a host material and can be arranged with atomic precision in two- and three-dimensional arrays [20, 21].

For both introduced solid state qubits robust single spin readout protocols are established. In the case of NVCs, there exists a very elegant optical method using a simple confocal microscope to read out single centers [34]. The spin state of a single phosphorus donor in silicon can be read electrically by utilizing a spin to charge conversion [35, 36]. On the other hand, single spin readout for MQBs is not studied in such detail.

2.1.3. Single spin readout of MQBs

Only few single spin readout experiments on molecules are published in literature. Usually, the spin is detected indirectly either using light (optical readout) or spin state dependent conductance (electrical readout).

Optical readout

Single spin readout of a single pentacene molecule in a p-terphenyl crystal with optical light was already demonstrated 1993 [37]. In a nutshell, a single diamagnetic pentacene molecule was exited with a green laser and its emission was monitored. Occasionally, the system enters a non degenerated triplet state where the molecule is essentially dark. The triplet life time depends on the spin state. Thus, the spin state can be indirectly

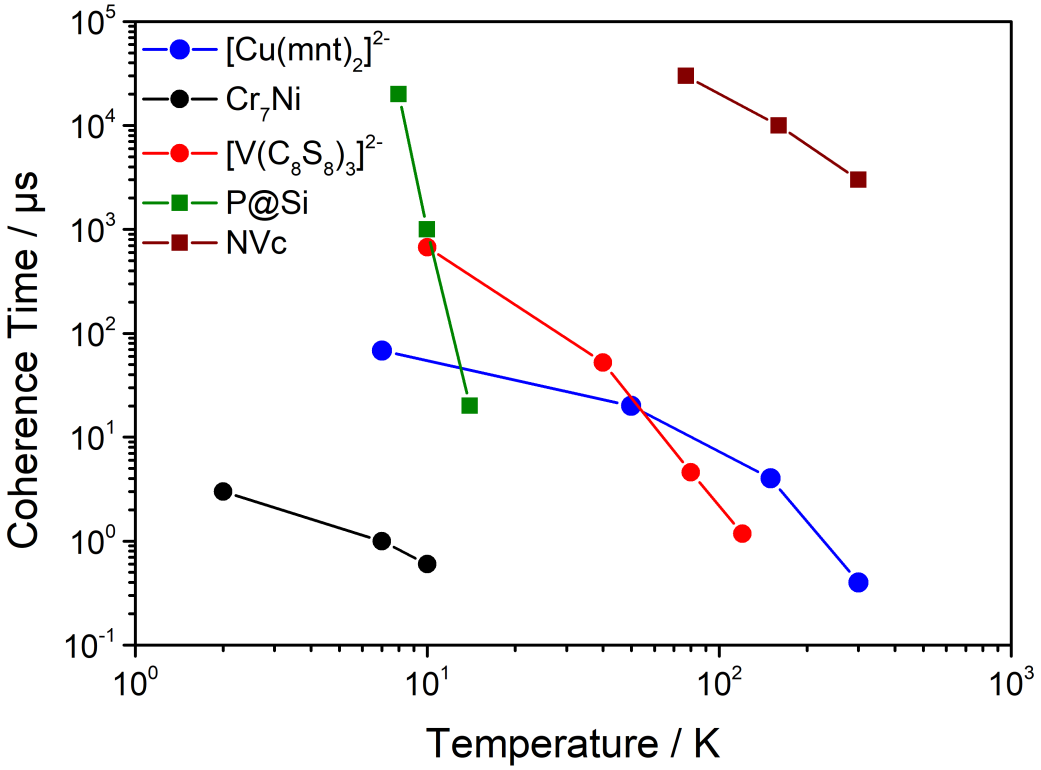

Figure 2.1.: Coherence times of the MQBs $[Cu(mnt)_2]^{2-}$ (blue circles and line [17]), Cr_7Ni (black circles and line [28]), $[V(C_8S_8)_3]^{2-}$ (red circles and line [31]) and the solid state qubits phosphourous in silicon (P@Si, dark green squares and line [32]) and nitrogen vacancy centers in diamond (NVC, dark red squares and line [33]) with respect to temperature.

measured by monitoring the emission intensity. Although the results are impressive, the pentacene molecule has no spin in its ground state, only in its excited triplet state. With regards to use such a system as a qubit, this would complicate the initialization procedure of the qubit.

To overcome this issue, nickle, vanadium, cobalt and chromium based MQBs were proposed as optically addressable candidates [38]. And in fact, in a very recent publication [39] the optical readout of the spin state in the electrical ground state of an ensemble of chromium (IV) MQBs was demonstrated. In a nutshell, a spin forbidden transition from the ground state with $S = 1$ to the electronically excite state with $S = 0$ is excited using light in the NIR region. Afterwards, photoluminescence from the transition back to the ground state is measured. As the transition from the $m_s = 0$ state yields a higher photoluminescence intensity, the spin state can be indirectly measured. Although the demonstrated method is not sensitive enough for a single spin readout yet, it demonstrates how flexible MQBs are.

Electrical readout

In an outstanding experiment [40] it was demonstrated, that it is possible to read out the spin state of a single terbium(III)bis(pthalocyaninato) ($TbPC_2$) molecule by measuring its conductance. Briefly, the molecule was deposited on a gold nanowire which was broken by applying a voltage ramp. A single $TbPc_2$ molecule enters the junction due to electromigration. The Pc ligand act as a quantum dot which is exchanged coupled with the nearby terbium ion. Changing the spin state of the terbium alters the differential conductance through the quantum dot making it possible to indirectly measure the spin state.

However, the described device is by far not easy to manufacture. Basically, many devices have to be prepared and measured to find a broke wire with a single molecule in the junction. Furthermore, the device only survives at mK temperatures. In order to provide an universal electrical access to MQBs, conducting polymers have been proposed to work as an interface between current and MQBs [41]. The idea is to exploit the interaction between spin polarized currents with the spin of the MQB. Within this concept, the polymer containing the MQBs is then processed as a thin film on an readout device. One aim of this thesis is to provide a method to characterize such films with pulsed EPR which will be discussed in chapter 4.

2.2. Electron paramagnetic resonance

The following section about EPR bases on the *Principles of Pulse Electron Paramagnetic Resonance* [42], a comprehensive book covering many facets of EPR.

2.2.1. Quantum mechanical description of the electron spin

The electron spin is an intrinsic property of the electron. It can be described by a quantum mechanical angular momentum represented by the spin operator $\vec{s}^T = \begin{pmatrix} \hat{s}_x & \hat{s}_y & \hat{s}_z \end{pmatrix}$ and characterized by the two quantum numbers $s = 1/2$ and $m_s = \pm 1/2$. This momentum is connected to an inherent spin magnetic moment of the electron $\vec{\mu}_{s,e} = -g_e \mu_\mathrm{B} \vec{s}/\hbar$ with the Bohr magneton μ_B, the reduced Plank constant $\hbar$ and the $g_e \approx 2$ factor arising from relativistic effects.

In molecules, a resulting spin exists in radicals or transition metal ions where the outer electrons are not fully paired. As there might be more than one unpaired electron in a molecule, the residual spin corresponds to the vector sum of single electron spins and will be described by an operator $\vec{S} = \sum_i^N \vec{s}_i/\hbar$ (division by $\hbar$ is introduced to keep the following equations more simple). Furthermore, the g_e factor is replaced by a symmetric tensor $\mathbf{g}$ as spin orbit interactions in molecules leads to an anisotropic behavior of the resulting magnetic moment with respect to the molecular frame. Through the rest of this thesis, the term spin magnetic moment will always correspond to the molecular spin magnetic moment $\vec{\mu}_S = -\mathbf{g}\mu_\mathrm{B}\vec{S}$.

The magnetic moment may interact with magnetic fields that can be described by a spin Hamiltonian $\mathscr{H}_{S,\mathrm{tot}}$. In the following, interactions with an applied static field, external fields originating from nuclear spins, internal fields from the unpaired electrons in the molecule and external fields from nearby molecular spins lead to a total spin Hamiltonian

$$\mathscr{H}_{S,\mathrm{tot}} = \mathscr{H}_\mathrm{Zeeman} + \mathscr{H}_\mathrm{HF} + \mathscr{H}_\mathrm{ZFS} + \mathscr{H}_\mathrm{EE} \tag{2.1}$$

Zeeman interaction $\mathscr{H}_\mathrm{Zeeman}$

The interaction of the spin magnetic moment with an applied external magnetic field $\vec{B}_0$ is called Zeeman interaction and can be described as a simple scalar product between the field and moment.

$$\mathscr{H}_{\text{Zeeman}} = -\vec{B}_0^T \vec{\mu}_S = \mu_{\text{B}} \vec{B}_0^T \mathbf{g} \vec{S} \tag{2.2}$$

The convention is that $\vec{B}_0$ is applied along the z-direction $\vec{B}_0^T = \begin{pmatrix} 0 & 0 & B_z \end{pmatrix}$ in the external/laboratory frame. As mentioned before, $\mathbf{g}$ is a symmetric tensor which can always be diagonalized. If the z-axis of the eigenframe of $\mathbf{g}$ coincides with the laboratory frame eq. 2.2 can be rewritten to

$$\begin{aligned} \mathscr{H}_{\text{Zeeman}} &= \mu_{\text{B}} \begin{pmatrix} 0 & 0 & B_z \end{pmatrix} \begin{pmatrix} g_{xx} & 0 & 0 \\ 0 & g_{yy} & 0 \\ 0 & 0 & g_{zz} \end{pmatrix} \begin{pmatrix} \hat{S}_x \\ \hat{S}_y \\ \hat{S}_z \end{pmatrix} \\ &= \mu_{\text{B}} B_0 g_{zz} \hat{S}_z \end{aligned} \tag{2.3}$$

A similar result may be obtained if $\mathbf{g}$ is isotropic by replacing g_{zz} in eq. 2.3 with the isotropic factor g. In the case above, the eigenstates of $\mathscr{H}_{\text{Zeeman}}$ correspond to the eigenstates of $\hat{S}_z$ which are characterized by the quantum number M_S. For a simple $S = 1/2$ systems this leads to the eigenstates $|\pm 1/2\rangle$ which are often depicted as $|+1/2\rangle \equiv |\uparrow\rangle$ and $|-1/2\rangle \equiv |\downarrow\rangle$.

In nearly every experiment presented here, the Zeeman interaction is the strongest interaction. In that case, it is usual to describe the eigenstates of the total spin Hamiltonian as a linear combination of the $\hat{S}_z$ eigenstates.

Hyperfine interaction $\mathscr{H}_{\text{HF}}$

In molecules it is nearly inevitable that nuclear spins (represented by the spin operator $\vec{I}$) are present in the vicinity of the electron spin. The magnetic moments of these nuclear spins produce a field which interacts with the electron spin. Usually, these interactions are described by the Hamiltonian

$$\mathscr{H}_{\text{HF}} = \sum_i \vec{S}^T \mathbf{A}_i \vec{I}_i \tag{2.4}$$

where $\mathbf{A}$ is a symmetric tensor for every case in this thesis which can be written as $\mathbf{A} = \alpha_{\text{iso}} \mathbf{1} + \mathbf{A}_{\text{aniso}}$. The isotropic part characterized by the scalar α_{iso} originates from the finite electron probability density of the spin bearing electron at the nucleus of interest. For transition metal ions α_{iso}/h lies in the order of 100 MHz. The anisotropic part $\mathbf{A}_{\text{aniso}}$

can be described by a simple dipolar interaction in most cases. It is usually a very weak interaction in the order of kHz to a few MHz. However, as there are often hundreds of nuclear spins in the vicinity of an electron spin, this interaction has a great effect on spin dynamics as we will see later on.

Zero field splitting $\mathscr{H}_{\mathrm{ZFS}}$

As already mentioned, the residual spin in molecules may originate from more than one unpaired electron for example in transition metal complexes. The spins of the single electrons can interact with each other by dipolar interactions or interact with the orbital momenta by the means of spin-orbit coupling (SOC). A prominent example would be Cr^{3+} in a metal complex. Here, the presence of three unpaired electrons leads to $S = 3/2$. Usually, the corresponding M_S states would be degenerate in the absence of an external field. However, the aforementioned interactions lead to the zero field splitting (ZFS) term

$$\mathscr{H}_{\mathrm{ZFS}} = \vec{S}\mathbf{D}\vec{S} \tag{2.5}$$

where **D** is a traceless symmetric tensor. Usually (in case of a diagonalized **D**), eq. 2.5 is written as

$$\begin{aligned}\mathscr{H}_{\mathrm{ZFS}} &= D_{xx}\hat{S}_x^2 + D_{yy}\hat{S}_y^2 + D_{zz}\hat{S}_z^2 \\ &= D\left[\hat{S}_z^2 - \frac{1}{3}S(S+1)\right] + E(\hat{S}_x^2 + \hat{S}_y^2)\end{aligned} \tag{2.6}$$

with $D = 3D_{zz}/2$ and $E = (D_{xx} - Dyy/2)$. In the above mentioned example with $S = 3/2$, a negative D and $E = 0$ lead to a twofold degenerate ground state with the eigenstates $|\pm 3/2\rangle$ and a twofold exited state $|\pm 1/2\rangle$. In the case of a low symmetry Cr^{3+} complex $E \neq 0$ is expected. This term leads to a mixing between the two doublets and thus the eigenstates have to be described as linear combinations of the M_S states.

Electron-electron interaction $\mathscr{H}_{\mathrm{EE}}$

In the preceding section, the interaction between electron spins was described by the ZFS Hamiltonian. There, the vector sum of the single electron spins was performed and the resulting M_S levels of the combined spin are split due to the interactions. This description is used, if the electrons resides on the same center like a transition metal in a complex. However, there are molecules featuring several spin centers which can interact. Furthermore, due to close packing of organic radicals in their corresponding crystal structure, electron spins of different molecules interact as well. This interaction between spin centers is described by the electron-electron interaction term

$$\mathscr{H}_{\mathrm{EE}} = \sum_{j>i} \vec{S}_i^T \mathbf{J} \vec{S}_j \tag{2.7}$$

The interaction tensor **J** depends on the type of interaction. For example, dipolar interaction leads to an anisotropic symmetric **J** tensor. Exchange interaction on the other hand can lead to an isotropic **J** tensor but also to an anisotropic asymmetric tensor. In this thesis, only isotropic exchange between two neighboring spin centers plays a role which leads to the Hamiltonian

$$\mathscr{H}_{\mathrm{EE}} = \vec{S}_1^T \begin{pmatrix} J_{\mathrm{iso}} & 0 & 0 \\ 0 & J_{\mathrm{iso}} & 0 \\ 0 & 0 & J_{\mathrm{iso}} \end{pmatrix} \vec{S}_2 \tag{2.8}$$

$$= J_{\mathrm{iso}}(\hat{S}_{x,1}\hat{S}_{x,2} + \hat{S}_{y,1}\hat{S}_{y,2} + \hat{S}_{z,1}\hat{S}_{z,2}) \tag{2.9}$$

In literature, different conventions for J_{iso} exist. The most important ones are $J_{\mathrm{iso}} = J$, $J_{\mathrm{iso}} = -J$ and $J_{\mathrm{iso}} = -2J$.

2.2.2. Electron paramagnetic resonance spectroscopy

Now that the spin system of a molecule is properly defined by a spin Hamiltonian $\mathscr{H}_{S,\mathrm{tot}}$, the question arises how to obtain numbers for all the different tensors and why are they so interesting. To give a short answer to the latter, some examples are presented. The **g** anisotropy of a copper molecule will be used in this thesis to understand its interaction with a surface. **A** can give insights on how a ligand coordinates with a transition metal.

D reveals more information about spin-orbit coupling in a complex which can help to understand the photo-physics of a molecule. Last but not least, **J** yields information on the distance between molecules and is responsible for the existence of permanent magnets.

In order to determine the spin Hamiltonian, EPR spectroscopy is a valuable tool. Within this method, the spin system interacts with the magnetic field of electromagnetic radiation. The radiation induces transitions between the eigenstates of the spin system. During this process, photons are absorbed which can be measured. In the following, a few, simple examples about how the spin Hamiltonian influences the EPR spectrum are given.

Example with Zeeman interaction only

A simple example would be a system only featuring isotropic Zeeman interaction with an external static magnetic field:

$$\mathscr{H}_{\text{Zeeman}} = \mu_{\text{B}} B_0 g \hat{S}_z \tag{2.10}$$

The eigenvalues of this system are

$$E(M_S) = M_S \mu_{\text{B}} B_0 g \tag{2.11}$$

The selection rules for the absorption of one photon is $\Delta M_S = \pm 1$ (conservation of angular momentum). Furthermore, the energy of the photon $E = h\nu$ is required to be equal to the energy difference ΔE of the involved eigenstates. Combining both requirements, the resonance condition

$$h\nu = \Delta E \tag{2.12}$$

$$= \Delta M_s \mu_{\text{B}} B_0 g = \mu_{\text{B}} B_0 g \tag{2.13}$$

can be formulated. In EPR spectroscopy, the frequency ν of radiation is usually kept fixed and the static magnetic field is swept. If the resonance condition is met, radiation will be absorbed which can be measured by a detector. From the resonance field it is possible to calculate g.

Example with Zeeman and hyperfine interaction

Hyperfine interaction usually leads to a splitting of the resonance line, as it leads to additional states with shifted energies depending on the orientation of the nuclear spin. Adding an isotropic hyperfine interaction of a single nuclear spin to the example before leads to the Hamiltonian

$$\mathscr{H}_{\text{Zeeman}} + \mathscr{H}_{\text{HF}} = \mu_{\text{B}} B_0 g \hat{S}_z + \alpha_{\text{iso}} (\hat{S}_x \hat{I}_x + \hat{S}_y \hat{I}_y + \hat{S}_z \hat{I}_z) \tag{2.14}$$

where $\alpha_{\text{iso}}(\hat{S}_x \hat{I}_x + \hat{S}_y \hat{I}_y)$ can be omitted in the high field limit ($\mu_{\text{B}} B_0 g \gg \alpha_{\text{iso}}$). The corresponding eigenvalues are

$$E(M_S, M_I) = M_S \mu_{\text{B}} B_0 g + M_s M_I \alpha_{\text{iso}} \tag{2.15}$$

The selection rules for allowed transitions are $\Delta M_S = 1$ and $\Delta M_I = 0$ as conservation of angular momentum allows only one spin flip per absorption of a photon. In the case of a nuclear spin with $I = 1/2$, following transitions are allowed

$$\Delta E(M_I = -1/2) = \mu_{\text{B}} B_0 g - (1/2)\alpha_{\text{iso}} \tag{2.16}$$

$$\Delta E(M_I = +1/2) = \mu_{\text{B}} B_0 g + (1/2)\alpha_{\text{iso}} \tag{2.17}$$

Compared to case without hyperfine interaction, the resonance line is split symmetrically by α_{iso} into two resonance lines.

Example with Zeeman and ZFS interaction

Last but not least, the effect of ZFS on the EPR spectrum will be discussed. Considering a system featuring ZFS with arbitrary D while $E = 0$ and including Zeeman interaction, following Hamiltonian can be formulated (the constant shift of the ZFS Hamiltonian is omitted)

$$\mathscr{H}_{\text{Zeeman}} + \mathscr{H}_{\text{ZFS}} = D S_z^2 + \mu_{\text{B}} B_0 g \hat{S}_z \tag{2.18}$$

The eigenvalues for this systems are

$$E(M_S) = M_S^2 D + M_S \mu_{\text{B}} B_0 g \tag{2.19}$$

In the case of $S = 3/2$ with $M_S = \pm 3/2, \pm 1/2$ this would lead to the eigenvalues

$$E(-3/2) = 9/4D - 3/2\mu_B B_0 g \tag{2.20}$$
$$E(-1/2) = 1/4D - 1/2\mu_B B_0 g \tag{2.21}$$
$$E(+1/2) = 1/4D + 1/2\mu_B B_0 g \tag{2.22}$$
$$E(+3/2) = 9/4D + 3/2\mu_B B_0 g \tag{2.23}$$

Keeping the selection rule $\Delta M_S = 1$ in mind, this leads to three different resonance conditions

$$\Delta E(-1/2 \rightarrow -3/2) = 2D - \mu_B B_0 g \tag{2.24}$$
$$\Delta E(+1/2 \rightarrow +3/2) = 2D + \mu_B B_0 g \tag{2.25}$$
$$\Delta E(-1/2 \rightarrow +1/2) = \mu_B B_0 g \tag{2.26}$$
$$\tag{2.27}$$

in the case of $D > 0$ and $2D > \mu_B B_0 g$. Thus, a resonance may be observed even in absence of a applied magnetic field if the frequency of radiation ν fulfills the condition $h\nu = 2D$.

Considering the high field limit ($\mu_B B_0 g \gg 2D$), the conditions changes slightly to

$$\Delta E(-3/2 \rightarrow -1/2) = \mu_B B_0 g - 2D \tag{2.28}$$
$$\Delta E(+1/2 \rightarrow +3/2) = \mu_B B_0 g + 2D \tag{2.29}$$
$$\Delta E(-1/2 \rightarrow +1/2) = \mu_B B_0 g \tag{2.30}$$
$$\tag{2.31}$$

Thus, three resonance lines in an EPR spectrum are expected again but the energetic order of the eigenstates changed. It has to be noted that the transition inside the $|\pm 1/2\rangle$ doublet is not affected by D. Typically, in a sample with many molecules D has a significant variance as very small geometrical changes lead to a measurable change in D. This is leading to a broadening of the resonance lines for the transitions between the two doublets. In the end, the resulting spectrum will feature one sharp transition covered by two flanks.

Simulation of complicated spin systems

Up to now, the spectra of the examples above are easy to interpret and the involved parameters could be extracted without any problem. Unfortunately, tensors are usually not isotropic. Furthermore, a molecule may feature anisotropic Zeeman interaction, hyperfine interaction with many nuclei and ZFS at the same time. The tensors involved are usually not collinear (especially **A** with respect to **g** and **D**). In addition, the tensors of molecules with non negligible spin orbit coupling are very sensitive to small geometrical perturbations which are inevitable if the sample is prepared for example in a frozen solution. This leads to a broadening of the resonance lines and complicates the interpretation of spectra even further. Luckily, the software *Easyspin* [43] was developed which allows the simulation and interpretation of EPR spectra including all the aforementioned particularities. Thus, any spin Hamiltonian parameters obtained in this thesis were extracted by fitting the spectra with this powerful tool.

Continuous wave EPR spectroscopy

The typical way to perform EPR experiments is called continuous wave (CW) EPR spectroscopy. Within this method, the sample is continuously irradiated with microwaves (typically 9.4 GHz or 35 GHz) and the magnetic field is swept. If the resonance condition is met, microwave energy will be absorbed which can be measured. As the interaction of the magnetic field of the microwaves with the sample is very weak, several methods are employed to increase the signal strength. First, the sample is placed inside a microwave resonator which enhances the microwave magnetic field and thus the interaction with the sample. Second, the static magnetic field is modulated. Third, the impedance of the microwave resonator is matched to an external microwave source. If the resonance condition is reached, the impedance of the resonator changes and thus microwaves will be reflected to the detector. The detector signal is demodulated at the field modulation frequency to further enhance the signal. As a result, the first derivative of the spectrum is obtained.

CW-EPR is a great tool in order to understand the spin Hamiltonian of a system. However, it does not tell us much about the spin dynamics of a system. Therefore, pulsed EPR is the method of choice which will be covered in the next section.

2.2.3. Pulsed electron paramagnetic resonance spectroscopy

Pulsed EPR is the most used technique in this thesis as it is one of the very few methods to actually manipulate and read out molecular qubits. Usually, it is introduced by summing up the magnetic moments of the single spins occurring in the sample to form a total magnetization which is manipulated by the electromagnetic field. In order to understand the qubit nature of spins a little bit better, pulsed EPR will be introduced here in a more quantum mechanical way.

Time dependent interaction between spins and microwave radiation

In a typical pulsed EPR system, an static magnetic field is applied to the spin system which is then irradiated with short and strong microwave pulse where the magnetic field component of the radiation is perpendicular to the applied static field. This can be summarized in the field vector $\vec{B}(t) = \begin{pmatrix} B_1 \sin(\omega t) & B_1 \cos(\omega t) & B_0 \end{pmatrix}$ where B_1 is the magnetic field strength and ω the frequency of the microwave radiation.

Considering only Zeeman interaction, the Hamiltonian

$$\mathscr{H} = \mu_B B_0 g \hat{S}_z + \mu_B B_1 g(\cos(\omega t)\hat{S}_x + \sin(\omega t)\hat{S}_y) \tag{2.32}$$

can be formulated. For a simple $S = 1/2$ system, following experiment would be feasible. First, no microwave is applied to the spin system thus $B_1 = 0$. Due to the static applied field, in thermal equilibrium the spin would reside in one of its eigenstates $|\pm 1/2\rangle$ with a higher probability for $|-1/2\rangle$ as it has the lower energy. Now, the electromagnetic field is switched on. A spin in the formerly $|-1/2\rangle$ state now starts to evolve under the Hamiltonian given in eq. 2.32 according to the Schrödinger equation. The time development of the state can be calculated analytically [44] however the derivation is quite lengthy. Briefly, the time dependence of the Hamiltonian is eliminated by transforming the coordinate system into a frame rotating with ω. Afterwards, the time dependent Schrödinger equation is solved. If the resonance condition $\omega = \mu_B B_0 g/\hbar$ is met, the time evolution in the rotating frame can be described with the time dependent state $|\phi(t)\rangle$

$$|\phi(t)\rangle = \cos(\frac{1}{2}\omega_1 t)\,|-\frac{1}{2}\rangle + i\sin(\frac{1}{2}\omega_1 t)\,|+\frac{1}{2}\rangle \tag{2.33}$$

with $\omega_1 = \mu_B B_1 g/\hbar$ as long as the microwave is switched on. The microwave radiation may be turn off after the time $t_{90} = \frac{\pi}{2\omega_1}$, in pulsed EPR terminology this is called a $\pi/2$ pulse. The resulting state would be then $|\phi(t_{90})\rangle = \frac{1}{\sqrt{2}}\left[|-\frac{1}{2}\rangle + i|+\frac{1}{2}\rangle\right]$. The result is important as we now have prepared the system in a coherent superposition of two eigenstates which is the fundamental feature of a qubit. Furthermore, $|\phi(t_{90})\rangle$ is a eigenstate of the $\hat{S}_y$ operator. Thus, a magnetization perpendicular to the applied field would be now measurable. It has to be noted that $|\phi(t_{90})\rangle$ is still described in a frame rotating with ω. In the static laboratory frame, the state rotates around the z-axis meaning that magnetization is rotating in the xy-plane as well.

Spin-echo

In a real pulsed EPR experiment, many spins are excited simultaneously. Thus, a sum of magnetic moments will be measured. However, each individual spin may have a slightly different resonance frequency due to inhomogenieties in the static magnetic field or distribution in the g factor. However, they can be still excited together if a short microwave pulse with a large bandwidth is employed. In any case, after excitation, the spins start to dephase as they rotate with different frequencies in the static frame. This means that the xy-magnetization quickly decays (the phenomena is called free induction decay FID) and eventually can not be measured anymore. To overcome this issue, a spin echo experiment can be employed. Within this experiment, a $\pi/2$-pulse rotates the all magnetization vectors for example around the x-axis onto the y- axis. For a time τ the system may dephase in the xy-plane. A π pulse is employed which rotates all magnetization vectors by 180° around the x-axis. As the spins will maintain their sense of rotation, after the total time 2τ all magnetization vectors will align on the y-axis again. The whole pulse sequence can be summarized using the following notation

$$\pi/2 - \tau - \pi - \text{echo} \tag{2.34}$$

Up to now, losses have been neglected regarding the spin dynamics. This would mean that after a $\pi/2$ pulse the spins will remain in their coherent superposition or we could bring a spin from $|-1/2\rangle$ to the energetically higher $|+1/2\rangle$ state where it would stay forever. Although this would be perfect for quantum computing, this is not the case for any real world system as the spins will always couple to the environment finally bringing the spin back to its thermal equilibrium.

Spin-lattice relaxation T_1

Spin-lattice relaxation ultimately limits the timescale on which a pulsed EPR experiment may be conducted. In a nutshell, it describes the relaxation of the spin system back to its thermal equilibrium. It is called spin-lattice relaxation as the energy stored inside the spin system is released to the lattice in the form of lattice vibrations (phonons). Spin-lattice relaxation can be observed, e.g., with the inversion recovery experiment. Here, the magnetization of the spins is inverted by the means of a π pulse. After a time T, a spin echo sequence is performed. As the magnetization is inverted, the phase of the spin echo is inverted as well compared to a spin echo starting from thermal equilibrium. Thus, the intensity of the echo is observed for different time T until it reaches the intensity A_{eq} of the spin system in thermal equilibrium. To recapitulate, the shorthand notation for the inversion recovery is

$$\pi - T - \pi/2 - \tau - \pi - \tau - \mathrm{echo} \tag{2.35}$$

Usually, the intensity of the echo with respect to T can be fitted with an exponential decay

$$A_{eq}(1 - 2\exp(-T/T_1)) \tag{2.36}$$

The constant T_1 is called spin lattice relaxation time or longitudinal relaxation time. It is very temperature dependent as the number of excited phonons depends on temperature. The exact temperature dependency of T_1 depends on the interaction mechanism between spins and phonons. In the literature, three main mechanism are frequently discussed. First one is the *direct* process, here the spin system deexcites by emitting a phonon with the energy $\mu_{\mathrm{B}} B_0 g$. For the direct process, a temperature scaling law $1/T_1 \propto T$ can be formulated. In most cases, this process is only relevant at temperatures below 4.2 K. At higher temperatures, phonon scattering processes like the *Raman* (scattering involves a virtual energy level) or *Orbach* (scattering involves a real energy level) processes are more efficient. The scaling laws are $1/T_1 \propto T^{-9}$ or $1/T_1 \propto T^{-7}$ in case of a *Raman* process depending on whether the spin system has a half-integer or integer spin. In case of the *Orbach* process, the scaling law is $1/T_1 \propto (\exp(-\Delta/k_{\mathrm{B}}T) - 1)$ where Δ is the energy difference between the ground and excited state. It has to be noted that these scaling laws are derived for ionic single crystal systems. For example, molecular vibrations are not included in the aforementioned processes. However, very recent publications [45, 46] show that they play a significant role in molecular systems. As a result, in many older publications the temperature dependency of T_1 in molecular

systems is fitted with an arbitrary polynomial which cannot be related directly to real physical processes. Thus, any discussion about the temperature dependency in this thesis will focus more on the aspect whether the system could be a usable qubit at higher temperatures.

Phase memory time T_m

T_1 tells us how long we could save a classical bit of information in the spin system. However, one main difference of a bit compared to a qubit is that the latter can be prepared in a coherent superposition of two states, just like the electron spin shown before. In pulsed EPR experiments, coherence always leads to a measurable magnetization in the *xy*-plane. Thus, the decay of the in-plane magnetization called T_2 may be used as a measure for the qubit's coherence time. However, we already seen that different resonance frequencies of the individual spins lead to a decay as the spins dephases. It is still possible to bring them back into phase with the spin echo experiment. This means that the individual spins are still in a coherent superposition. Thus, the time T_m (phase memory time) will be used as a measure of the qubit coherence time. It is measured by performing the spin echo experiment described in 2.34 at different τs. The echo intensity with respect to τ can usually be fitted with an exponential decay

$$A_0 \exp(-2\tau/T_m) \tag{2.37}$$

from which T_m can be extracted. The main contributor to T_m in molecular systems is spin diffusion [17, 19]. In a nutshell, coherence is irreversibly transferred to neighboring electron spins (spin-spin diffusion) or nuclear spins (nuclear spin diffusion). Both processes depend on the dipolar coupling of the spin of interest with the spins in the vicinity. Thus, it is possible to suppress spin-spin diffusion by simply diluting the investigated system in some diamagnetic matrix like a solvent. Nuclear spin diffusion on the other hand is much harder to avoid. A prominent example is to remove protons from the environment by deuterating the matrix [17]. Deuterium still has a nuclear spin, but its magnetic moment and thus its dipolar interaction is three times weaker.

Nuclear spin diffusion is an *irreversible* transfer of coherence to a bath of nuclear spins in the environment. However, in pulsed EPR it is possible to observe a *reversible* transfer of coherence to hyperfine coupled nuclei inside the molecule.

Electron spin echo envelope modulation

The echo intensity in a simple spin echo decay experiment usually decreases exponentially with respect to the time delay τ. However, in some cases, this decay is superimposed by several oscillations. They occur, if the electron spin is coupled to one or more nuclei via anisotropic hyperfine interactions $\mathbf{A}$. Considering a spin system with $S = 1/2$ and $I = 1/2$, the observable frequencies are

$$\omega_\alpha = \sqrt{(\omega_I + A/2)^2 + \frac{B^2}{4}} \tag{2.38}$$

$$\omega_\beta = \sqrt{(\omega_I - A/2)^2 + \frac{B^2}{4}} \tag{2.39}$$

$$\omega_+ = \omega_\alpha + \omega_\beta \tag{2.40}$$

$$\omega_- = \omega_\alpha - \omega_\beta \tag{2.41}$$

with $A = A_{zz}$, $B = \sqrt{A_{zx}^2 + A_{zy}^2}$ and $\omega_I = \mu_\mathrm{B} B_0 g_N/\hbar$ being the Larmor frequency of the nuclear spin. The modulation depth $k = \left(\frac{\omega_I B}{\omega_\alpha \omega_\beta}\right)^2$ depends on the anisotropy of the hyperfine interaction and the direction of the static magnetic field as $B = 0$ if the field is applied along one of the principal axes of the $\mathbf{A}$ tensor. In order to understand the effect a little bit, a short qualitative explanation for the phenomenon is given.

We assume a static magnetic field along the z-direction resulting in a Zeeman interaction being much stronger than any other interaction. Then, the system can be described very well in the product basis of $\hat{S}_z$ and $\hat{I}_z$ operators leading to the states $|M_S, M_I\rangle$. Allowed transitions require $\Delta M_S = 1$, thus a $\pi/2$ pulse can create coherence between the $|-1/2,-1/2\rangle$ and $|+1/2,-1/2\rangle$ or $|-1/2,+1/2\rangle$ and $|+1/2,+1/2\rangle$ states. However, an anisotropic $\mathbf{A}$ enables a microwave pulse to flip the nuclear spin as well. The reason for this is that due to the anisotropy the nuclear spin experiences an effective field from electron spin with an direction slightly tilted from the original z-axis. As the spin is manipulated by the microwave pulse, this transverse field component leads to a nuclear spin flip.

As a result, a $\pi/2$ pulse will not only generate coherence on the two allowed transitions but on the two forbidden ones ($\Delta M_S = 1, \Delta M_I = 1$) as long as the bandwidth of the pulse is large enough. As the transitions have different resonance frequencies, the rotation of the four coherences in the xy-plane differs as well. Thus, a beating of the four transitions would be observable in the FID. One may think that a π pulse would lead to an refocusing of the FID. However, coherence created by the $\pi/2$ on one transition

will be distributed again to all four transitions during the π pulse. This means that only a part of the originally created coherence will be refocused again. The distributed part of it may refocus depending on the rotation frequency of the other transitions and time delay τ.

In the end, this leads to a oscillation in the spin echo decay where the frequencies of oscillation are given in 2.38-2.41. Of course, things are getting more complicated for spin systems with more then one nuclear spin. Furthermore, the nuclear spin may be affected by quadrupolar splitting as well. More advanced correlation pulse sequences are available to simplify things somewhat, but in the end a lot of experience is needed in order to fully understand nuclear modulations in EPR experiments.

2.3. Microwave resonators

All pulsed EPR experiments require pulses with a specific rotation angle $\beta = \omega_1 t$ with $\omega_1 = \mu_B B_1 g/\hbar$. Often it is desirable to keep t very short because of two reasons. First, any relaxation during the pulses is unwanted. Second, a short t leads to a larger bandwidth of the excitation pulse and thus a stronger signal. Typical pulse lengths are on the order of tens of ns. In order to achieve a rotation angle of $\pi/2$ in 20 ns, a field of approximately 0.4 mT is needed. The pulsed EPR spectrometer used in this thesis operates at 35 GHz. The average magnetic field of 35 GHz microwave radiation in the employed WR28 waveguide is around $0.01\frac{\mathrm{mT}}{\sqrt{\mathrm{W}}}$. Thus, a microwave power of 1.6 kW is needed in order achieve the desired angle of rotation. Therefore, the spectrometer would need many high power components which are very expensive. To overcome this issue, a resonator can be used which confines the microwave radiation in space. As the development of a new microwave resonator is part of this thesis, the next section will cover some basics of 3D microwave resonators.

2.3.1. Resonator basics

A 3D microwave resonator can be generally described as a cavity enclosed by metal walls filled with a dielectric material. The geometry of the cavity has to fulfill certain conditions such as that a standing wave of microwave radiation of a specific frequency may build up inside.

To keep it simple, a theoretical resonator which can be explained with simple plane waves is discussed from which the basic rules may be transferred to practical 3D resonators. It is described by two infinite large conducting walls which are spaced by a distance d. The walls are parallel to the xy-plane. Maxwell's equations lead to several boundary conditions for the electromagnetic field in such a system. First, the functions describing $\vec{\mathbf{E}}(\vec{r},t)$ and $\vec{\mathbf{B}}(\vec{r},t)$ have to fulfill the wave equation. Second, at the plane surfaces, the components of the electric field vector $\vec{\mathbf{E}}(\vec{r},t)$ tangential to the walls have to vanish. The same is true for the magnetic field component of the magnetic field vector $\vec{\mathbf{B}}(\vec{r},t)$ normal to the wall. The solution of the wave equation considering these boundary conditions is

$$\vec{\mathbf{E}}(t,z) = \mathscr{E}_0 \sin\left(\frac{2\pi z}{\lambda}\right)\sin(\omega t)\vec{x} \tag{2.42}$$

$$\vec{\mathbf{B}}(t,z) = B_0 \cos\left(\frac{2\pi z}{\lambda}\right)\cos(\omega t)\vec{y} \tag{2.43}$$

with the angular frequency $\omega = 2\pi f$. The a spacing $d = (n+1)\frac{\lambda}{2}$ between the two walls is an integer multiple n of half the wavelength λ. This solutions describe a standing plane wave with a plane normal in z direction which oscillates at the frequency $f = \frac{c}{\lambda}$. The speed of light $c = \frac{c_0}{\sqrt{\mu_r \varepsilon_r}}$ depends on the relative permittivity ε_r and permeability μ_r of the material between the walls. Combining both, the resonance frequency of the theoretical resonator can be calculated with

$$f_{\text{res}} = (n+1)\frac{c}{2d\sqrt{\mu_r \varepsilon_r}} \tag{2.44}$$

n is called the mode number, for a fixed resonance frequency a higher mode number translate into a larger distance d. With the formalism presented here, n directly corresponds to the number of knots observed in the standing wave with $n = 0$ being the fundamental mode. However, sometimes in literature the fundamental mode is described with $n = 1$ leading to $n+1 \to n$ in eq. 2.44. Figure 2.2 shows the amplitudes of the field components with respect to the z direction for $n = 1$.

Two important aspects about cavities can be emphasized by discussing the energy stored inside the cavity. The energy density $u(t,z)$ is given by Poynting's theorem

$$u(t,z) = \frac{1}{2}\varepsilon_r \varepsilon_0 \vec{\mathbf{E}}^2(t,z) + \frac{1}{\mu_r \mu_0}\vec{\mathbf{B}}^2(t,z) \tag{2.45}$$

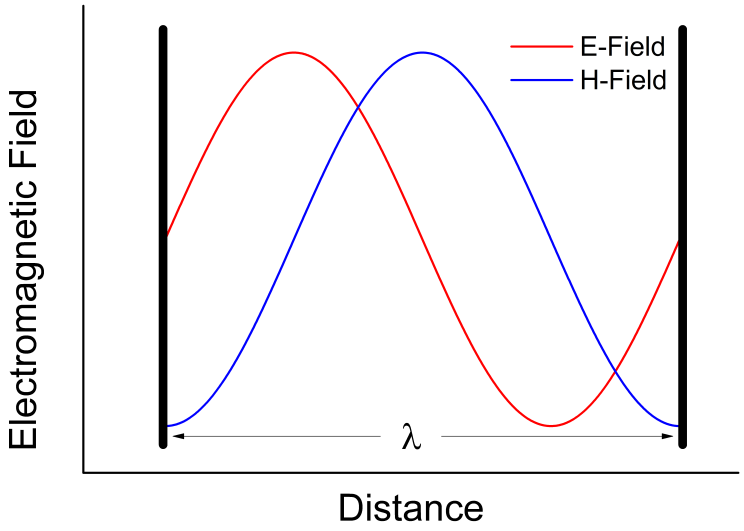

Figure 2.2.: Amplitudes of the electric (red curve) and magnetic (blue curve) field components inside a theoretical resonator (see text for the boundary conditions) with respect to the z-axis.

As we have a standing wave inside the cavity, the spatial and the time dependent parts of the fields are decoupled; thus we can write

$$\tilde{\mathbf{E}}(t,\vec{r}) = \mathbf{E}(\vec{r})\sin(\omega t) \tag{2.46}$$

$$\tilde{\mathbf{B}}(t,\vec{r}) = \mathbf{B}(\vec{r})\cos(\omega t) \tag{2.47}$$

Integrating eq. 2.45 over the cavity volume yields the stored field energy E_{cav}

$$E_{\mathrm{cav}}(t) = E_{\mathrm{el.}}(t) + E_{\mathrm{mag.}}(t) \tag{2.48}$$

$$E_{\mathrm{el.}}(t) = \frac{1}{2}\varepsilon_r\varepsilon_0\mathscr{E}_0^2 V_{\mathrm{mode}}\sin^2(\omega t) \tag{2.49}$$

$$E_{\mathrm{mag.}}(t) = \frac{1}{2\mu_r\mu_0}B_0^2 V_{\mathrm{mode}}\cos^2(\omega t) \tag{2.50}$$

where the mode volume V_{m} describes the effective volume in which the energy of the electromagnetic field is distributed. It is defined as

$$V_{\mathrm{m}} = \frac{\int^V |\mathbf{E}(\vec{r})|^2 d\vec{r}}{\max|\mathbf{E}(\vec{r})|^2} = \frac{\int^V |\mathbf{B}(\vec{r})|^2 d\vec{r}}{\max|\mathbf{B}(\vec{r})|^2} \tag{2.51}$$

The first important aspect about cavities can be directly seen in the equations 2.48-2.50. Here, we can see that the field energy oscillates between the electric $E_{\text{el.}}$ and magnetic $E_{\text{mag.}}$ field energy. Thus, the field behaves like a harmonic oscillator.

A second aspect is the mode volume. For our example, it can be calculated according to

$$V_{\text{m}} = \int_0^b \int_0^a \int_0^d \sin^2\left(\frac{2\pi z}{\lambda}\right) \mathrm{d}z\,\mathrm{d}y\,\mathrm{d}x \tag{2.52}$$

$$= A\frac{\lambda(n+1)}{4} \tag{2.53}$$

with the integrated area $A = ab$ of the plane wave and keeping in mind that $d = (n+1)\lambda/2$. First, from eq. 2.50 we see that a smaller mode volume results in higher field amplitudes $\mathscr{E}_0 \propto \frac{1}{\sqrt{V_{\text{m}}}}$ and $B_0 \propto \frac{1}{\sqrt{V_{\text{m}}}}$. As we are interested in high fields for spin manipulation in ERP, a small mode volume is generally desired. This can be achieved by increasing the frequency and using the fundamental mode of a resonator.

This theoretical resonator is an example which might be relatively easy to understand as the mode pattern is simply a standing plane wave. However, any realistic type of resonator can not include infinitely large metal plates. Thus two additional boundaries appear which introduce two more mode numbers and thus fix the undetermined area A in eq. 2.53. However, the general aspects and definitions introduced here are still valid for such 3D resonators.

2.3.2. Losses

Up to now, losses inside a resonator were neglected. This means that we can store as much energy as we like inside a resonator to achieve large fields. However, in any realistic resonator losses occur due to three basic loss mechanism. First, if a dielectric material is employed, dielectric losses $Q_{\text{diel.}}$ occur. Second, the metal walls where the radiation is reflected usually have a finite surface resistance. Thus, currents induced by the field experience a resistance causing losses $Q_{\text{res.}}$. Last but not least, energy needs to be coupled into a resonator. This, however, means that radiation losses $Q_{\text{coupl.}}$ due to the coupling are induced. The losses can be quantitatively described by the Q(uality)-factor

$$Q = 2\pi\frac{W}{V} \tag{2.54}$$

Where W is the amount of stored energy inside the resonator at the beginning of one period of oscillation and $V = \frac{2\pi}{\omega}$ the amount of energy which is dissipated during this period with the power of dissipation P. For each loss mechanism, a separate Q-factor can be formulated and the total loaded Q_L-factor then reads

$$Q_\mathrm{L}^{-1} = Q_\mathrm{diel.}^{-1} + Q_\mathrm{res.}^{-1} + Q_\mathrm{coupl.}^{-1} \tag{2.55}$$

Usually, the Q_L is divided into an unloaded part $Q_0 = \frac{1}{Q_\mathrm{diel.}^{-1}+Q_\mathrm{res.}^{-1}}$ considering losses inside the resonator and an external part $Q_\mathrm{ext.} = Q_\mathrm{coupl.}$ considering the coupling. The reason for this is that maximum energy transfer from a source to the resonator is achieved if $Q_0 = Q_\mathrm{ext.}$. The coupling coefficient $\kappa = \frac{Q_\mathrm{ext.}}{Q_0}$ indicates whether the losses are dominated by internal losses or by the coupling itself. The resonator is said to be under coupled for $\kappa < 1$, critically coupled for $\kappa = 1$ and over-coupled for $\kappa > 1$.

The Q_L is important for pulsed EPR because of mainly two reasons. First, it defines the bandwidth $\Delta f_\mathrm{BW} = \frac{f_\mathrm{res}}{Q_\mathrm{L}}$ of the resonator. Thus, for very short pulses the excitation bandwidth may be limited by the resonator. Second and most important, after the microwave pulse the energy stored inside the resonator will start to decay with a time constant $\tau = \frac{2Q_\mathrm{L}}{2\pi f_\mathrm{res}}$. Thus, directly after the pulse the decaying field might overload the detector of the spectrometer. Usually, the detector is then protected for a time 5τ which is called dead time. During the dead time, no measurements can be performed which makes it impossible to measure for example spin systems with a relaxation time $T_\mathrm{m} \ll \tau$.

2.4. Cavity quantum electrodynamics

In the previous sections, the interaction between microwaves (light) and spins (matter) was described as an interaction between the quantum mechanical spin and the classical electromagnetic radiation. This description perfectly describes many experiments involving spectroscopy. However, under certain conditions, the classical treatment of the light is no longer appropriated. This is usually the case, when the light-matter interaction strength exceeds any losses involved and/or the electromagnetic field is very weak such that the particle nature (photons) has to be considered. The field of research dealing with the interaction of matter with quantized electromagnetic radiation is called Cavitiy Quantum Electrodynamics (CQED) as it is usually necessary to confine the electromagnetic fields in a cavity in order to observe the quantum mechanical behavior of the

light-matter interaction. One of the most important aspects is that CQED allows the reversible transfer of quantum information between a single photon and matter. This leads to potential applications as for example quantum memories [47], quantum repeaters [48, 49] and quantum computers [50, 51].

In the following, the quantized electromagnetic field will be introduced. The fully quantum mechanical treatment of the interaction between the electromagnetic field and matter follows. The section concludes with the theoretical treatment of the experiments performed in this thesis. It bases on a few textbooks [52, 53], PhD theses [54–56] and research papers [57–60].

2.4.1. Electromagnetic field in a cavity

As we have seen in section 2.3.1, the electromagnetic field inside a cavity behaves like a harmonic oscillator. Thus, it can be quantized in analogy to the standard textbook example of a harmonic oscillator leading to the Hamiltonian

$$\mathscr{H}_{\text{cav.}} = \hbar\omega(a^\dagger a + \frac{1}{2}) \tag{2.56}$$

with the bosonic creation $a^\dagger$ and annihilation a operators. Comparing eq. 2.56 with the classical energy $E = \frac{1}{2}\int \varepsilon_0 E^2 + \frac{1}{\mu 0} B^2$ of a cavity, the field operators $\hat{E}$ for the electric and $\hat{B}$ for the magnetic field can be deduced

$$\hat{E} = \sqrt{\frac{\hbar\omega}{2\varepsilon_0 V_{\text{mode}}}}(a + a^\dagger) \tag{2.57}$$

$$\hat{B} = -i\sqrt{\frac{\hbar\omega\mu_0}{2V_{\text{mode}}}}(a - a^\dagger) \tag{2.58}$$

2.4.2. Spins coupled to photons inside a Cavity

Jaynes-Cummings model for a single spin

The classical interaction between an electromagnetic field and a spin in a static magnetic field is a typical textbook [44] example of the phenomenon we call excitation. In this example, the eigenstates of the spin $|\uparrow\rangle$ and $|\downarrow\rangle$ are split in energy by $\hbar\omega_s$ due to Zeeman interaction with the external field. Applying an electromagnetic driving field with the

frequency $\omega_{\text{drive}} = \omega_{\text{s}}$ leads to transitions from the $|\uparrow\rangle$ to the $|\downarrow\rangle$ state and vice versa. The probability for a transition can be calculated to $p_{|\downarrow\rangle\rightarrow|\uparrow\rangle} = p_{|\uparrow\rangle\rightarrow|\downarrow\rangle} = \left|\sin(\frac{\Omega_1}{2})\right|^2$ thus the spin oscillates between the up and down state during the drive. These oscillations are called Rabi oscillations where the Rabi frequency $\Omega_1 \propto B_1$ scales linearly with the magnetic field strength of the electromagnetic radiation. However, this example neglects that electromagnetic energy is absorbed and emitted during the process, which is a valid approximation as long as the amplitude of the field is large and thus contains many photons. If the field is, however, very weak it has to be treated quantum mechanically. The latter case can be described by the Jaynes-Cummings model [61] for a single spin coupled to a single mode of an electromagnetic field in a cavity. The corresponding Hamiltonian $\mathscr{H}$ consists of three parts, the quantized field inside the cavity $\mathscr{H}_{\text{cavity}} = \hbar\omega_{\text{c}} a^\dagger a$ derived in section 2.4.1, the spin part $\mathscr{H}_{\text{spin}}$ and the interaction between the spin and photons $\mathscr{H}_{\text{int}}$.

$$\mathscr{H} = \mathscr{H}_{\text{cavity}} + \mathscr{H}_{spin} + \mathscr{H}_{\text{int.}} \tag{2.59}$$

For simple spin systems, only the Zeeman interaction needs to be considered leading to $\mathscr{H}_{spin} = g\mu_{\text{B}} B_{0,z}\hat{S}_z = \hbar\omega_{\text{s}}\hat{S}_z$. The interaction between the spin and photons can be derived from the semi-classical point-dipole interaction $-\vec{\mu}_S B_x \vec{e}_1$ using the quantized magnetic field component $B \rightarrow \hat{B}$ derived in section 2.4.1 that is linear polarized in x-direction denoted by the first unit vector $\vec{e}_1$.

$$\begin{aligned}\mathscr{H}_{\text{int}} &= -\vec{\mu}_S B_x \vec{e}_1 \\ &= g\mu_{\text{B}}\hat{S}_x i\sqrt{\frac{\hbar\omega\mu_0}{2V_{\text{mode}}}}(a - a^\dagger) \\ &= -i\hbar g_{\text{s}}(a - a^\dagger)(\hat{S}_+ + \hat{S}_-)\end{aligned} \tag{2.60}$$

The interaction strength is described by a single spin coupling constant $g_{\text{s}} = \sqrt{\frac{\hbar\omega\mu_0}{2V_{\text{mode}}}}\frac{g\mu_{\text{B}}}{2\hbar}$ which mainly depends on the frequency of radiation and the mode volume inside the cavity. In 3D-cavities, where the mode volume depends on the wavelength, g_{s} lies in the order of 100 mHz for 35 GHz radiation. The full Jaynes-Cummings Hamiltonian reads:

$$\mathscr{H} = \hbar\omega_{\text{c}} a^\dagger a + \hbar\omega_{\text{s}}\hat{S}_z - i\hbar g_{\text{s}}(a - a^\dagger)(\hat{S}_+ + \hat{S}_-) \tag{2.61}$$

The interaction term contains the products $a^\dagger \hat{S}_+$ and $a\hat{S}_-$ which describe processes where a photon is created/destroyed while the spin simultaneously gets excited/deexcited. These terms can be neglected as long as $g_s \ll \omega_c, \omega_s$ which is called Rotating-Wave-Approximation (RWA)[52]. For the investigations in this thesis this is a very good approximation. The Jaynes-Cummings Hamiltonian in the RWA reads

$$\mathscr{H}_{\mathrm{RWA}} = \hbar\omega_c a^\dagger a + \hbar\omega_s \hat{S}_z - i\hbar g_s (a\hat{S}_+ - a^\dagger \hat{S}_-) \tag{2.62}$$

In order to illustrate the consequences of this Hamiltonian, its eigenstates and energies may be evaluated for a simple $S = 1/2$ system in a single mode cavity. The states can be described in the basis of the Fock state $|n\rangle$ describing the numbers of photons as well as of the eigenstates of the $\hat{S}_z$ operator $|\frac{1}{2}\rangle = |\uparrow\rangle$ and $|-\frac{1}{2}\rangle = |\downarrow\rangle$ describing the spin. Both eigenvalues and eigenstates can be derived analytically [62]

$$\mathscr{H}_{\mathrm{RWA}} |0,\downarrow\rangle = -\hbar\frac{\omega_s}{2} |0,\downarrow\rangle \tag{2.63}$$

$$\mathscr{H}_{\mathrm{RWA}} |\psi_n^\pm\rangle = \hbar \left[\omega_c (n+1/2) \pm \frac{\Omega_{n,\Delta}}{2} \right] |\psi_n^\pm\rangle \tag{2.64}$$

$$|\psi_n^\pm\rangle = \begin{pmatrix} \cos\theta_n \\ -\sin\theta_n \end{pmatrix} |n+1,\downarrow\rangle \pm \begin{pmatrix} \cos\theta_n \\ \sin\theta_n \end{pmatrix} |n,\uparrow\rangle \tag{2.65}$$

$$\Omega_{n,\Delta}^2 = 4|g_s|^2(n+1) + \Delta^2 \qquad \Delta = \omega_s - \omega_c \qquad \tan\theta_n = \frac{2g_s\sqrt{n+1}}{\Omega_{n,\Delta} - \Delta} \tag{2.66}$$

with $n = 0, 1, 2, ..., \infty$.

In the rather unspectacular ground state $|0,\downarrow\rangle$ (Equation 2.63), the spin is in its ground state and the field is in the vacuum state. The excited states, however, are more interesting. In the case of zero detuning $\omega_{(s} = \omega_c$ and $n = 0$ the first two excited states can be described with the wavefunction $|\psi_0^\pm\rangle = \frac{1}{\sqrt{2)}}(|1,\downarrow\rangle \pm |0,\uparrow\rangle) = |\pm\rangle$. Compared with the single, uncoupled systems (cavity and spin), where an excitation can be localized in the number of photons or the orientation of the spin, the coupled system shares one excitation equally between the cavity and the spin. The resulting quasiparticle is commonly called polariton with the polariton modes $|\psi_n^\pm\rangle$. Furthermore, if the coupled system is prepared for example in the state $|0,\uparrow\rangle = \frac{1}{\sqrt{2}}(|+\rangle + |-\rangle)$ where only the spin is excited (no eigenstate of the coupled system), the system starts to oscillate between the states $|0,\uparrow\rangle$ and $|1,\downarrow\rangle$ according to the Schrödinger equation.

$$\frac{1}{\sqrt{2}} \left(e^{-i\Omega_{0,0}t/2} |+\rangle + e^{i\Omega_{0,0}t/2} |-\rangle \right) = \cos(\Omega_{0,0}t/2) |1\downarrow\rangle - i\sin(\Omega_{0,0}t/2) |0\uparrow\rangle$$

Because the system exchanges energy with the electromagnetic field even in the absence of any applied radiation, these oscillations are called vacuum Rabi oscillations.

The magnitude of g_s plays an important role for the exchange of quantum information on a single photon level. The reason for this is dissipation which occurs in any real world system. Only as long as g_s is larger than the dissipation rate κ, which accounts for photon dissipation inside the cavity, and the rate γ accounting for spin relaxation, it is possible for a single photon to fully interact with the spin during its lifetime (strong coupling limit) [63]. For non-superconducting 3D-Cavities operating at 35 GHz κ lies in the order of several MHz [64]. Spin relaxation times of radicals lie in the order of μs [65] leading to a γ in the MHz range as well. These rates are 10^7 times larger than the typical single spin coupling constant g_s for this kind of systems which seems to put the strong coupling limit out of range. However, it is possible to collectively enhance the coupling by using a spin ensemble instead of a single spin as we will see in the next section.

Tavis-Cummings model for an ensemble of spins

Instead of having a single spin coupled to the cavity mode, an ensemble with N spins can be coupled to a single mode. Assuming no interactions between the spins, the corresponding Hamiltonian reads

$$\mathscr{H}_\mathrm{RWA} = \hbar\omega_\mathrm{c} a^\dagger a + \sum_i^N \hbar\omega_{\mathrm{s},i}\hat{S}_{z,i} - i\hbar\sum_j^N g_{\mathrm{s},j}(a\hat{S}_{+,j} - a^\dagger \hat{S}_{-,j}) \tag{2.67}$$

If all spins posses the same transition $\omega_{\mathrm{s},i} = \omega_\mathrm{s}$ and interaction frequencies $g_{\mathrm{s},j} = g_\mathrm{s}$, Equation 2.67 can be rewritten using $\sum_i^N \hat{S}_{z,i} = \hat{S}_{z,\mathrm{tot}}$ and $\sum_i^N \hat{S}_{\pm,i} = \hat{S}_{\pm,\mathrm{tot}}$

$$\mathscr{H}_\mathrm{RWA} = \hbar\omega_\mathrm{c} a^\dagger a + \hbar\omega_\mathrm{s}\hat{S}_{z,\mathrm{tot}} - i\hbar g_\mathrm{s}(a\hat{S}_{+,\mathrm{tot}} - a^\dagger \hat{S}_{-,\mathrm{tot}}) \tag{2.68}$$

which resembles eq. 2.62. Thus, in the case of N identical spins the Hamiltonian is the same as for the single spin case. However, the evaluation of the Hamiltonian has to be performed under the consideration of a spin system with $S = N/2$. In order to discuss such a system, the non-linear Holstein-Primakoff transformation [66] can be very useful. Here, the spin operators $\hat{S}_{-,\mathrm{tot}} = \sqrt{N}\sqrt{1-\frac{b^\dagger b}{N}}b^\dagger$, $\hat{S}_{-,\mathrm{tot}} = \sqrt{N}\sqrt{1-\frac{b^\dagger b}{N}}b$ and $\hat{S}_{z,\mathrm{tot}} = N - b^\dagger b$ are bosonized with the bosonic annihilation and creation operators b and $b^\dagger$. The bosons resulting from the transformation are called magnons which are collective spin excitations. The corresponding vacuum state corresponds to the state where the

spin system is fully polarized. In the context of cavity QED, due to the light-matter interaction, photons excite magnons and vice versa. If the number of photons/magnons represented by the number operators $a^\dagger a$ and $b^\dagger b$ are small compared to the total number of spins N the bosonized spin ladder operators reduce to $\hat{S}_{-,\mathrm{tot}} \approx \sqrt{N} b^\dagger$ respectively $\hat{S}_{+,\mathrm{tot}} \approx \sqrt{N} b$. This leads to the Hamiltonian

$$\mathscr{H}_{\mathrm{RWA,H-P}} = \hbar\omega_\mathrm{c} a^\dagger a - \hbar\omega_\mathrm{s} b^\dagger b - i\hbar\Omega_\mathrm{eff}(ab^\dagger - a^\dagger b) \tag{2.69}$$

of two interacting harmonic oscillators. This result is important as it shows that photons excite collective spin states (magnons) and not single spins in a cavity. Compared to the single spin case, the interaction strength $\Omega_\mathrm{eff} = \sqrt{N} g_\mathrm{s}$ is enhanced by the factor $\sqrt{N}$ due to the collective nature of interaction. Thus, it is possible to overcome the loss rates κ and γ in order to realize a coherent exchange of a photon between the cavity and spins.

The Holstein-Primakoff transformation helps to understand the collective behavior of an ensemble of spins coupled to a single mode inside a cavity. However, in reality, spins usually do not have the same transition frequency due to several interactions with the environment. Therefore, models are needed which include an inhomogeneous distribution of spin transition frequencies in order to describe most of the experiments performed in this thesis. The following two sections cover models to describe the response of an ensemble of spins coupled to a cavity to external stimuli in the frequency and time domains.

2.4.3. Probing CQED systems

Probing the light-matter interaction of spins with photons in a cavity can be achieved by initializing the cavity in a defined state and measuring the resulting fields inside the cavity. Initialization can be done by coupling the system to a coherent photon source while the detection of the cavity field requires a coupling of the system to a detector. For a spin ensemble coupled to a 3D cavity in the microwave regime, waveguides can be used to transport microwaves from a source to the cavity. The coupling can be achieved by using a small coupling hole between the waveguide and the cavity which allows microwave energy to enter the cavity with a rate $2\kappa_\mathrm{e}$. Of course, microwave energy inside the cavity couples out with the same rate. Thus, an indirect detection of the fields inside the cavity is possible by observing the radiation coupled out. The coupling of a coherent source to the system can be modeled with the driving Hamiltonian $\mathscr{H}_\mathrm{drive} = i\hbar\sqrt{2\kappa_\mathrm{e}}(\beta_\mathrm{in}(t)a^\dagger - \beta_\mathrm{in}^*(t)a)$ where $\beta_\mathrm{in}(t)$ describes an arbitrary coherent field generated by the source and $|\beta_\mathrm{in}(t)|^2$ corresponds to the number of incoming photons per second.

It can be shown [53] that the output field $\beta_{\text{out}}(t)$ is related with the input field $\beta_{\text{in}}(t)$ and cavity field $\langle a \rangle (t)$ by

$$\beta_{\text{in}}(t) + \beta_{\text{out}}(t) = \sqrt{2\kappa_{\text{e}}} \langle a \rangle (t) \tag{2.70}$$

in case of a one sided cavity (only one coupling hole) if κ_{e} is constant over the frequency range of interest. In order to calculate the output field, which is the quantity being measured by a detector, the expectation value $\langle a \rangle (t)$ is required. As losses occurring in the system should be considered as well, the Lindblad equation in the Heisenberg picture

$$\frac{\mathrm{d}}{\mathrm{d}t} \langle O \rangle = \langle \dot{O} \rangle = \frac{i}{\hbar} \langle [\mathscr{H}, O] \rangle + \frac{1}{2\hbar} \sum_k \left(V_k^\dagger [O, V_k] + [V_k^\dagger, O] V_k \right) \tag{2.71}$$

can be used to calculate this quantity. In the following, the Tavis-Cummings Hamiltonian

$$\begin{aligned} \mathscr{H}_{\text{RWA}} = \hbar\omega_{\text{c}} a^\dagger a + \sum_i^N \hbar\omega_{\text{s},i} \hat{S}_{z,i} + i\hbar \sum_j^N g_{\text{s},j} (a\hat{S}_{+,j} - a^\dagger \hat{S}_{-,j}) \\ + i\hbar\sqrt{2\kappa_{\text{e}}} (\beta_{\text{in}}(t) a^\dagger - \beta_{\text{in}}^*(t) a) \end{aligned} \tag{2.72}$$

including the driving term will be used to model the systems response in the frequency and time domains in the following sections. Furthermore, the jump operator $V_1 = \sqrt{2\hbar\kappa} a$ with $\kappa = \kappa_{\text{e}} + \kappa_{\text{i}}$ will be used to model photon dissipation due to intrinsic κ_{i} and external κ_{e} losses originating from the finite Q-factor of the cavity respectively from the out coupling of radiation. Dephasing of the spins due to magnetic field fluctuations in z-direction are modeled with the jump operators $V_i = \sqrt{2\hbar\gamma} \hat{S}_{z,i}$. As spin dephasing is usually the most important spin loss mechanism for the measurements presented in this thesis, other loss mechanisms like spin-lattice relaxation are neglected.

Frequency domain

A vector network analyzer is the perfect tool to probe the cavity spin system in the frequency domain. In the case of a one sided cavity, it measures the scattering parameter $S_{11}(\omega)$ which corresponds to the ratio $\frac{\beta_{\text{out}}(\omega)}{\beta_{\text{in}}(\omega)}$ between the output and input fields in frequency domain. In order to calculate $S_{11}(\omega)$, the Lindblad equations for $\langle \dot{a} \rangle$ and

$\langle \dot{S}_{-,i} \rangle$ are needed in order to get rid of the time dependency.

$$\langle \dot{a} \rangle = -i\omega_c \langle a \rangle (t) + \sum_i g_{s,i} \langle S_{-,i}(t) \rangle - \kappa \langle a \rangle (t) + \sqrt{2\kappa_e}\beta_{in}(t) \langle a \rangle (t) \tag{2.73}$$

$$\langle \dot{S}_{-,i} \rangle = -i\omega_c \langle S_{-,i} \rangle (t) + 2g_{s,i} \langle a \rangle (t) \langle S_{z,i} \rangle - \gamma \langle S_{-,i} \rangle (t) \tag{2.74}$$

Here, the correlations between the photons and the spins are neglected by the approximation $\langle aS_{z,i} \rangle (t) = \langle a \rangle (t) \langle S_{z,i} \rangle (t)$ which is valid as long the numbers of photons inside the cavity N_{phot} is much smaller than the number of spins N [58]. Utilizing the same argument, $\langle S_{z,i} \rangle$ is assumed to be constant as only very few spins are excited due to the low number of photons. The frequency response can be obtained by using the Fourier representation $f(t) = \sum_\omega f(\omega) e^{-i\omega t}$ of the equations 2.73 and 2.74.

$$-i\omega \langle a \rangle (\omega) = -i\omega_c \langle a \rangle (\omega) + \sum_i g_{s,i} \langle S_{-,i} \rangle (\omega) - \kappa \langle a \rangle (\omega) + \sqrt{2\kappa_e}\beta_{in}(\omega) \tag{2.75}$$

$$-i\omega \langle S_{-,i} \rangle (\omega) = -i\omega_c \langle S_{-,i} \rangle (\omega) - 2g_{s,i} \langle a \rangle \langle S_{z,i} \rangle (\omega) - \gamma_i \langle S_{-,i} \rangle \tag{2.76}$$

Solving equation 2.76 for $\langle S_{-,i} \rangle (\omega)$, plugging in the result in equation 2.75 and using the relation between input and output field (Equation 2.70) the scattering parameter $S_{11}(\omega)$ can be obtained.

$$\frac{\beta_{out}(\omega)}{\beta_{in}(\omega)} = S_{11}(\omega) = 1 - \frac{2\kappa_e}{i(\omega_c - \omega) + \kappa + \sum_j \frac{-2g_{s,j}^2 \langle \hat{S}_{z,j} \rangle}{i(\omega_{s,j} - \omega) + \gamma_j}} \tag{2.77}$$

In the case of N_{id} spins with identical transition frequencies $\omega_{s,j} = \omega_s$, couplings $g_{s,j} = g_s$ and dissipation rates $\gamma_j = \gamma$ the sum occurring in equation 2.77 can be rewritten as

$$\begin{aligned} \sum_{j=1}^{N_{id}} \frac{-2g_{s,j}^2 \langle \hat{S}_{z,j} \rangle}{i(\omega_{s,j} - \omega) + \gamma_j} &= \frac{-2N_{id} g_s^2 \langle \hat{S}_z \rangle}{i(\omega_s - \omega) + \gamma} \\ &= \frac{\Omega_{eff}^2}{i(\omega_s - \omega) + \gamma} \end{aligned} \tag{2.78}$$

with an effective collectively enhanced coupling

$$\Omega_{eff} = \sqrt{-2N_{id.} \langle \hat{S}_z \rangle} g_s \tag{2.79}$$

Usually, experiments in the strong coupling limit are carried out at low temperatures, where $\langle \hat{S}_z \rangle = -0.5$ and thus $\Omega_{\text{eff}} = \sqrt{N_{\text{id.}}} g_{\text{s}}$. In the experiments presented in this thesis, this is not the case. Therefore, $\langle \hat{S}_z \rangle$ has to be calculated for the temperatures at which the measurements are performed.

Typically, spins in an ensemble do not have the same resonance frequency due to inhomogeneities in the static magnetic field and strains in the material. This inhomogeneous distribution in frequency can be either described by a continuous $\rho(\omega_{\text{s}})$ or by a discretized $\rho(\omega_{\text{s},j})$ spectral density function. In order to avoid including every single spin, the ensemble can be discretized in $\mathcal{N}$ sub ensembles (spin packets) which are said to have the same resonance frequency. The number of spins in each sub ensemble $N_{\text{id,j}}$ can be calculated from $\rho(\omega_{\text{s},j})$.

$$N_{\text{id,j}} = \frac{N\rho(\omega_{\text{s},j})}{\sum^{\mathcal{N}} \rho(\omega_{\text{s},j})} \tag{2.80}$$

In order to avoid errors due to the discretization, the frequency spacing $\omega_{\text{s},j+1} - \omega_{\text{s},j} < \gamma$ should be smaller than the half-width γ of the packet caused by relaxation to guarantee spectral overlap of the packets. S_{11} in case of inhomogeneous broadening can be then calculated with

$$S_{11} = 1 - \frac{2\kappa_{\text{e}}}{i(\omega_{\text{c}} - \omega) + \kappa + \sum^{\mathcal{N}} \frac{-2N_{\text{id,j}} g_{\text{s}}^2 \langle \hat{S}_{z,j} \rangle}{i(\omega_{\text{s},j} - \omega) + \gamma}} \tag{2.81}$$

Time domain

To model the a spin-cavity system in time domain, a similar approach as presented in the section before can be employed. However, instead of performing a Fourier transformation, one can for example obtain a closed set of differential equations and solve them numerically. This was done by Julsgaard *et al.* [60] for an ensemble of inhomogeneously broadened spins. The method they developed will be described briefly in this section.

First, the Javis-Cummings Hamiltonian including the driving term is transformed into a frame rotating with $\omega_{\text{s,c}}$ which is the frequency of the spins in the center of their distribution.

$$\mathscr{H}_{\mathrm{RWA}} = \hbar\Delta_{\mathrm{cs}} a^{\dagger}a + \sum_{i}^{N} \hbar\Delta_{\mathrm{s},i}\hat{S}_{z,i} - i\hbar\sum_{j}^{N} g_{\mathrm{s},j}(a\hat{S}_{+,j} - a^{\dagger}\hat{S}_{-,j}) + i\hbar\sqrt{2\kappa_{\mathrm{e}}}(\beta_{\mathrm{in}}^{'}(t)a^{\dagger} - \beta_{\mathrm{in}}^{'*}(t)a) \tag{2.82}$$

Here, $\Delta_{\mathrm{cs}} = \omega_{\mathrm{c}} - \omega_{\mathrm{s,c}}$ is the difference between the cavity resonance and the central spin frequency. Furthermore, $\Delta_{\mathrm{s},i} = \omega_{\mathrm{s},i} - \omega_{\mathrm{s,c}}$ is the difference between the resonance frequency of each individual spin with the central spin frequency. Again, the ensemble is divided into $\mathscr{N}$ homogeneous sub ensembles containing N_{m} identical spins. To form a closed set of differential equations, the following operators are needed

$$\hat{X} = \frac{a + a^{\dagger}}{\sqrt{2}} \tag{2.83}$$

$$\hat{P} = \frac{-i(a - a^{\dagger})}{\sqrt{2}} \tag{2.84}$$

$$\hat{S}_{x,\mathrm{m}} = \sum_{j}^{N_{\mathrm{m}}} \frac{\hat{S}_{+,j} + \hat{S}_{-,j}}{2} \tag{2.85}$$

$$\hat{S}_{y,\mathrm{m}} = -i\sum_{i}^{N_{\mathrm{m}}} \frac{\hat{S}_{+,j} - \hat{S}_{-,j}}{2} \tag{2.86}$$

$$\hat{S}_{z,\mathrm{m}} = \sum_{i}^{N_{\mathrm{m}}} \hat{S}_{z,j} \tag{2.87}$$

Instead of the pure creation and annihilation operators, the authors use the field quadratures $\hat{X}$ and $\hat{P}$ which is a matter of taste. The operators are then linearized about their mean values with $\hat{X} = X + \delta\hat{X}$, $\hat{P} = P + \delta\hat{P}$ and $\hat{S}_{k,\mathrm{m}} = S_{k,\mathrm{m}} + \delta\hat{S}_{k,\mathrm{m}}$ for $k = x, y, z$. This leads to the Lindblad equations

$$\frac{\mathrm{d}X}{\mathrm{d}t} = -\kappa X + \Delta_{\mathrm{cs}} P - \sum_{m} \sqrt{2} g_m S_{y,m} + 2\sqrt{\kappa}\beta_{\mathrm{R}}^{'} \tag{2.88}$$

$$\frac{\mathrm{d}P}{\mathrm{d}t} = -\kappa P - \Delta_{\mathrm{cs}} X - \sum_{m} \sqrt{2} g_m S_{x,m} + 2\sqrt{\kappa}\beta_{\mathrm{I}}^{'} \tag{2.89}$$

$$\frac{\mathrm{d}S_{x,m}}{\mathrm{d}t} = -\gamma_{\perp} S_{x,m} - \Delta_{s,m} S_{y,m} - \sqrt{2} g_m \left(S_{z,m} P + \left\langle \delta\hat{S}_{z,\mathrm{m}} \delta\hat{P} \right\rangle\right) \tag{2.90}$$

$$\frac{\mathrm{d}S_{y,m}}{\mathrm{d}t} = -\gamma_{\perp} S_{y,m} + \Delta_{s,m} S_{x,m} - \sqrt{2} g_m \left(S_{z,m} X + \left\langle \delta\hat{S}_{z,\mathrm{m}} \delta\hat{X} \right\rangle\right) \tag{2.91}$$

$$\frac{\mathrm{d}S_{z,m}}{\mathrm{d}t} = \sqrt{2} g_m \left(S_{x,m} P + \left\langle \delta\hat{S}_{x,\mathrm{m}} \delta\hat{P} \right\rangle + S_{y,m} X + \left\langle \delta\hat{S}_{y,\mathrm{m}} \delta\hat{X} \right\rangle\right) - \gamma_{\parallel}(S_{z,m} + N_m) \tag{2.92}$$

where $\beta_{\mathrm{R}}^{'}$ is the real part of the driving field and $\beta_{\mathrm{I}}^{'}$ corresponds to the imaginary part. $\gamma_{\perp}$ describes the in plane dissipation governed by T_{m} where $\gamma_{\parallel}$ describes transversal dissipation governed by T_1. The driving field is noted as $\beta^{'}(t)$ as it corresponds to the down converted field $\beta^{'}(t) = \beta(t)e^{-i\omega_{\mathrm{s,c}}t}$. These equations contain correlations between the cavity field and the spins (like $\left\langle \delta\hat{S}_{z,\mathrm{m}}\delta\hat{P}\right\rangle$) which means that they do not form a closed set. The authors included them in their calculations up to second order and came to the conclusion that they can be neglected for their purpose. As the conditions under which they used these equations are similar to what is presented in this thesis (mostly that the numbers of photons is smaller than the number of spins), the correlations are neglected and thus the equations form a closed set. The differential equations may be solved numerically ensuring that the spin packets have enough spectral overlap. The initial conditions for thermal equilibrium then reads

$$X = 0 \tag{2.93}$$

$$P = 0 \tag{2.94}$$

$$S_{x,\mathrm{m}} = 0 \tag{2.95}$$

$$S_{y,\mathrm{m}} = 0 \tag{2.96}$$

$$S_{z,\mathrm{m}} = N_{\mathrm{id,m}}\left\langle \hat{S}_{z,\mathrm{m}}\right\rangle \tag{2.97}$$

Where $N_{\mathrm{id,m}}$ can be calculated with equation 2.80 and $\left\langle \hat{S}_{z,\mathrm{m}}\right\rangle$ has to be calculated for the temperature of interest. Simulations based on this equations were performed with *Matlab*. The scripts for solving the differential equations are shown in the appendix A.3.

3. $[Cr(ddpd)_2][BF_4]_3$ a photoactive molecular quantum bit

This chapter is based on the research paper

Chromium(III)-based potential molecular quantum bits with long coherence times, S. Lenz, H. Bamberger, P. P. Hallmen, Y. Thiebes, S. Otto, K. Heinze and J. van Slageren, *Phys. Chem. Chem. Phys.*, 2019, 21, 6976-6983

and uses parts of it. The publication was a joint collaboration with the Heinze Group from the Johannes Gutenberg University Mainz who provided the compound $[Cr(ddpd)_2][BF_4]_3$ and its deuterated analogue. $[Cr([D_9]\text{-}ddpd)_2][BF_4]_3$.

3.1. Introduction

Many advantages of MQBs have been impressively demonstrated. Tailoring by chemical synthesis has improved the coherence time of MQBs in a rational way [17, 19, 30, 31] from hundreds of nanoseconds to nearly one millisecond. It has been shown [67, 68] that it is possible to build up two qubit gates by molecular design and thus make universal quantum computing possible. However, the readout of MQBs is nearly exclusively performed on ensembles of MQBs in the bulk material by the means of pulsed EPR [17, 19, 30, 31, 69–72]. For a practical quantum computer, it would be necessary to readout single MQBs in order to scale up the system. Using standard pulsed EPR techniques this is, unfortunately, not possible yet, as the energy of single microwave photons is very low. On the other hand, for spin defects in diamond [34] it has been demonstrated that a single spin readout is possible by exploiting the optical properties of the system. Here, the readout is transferred to the optical region, where single photons have a five orders of magnitude larger energy compared to microwave photons. This, however, requires optical transitions coupled to spin transitions via spin-orbit coupling [73] in a favorable way.

Out of the many introduced MQB systems, mononuclear chromium(III) complexes are particularly interesting in this regard. Besides reasonable coherence times [74, 75], chromium(III) complexes often possess luminescent properties which are being proposed to be useful for optical addressing of the qubit [38]. However, only chromium defect centers in alumina (ruby) [76] are proven to be useful optically addressable qubits up to now. In order to get access to the benefits of a molecular system, a chromium complex featuring similar optical properties as ruby would be desirable.

Fortunately, a very promising chromium (III) complex $[Cr(ddpd)_2][BF_4]_3$, where ddpd stands for N,N'-dimethyl-N,N'-dipyridine-2-ylpyridine-2,6-diamine , was synthesized recently and its optical properties studied extensively [77]. It features luminescent properties similar to ruby and is very stable under ambient conditions. Thus, the complex seems to be the optimal candidate for a MQB which can be addressed optically. In order to explore its potential, the compound was studied by the means of magnetic measurements, CW and pulsed EPR, MCD and luminescent spectroscopy and finally by a combination of optical and EPR spectroscopy.

3.2. SQUID magnetometry

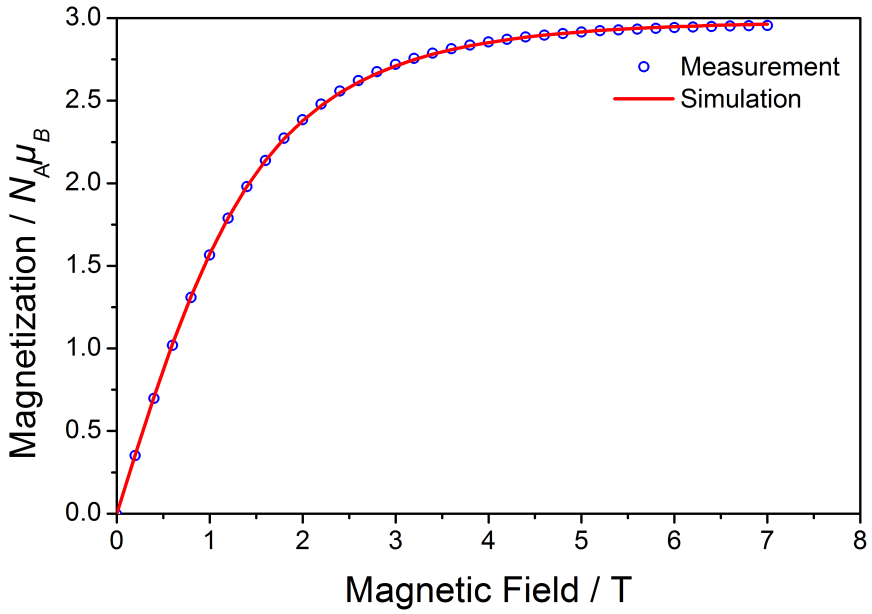

Figure 3.1.: Measured magnetization M of **Cr-H** (blue dots) at 1.8 K and a simulation performed with *Easyspin* (red line) based on the spin hamiltonian parameters $S = 3/2$ $g = 1.98$ $D = 0.5$ cm^{-1}.

Initial magnetic characterization of **Cr-H** was achieved by the means of SQUID magnetometry. First, the magnetization of a pressed pellet of 8.5 mg **Cr-H** from 0 T to 7 T at 1.8 K was measured. As can be seen in Figure 3.1, the magnetization behaves linear with respect to an applied field of up to 1 T and saturates at around 2.97 $N_A\mu_B$ in high fields as expected for a Cr^{3+} complex. Next, the molar magnetic susceptibility χ was measured from 1.8 K to 300 K at 100 mT. Figure 3.2 shows the product χT which features a constant value of 1.86 cm^3 K mol^{-1} above 10 K, whereas at lower temperature it starts to decrease. The high temperature behavior of χT can be perfectly described by Curie's law. Assuming a Spin $S = 3/2$ and a typical Cr^{3+} g-value of 1.98 [78], a Curie constant $C = 1.86$ cm^3 K mol^{-1} can be calculated, which fits very well to the observed value. The deviation from Curie's law at lower temperature could be explained by a small zero field splitting. Indeed, a simulation performed with *Easyspin*, which calculates χT based on the spin Hamiltonian in eq. 3.1 by solving the Van Vleck equation, fits perfectly to the measurement.

$$\mathscr{H} = g\mu_B \hat{S}_z B_z + D(\hat{S}_z^2 - S(S+1)/3) \tag{3.1}$$

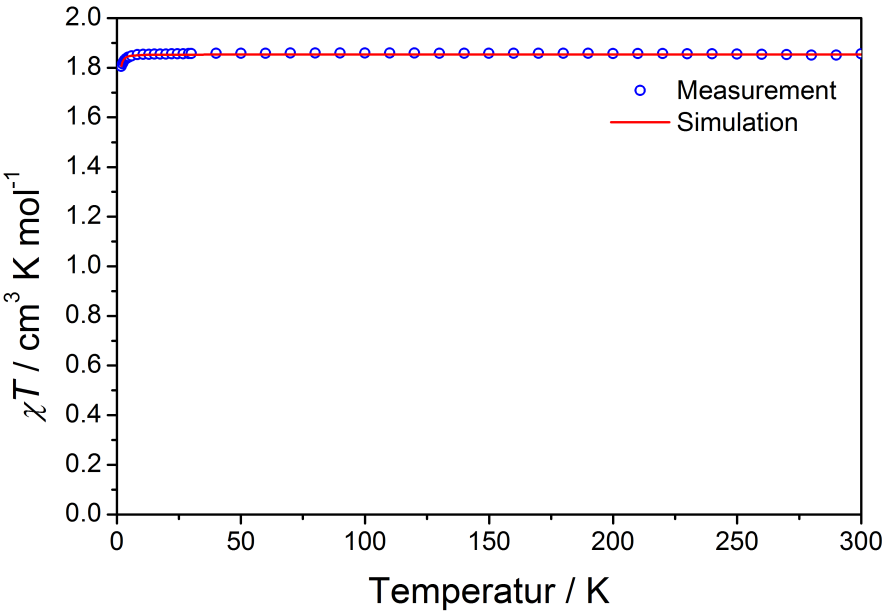

Figure 3.2.: Measured product of the molar susceptibility and temperature χT of **Cr-H** (blue dots) and a simulation performed with *Easyspin* (red line) based on the spin hamiltonian parameters $S = 3/2$ $g = 1.98$ $D = 0.5$ cm^{-1}.

Here, a zero field splitting parameter $D = 0.5 \pm 0.3$ cm^{-1} was used, which is a typical value for Cr^{3+} [78–80]. Using the same parameters, the behavior of the magnetization in Figure 3.1 can be reproduced perfectly as well including the saturation magnetization of $2.97\, N_A \mu_B$. It should be noted, however that SQUID magnetometry is not very sensitive with respect to D resulting in large relative error of about 50 %.

In summary, the SQUID measurements show that the magnetism of **Cr-H** can be described very well with the spin-only magnetism of a $S = 3/2$ system as expected, no phase transitions are visible over the whole temperature and field range of interest and the compound exhibits a small zero field splitting. These results are important for the following EPR investigations, as they will simplify the interpretation of the spectra and temperature dependencies.

In the next section, high field EPR measurements will be employed in order to obtain more precise zero field splitting parameters. This will be important for further pulsed EPR measurements as D is on the same order as the energy of the radiation used in the pulsed spectrometer.

3.3. High-field EPR spectroscopy

High-Field EPR (HFEPR) spectroscopy is an excellent method to study paramagnetic molecules with a spin larger than $S = 1/2$ and possessing a zero field splitting. The reason for this is that the interpretation of spectra greatly simplifies, when the energy of the radiation exceeds the zero field splitting (high-field limit). The same 8.4 mg pellet of **Cr-H** used for the SQUID measurements was investigated in a home built HFEPR spectrometer from 0 T to 14 T at frequencies from 95 GHz to 370 GHz at 10 K (Figure 3.3). Furthermore, temperature dependent measurements were carried out at 370 GHz from 10 K to 80 K (Figure 3.4). The field domain measurements at different frequencies can be seen in Figure 3.3. The spectra show a sharp central line accompanied by two broad flanks. The central line is distorted due to admixture of dispersion to the absorption signal, a common problem in HFEPR [81]. Figure 3.4 shows the spectrum of **Cr-H** at 370 GHz and different temperatures in the region of interest. By increasing the temperature, both flanks decrease equally while the distortion of the central line vanishes at higher temperatures.

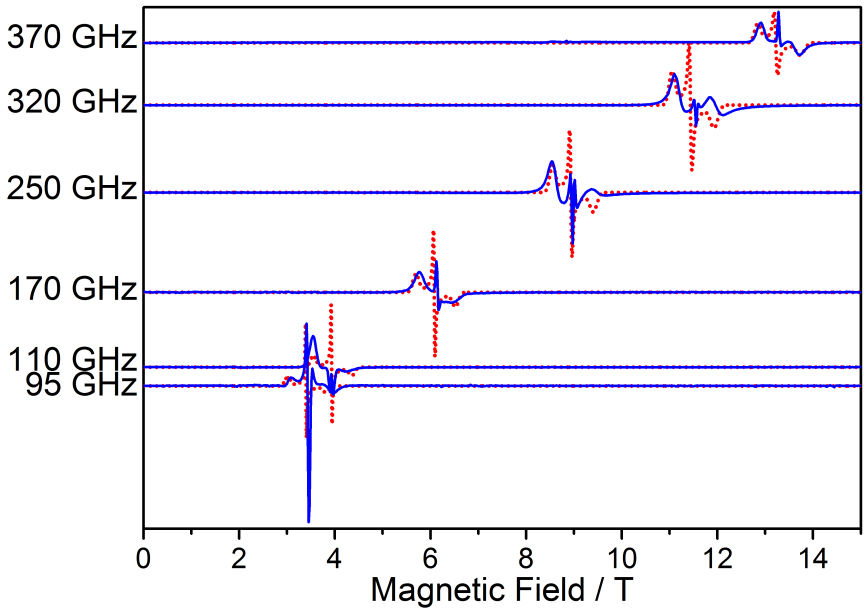

Figure 3.3.: HFEPR spectra (blue line) of a pressed pellet of 8.4 mg **Cr-H** recorded at frequencies from 95 GHz to 370 GHz at 10 K. Simulations of the spectra (red dotted line) were performed with *Easyspin* using the spin Hamiltonian parameters $S = 3/2$, $g_{\perp} = 1.99$, $g_{\parallel} = 1.98$, $D = 0.18$ cm^{-1} and $E = 0.06$ cm^{-1}

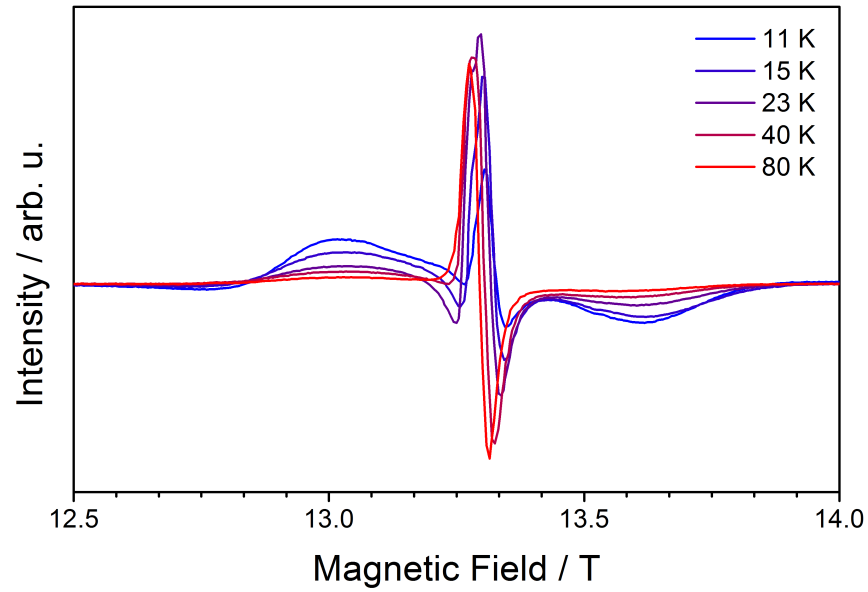

Figure 3.4.: HFEPR spectra (colored lines) of a pressed pellet of 8.4 mg **Cr-H** recorded at temperatures between 11 K and 80 K at 370 GHz.

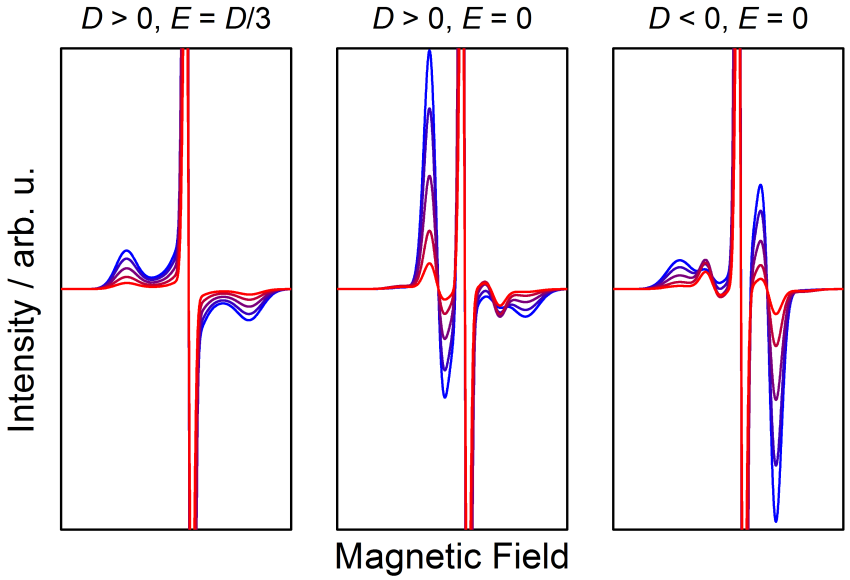

Figure 3.5.: Simulated temperature dependence of a $S = 3/2$ with different zero field splitting parameters in the high field limit.

The field domain spectra in Figure 3.3 can be simulated reasonably well using *Easyspin* which calculates the spectrum on the basis of the spin Hamiltonian given in eq. 3.2 using the parameters $S = 3/2$, $g_\perp = 1.99$, $g_\parallel = 1.98$, $D = 0.18 \pm 0.02$ cm^{-1} and $E = -0.06 \pm 0.005$ cm^{-1}. The flanks are broadened by a statistical distribution of the D and E parameter. Therefore, strain parameters (FWHM of a Gaussian distribution) $\Delta D = 0.027$ cm and $\Delta E = 0.001$ cm were used for the simulations. The distribution of D arises from molecular distortions [82, 83] in the micro-crystalline powder which influence the ligand field and therefore D.

$$\mathscr{H} = \hat{S}\mu_B \mathbf{g}\mathbf{B} + D(\hat{S}_z^2 - S(S+1)/3) + E(\hat{S}_+^2 + \hat{S}_+^2)/2 \tag{3.2}$$

The temperature dependent measurements shown in Figure 3.4 confirm the strong rhombicity $E \approx D/3$ as both flanks decrease equally with increasing temperature. In the axial case $E = 0$, one flank would increase more with temperature depending on the sign of D. This temperature dependent behavior of a $S = 3/2$ system is summarized in Figure 3.5.

In conclusion, HFEPR measurements on **Cr-H** pinned down the magnitude of the zero field splitting parameter D from $D = 0.5 \pm 0.3$ cm^{-1} to $D = 0.18 \pm 0.02$ cm^{-1} and revealed a strong rhombicity reflected by the parameter $E = -0.06 \pm 0.005$ cm^{-1}. As the zero field splitting lifts the degeneracy of the spin microstates, the latter ones can be addressed individually in pulsed EPR by tuning the magnetic field. Thus, the chromium complex could be used as qudit, which is a qubit with more than two defined states [84]. The usability of the compound as qubit/qudit will be explored in the next section, where the dynamical properties of the system will be investigated by the means of pulsed EPR at 35 GHz.

3.4. Pulsed EPR

Pulsed EPR is commonly used to probe spin dynamics in a system of interest. The method is only applicable if the phase memory time T_m (sometimes called T_2 depending on the convention) and thus the coherence time of a superposition of two spin states, is longer than the dead time of the spectrometer. Usually, the phase memory time of concentrated paramagnetic compounds is too short compared to the dead time [42] due to spin-spin diffusion. Furthermore, nuclear spins in the vicinity of the paramagnetic

center induce nuclear spin-spin diffusion which decreases T_m as well. Therefore, it is common to dilute the compounds either in a frozen solution or in a diamagnetic analog. Deuteration of the host further decreases the effect of nuclear spin diffusion [17, 19] as the gyromagnetic ratio of deuterons is about 6.5 times smaller compared to protons.

Therefore, pulsed EPR measurements at 35 GHz were carried out on 1 mM frozen solutions of **Cr-H** and its partially deuterated analog **Cr-D** in H_2O/Glycerol 1:1 vol. (**sol-H**) and D_2O/Glycerol-d_8 1:1 vol. (**sol-D**) at temperatures between 7 K and 80 K. The measurements and preliminary evaluation of the data were performed by Yannic Thiebes during his research internship.

3.4.1. ESE-detected EPR spectra

First, electron spin echo (ESE-)detected spectra were recorded in the range of 800 mT to 1500 mT at temperatures of 7 K, 20 K, 35 K, 50 K and 80 K. A spectrum of 1 mM **Cr-H** in **sol-H** at 7 K and a simulation performed with *Easyspin* is shown in Figure 3.6. Because the external magnetic field is not modulated, this technique yields the absorption spectrum, in contrast to standard CW (HF)EPR techniques. Again, the spectrum features two broad flanks and a sharp central line.

The spectrum was simulated with $S = 3/2$, $g_\perp = 1.99$, $g_\parallel = 1.987$, $D = 0.12 \pm 0.02$ cm^{-1} and $E = -0.04 \pm 0.005$ cm^{-1}. Furthermore, the strain parameters $\Delta D = 0.08$ cm^{-1} and $\Delta E = 0.03$ cm^{-1} were used to account for the broadening of the flanks. Compared to the HFEPR measurements ($D = 0.18 \pm 0.02$ cm^{-1}, $E = -0.06 \pm 0.005$ cm^{-1}), D and E are a little bit smaller but not by much. The strains, however, are about ten times larger than those found by the HFEPR measurements. The reason for this is most likely that the pulsed measurements are carried out on frozen solutions, thus molecular distortions could be much larger as in a microcrystalline powder. The spectra of the other three compound/solvent combinations are essentially the same (see Appendix Figure A.1) and the temperature behavior is in accordance with the HFEPR measurements (see Appendix Figure A.2).

3.4.2. Rabi nutation measurements

As mentioned in section 3.3, the zero field splitting lifts the degeneracy of the $|\pm 3/2\rangle$ and $|\pm 1/2\rangle$ states of the $S = 3/2$ system. This allows to separate transitions between $|-3/2\rangle \rightarrow |-1/2\rangle$, $|-1/2\rangle \rightarrow |+1/2\rangle$ and $|1/2\rangle \rightarrow |3/2\rangle$ by applying an appropriated field. Therefore, it is possible to access all four levels in the system individually. The

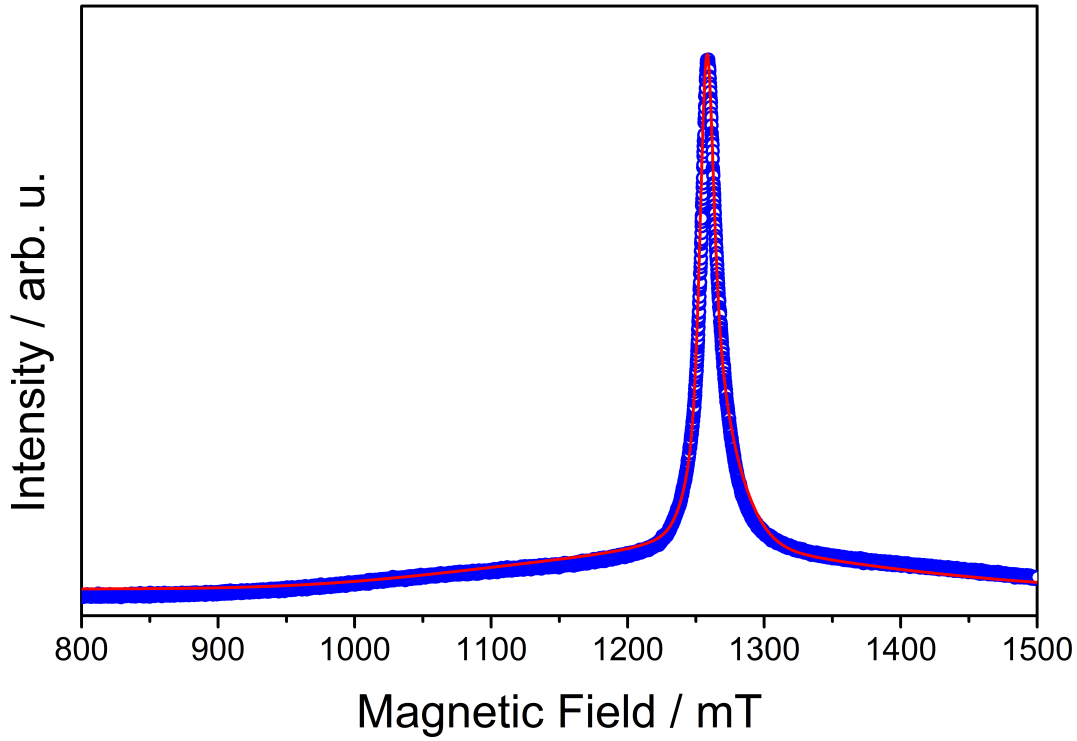

Figure 3.6.: ESE-detected EPR spectrum (blue dots) of 1 mM **Cr-H** in **sol-H** at 7 K and 35 GHz. A simulation (red line) with the spin parameters $S = 3/2$, $g_{\perp} = 1.99$, $g_{\parallel} = 1.987$, $D = 0.12 \pm 0.02$ cm^{-1} and $E = -0.04 \pm 0.005$ cm^{-1} carried out with *Easyspin* is shown as well.

strain parameter ΔD only affects transitions between $|\pm 3/2\rangle$ and $|\pm 1/2\rangle$ thus it can be deduced that these transitions occur in the broad flanks of the spectrum and the intra doublet transition $|-1/2\rangle \rightarrow |+1/2\rangle$ at the sharp central line. In order to verify this, Rabi nutation measurements were performed on **Cr-D** in **sol-H** at 7 K at 1258.9 mT (central line) and 1200.0 mT (left flank). The measurements are presented in Figure 3.7.

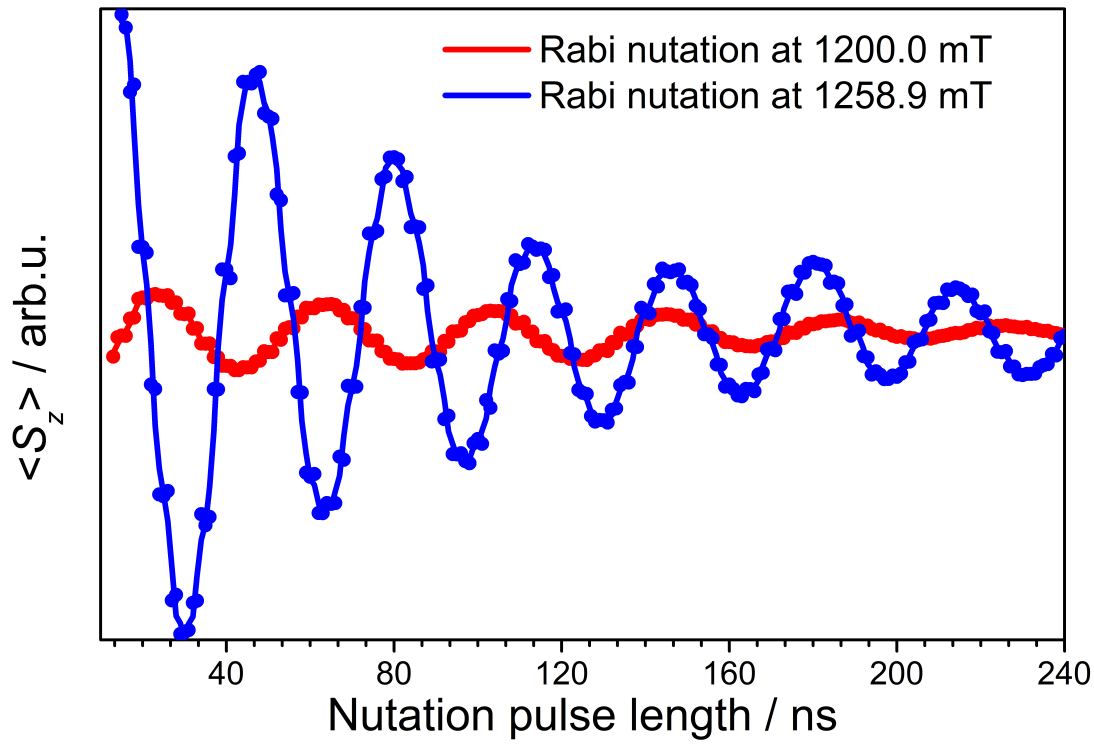

Figure 3.7.: Rabi nutation experiments of 1 mM **Cr-D** in **sol-H** at 7 K, 35 GHz, 1258.9 mT (blue dotted line) and 1200.0 mT (red dotted line).

Here, the integrated echo intensity, which correlates with the samples-magnetization in z-direction, oscillates as the nutation pulse length is increased. The observation of Rabi nutations already proves that coherent manipulations of at least two states are possible. In Figure 3.8, the fast Fourier transform of both oscillations is shown. The magnetization oscillates with $\omega_{\text{nut,central}}/2\pi = 31(1)$ MHz at the central line and with $\omega_{\text{nut,flank}}/2\pi = 26(1)$ MHz at the flank.

The frequency of nutation ω_{nut} is related to the excited transition according to the equation [42]

$$\omega_{\text{nut}}(m_s, m_s+1) = \frac{g\beta_e B_1}{\hbar}\sqrt{S(S+1) - m_s(m_s+1)} \tag{3.3}$$

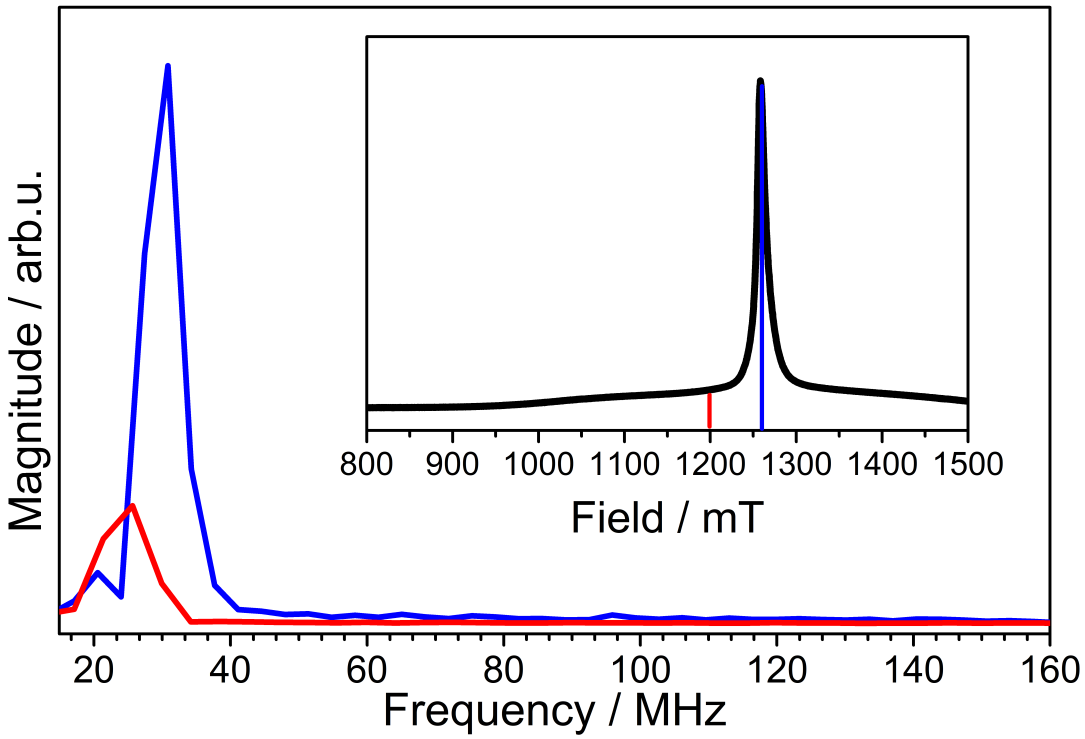

Figure 3.8.: FFT of the Rabi nutation experiments shown in Figure 3.7. The red line corresponds to the measurement at 1200 mT and the blue line to the one ate 1258.9 mT.

Following this equation, transitions inside the $m_s = \pm 1/2$ manifold should have a Rabi frequency 1.15 times larger compared that of transitions between the $m_s = \pm 1/2$ and $m_s = \pm 3/2$ manifolds. $\frac{\omega_{\text{nut,central}}}{\omega_{\text{nut,flanks}}} = 1.19(8)$ further confirms that intra doublet transitions are excited at the central line and transitions between the manifolds at the flanks.

The Rabi nutation measurements already show that the chromium complex can be potentially used as a qubit or even as a qudit. In the next section, the relaxation times of the system will be investigated which are important for a potential application as a qubit.

3.4.3. Relaxation times measurements

To determine the relaxation times T_1 and T_m, Hahn-echo decays respectively inversion recovery experiments were performed. Those relaxation times are important properties of a qubit as they corresponds to the lifetime of classical information (T_1) and quantum information (T_m) in a qubit.

The experiments were performed on all four compound/solvent combinations at temperatures between 7 K and 80 K at a field of 1258.9 mT (central line). Figure 3.9 shows the Hahn-echo decays at 7 K. As the inter pulse delay τ is increased, the echo intensity decreases. Each decay is superimposed by an oscillation at short values of 2τ.

The oscillation is attributed to Electron Spin Echo Envelope Modulation (ESEEM) caused by nuclear spins in the direct vicinity of the chromium. The frequency spectrum of the ESEEM was obtained by applying a FFT to the decays after subtracting the decaying background and is shown in Figure 3.9 as well. Peaks at 3.2 MHz and 12.9 MHz occur. These frequencies are attributed to the double quantum transitions $\omega_\text{dq}(m_s)$ of the coordinating ^{14}N nuclear spins. These transitions are insensitive regarding the orientation of the molecule to the magnetic field. Thus, they do not smear out in a frozen solution. The strong modulation depth implies that the condition of cancellation, where half the hyperfine interaction constant $a_\text{iso}/2$ is equal to the nuclear Larmor frequency $\omega_{^{14}\text{N}}$, is (nearly) fulfilled and the quadrupole interaction is of the same order of magnitude compared to both of these quantities [42, 85]. The frequencies of $\omega_\text{dq}(m_s)$ can be calculated with the equation

$$\omega_\text{dq}(ms) = 2\sqrt{(m_s a_\text{iso} + \omega_{^{14}\text{N}}) + K^2(3+\eta^2)} \tag{3.4}$$

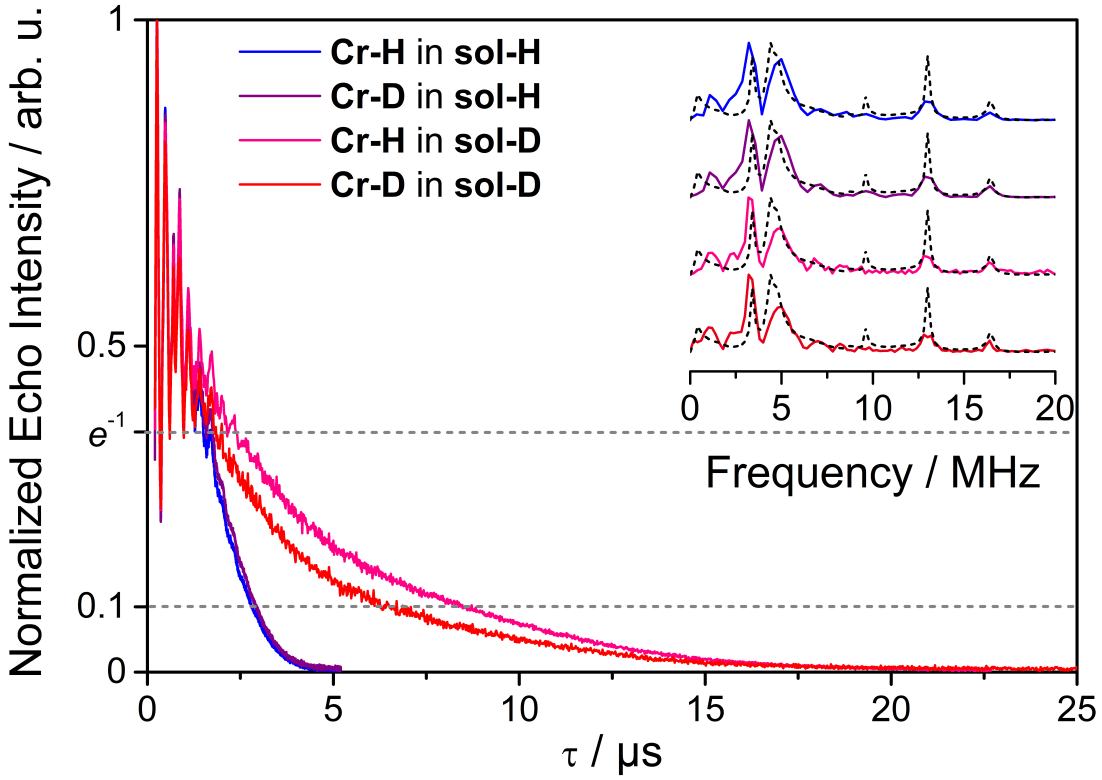

Figure 3.9.: Hahn-Echo decays of 1 mM **Cr-H**/**Cr-D** in **sol-H**/**sol-H** at 7 K, 35 GHz and 1258.9 mT. The inset shows the FFT of the oscillations (ESEEM) after subtraction of the exponential background. An simulation (see text for further information) of the frequency spectrum of the ESEEM (black dashed line) is shown as well.

In the previous section it was shown that mainly transitions in the $m_s = \pm 1/2$ manifold are excited at the central line. Thus, a hyperfine interaction $a_{\mathrm{iso}} = 5.12$ MHz can be calculated from the observed double quantum transitions estimating the quantity $K^2(3+\eta^2)$ of the quadrupole tensor to 1 MHz^2 which is a typical value for ^{14}N [85]. Indeed, a simulation (black dotted line in Figure 3.9) performed with *Easyspin* using $K = 0.58$ MHz and $\eta = 0.9$ perfectly fits to the observed frequency spectrum. The ESEEM frequency spectrum does not change upon deuteration of the compound or solvent. Therefore it can be deduced that the electron spin density is negligible on the protons/deuterons of the complex.

The Hahn-echo decays of the compounds in **sol-D** decay more slowly than the ones of the compounds in **sol-H**. Furthermore, the deuteration of the ligand seems to have no significant effect on the decays in **sol-H** and only a minor one in case of **sol-D**. Deuteration of the solvent reduces the effect of Nuclear Spin Diffusion (NSD) caused by protons which is often one of the main contributor to the Hahn-echo decay. In a nutshell [19, 42, 86, 87], energy conservative nuclear spin flip-flops between bath nuclei with the same Larmor frequency change the precession frequency of the electron spin after the $\pi/2$ pulse. As this is a dynamic process, it can not be refocused with the π pulse. This mechanism depends on the dipolar coupling between the nuclear spins themselves and between the nuclear spins and the electron spin. As the gyromagnetic ratio of deuterium is about six times smaller compared to protons, the dipolar couplings are decreased as well which leads to smaller contribution of NSD to the phase memory time. NSD depends on the bath nuclei and thus it is not surprising that the deuteration of the ligand has only a minor effect. In fact, T_{m} is longer for **Cr-H** in **sol-D** compared to its partially deuterated analog. Most recent investigations [88] show that partially replaced protons in the ligand of a metal complex can lead to either a increase or decrease of the characteristic decay time depending on the pattern in which protons are being replaced.

The decays themselves can be fitted with the equation of a stretched exponential decay in case of the compounds in **sol-H**

$$I(\tau) = Ae^{-\left(\frac{2\tau}{T_{\mathrm{m}}}\right)^k} \tag{3.5}$$

while the decays in **sol-D** can be fitted with a monoexponential decay ($k = 1$). The fitting parameters are summarized in Table 3.1. The longest phase memory time $T_{\mathrm{m}} = 8.4$ µs is reached for **Cr-H** in **sol-D** which is about a factor of four times longer compared to similar, largely nuclear spin free chromium complexes $K_3[Cr(C_2O_4)_3]$ (2.79 µs at 213.0 mT and 5 K) [75] and $(PPh_4)_3[Cr(C_3S_5)_3]$ (1.81 µs at 350.0 mT and 5 K) [74]. Compared to **Cr-H** and **Cr-D**, the trisoxalate ($D = 0.71$ cm^{-1}) and tristhiolate ($D = 0.33$ cm^{-1},

($E = -0.11$ cm^{-1})) complexes exhibit a larger ZFS. T_m is governed by fluctuating fields which can be induced by ZFS modulation. A weaker ZFS would lead to a smaller modulation amplitude which could be beneficial for longer coherence times, thus a small zero field splitting can be a design criterion for molecular quantum bits with $S > 1/2$.

Table 3.1.: Fitting parameters of the Hahn-echo decays shown in Figure 3.9 fitted with equation 3.5. k was fixed to 1 for the compounds in **sol-D**. Furthermore, the time $T_{m,10\%}$ where the decays decreased to 10% of their initial intensity are given.

	Cr-H/sol-H	**Cr-D/sol-H**	**Cr-H/sol-D**	**Cr-D/sol-D**
T_m / µs	4.47(3)	4.24(4)	8.4(1)	6.629(5)
k	2.29(6)	2.09(5)	1	1
$T_{m,10\%}$ / µs	5.60	5.83	16.96	12.56

A stretch factor $1 < k < 4$ indicates that nuclear spin diffusion is the main cause of decoherence [86, 87]. The stretch factor $1 < k$ arise from the non-Markovian dynamic of nuclear spin diffusion. Usually, T_m increases by a factor of six to ten [17, 28] upon deuteration of the host solvent/material. In this case, however, T_m increase only a factor of about 1.5 to 2 depending on the compound. The reason for this behavior is that the type of decay changes from a stretched exponential to a monoexponential decay. $T_m/2$ marks the time when the intensity $I(\tau)$ decreases to I_0/e. A stretched exponential with $k > 1$, however, decays slower than a monoexponential decay as long as $\tau < T_m/2$ and faster when $\tau > T_m/2$. In Figure 3.9 it can be seen that all decays decayed to $1/e$ at similar times but in the case of **sol-D** the tail is much longer. To avoid ambiguities when talking about numbers only, it was suggested [89] to compare the times $T_{m,10\%}/2$ where $I(\tau) = I_0/10$ and therefore the effect of a stretch factor is nearly canceled out. This numbers are given in Table 3.1 as well. Here, the effect of deuteration is more pronounced as the relaxation times increase by a factor of 2 to 3 upon deuteration. Still, the deuterated solvent does not increase T_m as expected. Therefore, other relaxation mechanism might contribute to the latter. This is further substantiated by the fact that the decay changes to a monoexponential decay upon deuteration. Recent investigations [89] suggest that a time dependent zero field splitting caused by molecular rotation and vibration influences T_m even in frozen solution at cryogenic temperatures which might be the additional source of decoherence.

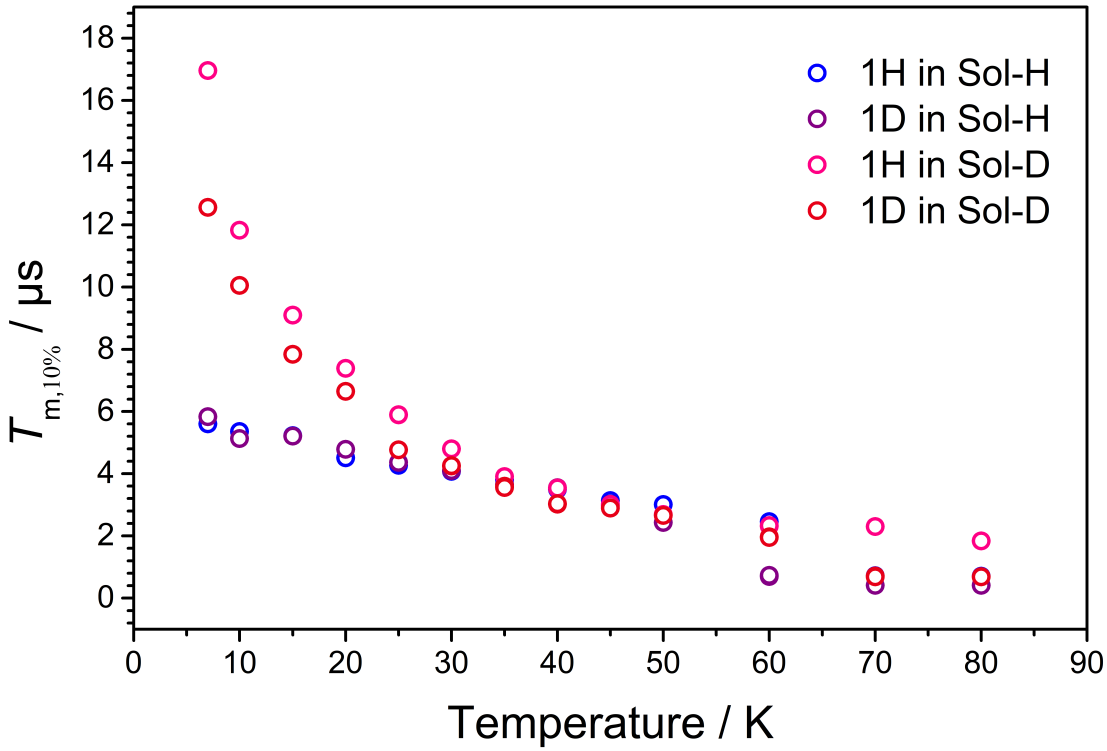

Figure 3.10.: Temperature dependence of the time $T_{m,10\%}$ of 1 mM **Cr-H**/**Cr-D** in **sol-H**/**sol-H** at 35 GHz and 1258.9 mT.

Figure 3.10 shows the temperature dependence of $T_{m,10\%}$ of all solvent/compound combinations. While the measurements in **sol-H** show a nearly temperature independent behavior, $T_{m,10\%}$ measured in **sol-D** is much more temperature dependent up to 35 K. Above this temperature, the solvent seems to have no effect anymore. This further supports the hypothesis that time dependent zero field splitting caused by molecular rotation and vibration plays an important role as it is strongly dependent on the temperature. At least, a temperature dependent effect on T_m is observed. The effect is not visible in **sol-H** as the NSD outweighs it in that case.

Compared to the Hahn-echo decays, the inversion recovery experiments are rather featureless as this type of experiment is not sensitive to the hyperfine field of nuclear spins. Monoexponential decays at all temperatures regardless of the degree of deuteration are observed (see Appendix Figure A.3-A.6). Furthermore, the extracted spin lattice relaxation time T_1 does not change significantly with respect to the solvent/compound combination. The temperature dependent behavior of T_1 together with T_m is shown in Figure 3.11

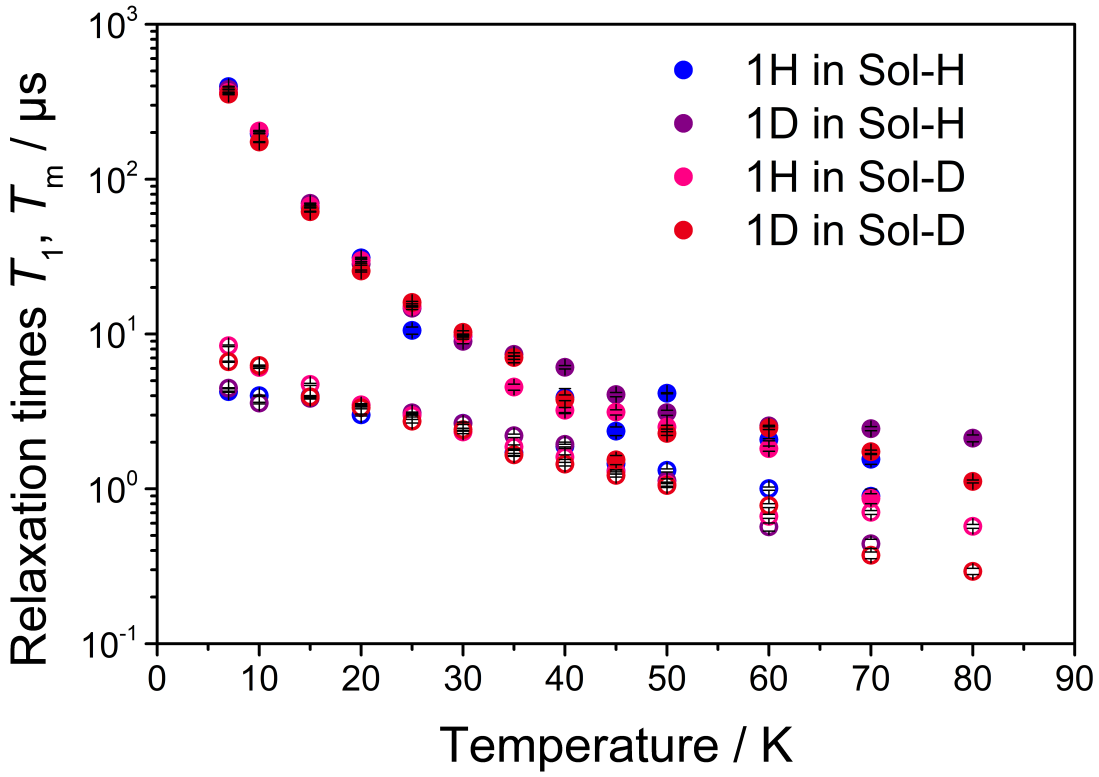

Figure 3.11.: Temperature dependence of the relaxation times T_1 and T_m of 1 mM **Cr-H**/**Cr-D** in **sol-H**/**sol-H** at 35 GHz and 1258.9 mT.

At 7 K a $T_1 \approx 400$ µs is observed which decreases to about 10 µs at 35 K. Above this temperature, T_m is dominated by T_1 which explains why $T_{m,10\%}$ does not depend on the solvent above this temperature. At temperatures above 80 K, the signal-to-noise is to low for a reliable measurement. The temperature dependence further shows that for a potential application of this qubit, the temperature should be at or below the temperature of liquid nitrogen (77 K) in order to have a reasonable coherence time.

To sum it up, the pulsed EPR measurements revealed one of the longest reported coherence time ($T_m = 8.4$ µs at 7 K of **Cr-H** in **sol-D**) of a chromium complex. In the protonated solvent NSD is the main decoherence source indicated by a stretched exponential decay with a stretch factor $k \approx 2$. Using a deuterated solvent improves T_m about a factor of two which is less compared to the usually reported [17, 28] factor of six. An additional temperature dependent contribution to T_m was found which explains weaker impact of using a deuterated solvent. Above temperatures of 35 K, T_m is bound by T_1. The partial deuteration of **Cr-H** has only a very minor effect on the relaxation times.

The investigations presented in this section demonstrated the qubit potential of **Cr-H**. In the next section, the combination of optical and EPR spectroscopy was employed in an attempt to ultimately read out the spin state using light in the visible/NIR region.

3.5. Combined optical and EPR spectroscopy

Besides the remarkable qubit properties of **Cr-H**, the complex has very interesting and promising optical properties. Upon excitation with blue light (about 435 nm), the complex emits in the NIR-Region (776 nm and 736 nm) with a remarkable lifetime $\tau = 1164$ µs and a quantum efficiency of $\phi = 14.2\%$. The optical properties were studied extensively [77, 90] and are summarized in the Jablonski diagram shown in Figure 3.12.

The complex can be excited from its ^4A_g ground state to $^4T_{2g}$ excited state (O_h notation). From the $^4T_{2g}$ excited state, an Inter System Crossing (ISC) happens to the systems doublet states. It was shown by transient UV/Vis-spectroscopy [90] that the ISC takes only a few picoseconds. After vibronic relaxation, the system relaxes from the doublet states $^2T_{1g}$ and ^2E_g back to the ground state via phosphorescence. Any back-ISC is prevented because of the very large energy difference between quartet and doublet states and thus the quantum efficiency is very high. It was speculated that the ISC populates $^2T_{2g}$ as well from which the system undergoes an Internal Conversion (IC) to ^2E_g.

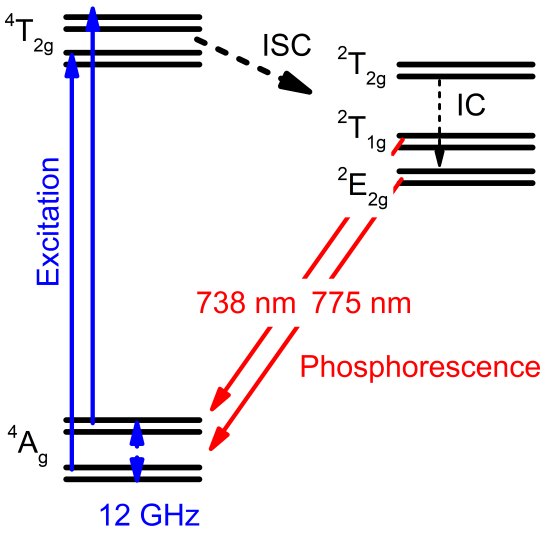

Figure 3.12.: Jablonski diagram of **Cr-H** based on the optical investigations presented in [77, 90]

In this section, the possibility of combining EPR and optical spectroscopy on **Cr-H** is explored. This combination is very promising, as it was shown a that single spin can be readout with optical light in favorable cases [34]. First, it was tried to optically detect the EPR transitions in the ground state and thus to read out the spin state via light. Here, two approaches utilizing the MCD effect respectively the phosphorescence in the complex were employed. Second, experiments on **Cr-H** in **sol-D** were performed on a pulsed EPR spectrometer which allows optical excitation with short laser pulses. The goal of this investigation was to investigate the spin dynamics of the complex in the exited ^2E_g state.

3.5.1. Magnetic circular dichroism spectroscopy

MCD is a great tool for investigating dd-transitions in metal ions as it offers a higher resolution in energy due to the signed nature of the MCD quantity. This allows to unravel broad absorption bands into their single components. Furthermore, the MCD effect depends on the magnetization of the sample. This allows in principle to detect the spin state of the complex as the magnetization depends on the spin state.

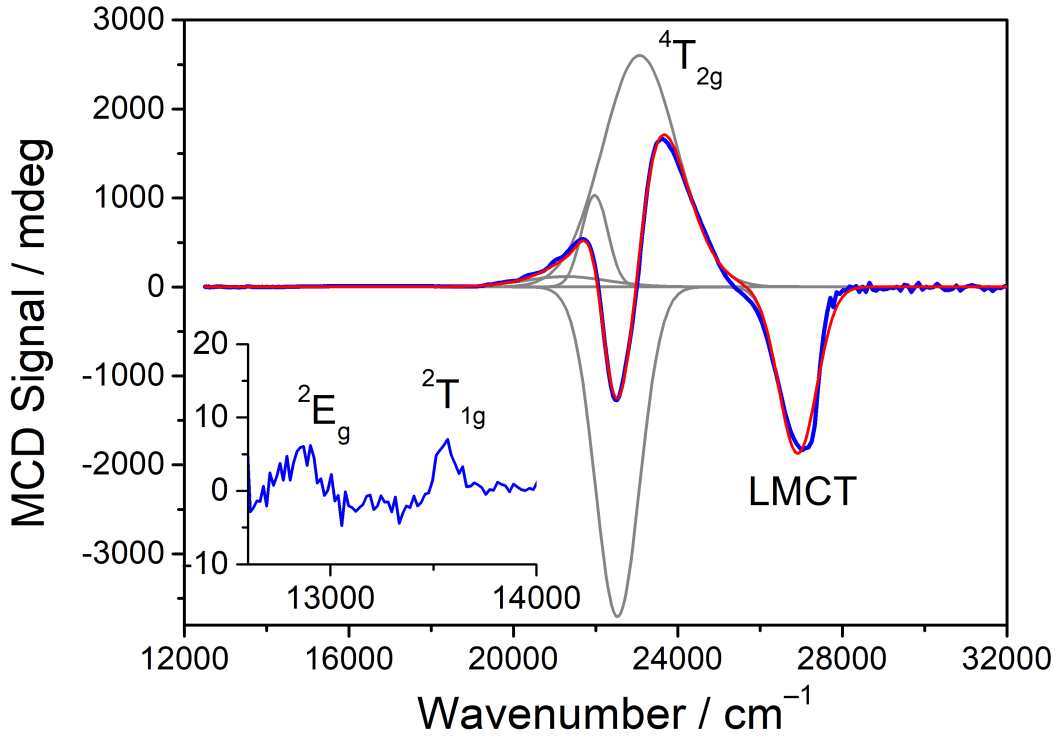

Figure 3.13.: MCD spectrum (blue line) of a frozen solution of 5 mM **Cr-H** in **sol-H** at 7 T and 7 K. The spectrum was fitted with three gaussians (red line). The single gaussian peaks are shown as well (grey lines). The inset shows two spin forbidden transitions (blue line) in the NIR region.

As a preparation for optical spin read out via the MCD effect, a MCD spectrum of 5 mM **Cr-H** in **sol-H** at 7 T and 7 K between 12500 cm^{-1} and 33333 cm^{-1} (300 nm and 800 nm) was recorded. The spectrum and its Gaussian deconvolution is shown in Figure 3.13. At lower energies, two sharp but weak bands are observed at 12887 cm^{-1} (776 nm) and 13568 cm^{-1} (737 nm). At higher energies, one broad band split in three components is observed at around 23000 cm^{-1} (435 nm). A Gaussian deconvolution of the spectrum yields the energies 21976 cm^{-1}, 22530 cm^{-1} (negative sign) and 23071 cm^{-1} of the three components. The band with the highest energy is observed at 27027 cm^{-1} (370 nm).

Cr-H was already characterized by UV/Vis-spectroscopy in great detail [77]. Three sharp and weak bands measured in a single crystal of **Cr-H** were observed at 776 nm, 736 nm and 697 nm. They were attributed to the spin forbidden $^4A_g \rightarrow {}^2E_g$, $^2T_{1g}$ and $^2T_{2g}$ (O_h notation) transitions. Two of this transitions are observed in the MCD spectrum as well (^2E_g at 12887 cm^{-1} and $^2T_{1g}$ at 13568 cm^{-1}). In the UV/Vis studies, a broad band at 435 nm was observed as well which was attributed to the $^4T_{2g}$ transition. Here, the MCD measurements allow to unravel this band into the three $^4T_{2g}$ components. These are split in energy as the complex possess D_2 symmetry instead of a O_h symmetry.

The zero field splitting parameters D and E can be derived (see Appendix Section A.1.2 for a detailed derivation) from the three components of the $^4T_{2g}$ transition with the equation

$$D = \frac{1}{2}\zeta^2 \left(\frac{8}{\Delta E_1} - \frac{4}{\Delta E_2} - \frac{4}{\Delta E_3} \right) \tag{3.6}$$

$$E = \frac{1}{2}\zeta^2 \left(\frac{4}{\Delta E_2} - \frac{4}{\Delta E_3} \right) \tag{3.7}$$

ΔE_1, ΔE_2 and ΔE_3 corresponds to the highest, midst and lowest transition energy of the $^4A_g \rightarrow {}^4T_{2g}$ band and $\zeta = 273$ cm^{-1} is the spin-orbit coupling constant of the free chromium(III) ion. The zero field splitting parameters $D = 0.48$ cm^{-1} and $E = 0.15$ cm^{-1} can be calculated from the MCD spectrum which is in a reasonable agreement with the EPR measurements and reflects again the strong rhombicity.

To sum it up, MCD measurements were carried out on **Cr-H** in **sol-H** in the UV-/Vis-/NIR- region. The transitions were assigned to the according dd-transitions occurring in the system. The splitting of the $^4T_{2g}$ state was resolved and connected to the zero field splitting in the system. The possibility of optically detected EPR measurements utilizing the MCD effect will be explored in the next section.

3.5.2. Optically detected EPR

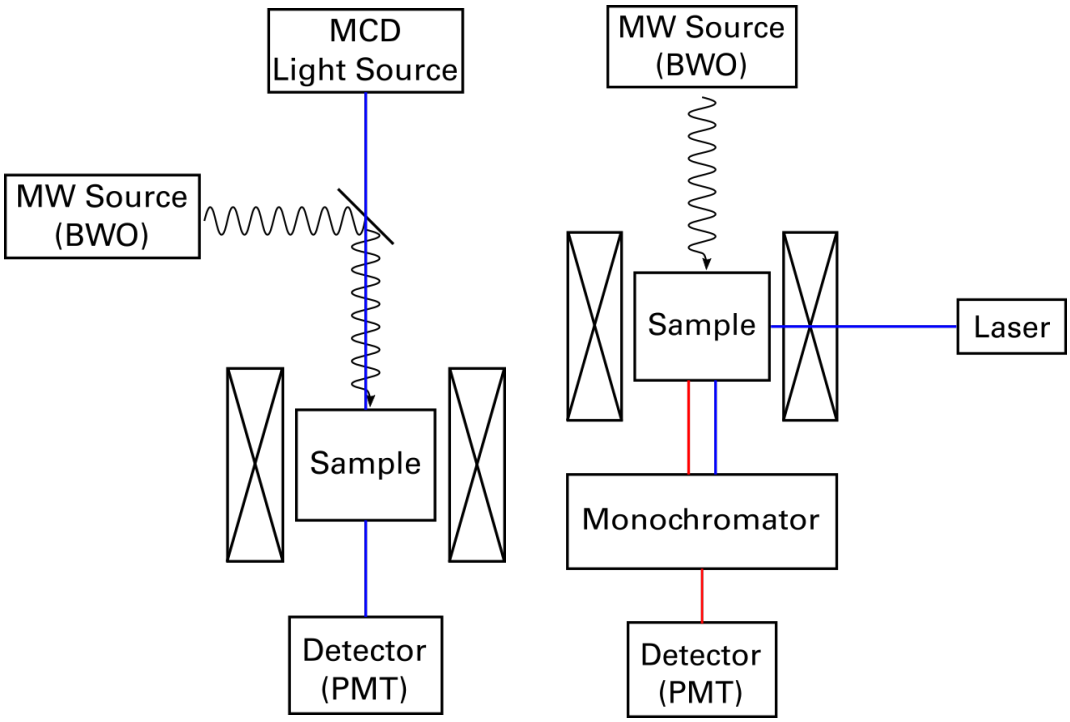

(a) MCD detected EPR setup **(b)** Luminescence detected EPR setup

Figure 3.14.: Schematics of the two ODMR setups used to investigate **Cr-H**

Optically detected EPR (ODMR) covers methods which indirectly detect EPR transitions with light in the UV/Vis/NIR region. Several optical properties, like the MCD effect [91–93] or luminescence from the sample [34, 94, 95], may be used for detection. Regardless of the exact mechanism of employed ODMR method, spin-orbit coupling is always necessary as it couples electronic transitions with spin transitions. ODMR is a very appealing technique for spin based quantum computing as it was demonstrated that it is possible [34, 94] to read out a single spin and thus a single qubit.

Several attempts were made to perform combined optical and EPR spectroscopy on **Cr-H**. Figure 3.14 shows the two setups which were used to combine both types of spectroscopy.

The first setup shown in Figure 3.14a includes the MCD spectrometer used to record the MCD spectrum in section 3.5.1. An additional ITO-Mirror, which lets UV/Vis-light pass but reflects microwaves, was put in the beam path of the spectrometer. Microwaves with a frequency of 147 GHz generated by a Back Wave Oscillator (BWO) and collimated by three Teflon lenses were focused on the sample with the help of this additional mirror.

The second setup shown in Figure 3.14b includes a superconducting magnet with four optical windows. One window was used to apply microwaves generated by a BWO in a quasi optical fashion. A 5 mw cw laser with a wavelength of 450 nm was used to irradiate the sample through the second window. Light coming from the sample was collected by a luminescence spectrometer, a longpass filter (550 nm) was put in front to exclude the laser radiation.

In the end, it was not possible to indirectly detect EPR via MCD effect or the luminescence. Nevertheless, the experiments performed on both setups will be presented in the following two sections together with an analysis why the experiments failed.

MCD detected EPR

The basic working principle of MCD detected is quite simple. The intensity of an MCD signal (the difference between the absorption of left and right circular polarized light) depends to the sample magnetization. The magnetization can be partially quenched by exciting an EPR transition in the system. The quench depends on the microwave power and spin relaxation time [91] of the investigated compound. Thus, if the EPR transition is excited, the MCD signal intensity will decrease. This technique was demonstrated for transition metal ions [91, 92] and lanthanides [93]. Usually, low microwave frequencies and fields are employed and cavities are used to enhance the microwave field at the sample. Here, microwaves with a frequency of 147 GHz are applied in a quasi optical way at high fields and without a cavity.

A 1 mM solution of **Cr-H** in **sol-H** sample was mounted in the setup. The quasi optical elements of the BWO assembly including the ITO-Mirror were adjusted by maximizing the radiation intensity after the sample with the help of a Golay cell. The sample's MCD signal intensity at 468 nm and 10 K was monitored while the sample was simultaneously irradiated with 147 GHz microwave radiation. The magnetic field was swept from 4 T to 6 T and again back to 4 T. The measurement is shown in Figure 3.15.

The MCD signal intensity increases upon increasing the magnetic field. This is expected as the samples magnetization increases as well. However, no drop in intensity can be observed which would indicate an EPR transition. The measurements were repeated for different MCD transitions occurring in **Cr-H** and at different temperatures. No EPR signal was observable at all.

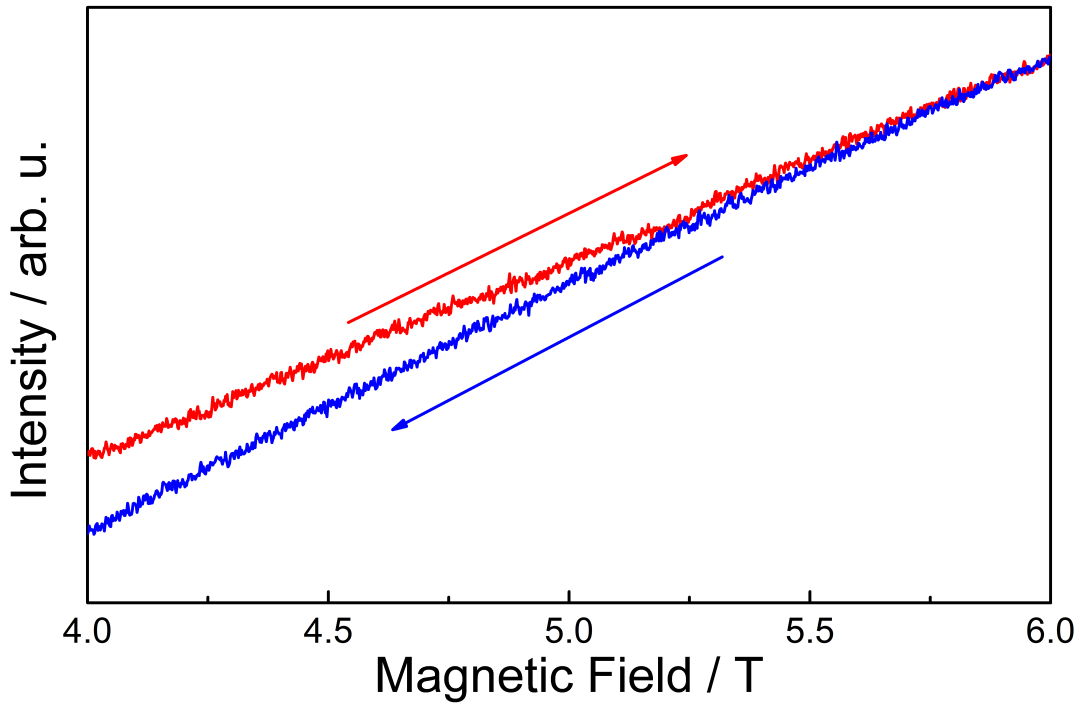

Figure 3.15.: MCD signal intensity of 1 mM **Cr-H** in **sol-H** with respect to a magnetic field sweep from 4 T to 6 T (red line) and back to 4 T (blue line). Microwave radiation with a frequency of 147 GHz was applied simultaneously.

The reason why no EPR signal was observable is most likely due to a too low microwave power. The BWO has a maximum output power of 20 mW at 147 GHz. Although no equipment was available to measure the power directly, measurements with a Golay cell indicate that not more than 1% of the available power reaches the sample. Thus, the change of the MCD signal is most probably below the noise level. Narrowbanding techniques like a Lock-In detection could circumvent that problem. However, it is not possible to directly access the MCD signal from the commercial spectrometer.

Therefore, it was tried to optically detect the EPR transition by monitoring the phosphorescence of the complex instead of the MCD effect.

Luminescence detected EPR

Optical detected EPR via luminescence received a high attention after it was demonstrated [34] that it is possible to detect the spin state of a single Nitrogen Vacancy (NV)-center in diamond. The working principle behind this technique can be explained by the Jablonski diagram of this defect shown in Figure 3.16a. The NV-Center can be excited to the ^{3}E state from the $^3A_2$ ground state with green (546 nm) light while preserving the magnetic state characterized by m_s. From the excited ^{3}E state the system can either undergo an ISC to a singlet state or relax back to $^3A_2$ via fluorescence (689 nm). The rate of the ISC strongly depends of the magnetic state and is much higher in case of $m_s = \pm 1$. After the ISC and an additional IC, the system relaxes back to $^3A_2$ via an ISC where the $m_s = 0$ state is populated exclusively. Due to this cycle, NV-Centers with $m_s = 0$ in the ground state have a higher chance to fluoresce then the ones with $m_s = 1$. The m_s state may be changed by applying microwaves with the appropriated energy which changes the fluorescence intensity. The cycle is still working in the presence of a magnetic field which lifts the degeneration of the $m_s = 1$ doublet.

The Jablonski diagram of **Cr-H** is shown again in Figure 3.16b. Similar to a NV-Center, the chromium complex can be excited with visible light (435 nm) from ^4A_g to $^4T_{2g}$. From this state, the system undergoes an ISC to either ^2T_1g or ^2E_g. At last, the system relaxes back to the ground state via phosphorescence. Only a very weak fluorescence from $^4T_{2g}$ was reported which means that the ISC is very efficient. The setup shown before in Figure 3.14b was used to monitor the phosphorescence upon applying a magnetic field and microwaves in order to check a magnetic state dependency of the phosphorescence similar to the fluorescence in NV-centers. The functionality of the setup was checked by Dennis Schäfter during his research internship with a NV-diamond sample from the Wrachtrup Group of the University of Stuttgart.

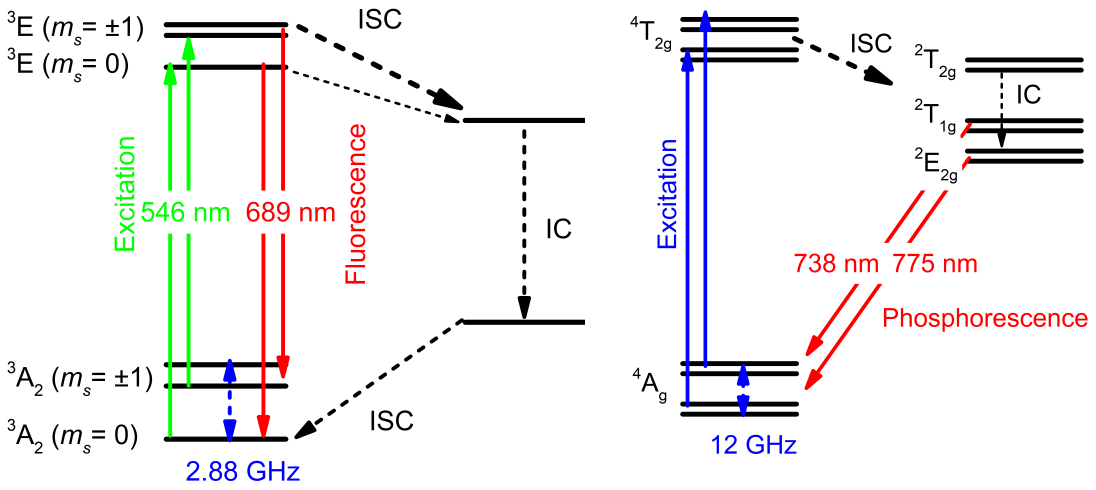

(a) Jablonski diagram of NV-centers in diamond based on [96].

(b) Jablonski diagram of **Cr-H** based on the optical investigations presented in [77, 90].

Figure 3.16.: Jablonski diagram of NV-centers in diamond (left) and of **Cr-H** (right).

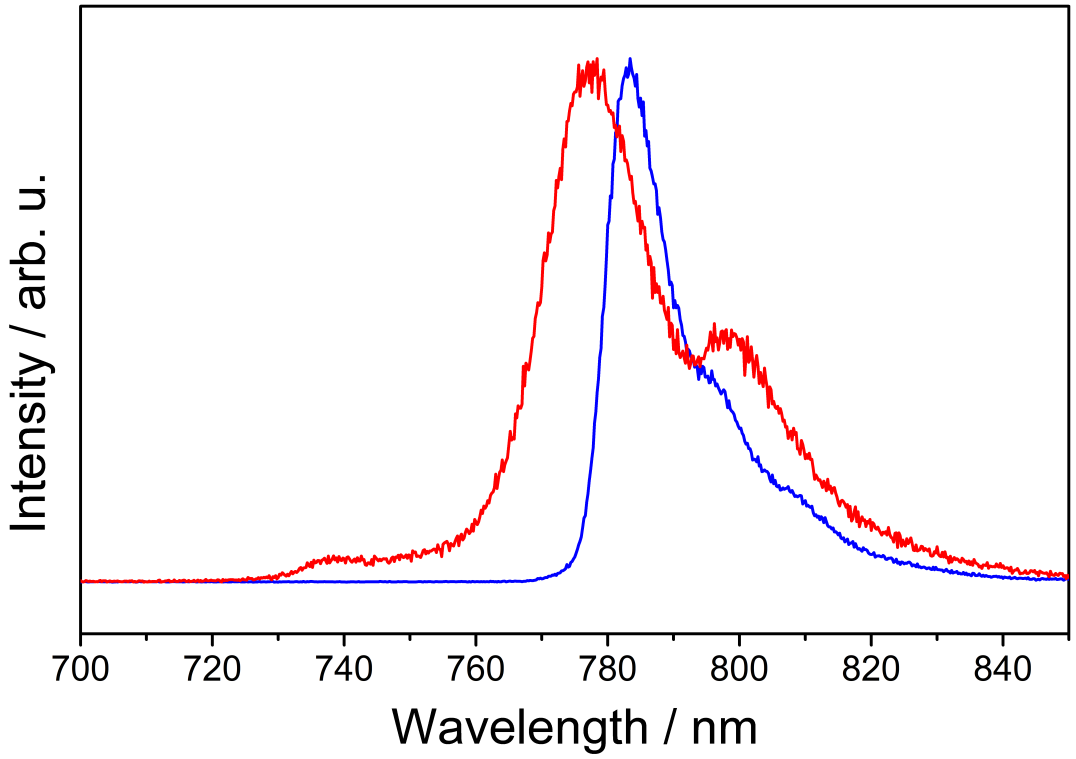

Figure 3.17.: Emission spectra of a **Cr-H** powder sample at 300 K (red) and 1.8 K (blue) in the luminescence detected EPR setup. The sample was excited with a 5 mW 450 nm laser.

First, a powder sample of **Cr-H** was mounted in the setup and excited by a 450 nm, 5 mW laser. The luminescence coming from the sample was collected by collimating the light using a plano-convex lens and filtered by a 550 nm longpass filter. The residual light was focused into a *AMINCO Bowman II* luminescence spectrometer. Figure 3.17 shows two emission spectra, one at 300 K and the other one at 1.8 K. The slit width of the monochromator was set to 2 nm. The spectrum at room temperature features three bands, a shoulder at 737 nm and two peaks at 776 nm and 800 nm. At 1.8 K, narrowing and a red shift of the peak at 776 nm can be observed while the shoulder at 737 nm vanishes.

The two spectra are in a good agreement with the already published [77] ones where the shoulder at 737 nm is attributed to the emission from $^2T_{1g}$ and the peak at 776 nm to the emission from ^2E_g. The peak at 800 nm may be attributed to a transition to a vibrationally exited ground state. As this peak was not observed before for this compound, it may originate from some glass impurities in the setup itself.

The emission at 776 nm and 737 nm coming from the sample was monitored upon the application of a magnetic field. Between 0 T and 7 T, no change of the emission intensity was observed. Furthermore, the sample was irradiated with 147 GHz microwave radiation coming from a BWO. No sign of an EPR transition was observed by sweeping the magnetic field between 0 T and 7 T. Beside the powder sample, a single crystal of **Cr-H** recrystallized from acetonitrile was investigated. Again, no magnetic field dependence or any sign of EPR transition in the emission could be observed. The reason for the absence of any spin state dependence might be explained as follows. Compared to the NV-Center, the ISC is very efficient in transition metal complexes. In fact, ISC in **Cr-H** happens on a picosecond time scale [90]. In contrast, the phosphorescent decay from ^2E_g happens on a millisecond time scale and therefore is the rate-determining step. Thus, even if the ISC is spin state sensitive like in NVCs, it would not be noticeable as the final emission rate is dominated by the ^2E_g decay rate. Furthermore, the phosphorescence rate is about 1 ms which is actually longer than the spin lattice relaxation rate in the ground state. Thus, even if the spin state is preserved in the ^2E_g state, it will most probably thermalize before the phosphorescent decay to the ground state. To sum it up, it was not possible to detect any magnetic field or spin state dependence of the phosphorescence from ^2E_g of **Cr-H** by exciting the $^4T_{2g}$ state using a 450 nm laser. In order to verify the assumption that spin lattice relaxation in the ^2E_g state is to fast in order to enable an optical readout, the ^2E_g state was investigated by the means of pulsed EPR combined with optical excitation in the next section.

3.5.3. Pulsed EPR with laser excitation

The lifetime of the ^2E_g state of **Cr-H** was determined to $\tau = 1164$ µs in **sol-D** and thus could be potentially investigated with pulsed EPR, which operates on a nanosecond time scale. Therefore, **Cr-H** was investigated in a pulsed EPR spectrometer capable of exciting the sample with visible light. The measurements were performed by Daniel Nohr in the group of Prof. Stefan Weber at the University of Freiburg.

A 5 mM frozen solution of **Cr-H** in **sol-D** was investigated at 7 K and 33.75 GHz. An ESE-detected spectrum between 6000 G and 15000 G was recorded, while the sample was excited with a 10 ns laser pulse with 435 nm and a pulse energy of 250 µJ directly before the Hahn-echo sequence. In a second measurement, no laser pulse was applied. Both spectra are shown in Figure 3.18.

The spectra look basically identical as the already presented one in section 3.4.1. Two broad flanks and a sharp central peak are observed. The intensity of the latter is smaller compared to the already presented spectrum. Furthermore, three sharp peaks are observed which are attributed to impurities inside the spectrometer. The spectrum with laser excitation exhibits an overall weaker intensity compared to the one without an applied laser pulse. To illustrate this behavior, a subtraction of both spectra is shown as well.

The intensity of the central line is weaker due to a blind spot caused by the nitrogen ESEEM and the chosen inter pulse delay of $\tau = 400$ ns. This was done on purpose in order to decrease the intensity of the ground state EPR spectrum. Although the laser pulse reversible quenches the ground state EPR spectrum, no additional signal from the ^2E_g state can be observed. In ruby [95], the principal values $g_{\parallel} = 2.445$ and $g_{\perp} \geq 0.16$ of the g-tensor in the ^2E_g were determined. As a frozen solution was investigated, this leads to a rather broad spectrum. Furthermore, spin lattice relaxation in the ^2E_g state might be just to fast in order to record a spectrum with pulse EPR.

To sum it up, a reversible quenching of the ground state EPR signal of **Cr-H** in **sol-D** was observable after the application of a 435 nm laser pulse. However, no EPR signal of the ^2E_g state could be observed. The reason for this might be a large g anisotropy of this excited state combined with a fast spin relaxation rate. This further substantiate the assumption that spin lattice relaxation rate in ^2E_g is to fast for an optical readout of the spin state.

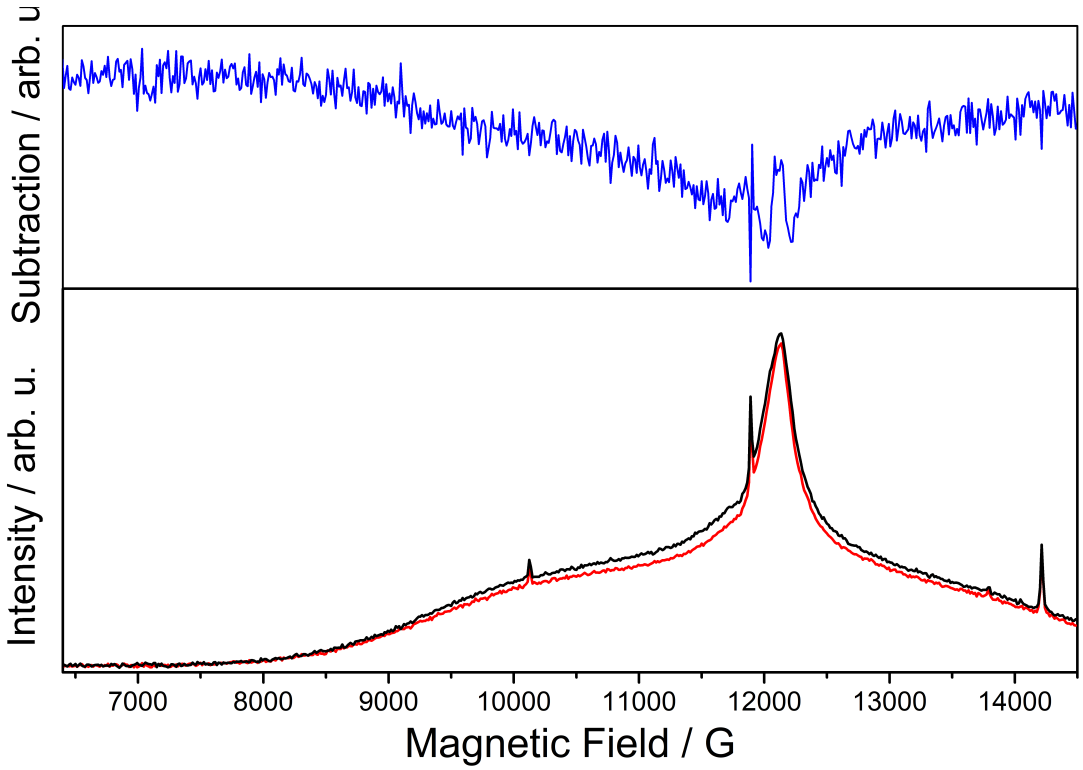

Figure 3.18.: ESE-detected EPR spectrum (blue dots) of 1 mM **Cr-H** in **sol-D** at 7 K and 33.75 GHz with (bottom, red line) and without (bottom, black line) laser excitation at 435 nm directly before the Hahn-echo sequence. A subtraction of the spectrum without excitation from the spectrum with excitation is shown as well (top, blue line)

3.6. Conclusion

Within this chapter, a comprehensive investigation of $[Cr(ddpd)_2][BF_4]_3$ in terms of its magnetic, optical and qubit properties was presented. SQUID and HFEPR measurements revealed a small ZFS with large rhombicity characterized by the parameters $D = 0.18 \pm 0.02$ cm^{-1} and $E = -0.06 \pm 0.005$ cm^{-1}. This was verified by MCD measurements, were the dd transitions were related to the magnetic properties of the complex. These findings suggest that the compound can not only be used as a qubit with two, but rather a qudit with four accessible quantum states. Pulsed EPR measurements demonstrated that the complex has a very long coherence time $T_m = 8.4$ µs which is the longest coherence time presented for a chromium based MQB so far. The investigations further showed that the coherence time is not limited by nuclear spin diffusion but rather by a temperature dependent effect which may be related to a fluctuating ZFS. In the end, it was not possible to optically detect the spin state of the complex via luminescence from the ^2E_g state by exciting the compounds $^4T_{2g}$ state. The reason for this is most probably that any transition rates preceding the emission from ^2E_g are much faster than the latter. Thus, a spin dependent emission is only expected if ^2E_g is spin polarized by the pump cycle. Unfortunately, spin relaxation in ^2E_g seems to happen much faster than the emission from this state and thus any possible spin polarization is lost before emission occurs.

In future experiments, this may be tackled by two different approaches. First, a chromium(III) complex could be designed where the emission rate from ^2E_g is faster than the spin relaxation. The emission rate can be controlled by the ligand of the complex [97]. However, up to now there is no recipe how to increase the spin relaxation time in the ^2E_g state by ligand design. Another approach could be to mimic NVCs by using a chromium(IV) complex instead which has a $S = 1$ ground state. First experiments into this direction seem to be very promising [39].

4. Pulsed EPR on thin film samples

This chapter is based on the research paper

Measurement of Quantum Coherence in Thin Films of Molecular Quantum Bits without Post-Processing, Samuel Lenz, Bastian Kern, Martin Schneider and Joris van Slageren, *Chem. Commun.*, 2019, 55, 7163-7166

and uses parts of it. Martin Schneider from the Brno Technical University and Bastian Kern from the Max-Planck Institute for Solid State Research contributed to this publication by providing the first drawing of the Fabry-Pérot resonator respectively providing the thin film of copper(II) phthalocyanine on sapphire.

4.1. Introduction

Many advantages of MQBs have been impressively demonstrated. Chemical engineering has improved the coherence time of MQBs in a rational way [17, 19, 30, 31] from several microseconds to nearly one millisecond. It has been shown [67, 68] that it is possible to build up two qubit gates by molecular design and thus make universal quantum computing possible. However, nearly all investigations of MQBs have been carried out in either the bulk material [17, 19, 69–71] or (frozen) solutions [30, 31, 72].

In a working device, it is needed to address single qubits and thus an ordered structure is necessary. 2D-arrays are very promising candidates, as CMOS compatible structures to control and read out spin based qubits [98] have been proposed which require a ordered 2D qubit layer on silicon. Here, MQBs are very attractive as in contrast to defect centers in diamond or silicon, molecules can be placed on a surface with atomic precision [99]. Before building such a device, the properties of MQBs on a surface have to be understood as they could change drastically due to the surface interaction. MQB characterization is carried out almost exclusively by pulsed EPR spectroscopy. Therefore, this would be the method of choice investigating MQBs on a surface. However, there

is basically only one study [100], where the dynamic properties of the MQB copper(II) phthalocyanine on a surface are investigated by the means of pulsed EPR. Furthermore, the sample studied was prepared as a 400 nm thin film and thus consists of hundreds of layers of molecules which may screen any surface interaction. Last but not least, the sample had to be sliced and packed into a glass tube in order to fit into the sample compartment.

The main reason for this shortcomings is the resonator used in the commercial available pulsed EPR spectrometers. Typically, cylindrical resonators are employed which are perfect for small powder samples or solutions inside a glass tube. But, due to the magnetic field distribution of microwaves in such resonators, they are unsuitable for large, flat samples. Here, Fabry-Pérot resonators have been proven useful which has been demonstrated for 2D electron gasses in semiconductors [101, 102]. The magnetic field distribution in such resonators fits perfectly to large but flat samples as they can be easily placed on a flat metal surface (see Figure 4.1).

The goal in this part of the thesis is to develop a setup which is capable of measuring pulsed EPR on very thin films in order to understand the spin dynamics of MQBs on surfaces. Therefore, a Fabry-Pérot resonator for our home-built pulsed EPR spectrometer operating at 35 GHz [103] was designed, constructed and characterized. Utilizing the manufactured resonator, the spin dynamics of thin films of thicknesses down to 10 nm of copper(II) pthalocyanine and the α,γ-bisdiphenylene-β-phenylallyl-benzene radical (BDPA·Bz) in a polymer matrix were studied.

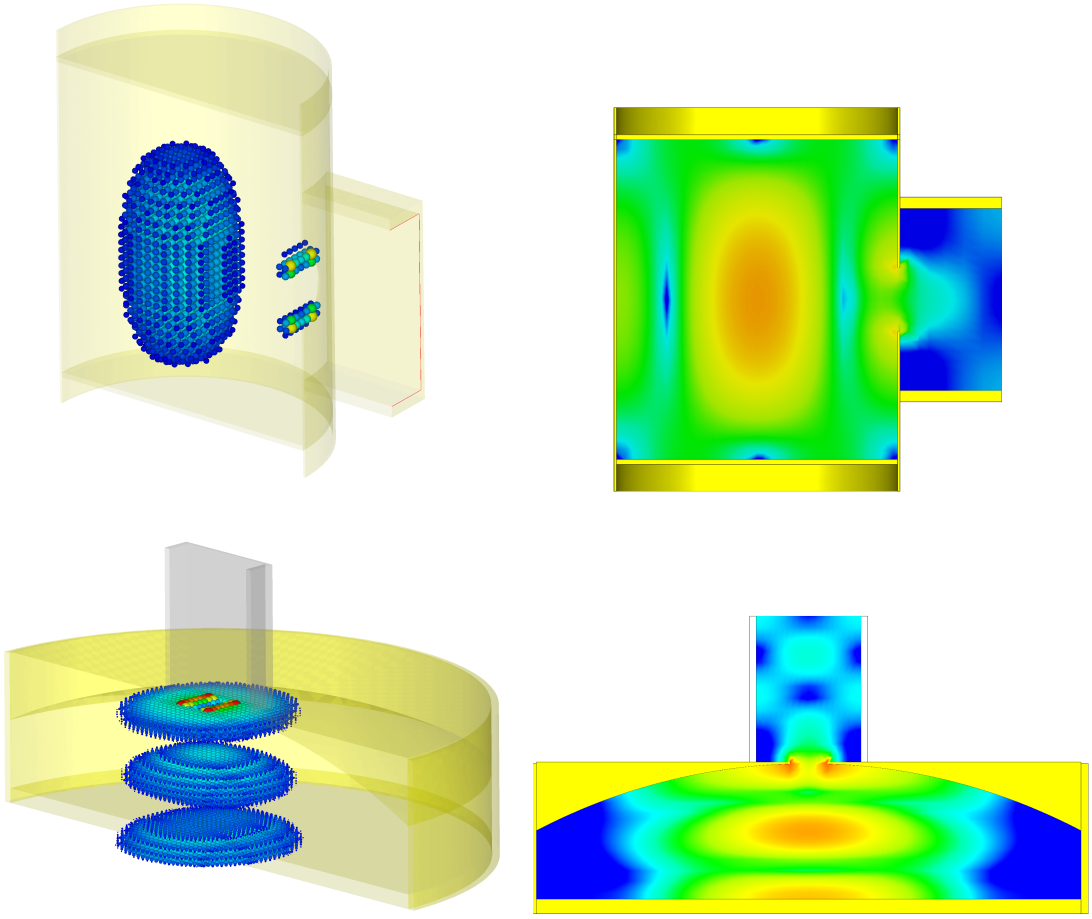

Figure 4.1.: 3D Magnetic field distribution of the TE_{011} mode (upper left) in a cylindrical resonator typically used for pulsed EPR. The sample is usually put into a glass tube which is inserted through the upper part of the cylinder. In contrast, the 3D magnetic field distribution of the TEM_{001} mode (lower left) in a Fabry-Pérot resonator allow it to put the sample on the bottom mirror. 2D slices for each field distribution (upper right, respectively lower right) are shown as well for the both types of resonator.

4.2. Fabry-Pérot resonator

4.2.1. Design

The Fabry-Pérot resonator is widely used in optics and high frequency EPR as it is the easiest 3D-resonator to manufacture for large frequencies and thus small structure sizes. The resonator consists out of two mirrors separated by the distance d facing each other. The mirrors can be either planar or spherical shaped, where the latter are characterized by their radius of curvature R.

Several issues have to be considered for the design of the resonator. First, the resonance frequency of the resonator is mainly determined by the distance of the mirrors. The two mirrors create a boundary condition for the electromagnetic field as the electric field component $\vec{E}$ has to vanish at the conducting metal surfaces. A standing wave and thus resonance occurs when the location-dependent part of the wave has a node at both metal surfaces. For a resonator with two planar mirrors this is fulfilled if the distance is a integral multiple $(n+1)$ with $n_{\min} = 0$ of half the wavelength λ of the electromagnetic wave. In vacuum, the resonance frequency then reads $f_{\text{res}} = (n+1)\frac{c_0}{2d}$. The electric and magnetic field for a 1D resonator on resonance ($n = 1$) is shown in Figure 4.2. It should be noted that the magnetic field, which is the important field component for EPR, is phase shifted by $\pi/2$ and thus has a maximum on the mirrors. As the resonator should operate at $f_{\text{res}} = 35$ GHz, the minimum distance needed would be $d = 4.28$ mm.

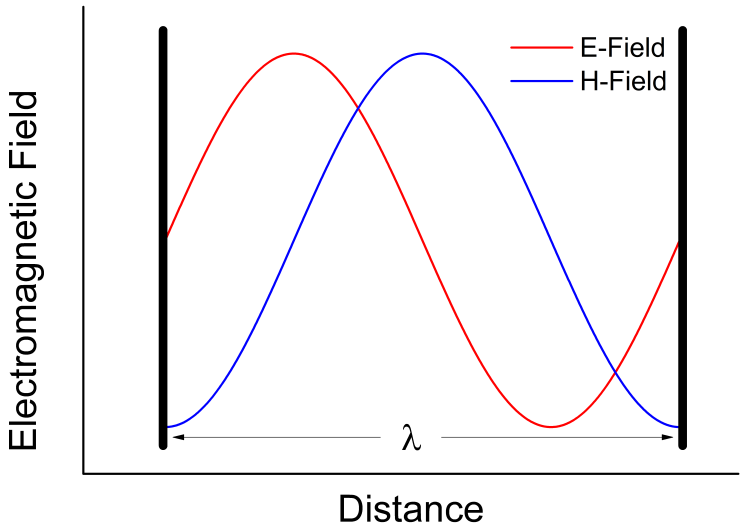

Figure 4.2.: Hypothetical field distribution in a 1D Fabry-Pérot resonator where the distance between the boundaries correspond to $d = \lambda$

The second issue to consider is the curvature R of the mirrors. As the magnetic field has a maximum on the surfaces of the mirror, planar mirrors would be perfect to mount flat samples on them. However, only little disturbances in the parallelity of the mirrors will already cause huge diffraction losses [101, 102, 104]. To overcome this problem, the mirrors can be shaped spherically. To combine the best of two worlds, a concave and a planar mirror can be used which is called a semiconfocal design. In general, the focal length and thus R of the curved mirror has to be equal or larger than the distance d between the mirrors in order to avoid diffraction losses [104] due to a growing beam. Furthermore, R determines the spot size of the magnetic field at the sample position. Thus, a larger R is desirable if the sample of interest is large.

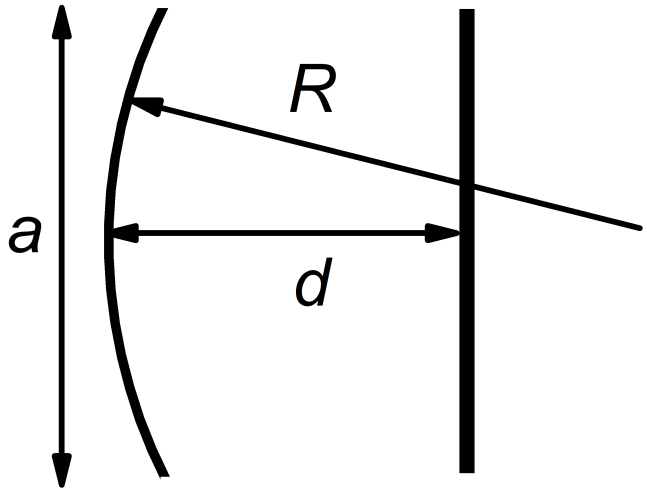

Figure 4.3.: 2D sketch of a Fabry-Pérot resonator with a semiconfocal configuration. The distance between the spherical mirror (left) and the planar mirror is is measured along the mirror axis. The radius of curvature R defines the focal length. The aperture (in this case the diameter of the mirrors) a should be as large as possible to avoid diffraction losses.

The eigenmodes of such a semiconfocal 3D-resonator can be described by the Hermite-Gaussian modes. They are called TEM_{pln} modes as the electric and magnetic field is transverse to the axis of propagation. The integers p, l and n correspond to the knots in radial, azimuthal and transversal directions, respectively. The resonance frequencies of these modes in a semiconfocal setup can be calculated analytically [104] with the following equation

$$f_{\mathrm{res}} = \left[(n+1) + \frac{1}{2\pi}(2p+l+1)\arccos\left(1-\frac{2d}{R}\right)\right]\frac{c}{2d} \tag{4.1}$$

Compared with the resonance frequency $f_{\mathrm{res}} = (n+1)\frac{c}{2d}$ of two planar mirrors, the concave mirror changes the resonance frequency a little bit and lifts the degeneracy of the TEM_{plx} modes. The modes with cylindrical symmetry ($p = 0, l = 0$) are particularly interesting as they have the most uniform field distribution over the planar mirror and the lowest losses. Based on a design of a resonator working at similar frequencies [102], $R = 43$ mm was chosen. Using equation 4.1 and the desired working frequency of $f_{\mathrm{res}} = 35$ GHz, the minimum distance for the TEM_{000} mode then would be $d = 4.75$ mm.

Another aspect to consider are the Fresnel numbers $\frac{a^2}{\lambda R}$ and $\frac{a^2}{\lambda d}$, where a is the diameter of the mirrors. These dimensionless numbers should be as large as possible in order to keep the diffraction losses low and at least above 1 for a TEM mode operation [105]. $a = 37$ mm was chosen which is the maximum possible diameter allowing the resonator to fit into our cryostat. This ensures that both Fresnel numbers are well above 1.

Beside of the geometry of the resonator, microwaves have to be coupled into the structure. The radiation is transported by a rectangular waveguide from the source. Coupling into the resonator can be achieved by a small coupling hole ($d_{\mathrm{hole}} \ll \lambda$) connecting the waveguide and the concave mirror. Generally, the hole should be placed in the center of the waveguide [106] for a maximum power transfer. As a rule of thumb, the diameter of the hole should be around $d_{\mathrm{hole}} \approx 0.3\lambda$ [101] to achieve a coupling near critical coupling. Therefore, a coupling hole diameter $d_{\mathrm{hole}} = 2.5$ mm was chosen.

Last but not least, the direction of polarization of the microwaves is important for EPR experiments. Generally, the magnetic field component should be polarized perpendicularly with respect to the applied static magnetic field. This can be either achieved by applying the static field along the axis of propagation inside the resonator as the field components of the TEM modes are always perpendicular to the axis of propagation. However, the setup presented in this thesis only allows applying the static field perpendicular to the axis of propagation. Still it is possible to achieve a perpendicular magnetic field component as the polarization is determined by the polarization of the waveguide. Thus, the magnetic field component inside the resonator is parallel to the long dimension of the waveguide.

Figure 4.4 shows the CAD-Drawing of the cavity, the distance of the two mirrors can be adjusted by a long screw. The lower mirror is connected to an upper round part with an brass casing (transparent in the drawing). The upper part can be moved on the steel rods with the long screw and thus moving the lower mirror. The waveguide ends at the top of the concave mirror. As the thickness of the coupling hole should be as thin as possible in order to avoid losses [106, 107], a waveguide was cut into the the concave mirror to achieve a thickness of 0.2 mm.

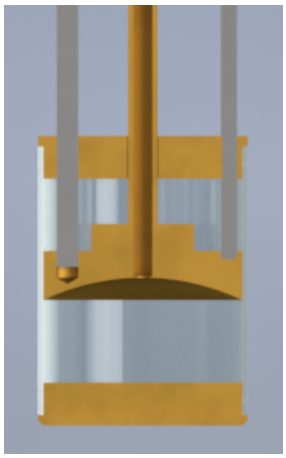

Figure 4.4.: CAD-Drawing of the cavity part of the resonator. A waveguide is cut into the upper concave mirror to reduces the thickness of the coupling hole.

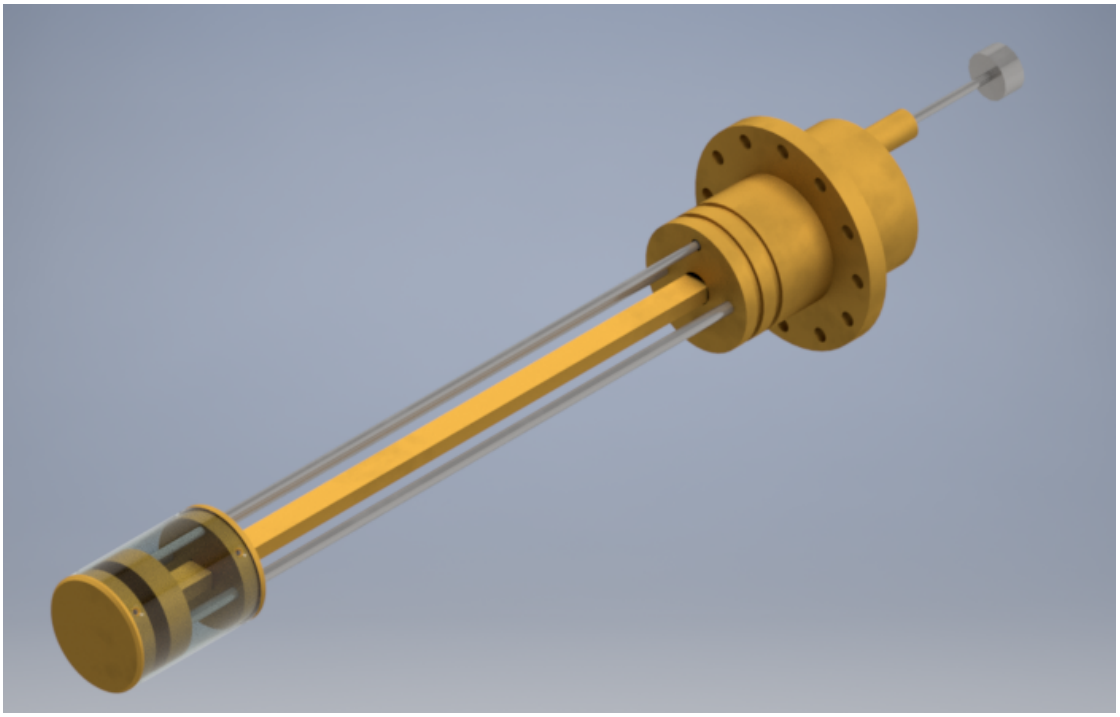

Figure 4.5.: CAD-Drawing of the Fabry-Pérot resonator including the flange on the top which complies with the Oxford CF-935 cryostat.

Figure 4.5 shows the drawing of the complete assembly which was designed to fit into an Oxford CF-935 cryostat. The long screw protrudes the top flange and is sealed with o-rings. Steel rods hold the concave mirror in place. On the top, the waveguide is sealed with a small piece of mica to in order to avoid air leakage into the cryostat.

Figure 4.6.: Cavity part of the manufactured resonator made of brass. The sample can be placed in the center of the flat mirror. The casing connects the lower mirror with the upper round brass part which can be moved by a screw. The waveguide is made from steel to reduce heat conduction.

Figure 4.6 shows the cavity part of the actual manufactured resonator made of brass. The sample can be mounted on the bottom flat mirror with small amounts of grease. After placing the sample, the casing is screwed to the bottom mirror and afterwards to the upper round brass part. The waveguide is made from steel, which increases the losses a bit but reduces heat leakage into the cryostat.

By definition, the Fabry-Pérot resonator is an open resonator which refers to the open boundaries on the sides. Any diffraction losses occurring due to the finite size of the mirrors will leak out there. However, the manufactured resonator is closed with a brass casing in order to avoid direct contact of the sample with the helium flow. Although the diameter of the mirrors is quite large ($a = 4.3\lambda$) this might change the Gaussian mode pattern a little bit. Thus, the resonator will be thoroughly characterized in the next section by a combination of measurements and simulations.

4.2.2. Characterization of the manufactured resonator

The manufactured resonator was characterized by three methods. In this way, the first four modes occurring at 35 GHz were analyzed by measuring their Q-factor with a Vector Network Analyzer (VNA), performing pulsed EPR measurements and simulating the field inside the resonator with the electromagnetic field simulation tool *CST-Studio*. All measurements were performed at room temperature with a 5 w.% α,γ-bisdiphenylene-β-phenylallyl (BDPA) in polystyrene sample. The sample was disc shaped with a diameter of 5 mm and a height of 0.2 mm.

Q-factors

The Q-factors were determined by recording the scattering parameter S_{11} at the input port of the resonator. The distance of the mirrors was increased while monitoring the magnitude of S_{11} in a range between 34.5 GHz to 35.5 GHz. The full S_{11} parameter was recorded, when a resonance occurs at about 35.00 GHz. This was performed for the first four modes which corresponds to intermirror distances d between 4.7 mm and 9.2 mm. d was measured after the respective VNA measurement with a caliper and is summarized in table 4.1.

Figure 4.7 shows the measured imaginary part of S_{11} against its real part of the first four modes. Characteristic semicircles with varying diameters are observed. With the exception of the first mode, the origins of the circles have an imaginary part close to zero. The diameter of the first mode circle is close to one, the fourth and second mode circles have a diameter larger then one and the third mode circle has a diameter slightly smaller than one.

Qualitatively, from the data it can be deduced that relatively large coupling losses occur in case of the first mode, because its origin has a small imaginary part [109]. From the diameters of the circles, the coupling regime can be deduced. A diameter of one corresponds to a critically coupled resonator, a diameter smaller or larger then one corresponds to a under respectively over coupled resonator.

The quantitative analysis including the determination of the Q-factors was performed by means of a method described in [109]. Briefly, the complex data of the reflection coefficient S_{11} was fitted with a circle by using a least squares method [108]. The diameter d of this circle can be used to calculate the coupling coefficient $\kappa = \frac{d}{2-d}$. In the next step, the fitted circle shown in Figure 4.7 is used to find the points Γ_{L} (S_{11} at resonance, nearest point to the origin) and Γ_{d} (S_{11} infinite far detuned from resonance, the point farthest away from the origin). Using these points together with each measured

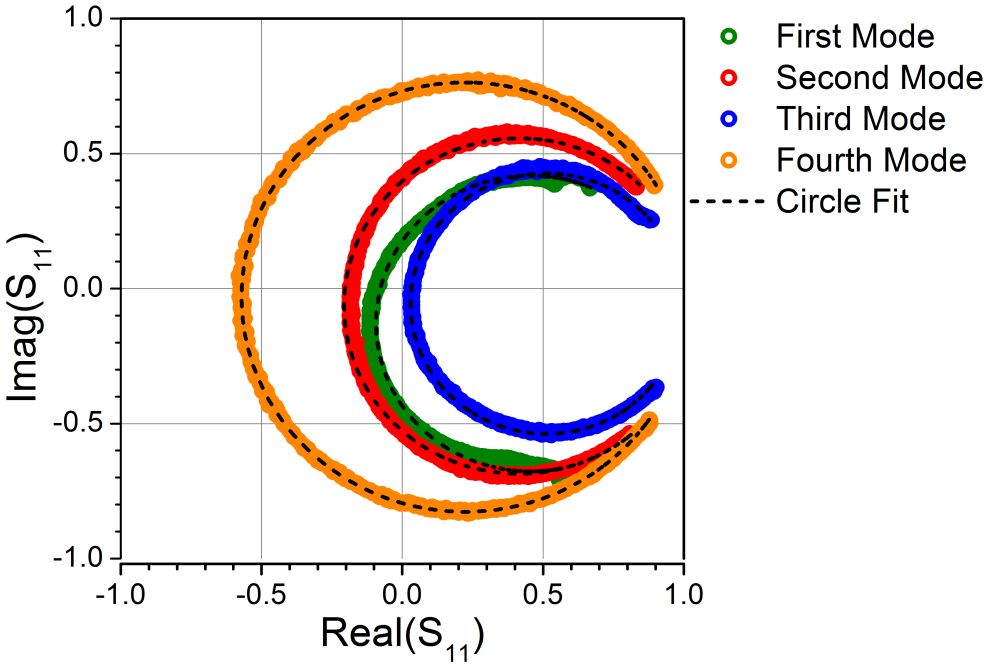

Figure 4.7.: Imaginary part of the measured S_{11} parameter (colored dots) against its real part of the first four modes occurring in the resonator. The data was fitted with the equation of a circle [108].

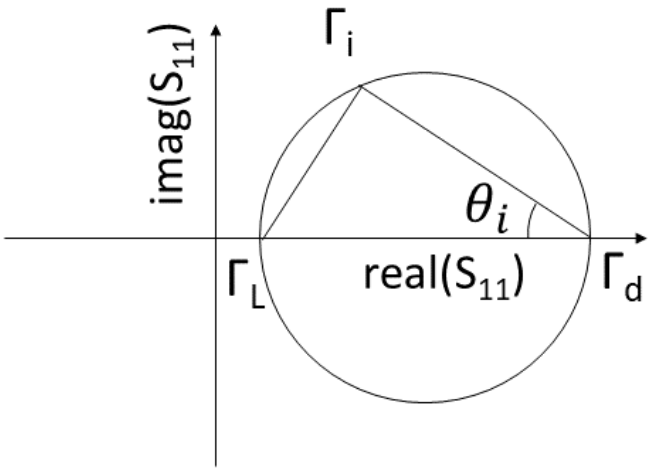

Figure 4.8.: Relevant points on the resonance circle used for the quantitative analysis [109]. Γ_i corresponds to the measured point, Γ_L is the point on resonance and Γ_d corresponds to the point infinitely far detuned from resonance. The three points form a triangle, the angle θ_i of this triangle is used to generate a linear frequency axis.

point Γ_i, triangles with the angle θ_i were constructed (see Figure 4.8). The tangents of these angles depend linearly on the frequency at which the points were measured. After fitting the tangents with a straight line (see Figure 4.9), the loaded Q-factor Q_L can be calculated from the intercept c with the equation $Q_\mathrm{L} = c/2$. Finally, the unloaded Q-factor Q_0 can be calculated from $Q_0 = Q_\mathrm{L}(1+\kappa)$.

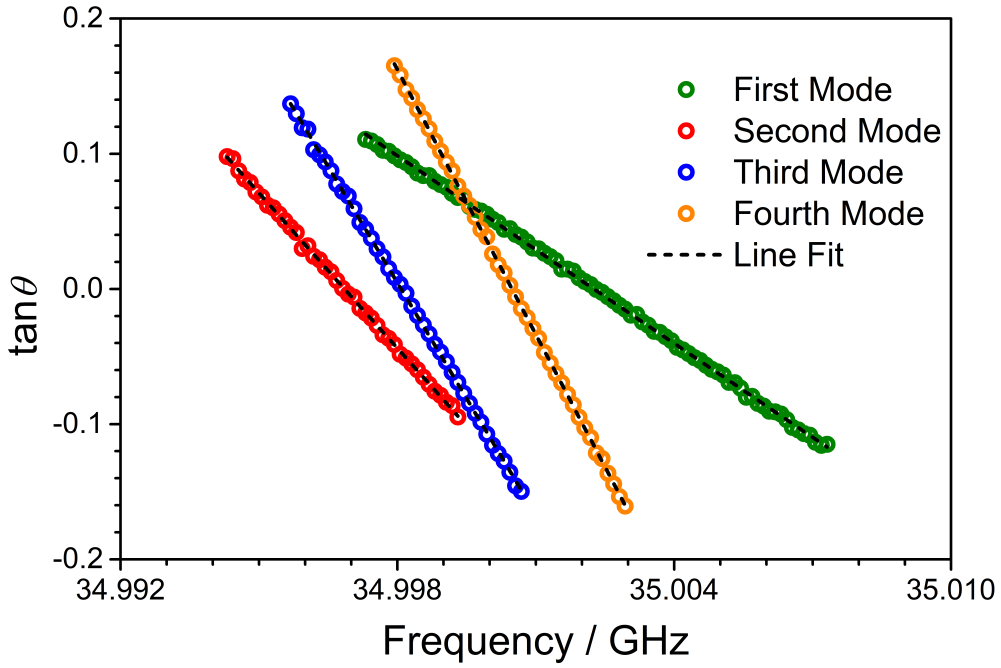

Figure 4.9.: The tangents of θ_i against the frequency for the first four modes (colored dots). A straight line fit is included from which the loaded Q_L factor can be determined.

The obtained Q-factors are summarized in Table 4.1. With the help of the resonance condition of a Fabry-Pérot resonator (equation 4.1), the intermirror distance d_th can be calculated for a given $\mathrm{TEM}_\mathrm{pln}$ mode at 35 GHz. As the intermirror distance d_exp was measured, this allows to identify the corresponding $\mathrm{TEM}_\mathrm{pln}$ modes. The mode assignment and d_theo are summarized in 4.1 as well.

With the exception of the third mode, κ is large than one meaning that the resonator is overcoupled. This is, however, desirable for pulsed EPR, as it reduces the dead time due to cavity ringing. The cavity ringing time constant $\tau = \frac{2Q_\mathrm{L}}{2\pi f_\mathrm{res}}$ for the fourth mode reaches 10 ns which is leading to a dead time of about 200 ns. It has been shown [110] that decreasing Q_L via overcoupling is much more beneficial for pulsed EPR compared to lowering the unloaded Q-factor Q_0 by the same amount.

Table 4.1.: Mode assignment, experimental d_{exp} and theoretical d_{th} intermirror distance d_{exp}, unloaded Q_0 and loaded Q_L factor and the coupling parameter κ of the first four modes. The modes were assigned using eq. 4.1

Mode	d_{exp} / mm	d_{th} / mm	Q_0	$Q_{0,th}$	Q_L	κ
1 (TEM_{000})	4.7(2)	4.75	900(40)	3300	404(1)	1.20(10)
2 (TEM_{100})	5.8(2)	5.82	1700(60)	4000	648(3)	1.70(4)
3 (TEM_{200})	7.2(2)	7.15	1930(30)	5000	997(3)	0.93(2)
4 (TEM_{001})	9.2(2)	9.22	5560(20)	6500	1142(2)	3.87(1)

The unloaded Q-factor $Q_{0,th} = 2\pi f_{res}\frac{2d}{c\beta}$ depends on the intrinsic losses β inside the resonator which are diffraction losses and electric losses due to the finite conductivity at the metal mirrors. The electric losses $\beta_e = 4\sqrt{\pi f_{res}\varepsilon_0\rho}$ of a reflection at one metal mirror can be calculated from the bulk resistivity ρ of the material [107] which is $\rho_{brass} = 6\cdot 10^{-8}\ \Omega\cdot$cm at room temperature for brass. If the electric losses dominate all losses, the total loss rate becomes $\beta = 2\beta_e$. $Q_{0,th}$ for each mode is shown in Table 4.1 next to the experimental values. For the lowest three TEM_{xx0} modes, the theoretical value differs more than 100% from the experimental values. Q_0 of the TEM_{002} mode is about 85% of the theoretical value.

Generally, the electric losses can increase by a factor up to two if the surface roughness of the metal mirrors is much larger than the skin depth of the radiation [111]. Thus, the slightly reduced Q_0 of the fourth mode (TEM_{001}) can be explained by a finite surface roughness of the mirrors. This does, however, not explain the much lower Q_0 of the three TEM_{xx0} modes. Here, additional losses like diffraction losses may occur. Therefore, the modes were simulated with the electromagnetic field simulation tool *CST-Studio* in the next section.

Microwave simulations

Microwave simulations were carried out using *CST-Studio 2018*. The Fabry-Pérot resonator was modeled as built and the Eigenmode Solver was used to simulate the field distributions of the different modes. A tetrahedral mesh in combination with the mesh refinement (frequency deviation of the modes < 0.001 GHz) was used.

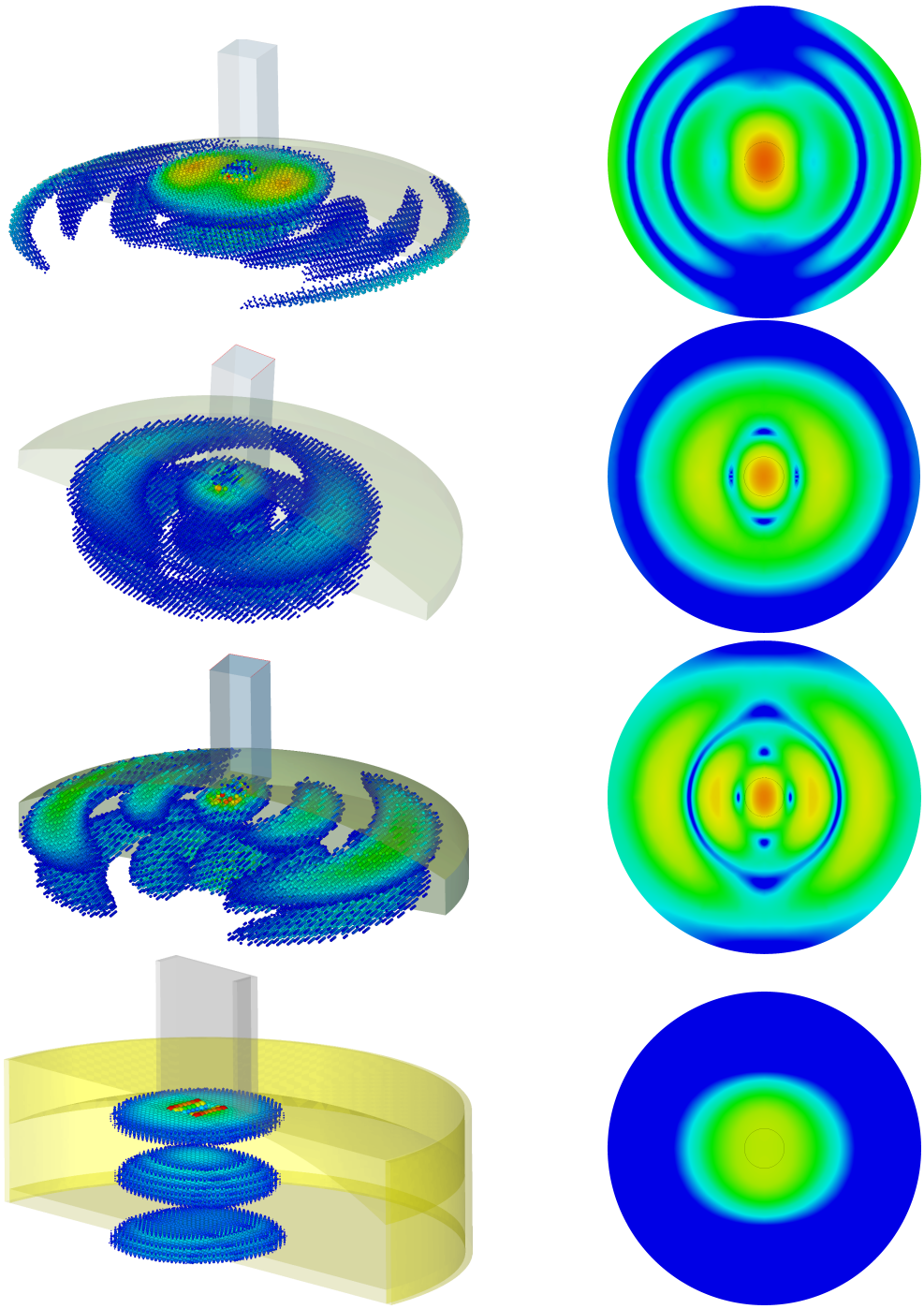

Figure 4.10.: Simulated 3D magnetic field distribution (left side) of the first four modes occurring in the Fabry-Pérot resonator. 2D field projections on the bottom mirror are shown as well (right side). The modes were originally assigned as TEM_{000} (first mode), TEM_{100} (second mode), TEM_{200} (third mode) and TEM_{001} (fourth mode). However, only the fourth mode shows a pure Gaussian mode behavior.

Figure 4.10 shows the 3D magnetic field distribution of the first four modes and a 2D projection of the field at the bottom mirror. All four modes exhibit a small degree of astigmatism due to the coupling from a rectangular wave guide. The first three modes deviate from the pure Gaussian modes which can be seen especially well for the first mode (assigned as TEM_{000}) which should have no nodes at all. The simulation of the fourth mode, on the other side, resembles perfectly the field distribution of a TEM_{001} Gaussian mode.

It is most likely that the decreased Q_0 originates from the field distribution of the first three modes. Especially the first mode has a significant magnetic field density at the edge of the mirrors and the casing leading to a surface current through the mirrors and the casing. The current paths can be easily disrupted if the casing does not sit perfectly tight. Furthermore, the modes have a much larger spot width compared to the real gaussian modes. Thus, diffraction losses can be larger.

From further simulations it turns out that the field distributions of the first three modes are strongly affected by the coupling hole size. Removing the hole completely would allow a perfect TEM_{000} mode as it can be seen in Figure 4.11 were the structure was simulated without a coupling hole. This is, of course, no option as the structure could no longer be fed with microwaves. Increasing the inter mirror distance and thus going to higher modes seems to tackle this problem as well as the TEM_{001} is already available in the built resonator. The reason for this behavior might be the interaction of the near field of the coupling hole with the lower mirror as the distance between them is only about $\lambda/2$ in case of the first mode.

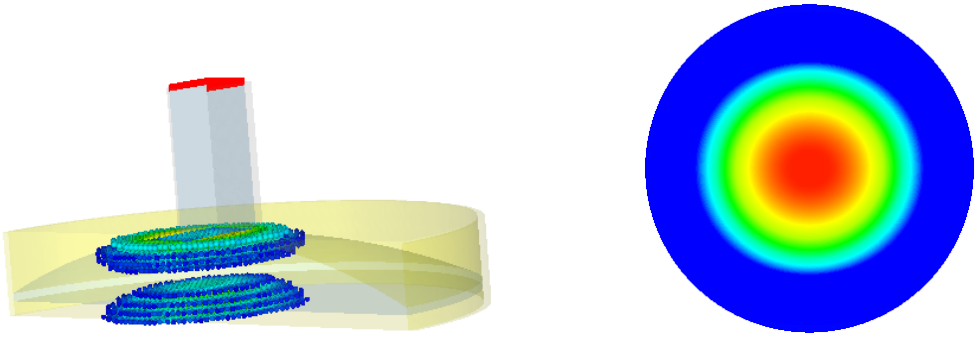

Figure 4.11.: Simulated 3D magnetic field distribution (left) and a 2D projection on the bottom mirror (right) of the first mode if no coupling hole is employed. A perfect Gaussian mode is obtained.

To conclude the characterization of the resonator, the next section will deal with the pulsed EPR performance of the first four modes.

Pulsed EPR

Pulsed EPR experiments were carried out on a 2.1 mg 5 w.% BDPA in polystyrene sample. The sample was disc shaped with a diameter of 5 mm and a height of 0.2 mm. Hahn-echo and Rabi nutation experiments were performed on the first four modes at 1249.2 mT, 35 GHz and room temperature. For the Hahn-echo measurements, the pulse lengths of the $\pi/2$ and π pulses were fixed at 20 ns and 40 ns, respectively. The microwave power was adjusted to achieve the maximum spin echo signal. For the first mode, it was not possible to achieve a full $\pi/2$ or π pulses even with the maximum available power at fixed pulse lengths. For the Rabi nutation experiments, the same pulse lengths were used for generating the spin echo. However, the maximum available power of 5 W was used for all experiments.

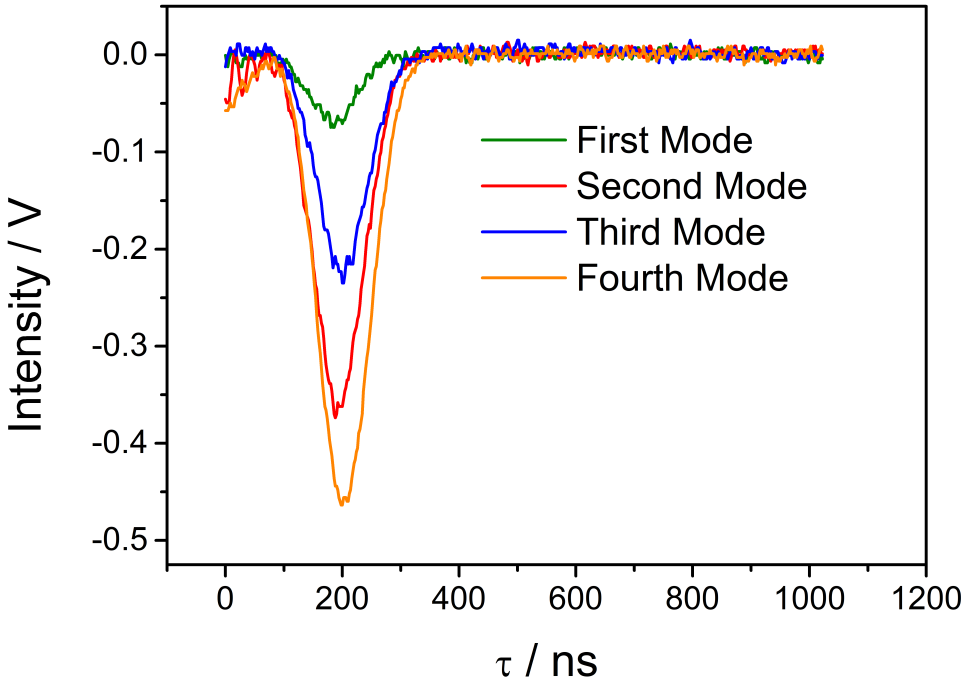

Figure 4.12.: Single shot Hahn-echos of a 2.1 mg 5 w.% BDPA in polystyrene sample at 1249.2 mT, 35 GHz and room temperature. Each echo was recorded while utilizing one of the first four modes.

Figure 4.12 shows the spin echos for the first four modes. The signal intensity does not change monotonically with the mode number. The largest intensity is reached using the fourth mode. The intensity decreases with the second mode to the third mode and finally to the first mode.

The intensity of the signal V_s is affected by Q_0, Q_L and the filling factor $\eta = \frac{\int_{sample} B_1^2 dV}{\int_{cavity} B_1^2 dV}$ with the equation [110, 112]

$$V_{s,th} \sim \eta \sqrt{Q_L Q_0 - Q_L^2} \tag{4.2}$$

The filling factor can be extracted from the simulations performed in *CST-Studio* considering the sample size. Using the measured Q-factors, the theoretical signal intensity normalized on the fourth mode $V_{norm,th} = V_{s,th}/V_{s,th,4}$ can be calculated . η, $V_{norm,th}$ and the experimental signal intensity $V_{norm,exp}$ normalized on the fourth mode are shown in Table 4.2.

Table 4.2.: Normalized signal intensities $V_{norm,exp}$ extracted from the Hahn-echos shown in Figure 4.12 of the first four modes. Additionally, the filling factor η calculated with *CST-Studio* and the theoretical signal intensity $V_{norm,th}$ based on equation 4.2 are shown. The theoretical intensity of the first mode marked with an asterisk includes a correction due to the imperfect pulse angles.

Mode	η	$V_{norm,exp}$	$V_{norm,th}$
1 (TEM_{000})	1.4%	0.15(1)	0.73 (0.15)*
2 (TEM_{100})	0.7%	0.78(5)	0.70
3 (TEM_{200})	0.4%	0.50(5)	0.46
4 (TEM_{001})	0.4%	1	1

With an exception of the first mode, the theoretical intensity matches very well to the observed intensity. The worse performance of first mode can be explained by the fact that not enough power was available to reach a full $\pi/2$ respectively π pulse. The real pulse angles for the first mode were determined by Rabi nutation measurements to $\pi/5$ respectively $2\pi/5$ (see Figure 4.13a). The expected echo intensity compared to a normal Hahn-echo sequence with $\pi/2$ and π pulses can be calculated with $I = |\sin\beta_1| \sin^2 \frac{\beta_2}{2}$ [42] where β_1 is the pulse angle of the first pulse and β_2 the angle of the second pulse. This results in a signal reduction by a factor of five for the first mode. The corrected value is shown in Table 4.2 as well and fits very nicely to the experiment.

Figure 4.13 shows the Rabi nutation experiments for all four modes. An oscillatory behavior of the echo intensity with respect to the nutation pulse length can be observed for all four modes. The damping behavior, however, is different for each mode. An exponential decay with the phase memory time $T_m = 680(10)$ ns measured before by a Hahn-echo decay measurement (see Appendix Figure A.7) is shown as well. Only the fourth mode is dampened with this time constant.

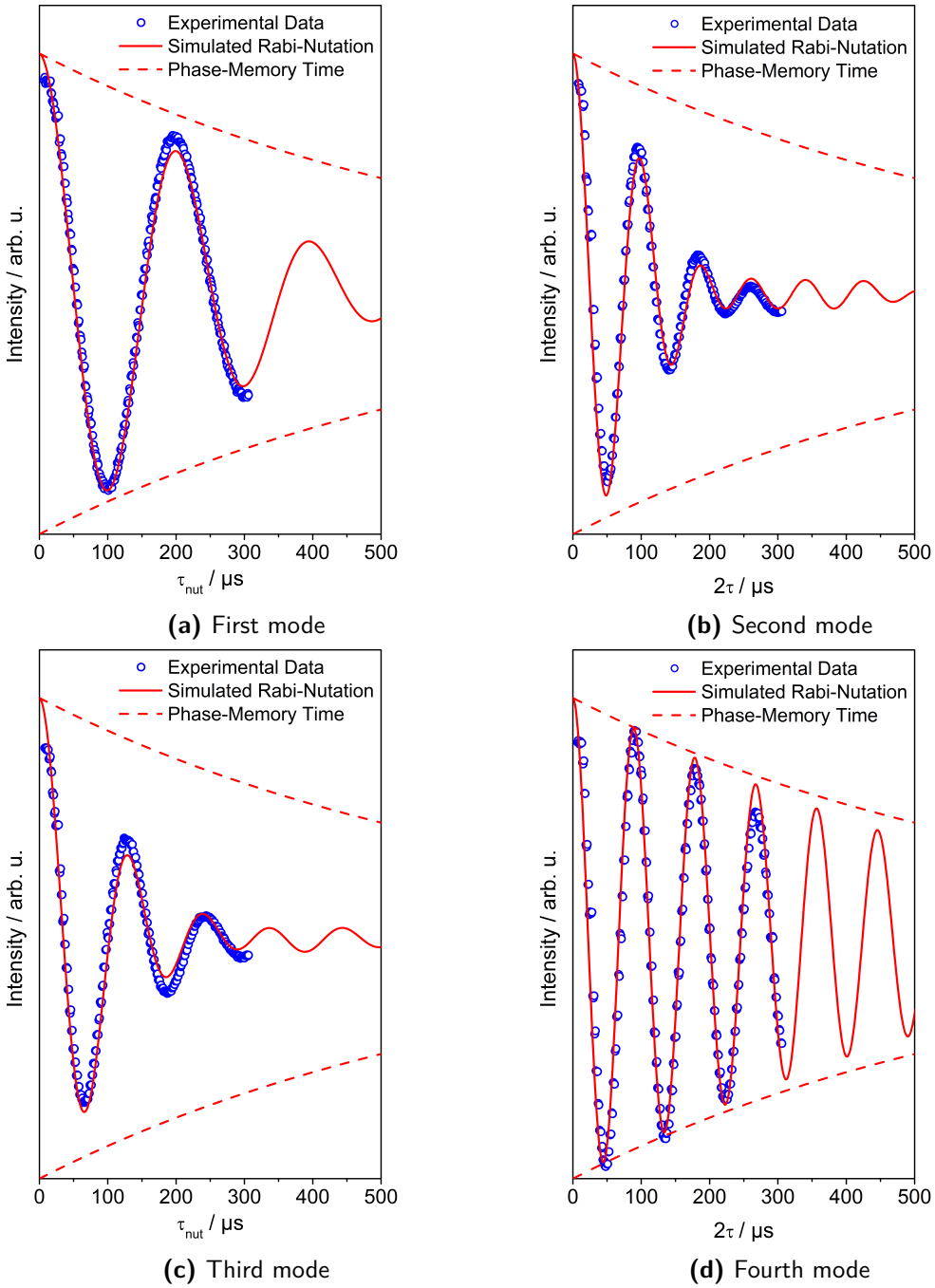

(a) First mode

(b) Second mode

(c) Third mode

(d) Fourth mode

Figure 4.13.: Rabi nutations (blue dots) of a 2.1 mg 5 w.% BDPA in polystyrene sample measured at 1249.2 mT, 35 GHz and room temperature. The nutations were measured utilizing the first four modes. An exponential decay based on $T_{\mathrm{m}} = 680(10)$ ns of the sample is shown as well (red dotted line). The nutations were simulated (red line) based on the simulated magnetic field distribution at the sample.

Theoretically, the damping of the Rabi nutations should be only affected by T_m. However, this assumes a homogeneous field distribution over the sample. If this is not the case, each spin depending on its spatial position experiences a different B_1 field and thus has a different nutation frequency ω_{nut}. In the end, this causes an additional damping as the oscillations of each spin sum up. The nutation frequency can be calculated with $\omega_{nut} = \frac{g\mu_B}{\hbar} B_1$. Thus, the B_1 field from the mode simulations shown before was sampled over the sample (approximatly 10^4 field points) for each mode. For each point, the Rabi nutation $I(\tau_{nut}) = \cos(\omega_{nut}\tau_{nut})$ was calculated. All calculated nutations were summed up and normalized by the number of points. The result for each mode is shown in Figure 4.13 as well which fit astonishingly well to the experiments. As the fourth mode has a very homogeneous field distribution over the sample, the damping is only caused by T_m.

To sum it up, the first four modes occurring in the Fabry-Pérot resonator were thoroughly characterized by a combining experimental and simulation methods. The modes were attributed to the TEM_{pln} modes according to the inter mirror distance d at which a resonance at 35 GHz occurs. Furthermore, the Q-factors and the couplings were characterized by measurements with a VNA. It turned out that the resonator is over coupled for most of the modes. The unloaded Q_0-factors of the first three modes did not fit to the theoretical predicted ones. By simulating the first four modes with *CST-Studio* it came to light that the first three modes can not longer be described by simple TEM_{pln} modes as the coupling hole strongly influences the modes if the inter mirror distance is short compared to the coupling hole size. Thus, the lower Q_0-factors were attributed to the disturbed field distributions. Beside the Q-factors, the EPR performance of the first four modes was investigated by the means of Hahn-echo and Rabi nutation experiments. Combining the Q-factor measurements and the field distributions of the modes obtained by the simulations, the experimental observed Hahn-echo intensity could be perfectly described. Furthermore, the Rabi nutation experiments confirm the field distribution inside the resonator. In the end, the fourth mode (TEM_{001}) delivered the best EPR performance due to its high Q_0 and homogeneous field distribution.

4.3. Thin films

After the characterization of the resonator, pulsed EPR measurements on thin films of MQBs were performed. First, a thin film of copper(II) phthalocyanine (CuPC) in a matrix of pure phthalocyanine (H_2Pc) on sapphire was prepared and measured. This system was chosen, as it was already studied as thin film before and thus the measurements performed in the new resonator can be compared to the already published ones.

Furthermore, the films of this system are very stable under ambient conditions and can be prepared on many substrates. The second measurement series was performed on thin films of BDPA in poly(methyl methacrylate) (PMMA) spin coated on silicon. The system was chosen for several reasons. First, the stable BDPA radical has a very narrow EPR line, thus it is possible to excite nearly all spins with a single pulse. The spin coating procedure was chosen as it allows to quickly produce thin films with a controllable thickness in the nanometer region. Spin coating works best in conjunction with a polymer. Furthermore, BDPA has to be dispersed in some medium anyway in order to reduce spin-spin diffusion. Here, PMMA was chosen because it is a well studied polymer used for spin coating [113]. Furthermore, during preliminary experiments it turned out that PMMA dissolves BDPA very well, even in thin films. Silicon as substrate was chosen to demonstrate that is in principle possible, to investigate a silicon based working device.

4.3.1. Copper(II) phthalocyanine thin films

A film of CuPc and H_2Pc in the ratio 1:5 was evaporated on a 2.5 cm square 0.2 mm thick sapphire substrate. AFM measurements (see Appendix Figure A.8) reveal a film thickness of about 60 nm. Dr. Bastian Kern at the Max-Planck Institute in Stuttgart prepared the films and performed the AFM characterization.

ESE-detected EPR spectrum

Pulsed EPR measurements at 7 K and 35 GHz were performed on this film utilizing the Fabry-Pérot resonator. First, an echo-detected EPR spectrum was recorded between 1100 mT and 1260 mT. The resulting spectrum can be seen in Figure 4.14.

The intensity of the spectrum increases step wise from 1120 mT to 1200 mT. From there, it increases further with a maximum at 1218 mT. Above this field, the intensity quickly decreases to the baseline.

The CuPc molecule has the typical *g*- and hyperfine anisotropy like many square planar copper(II) complexes and can be described with the spin Hamiltonian in equation 4.3 [114]. The four steps at lower fields in the spectrum are the hallmark of a axial copper(II) powder EPR spectrum. Here, resonances of the CuPc molecules oriented with the $g_{zz} = g_{\parallel}$ axis parallel to the magnetic field can be observed. Furthermore, the resonances are split in four lines due to the parallel component of the copper hyperfine interaction $A_{\mathrm{Cu},\parallel}$. Typically, at higher fields a large peak can be observed due

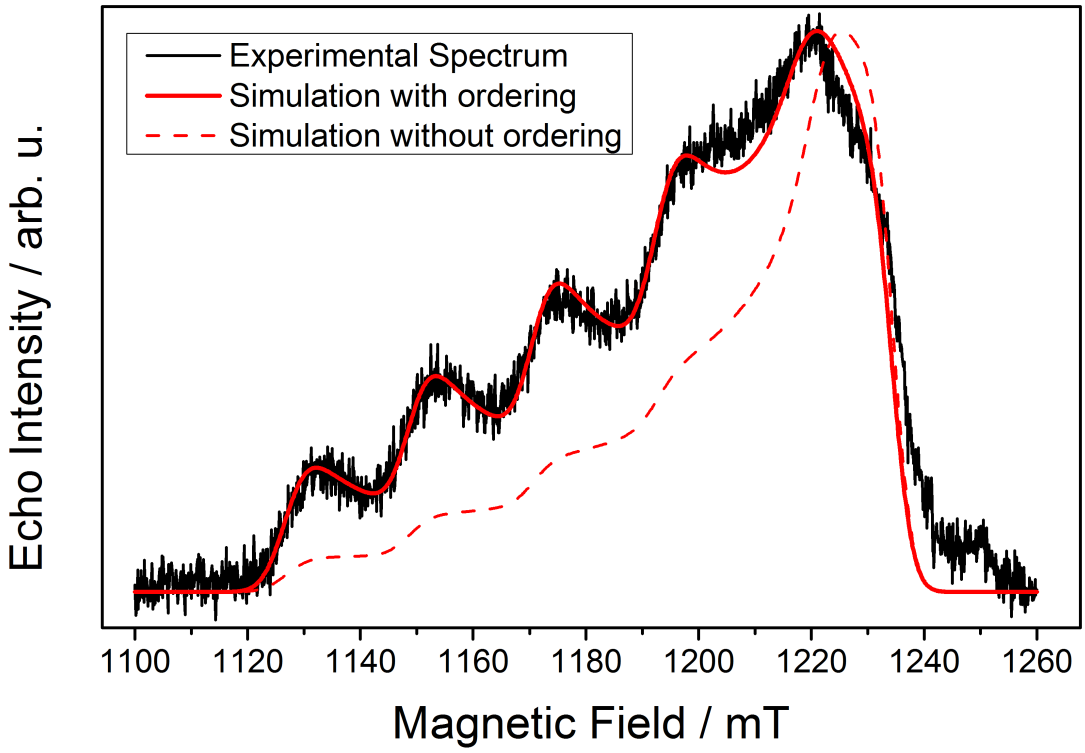

Figure 4.14.: ESE-detected EPR spectrum (black line) of the 60 nm CuPc and H_2Pc (1:5) film on sapphire measured at 7 K and 35 GHz. Two simulations based on the spin Hamiltonian parameters published in [114] are shown. The first simulation (red dotted line) assumes a full powder average. The second (red solid line) includes a partial ordering of the molecules as described in the text.

to resonances of molecules where the magnetic field lies in the $g_{xx} = g_{yy} = g_\perp$ plane. Sometimes, depending on the line width caused by strains, this peak is split in four lines as well due to the axial component of the copper hyperfine interaction $A_{\mathrm{Cu},\perp}$. However, in the observed spectrum no splitting at $g_\perp$ is visible.

$$\mathscr{H} = g_\parallel \mu_\mathrm{B} \hat{S}_z B_z + g_\perp \mu_\mathrm{B} (\hat{S}_x B_x + \hat{S}_y B_y) + A_{Cu\parallel} \hat{S}_z \hat{I}_z + A_{Cu\perp} (\hat{S}_x \hat{I}_x + \hat{S}_y \hat{I}_y) \tag{4.3}$$

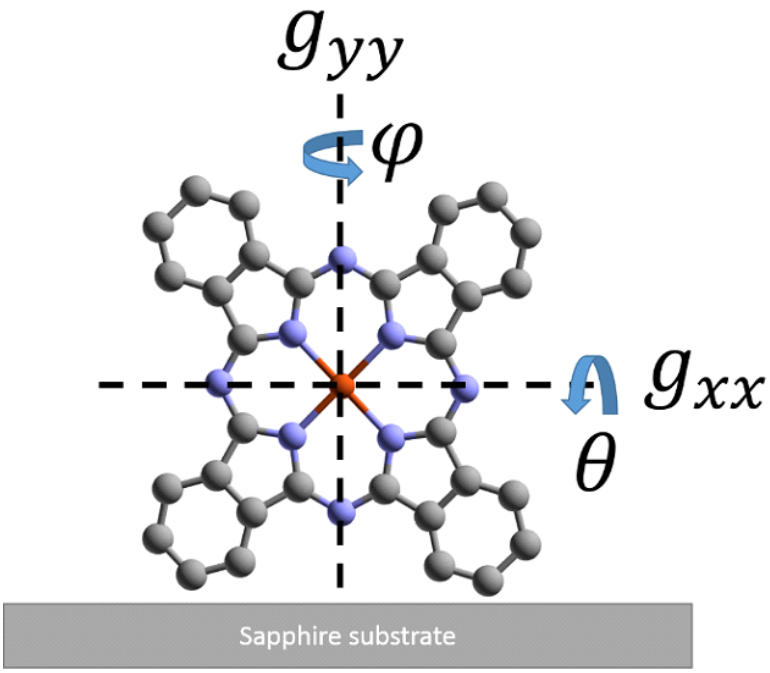

Figure 4.15.: Sketch of a standing CuPc molecule on a sapphire substrate. The principal axes g_{xx} and g_{yy} are implied as well as the angles θ and ϕ which describe the rotational orientation of the molecule.

A simulation (red dashed line) of a powder spectrum of CuPc based on the known [114] spin Hamiltonian parameters is shown in Figure 4.14 as well. It can be seen that the $g_\perp$ peak in the observed spectrum is much smaller compared to the simulation. Furthermore, the steps at $g_\parallel$ are not flat anymore. The discrepancies can be explained with a partial ordering of the molecules on the surface. It has been shown [115] that CuPc molecules tend to stand (illustrated in Figure 4.15) on technical substrates like ITO or sapphire and lie flat on very smooth surfaces like on Si(111) [116].

Partial ordering can be included in a spectrum simulation with *Easyspin*. Instead of performing a full powder average and thus including any possible orientation of the molecule with respect to the field, a weighted average can be calculated. Figure 4.15 shows the relevant angles θ and ϕ for the molecular orientation and the axes of g_{xx} and g_{yy} which lie in the plane of the phthalocyanine ligand. Here, the g_{yy} axis is parallel to the surface normal and g_{xx} perpendicular to it. In the bulk material, these axes are equivalent but this may change on a surface due to surface interactions. The angle ϕ describes a rotation about the surface normal, while θ is connected to a rotation around the g_{xx} axis.

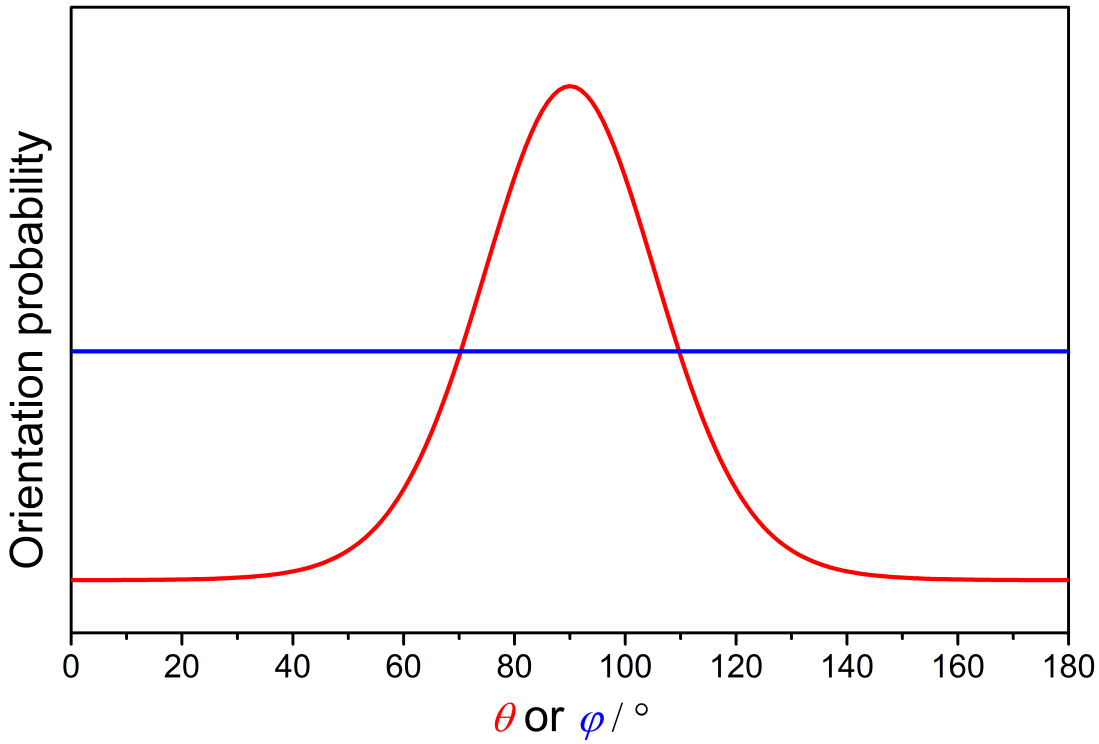

Figure 4.16.: Orientation probability for the angles θ and ϕ used for the simulation in Figure 4.14 including partial ordering.

Table 4.3.: Spin Hamiltonian parameters used to simulated the spectrum shown in Figure 4.14 as well as the values published before.

Sample	g_{xx}	g_{yy}	g_{zz}	$\lvert A_{\mathrm{Cu},xx}\rvert$	$\lvert A_{\mathrm{Cu},yy}\rvert$	$\lvert A_{\mathrm{Cu},zz}\rvert$
60 nm Film	2.039(1)	2.070(1)	2.158(1)	80(20)	80(20)	650(2)
Powder [114]	2.0390(5)	2.0390(5)	2.1577(5)	83(3)	83(3)	648(3)

For a simulation including partial ordering, the weighting function $p(\theta) = \exp\left(\frac{\lambda}{2}(3\cos^2\theta - 1)\right)$ with $\lambda = -4.5$ for the angle θ was used while the angle ϕ was not restricted (see Figure 4.16). Furthermore, the known spin hamiltonian parameters (see Table 4.3) were used with an exception of g_{yy} which was chosen slightly smaller. The resulting simulation is shown in Figure 4.14 (red solid) as well. The simulation perfectly agrees with the measured spectrum. Thus, EPR can be a valuable tool to determine the molecular ordering on a surface. The film is much thicker than a potential monolayer of molecules. Still, the ordering is visible, thus it is propagating along the molecular layers.

Relaxation times

The relaxation times T_1 and T_m of the 60 nm CuPc and H_2Pc film were measured as well. Here, inversion recovery respectivley Hahn-echo decay experiments were performed at 35 GHz, 7 K and 1218 mT which corresponds to the intensity maximum in the spectrum shown before. The resulting decays can be seen in Figure 4.17.

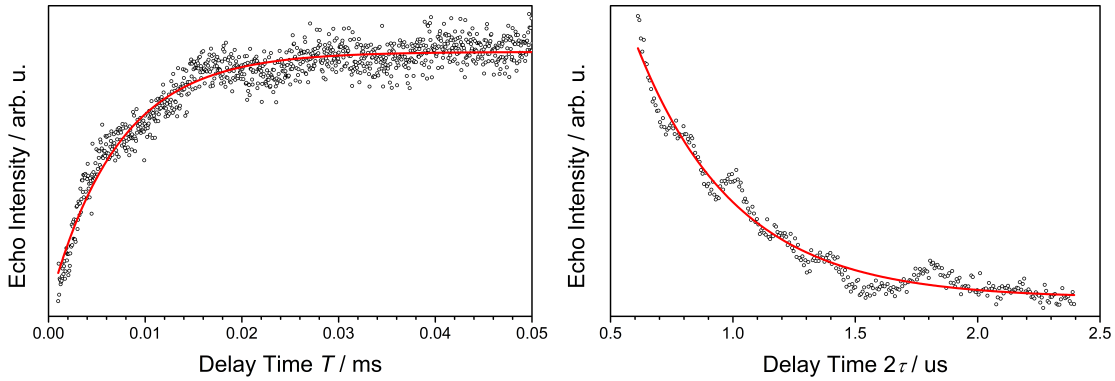

(a) Inversion recovery experiment **(b)** Hahn-echo decay

Figure 4.17.: Measured (black dots) inversion recovery experiment and Hahn-echo decay of the 60 nm CuPc and H_2Pc (1:5) film on sapphire at 7 K, 35 GHz and 1218 mT. A single exponential fit (red line) is shown as well.

Both decays show a exponential behavior and are imposed by a small oscillation. With a monoexponential fit, the relaxation times $T_1 = 7.1(1)$ µs and $T_m = 400(19)$ ns can be extracted from the inversion recovery experiment respectively Hahn-echo decay. These rather short times can be explained by the high concentration of CuPc which causes electron spin-spin diffusion. In previous investigations [100], the concentration dependency of T_1 and T_m of CuPc in H_2Pc was studied. Although the highest concentration measured was 10%, the measured relaxation times here fit very well to the expected extrapolated values for a 20% concentration $T_{1,ext} \approx 10$ µs and $T_{m,ext} \approx 300$ ns.

The CuPc and H_2Pc film was about 60 nm thick, nearly one order of magnitude thinner compared to previous studies. Furthermore, the film sample was not mechanically processed and thus measured in situ. This demonstrates that the Fabry-Pérot resonator is an excellent tool for the investigation of MQBs on surfaces.

60 nm is already quite thin but still far away from a single layer of MQBs and thus any surface effects except the ordering might be screened. The signal-to-noise ratio in the measurements presented was already quite low (about 0.5 for a single shot measurement) thus going to lower thicknesses with this system will be tricky. Increasing the copper concentration is no option as it would further decrease T_m which is already close to the spectrometers deadtime. One of the main problems of the presented system is the large anisotropy of CuPc. Therefore, even at the field where the spectrum reaches its maximum in intensity, a 20 ns pulse only excites about 1% of all spins.

To overcome this issue, a different system will be investigated in the next section containing the organic radical BDPA, which has a much more narrow spectrum.

4.3.2. Spin coated polymer films with organic radicals

Pulsed EPR measurements on thin films of 5% BDPA in PMMA with thicknesses ranging from 10 nm to 100 nm (thickness determined by AFM, see Appendix Figure A.9-A.14) spin coated on a quadratic silicon wafers (1.5 x 1.5 x 0.05 cm) were performed at 35 GHz and 7 K utilizing the Fabry-Pérot resonator. Furthermore, a 1 mg bulk sample of 5% BDPA in PMMA was measured for comparison.

ESE-detected EPR spectra

First, ESE-detected EPR spectra of all films and the bulk sample were recorded between 1240 mT and 1255 mT. The resulting spectra, which were measured with the exactly same settings, can be seen in Figure 4.18 (see Appendix Figure A.15 and A.16 for the decays).

A single line (FWHM about 2 mT) can be observed for all films. The intensity increases as the film thickness increases with an exception of the 40.8 nm thick film which is a little bit less intense. The spectrum of the bulk sample looks essentially the same as the film spectra.

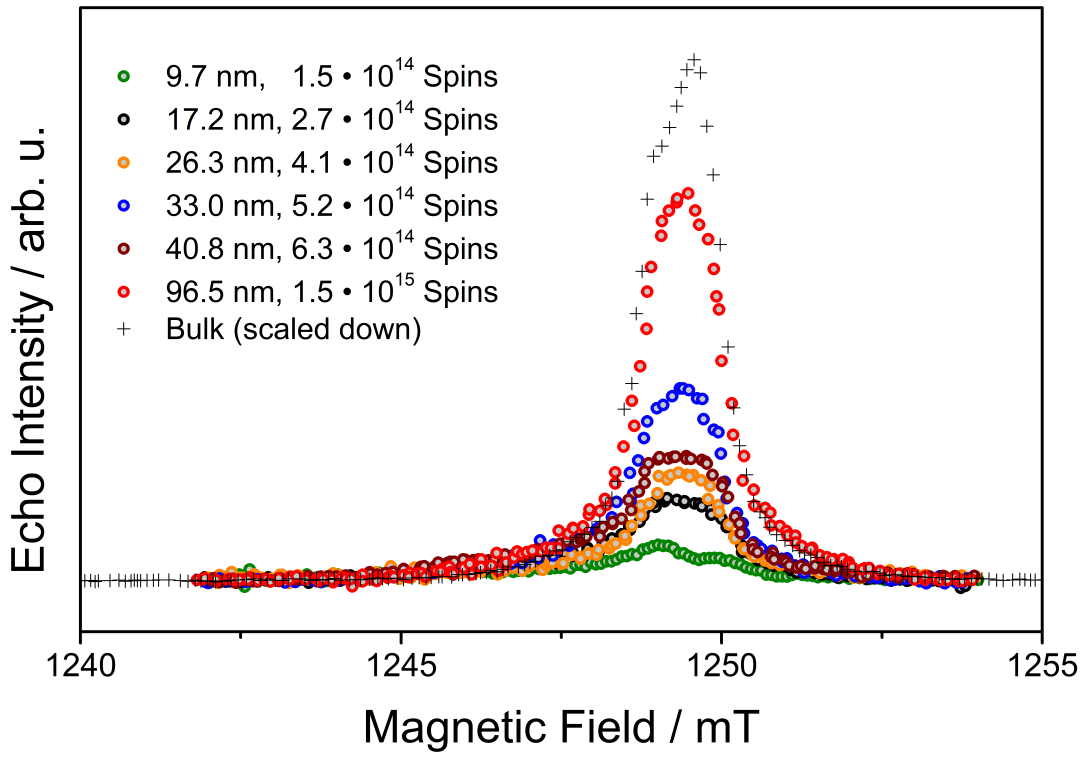

Figure 4.18.: ESE-detected EPR spectra (colored dots) of the spin coated thin films of 5% BDPA in PMMA measured at 7 K and 35 GHz. Furthermore, the measurement of the bulk sample is shown as well (black crosses).

First of all, the more or less linear increase of intensity with the film thickness is a good sign that the BDPA concentration is more or less the same for all films measured. Thus, aggregation of BDPA, commonly observed for small molecules in thin films [117], does not play a significant role. The spectrum of the thinnest film (9.7 nm) looks a little bit different compared to the rest as it has a small shoulder at 1250 mT. Here, surface effects might already effect the EPR spectrum as the thickness of the film corresponds to about ten monolayers. However, as the echo intensity of this film was already very low, experimental imperfections may be the reason for this as well. To further investigate this matter, the relaxation times of the sample were measured.

Relaxation times

The relaxation times T_1 and T_m of all films and the bulk sample were determined at 1249 mT utilizing the Saturation by Fast Repetition (SFR) respectively Hahn-echo decay sequence. The resulting relaxation times are visualized in Figure 4.19.

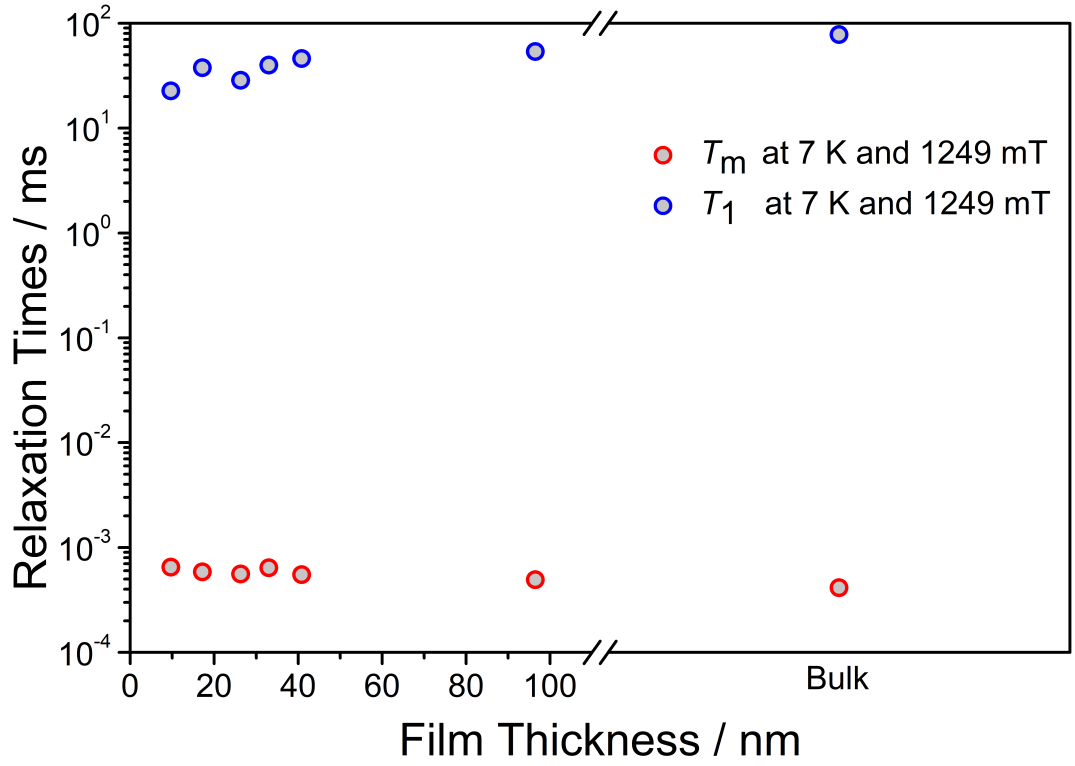

Figure 4.19.: Relaxation times T_1 (blue dots) and T_m red dots of the spin coated thin films of 5% BDPA in PMMA measured at 7 K, 35 GHz and 1249 mT. As a comparison, the relaxation times of the bulk sample are shown as well.

T_m and T_1 are nearly constant over the whole thickness range with a small tendency for T_m to decrease and for T_1 to increase. The bulk sample has essentially the same relaxation times as the films. Although this seems to be rather unspectacular, it shows that the properties of MQBs are very robust even when they prepared as a very thin film.

To sum it up, it was possible to measure a very thin film of 9.7 nm of BDPA 5 w.% in PMMA on a silicon substrate without any mechanical treatment of the sample. This is a very promising step towards characterizing spins on a potential silicon based quantum chip. The important relaxation times of the films were fairly unaffected by the film thickness and are essentially the same as the ones of the bulk sample. This demonstrates the excellent robustness of the system for further investigations like contacting the spins electrically.

4.4. Conclusion

In this chapter, it was shown that pulsed EPR on very thin films can be performed very comfortably with a Fabry-Pérot resonator. The principals of how to design such a resonator for EPR measurements were explained in the first part of this chapter. The manufactured resonator was thoroughly characterized by a combination of VNA and pulsed EPR measurements with electromagnetic field simulations in *CST-Studio*. It turned out that the field distribution of the first four modes occurring in the resonator are strongly affected by the coupling hole through which the microwaves are coupled in. This leads to a lower Q-factor and worse field homogeneity of these modes. Thus, the best mode in terms of field homogeneity and signal strength was the fourth mode occurring in the resonator which was identified to be the TEM_{001} mode. The resonator was used to measure a 60 nm thin film of CuPc in H_2Pc (1:5). The film was prepared on a 2.5x2.5 cm sapphire substrate, still it was possible to measure this film without any mechanical treatment like cutting thanks to the large dimension of the resonator. The measurements were in a good agreement with measurements performed before [100] on a much thicker film (400 nm). Furthermore, it was possible to observe ordering of the CuPc molecules by interpreting the EPR spectrum under consideration of partial ordering. Therefore, EPR can be a great addition for investigating molecules on surfaces. In the end it was demonstrated that it is possible to investigate spins on the semiconducting platform silicon. Here, pulsed EPR measurements on thin films of 5 w.% BDPA

in PMMA were performed. The system proven to be very robust which manifest into thickness independent relaxation times down to a thickness of 9.7 nm. Again, the thin films were directly measured without any post mechanical treatment which is necessary if a smaller resonator is used.

The results are a very promising step towards the characterization of spins in an actual working quantum chip based on, for example, a silicon interface. The resonator was already employed to characterize MQBs in a thin film of conducting polymer [41] which will be used to electrically address the incorporated MQBs. In a next step, the film could be coated on an electrical readout structure where the spins are controlled utilizing the resonator and read out through the electrical interface.

5. Strong coupling of photons with molecular quantum bits

This chapter is based on the research papers

Strong coupling between resonators and spin ensembles in the presence of exchange couplings, Samuel Lenz, David Hunger and Joris van Slageren, *Chem. Commun.*, 2020, 56, 12837-12840

and

Room-Temperature Quantum Memories Based on Molecular Electron Spin Ensembles, Samuel Lenz, Dennis König, David Hunger and Joris van Slageren, *Chem. Commun.*, 2019, 55, 7163-7166

and uses parts of it. David Hunger performed the temperature dependent measurements (SQUID and VNA) on both spin ensembles , Dennis König provided additional measurements of the quantum memory efficiency which are not included in this Chapter.

5.1. Introduction

In order to perform quantum computing, qubits are obviously one of the main ingredient for processing quantum information (QIP). However, during computation information has to be transferred and stored in analogy to our classical computers. Photons are the natural choice for transporting quantum information as those quantum objects travel with the speed of light. For a highly efficient transfer of quantum information from a matter based MQBs to a photon, it is necessary to strongly couple the spins of MQBs with the electromagnetic field of a photon. Devices operating in the strong coupling regime can act as a quantum memory [47, 118] and could play an important role as a quantum repeater in a photon based quantum network [119].

In this context, strong coupling means that the interaction between photons and MQBs has to exceed all losses occurring during the interaction. In order to enter this regime, the electromagnetic field of a photon is enhanced by using a cavity confining the field [61]. However, the interaction between a spin and the magnetic field of a photon is usually to weak to satisfy the strong coupling condition. Fortunately, the interaction can be enhanced as an ensemble of spins collectively interacts with the photon [118, 120].

Currently, strong coupling between microwave photons and spins has been demonstrated for NV-Centers in diamond [59, 121], phosphorus impurities in silicon [58], several molecular systems like transition metal ions [122] and organic radicals[123, 124]. It has been demonstrated that inhomogeneous broadening of a spin ensemble could be the key for storing quantum information [47, 60, 125] in strongly coupled systems as it allows a controllable coupling between spins and photons by utilizing dark states.

Most of the studies involve superconducting cavities and/or millikelvin temperatures in order to achieve the strong coupling limit. Furthermore, only very few studies cover the dynamics of the system and only present steady state results. Last but not least, the interaction between spins is usually neglected.

In order to tackle this open ends, strong coupling using simple molecular radical systems as α,γ-bisdiphenylene-β-phenylallyl-benzene (BDPA) complex and 2,2-diphenyl-1-picrylhydrazyl (DPPH) will be demonstrated utilizing the Fabry-Perot resonator presented in Chapter 4. The investigations show that high cooperativities up to room temperature are possible. Furthermore, the interaction between spins will be observed and included in the theoretical description of the system. Last but not least, the dynamics of the the strongly coupled systems will be explored utilizing a simple pulsed EPR setup.

5.2. Magnetic characterization of the spin ensembles

The coupling of a spin ensemble with a microwave resonators is dependent on the number of active (e.g. unpaired) spins in the ensemble. Therefore, samples of BDPA·Bz and DPPH which will be used for the following experiments were characterized by the means of SQUID magnetometry. This technique allows to extract the number of active spins per mass of the material for a wide range of temperature.

5.2.1. SQUID magnetometry of BDPA·Bz

The magnetic moment μ of a 18.0 mg pressed pellet of BDPA·Bz was measured from 1.8 K to 50 K at 1000 Oe and from 50 K to 300 K at 10000 Oe applied magnetic field. From the data, the molar paramagnetic susceptibility $\chi = \mu/(nH)$ was calculated where n is the amount of sample in mol and H the magnetic field strength in Oe. The data was corrected for a diamagnetic contribution of -550 $cm^3 \cdot mol^{-1}$ in order to obtain the correct behavior at high temperatures. Figure 5.1 shows the measurement (left, black dots), χ increases towards lower temperatures until 5 K, where it reaches a plateau and then again starts to rise. The product χT is shown as well (right, black dots), it features a constant value of 0.371 cm^3 K mol^{-1} above 200 K, whereas at lower temperature it bends towards zero. In order to reach the expected high temperature value of 0.371 cm^3 K mol^{-1}, an amount of sample n half as much as calculated for a 18 mg BDPA·Bz pellet and a diamagnetic contribution double as large as expected from the molar mass has to be assumed. This indicates that the sample, although freshly bought, contains only 50% active spins. This will be confirmed by the steady state measurements of the strongly coupled system in Section 5.3.

The high temperature behavior of χT can be described by Curie's law. Assuming a spin with $S = 1/2$ and a g-value of 2.0027 [78], a Curie constant $C = 0.375$ cm^3 K mol^{-1} can be calculated, which fits very well to the observed value and to what was reported in the past [126]. At lower temperatures, χT starts to deviate from the Curie's law due to antiferromagnetic interactions. It was reported [126] that BDPA·Bz behaves like a Heisenberg antiferromagnet described by the Hamiltonian

$$\mathscr{H} = g\mu_B B_0 \sum_i^{Nc} \hat{S}_{z,i} - 2J \sum_i^{Nc} \hat{S}_i \hat{S}_{i+1} \tag{5.1}$$

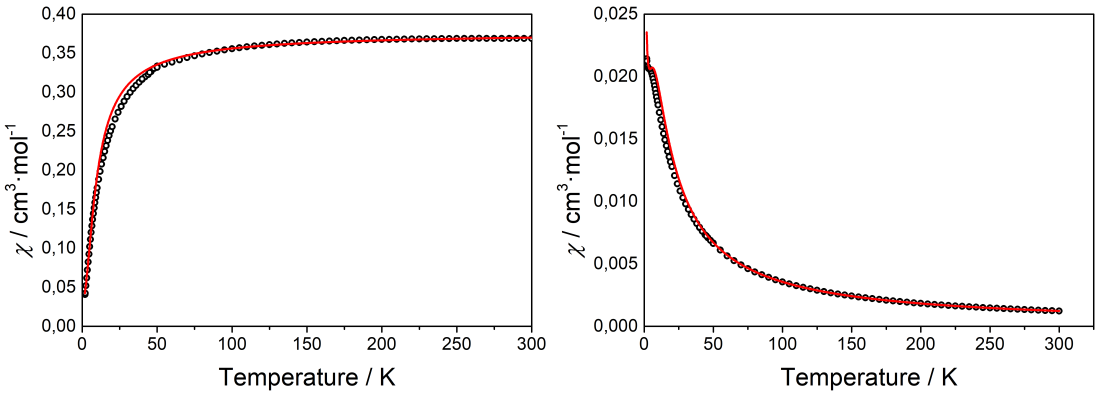

Figure 5.1.: Magnetic susceptibility χ of the BDPA·Bz sample (left, black dots) and the product χT (right, black dots) in the temperature range of 1.8 K to 300 K. A corresponding calculation (left and right, red line) based on the Hamiltonian in eq. 5.1 is shown as well.

with an exchange constant J and the chain length $N_c \to \infty$. The magnetic susceptibility χ_{AF} of such a system can be approximated by a ring with a finite N_c [127]. The result improves, if the susceptibility is calculated for an even and odd number of spins to form the mean $\bar{\chi} = [(N_c-1)\chi_{N_c} + (N_c)\chi_{N_c-1}]/(2N_c-1) \approx \chi_{AF}$. Therefore, the magnetic susceptibility was calculated for rings of the size $N_c = 12, 11$ using the Matlab package Easyspin and the mean was formed. The resulting χ and χT per single spin with $J/k_B = -4.9$ K are shown in Figure 5.1 as well (red solid line). To account for the small rise at very low temperatures, an uncoupled $S = 1/2$ impurity (4% with respect to the coupled amount) with $g = 2$ was added to the calculation. The calculate χ and χT are in a good agreement with the measured susceptibility. The fitted exchange constant $J/k_B = -4.9$ K is in a perfect agreement with the reported [127, 128] values of -4.2 K to -5.75 K for BDPA·Bz so far.

In summary, the BDPA·Bz sample contains about 50% active spins and still shows the expected behavior of a antiferromagnetic chain with an exchange constant $J/k_B = -4.9$ K. Therefore, it is most likely that beside BDPA·Bz the sample contains a very similar diamagnetic impurity. As the antiferromagnetic properties match the ones from pristine material, it will be still used for the hybrid system measurements keeping in mind the lower amount of active spins.

5.2.2. SQUID magnetometry of DPPH

SQUID magnetometry and preliminary data analysis on the DPPH used for the hybrid systems was performed by David Hunger during his master thesis.

The magnetic moment μ of a 11.4 mg pressed pellet of DPPH was measured from 1.8 K to 300 K at 1000 oe. The data was corrected for a diamagnetic contribution of -330 $cm^3 \cdot mol^{-1}$. Figure 5.2 shows that χ increases towards lower temperatures until 9 K where it reaches a maximum after which it decreases towards 2 K. A small increase at temperatures below 2 K can be observed. The product χT is shown as well (right, black dots), it features a constant value of 0.368 cm^3 K mol^{-1} above 200 K, whereas at lower temperature it bends towards zero. In order to reach the expected high temperature value of 0.368 cm^3 K mol^{-1}, an amount of sample $n = 0.84 n_w$, where n_w is the amount calculated for a 11.4 mg DPPH pellet, has to be assumed. This indicates that the sample contains about 84% active spins. This will be confirmed by the steady state measurements of the strongly coupled system in Section 5.3.

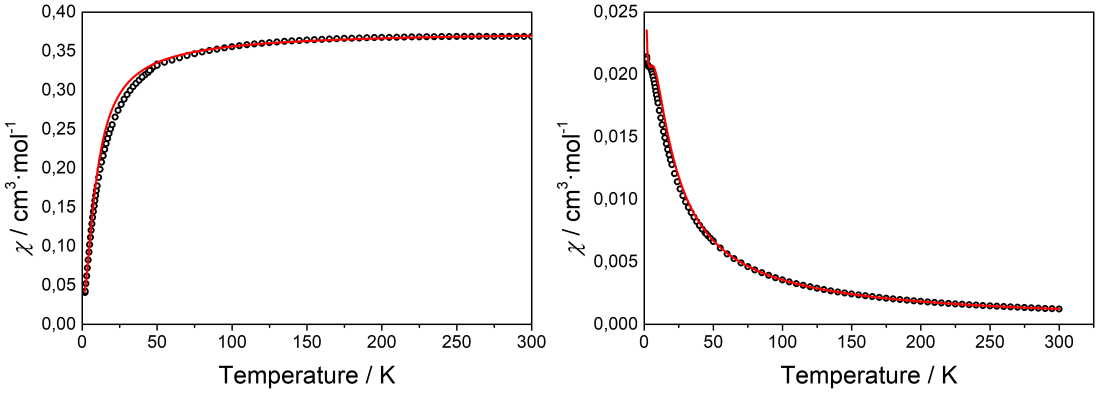

Figure 5.2.: Magnetic susceptibility χ of the DPPH·Bz sample (left, black dots) and the product χT (right, black dots) in the temperature range of 1.8 K to 300 K. A corresponding calculation (left and right, red line) based on the Hamiltonian in eq. 5.1 is shown as well.

The high temperature behavior of χT can be described by Curie's law. Assuming a spin with $S = 1/2$ and a g-value of 2.0036 [129], a Curie constant $C = 0.375$ cm^3 K mol^{-1} can be calculated, which fits very well to the observed value of 0.368 cm^3 K mol^{-1} and to what was reported [129] recently. At lower temperatures, χT starts to deviate from the Curie's law due to antiferromagnetic interactions. It was reported [129, 130] that solvent free DPPH forms antiferromagnetic dimers described by the Hamiltonian

$$\mathscr{H} = g\mu_B B_0(\hat{S}_{z,1} + \hat{S}_{z,2}) - 2J\hat{S}_1\hat{S}_2 \tag{5.2}$$

with an exchange constant J. These dimers contribute with $\chi_{\text{Dim.}}$ to the total magnetic susceptibility. Even in freshly prepared DPPH single crystals, approximately 10% uncoupled ($J = 0$) spins are present [129] giving a contribution $\chi_{\text{uncoupled}}$ to the total susceptibility. In order to extract J from the SQUID measurements, the magnetic susceptibility $\chi_{\text{tot.}} = a\chi_{\text{Dim.}}/2 + (1-a)\chi_{\text{uncoupled}}$ was calculated using the Matlab package Easyspin. The resulting χ and χT per single spin with $2J/k_B = -17.7$ K and $a = 0.92$ are shown in Figure 5.2 as well (red solid line). The calculate χ andχT are in a good agreement with the measured susceptibility. The fitted exchange constant $2J/k_B = -17.7(5)$ K is in a perfect agreement with the reported [129, 130] value of -17.5 K for DPPH.

In summary, the DPPH sample contains about 84% active spins and shows the behavior of antiferromagnetic dimers with an exchange constant $2J/k_B = -17.7(5)$ K. About 8% uncoupled spins are present in the sample. It will be interesting to see, whether the type of antiferromagnetism (chain or dimer) has any influence on the hybrid systems

5.3. Steady-state measurements

A simple way to investigate a spin ensemble in the strong coupling regime, is to perform reflection measurements on the system by the means of a VNA. The data can be evaluated using the Equation 2.77 in order to extract the dissipation rates κ, γ and the collective coupling Ω_{eff}.

5.3.1. Mode dependent measurements

Initial measurements were performed on a 18 mg, 5 mm pressed pellet of BDPA·Bz containing approximately $N = 1.1 \cdot 10^{19}$ spins. The spin ensemble was tuned into resonance using an electromagnet. The used sweep range of the magnet was 1230 mT to 1260 mT. Before the magnetic field was applied, the resonator was tuned to 35.00 GHz with the sample mounted and S_{11} was measured in order to extract the dissipation rates κ_{i} and κ_{e} by fitting the data as described in Section 4.2.2. Measurements were performed for the first four modes occurring in the resonator.

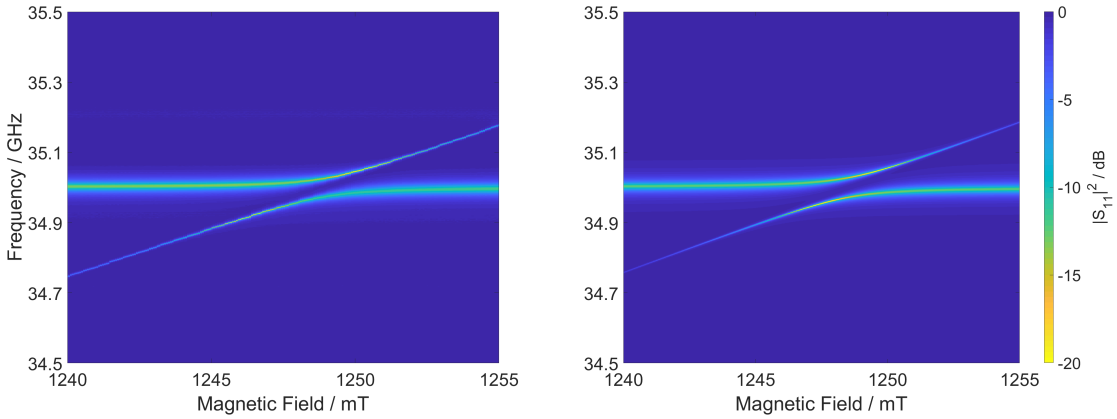

(a) Experiment **(b)** Simulation

Figure 5.3.: Magnitude of the measured reflection parameter S_{11} (left Figure) at room temperature of a 18 mg, 5 mm pressed pellet of BDPA·Bz inside a copper Fabry-Pérot (first mode) resonator as a function of the probe frequency and the applied external magnetic field. An anti-crossing is visible when ω_{s} approaches ω_{c} indicating that the system is in the strong coupling regime. A simulation based on Equation 2.77 using the parameters from Table 5.1 is shown on the right side. Slices along specific fields for both experiment and simulation are shown in Figure 5.4.

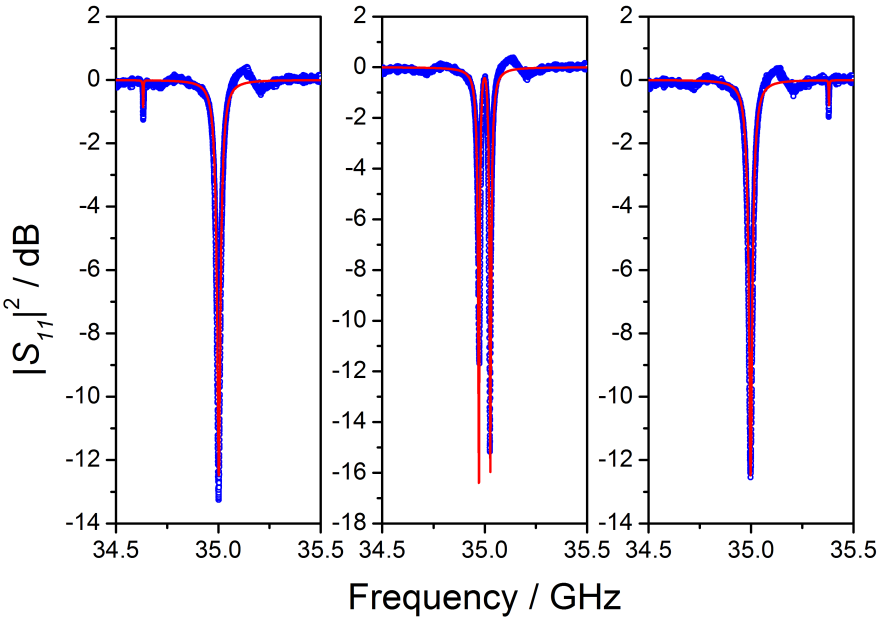

Figure 5.4.: Slices trough the exerimental data (blue dots) and simulation (red line) presented in Figure 5.3 at the fields 12355.7 Gauss(left), 12485.4 Gauss (middel) and 12620.8 Gauss (right)

Figure 5.3a shows a measurement of the system at room temperature utilizing the first mode of the Fabry-Pérot resonator. At 1240 mT, the broad cavity resonance can be seen at $\omega_c/2\pi = 35.00$ GHz while the spin resonance occurs at about $\omega_s/2\pi = 34.75$ GHz. By increasing the magnetic field, ω_s increases linearly and eventually reaches $\omega_c = \omega_s$. A clear anti-crossing is observed in this region. S_{11} was fitted to the data according to eq. 2.77, and the simulation can be seen in Figure 5.3b. The parameters $\Omega_{eff}/2\pi = 28.0(5)$ MHz, $\kappa_i/2\pi = 8(1)$ MHz, $\kappa_e/2\pi = 13(1)$ MHz and $\gamma/2\pi = 1.5(5)$ MHz were used and ω_s was calculated from the magnetic field B_0 assuming only isotropic Zeeman-interaction $\omega_s = \frac{g_{iso}\mu_B B_0}{\hbar}$ with $g_{iso} = 2.0028$. For a better comparison, the data and calculation were sliced at different fields which can be seen Figure 5.4.

The measurement on the next three modes were analyzed in the same way, and the parameters are summarized in Table 5.1.

The observation of an anti-crossing already demonstrates that the system is in the strong coupling regime. The fulfillment of the condition $\kappa, \gamma < \Omega_{eff}$, derived from the fits, further confirms this. A collective coupling of $\Omega_{eff} = 28$ Mhz is one of the largest couplings at room temperature reported for strongly coupled radicals so far [123, 124, 131]. For a coherent exchange of a single photon, Ω_{eff} has to be compared to

the dissipation rates γ and $\kappa = \kappa_i + \kappa_e$. The Figure of merit here is the cooperativity $C = \frac{\Omega^2}{\gamma\kappa}$. An outstanding value of $C = 24.9$ is reached for the first mode, comparable to other similar hybrid system which, however, operate at millikelvin temperatures [59, 132, 133].

Table 5.1.: Measured dissipation rates, collective coupling constants and cooperativities of a 18 mg BDPA·Bz sample inside the copper Fabry-Pérot resonator at room temperature. The values were obtained by fitting eq. 2.77 to the measured reflection data. The single spin coupling constant was calculated from CST-Simulations of the first four modes inside the Resonator.

Mode	$\gamma/2\pi$ (MHz)	$\kappa_i/2\pi$ (MHz)	$\kappa_e/2\pi$ (MHz)	$\Omega_{eff}/2\pi$ (MHz)	$g_{s,sim}/2\pi$ (Hz)	C
First	1.5(2)	8.0(5)	13.0(5)	28.0(5)	0.139	25(5)
Second	1.5(2)	6.5(5)	7.0(5)	19.0(5)	0.099	17(3)
Third	1.5(2)	4.0(5)	7.0(5)	12.0(5)	0.072	9(2)
Fourth	1.5(2)	4.0(5)	4.0(5)	13.0(5)	0.076	14(2)

At a first glance, it seems to be a little odd that such a dense spin ensemble can be described by just an isotropic g_{iso} value with a very narrow linewidth of $\gamma/2\pi = 1.5$ MHz. The line should be heavily broadened by unavoidable dipolar interactions $\omega_{dip}/2\pi \approx 50$ MHz calculated from the crystal structure [134] of BDPA·Bz. However, an isotropic antiferromagnetic exchange $J/k_B = -4.9$ K much larger then the dipolar fields is present in crystalline BDPA·Bz [126] leading to an effect called exchange narrowing. In a nutshell, the exchange averages out the dipolar interactions in time leading to a much narrower line which eventually becomes lorentzian if $J/\hbar \gg \omega_{dip}$ [135]. In summary, this effect leads to an effective description of the spin system were a spin ensemble of identical spins with a single resonance frequency ω_s and a single relaxation rate γ can be assumed.

The collective coupling $\Omega_{eff} = \sqrt{-2N\langle\hat{S}_z\rangle}g_s$ (see Equation 2.77) depends on the number of spins $N = 1.1 \cdot 10^{19}$, their polarization $\langle\hat{S}_z\rangle$ and the single spin coupling constant $g_s = |B_{x,Photon}|\frac{g\mu_B}{2\hbar}$ which depends on the magnetic field strength of a single photon inside the cavity. $|B_{x,Photon}|$ can be derived from the microwave simulations of the Fabry-Pérot modes discussed in chapter 4. This is accomplished by normalizing the simulated field $|B_{x,sim}|$ on the number of photons $|B_{x,Photon,sim}| = |B_{x,sim}|/\sqrt{N_p}$ [59]. The numbers of photons can be estimated from the stored energy inside the resonator. As CST microwave simulations using the Eigenmode-Solver always normalize the stored energy to

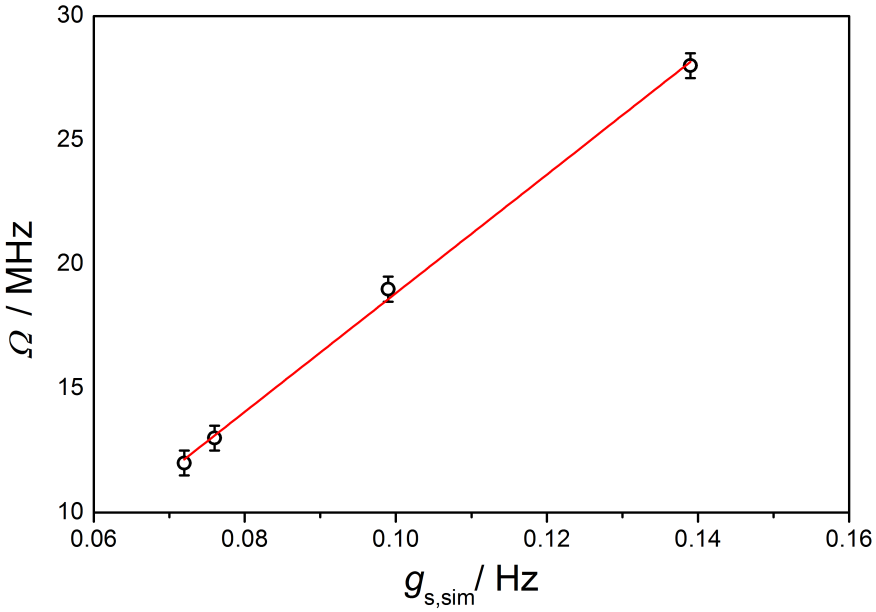

Figure 5.5.: Measured collective coupling Ω_{eff} (black dots) of the 18 mg BDPA·Bz sample for the first four modes occurring in the Fabry-Pérot resonator with respect to the simulated single spin coupling of the given mode. The values are presented in Table 5.1 as well.

1 J, the simulated fields correspond to $N_{\text{p}} = 1\,\text{J}/\hbar\omega_{\text{c}} \approx 4.3 \cdot 10^{22}$ photons. The resulting single spin coupling constants $g_{\text{s,sim}}$ for each mode are shown in Table 5.1. In addition, Figure 5.5 shows Ω_{eff} plotted against $g_{\text{s,sim}}$. A clear linear relationship can be observed proving the reliability of the microwave simulations.

For a reliable calculation of $g_{\text{s,exp}}$ the exception value $\langle \hat{S}_z \rangle$ has to be know (see eq. 2.79. With a probe power of -20 dBm, the VNA populates the resonator with approximately $1 \cdot 10^9$ photons, i. e. much less then the number of spins. Therefore, the polarization of the spins does only change insignificantly due to excitation and can be approximated with the thermal equilibrium polarization $\langle \hat{S}_z \rangle_{\text{eq}}(T) \approx \langle \hat{S}_z \rangle$ which only depends on the temperature T. As this quantity should be affected by the antiferromagnetic exchange coupling, it will be investigated in more detail in the following section by the means of temperature depended measurements.

5.3.2. Temperature dependence of strong coupling in BDPA·Bz

Temperature dependent measurements of BDPA·Bz and preliminary data analysis were performed by David Hunger during his master thesis. The measurements in the range of 7 K to 293 K were performed on a 9.4 mg, 5 mm pressed pellet of BDPA·Bz containing approximately $N = 0.6 \cdot 10^{19}$ spins. The sample was mounted in a copper Fabry-Pérot resonator in a way as shown in Figure 4.6. The spin ensemble was tuned into resonance using an electromagnet. The used sweep range of the magnet was 1230 mT to 1260 mT. Before the magnetic field was applied, the resonator was tuned to 35.00 GHz with the sample mounted and S_{11} was measured in order to extract the dissipation rates κ_i and κ_e by fitting the data as described in Section 4.2.2. The first mode occurring in the resonator was used for all measurements.

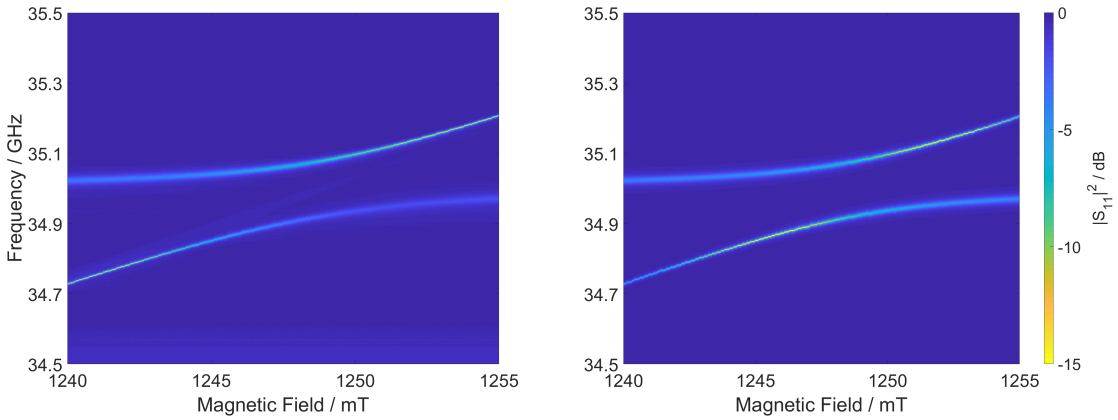

(a) Experiment **(b)** Simulation

Figure 5.6.: Magnitude of the measured reflection parameter S_{11} (left Figure) at 7 K of a 9.4 mg, 5 mm pressed pellet of BDPA·Bz inside the copper Fabry-Pérot (first mode) resonator with respect to the probe frequency and an applied external magnetic field. An anti-crossing is visible when ω_s approaches ω_c indicating that the system is in the strong coupling regime. A simulation based on Equation 2.77 using the parameters from Table 5.2 is shown on the right hand side.

Figure 5.6b shows a measurement at 7 K, again the cavity resonance can observed at 35 GHz and the spin resonance at 34.7 GHz at 1240 mT. Compared to the room temperature measurements shown in Figure 5.3a before, the gap of the anti-crossing is much larger. Furthermore, a faint line passing the anticrossing is visible which will be discussed in Section 5.3.4 To extract the relevant parameters, the data was fitted using eq. 2.77. The resulting simulation for 7 K can be seen in Figure 5.3b. The same procedure

to analyze the data was carried out on the measurements at higher temperatures. The resulting parameters are summarized in Table 5.2. $\Omega_{\text{eff}}(T)$ is visualized in Figure 5.7 for all measured temperatures. As the larger gap in Figure 5.6b already suggests, Ω_{eff} increases towards lower temperature.

Table 5.2.: Measured dissipation rates, collective coupling constant and cooperativity of a 9.4 mg BDPA·Bz sample inside the copper Fabry-Pérot resonator at different temperatures. The values were obtained by fitting eq. 2.77 to the measured reflection data.

Temperature K	$\gamma/2\pi$ (MHz)	$\kappa_{\text{i}}/2\pi$ (MHz)	$\kappa_{\text{e}}/2\pi$ (MHz)	$\Omega_{\text{eff}}/2\pi$ (MHz)	C
7	1.5(5)	2.0(5)	13.0(5)	80(3)	290(90)
9	1.5(5)	2.0(5)	13.0(5)	78(3)	270(90)
11	1.5(5)	2.0(5)	13.0(5)	73(3)	240(80)
13	1.5(5)	2.0(5)	13.0(5)	71(3)	220(70)
15	1.5(5)	2.0(5)	13.0(5)	68(2)	200(70)
20	1.5(5)	2.0(5)	13.0(5)	62(2)	170(60)
25	1.5(5)	2.0(5)	13.0(5)	58(2)	150(50)
30	1.5(5)	2.0(5)	13.0(5)	53(2)	120(40)
50	1.5(5)	2.0(5)	13.0(5)	41(2)	70(20)
70	1.5(5)	2.5(5)	13.0(5)	36(2)	60(20)
90	1.5(5)	2.5(5)	13.0(5)	31(2)	40(10)
100	1.5(5)	2.5(5)	13.0(5)	31(2)	40(10)
120	1.5(5)	2.5(5)	13.0(5)	29(2)	40(10)
180	1.5(5)	3.0(5)	13.0(5)	24(2)	25(10)
200	1.5(5)	3.5(5)	13.0(5)	23(2)	21(7)
240	1.5(5)	4.5(5)	13.0(5)	20(2)	15(5)
291	1.5(5)	5.5(5)	13.0(5)	19(2)	13(5)

An increase of Ω_{eff} is expected as the absolute value of the spin polarization $\langle \hat{S}_z \rangle$ should increases at lower temperature. For simple spin $S = 1/2$ system, the polarization can be calculated according to Boltzmann with the equation

$$\langle \hat{S}_z \rangle_{\text{eq.}}(T) = -0.5 \tanh \frac{\hbar \omega_{\text{s}}}{kT} \tag{5.3}$$

Using the definition $\Omega_{\text{eff}} = \sqrt{-2N \langle \hat{S}_z \rangle} g_{\text{s}}$ together with $N = 0.6 \cdot 10^{19}$ and eq. 5.3, the measured $\Omega_{\text{eff}}(T)$ can be fitted using a single spin coupling constant $g_{\text{s}}/2\pi = 0.14(1)$ Hz (Figure 5.7, red dashed line). However, the fit deviates quite a lot from the experimental values at lower temperatures. The reason for this is the antiferromagnetic

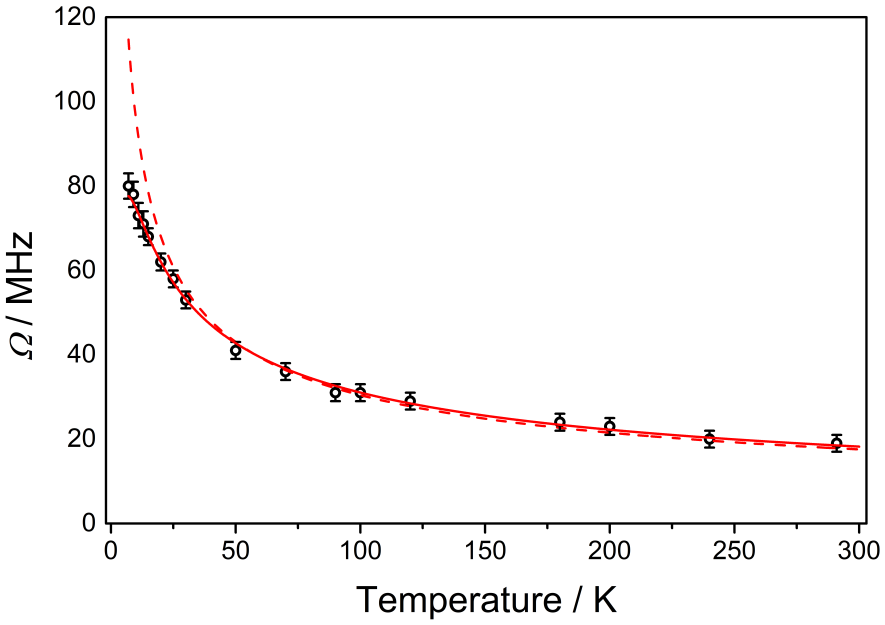

Figure 5.7.: Measured collective coupling constants of a 9.4 mg BDPA·Bz sample inside the copper Fabry-Pérot resonator (black dots) at temperatures between 7 K to 293 K utilizing the first mode. Two fits are included, the first one (red dotted line) assumes a temperature dependent spin polarization of a single $S = 1/2$ system (eq. 5.3) and the second one (red solid line) uses a spin polarization based on a linear antiferromagnetic chain (see text for details) with 12 chain members.

exchange present in pure BDPA·Bz, which has a strong impact on the polarization. As pointed out in Section 5.2.1, the antiferromagnetism of BDPA·Bz sample can be described with the Hamiltonian described in eq. 5.1 with an exchange constant $J/k_{\mathrm{B}} = -4.9$ K and the chain length $N_{\mathrm{c}} = 12$.

The *Matlab* package *Easyspin* was used to calculate $\left\langle \hat{S}_{z,i} \right\rangle_{\mathrm{eq.}}(T)$ for every chain member. The mean polarization of a single spin inside the chain was calculated using the equation $\left\langle \hat{S}_z \right\rangle_{\mathrm{eq.}}(T) = 1/N_{\mathrm{c}} \sum_i \left\langle \hat{S}_{z,i} \right\rangle_{\mathrm{eq.}}(T)$. Again, the measured $\Omega_{\mathrm{eff}}(T)$ was fitted using the calculated mean polarization of a linear chain with $N_{\mathrm{c}} = 12$ and a single spin coupling constant $g_{\mathrm{s}}/2\pi = 0.145(6)$ Hz. The result is shown in Figure 5.7 as a red solid line. It fits perfectly over the whole temperature range proving that the antiferromagnetic exchange can not be neglected in order to understand the temperature dependent behavior. The fitted single spin coupling constant $g_{\mathrm{s}} = 0.145(6)$ Hz is in a very good agreement with the simulated constant of the first mode $g_{s,\mathrm{sim}}/2\pi = 0.14$ Hz.

According to the definition of Ω_{eff}, it should scale with square root of the number of total spins $\sqrt{N_{\mathrm{S}}}$ as well. The temperature dependent measurements where carried out on a 9.4 mg sample which approximately contains halve as much spins then the one used for the mode dependent measurements. In fact, the collective coupling at room temperature of the 18 mg sample used for the mode dependent measurements is $\Omega_{\mathrm{eff,18mg}}/2\pi = 28$ MHz which is very close to $\sqrt{2}\Omega_{\mathrm{eff,9.4mg}} = 27$ MHz. The maximum reasonable amount of sample for the first mode is approximately 30 mg of BDPA·Bz before the pellet size becomes bigger than the mode volume. Therefore, a collective coupling constant $\Omega_{\mathrm{eff,30mg}}/2\pi = 140$ MHz could be reached for BDPA·Bz at 7 K implicating a cooperativity $C \approx 1000$. Unfortunately, this measurement was not possible due to the availability of the material.

Besides the collective coupling, the internal loss κ_{i} inside the resonator decreases with the temperature as well. This is not unexpected, as κ_{i} depends on the resistivity of the resonator material which decreases with temperature. In the case of copper used for machining, the resistivity does not further decrease at temperatures below 50 K due to impurities inside the metal [136]. This explains why κ_{i} does not decrease below 50 K.

In summary, the temperature dependent behavior of BDPA·Bz can be perfectly described with the antiferromagnetic chain model introduced in Section 5.2.1 and the extracted single spin coupling constant $g_{\mathrm{s}} = 0.145(6)$ Hz fits very well to the electromagnetic field simulations of the resonator. In order to cross check the influence of the exchange coupling, the temperature dependent behavior of DPPH will be investigated which features a pair-wise antiferromagnetic exchange interaction.

5.3.3. Temperature dependence of DPPH

Temperature dependent measurements of DPPH and preliminary data analysis were performed by David Hunger during his master thesis. The measurements in the range of 7 K to 293 K were performed on a 11.4 mg, 5 mm pressed pellet of DPPH containing approximately $N = 1.46 \cdot 10^{19}$ spins. The spin ensemble was tuned into resonance using an electromagnet. The used sweep range of the magnet was 1230 mT to 1260 mT. Before the magnetic field was applied, the resonator was tuned to 35.00 GHz with the sample mounted and S_{11} was measured in order to extract the dissipation rates κ_i and κ_e by fitting the data as described in Section 4.2.2. The first mode occurring in the resonator was used for all measurements.

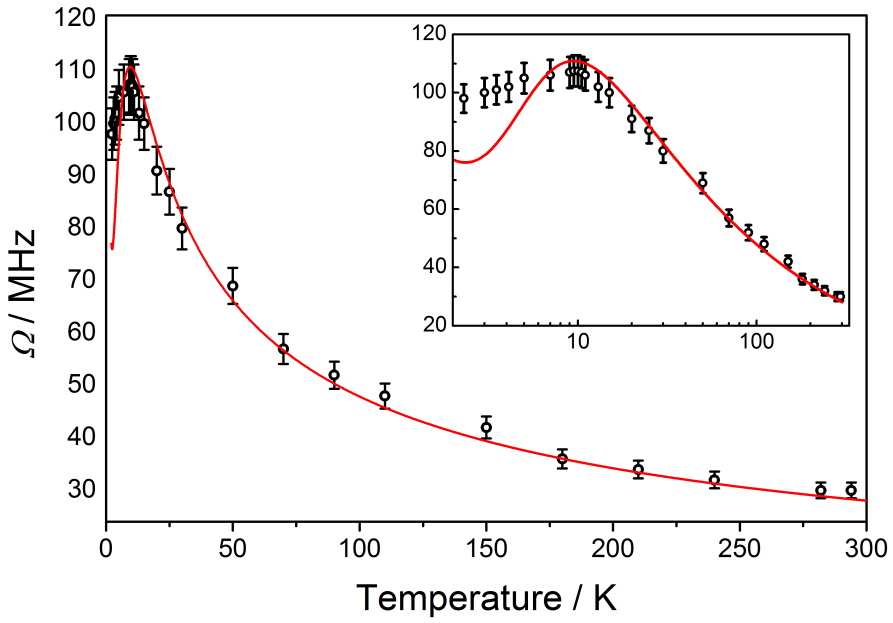

Figure 5.8.: Measured collective coupling constants of a 11.4 mg DPPH sample inside the copper Fabry-Pérot resonator (black dots) at temperatures between 7 K to 293 K utilizing the first mode. The fit (red line) included is based on the spin polarization of an antiferromagnetic dimer as determined in the SQUID measurements in Section 5.2.2

The evaluation of the data was performed analogically to the BDPA·Bz sample in Section 5.3.2 using Equation 2.77 to extract the relevant parameters which are summarized in Table 5.3. Again, κ_i starts to increase at temperatures above 70 K due to the increase in the electrical resistance of the copper. Furthermore, the spin line width γ increases

Table 5.3.: Measured dissipation rates, collective coupling constant and cooperativity of a 11.4 mg DPPH sample inside the copper Fabry-Pérot resonator at different temperatures. The values were obtained by fitting eq. 2.77 to the measured reflection data.

Temperature (K)	$\gamma/2\pi$ (MHz)	$\kappa_i/2\pi$ (MHz)	$\kappa_e/2\pi$ (MHz)	$\Omega_{eff}/2\pi$ (MHz)	C
2.3	13(2)	2.0(5)	13.0(5)	98(3)	50(10)
3	12(2)	2.0(5)	13.0(5)	100(3)	60(10)
3.5	13(2)	2.0(5)	13.0(5)	101(3)	50(10)
4.1	10(2)	2.0(5)	13.0(5)	102(3)	70(20)
5	5.0(5)	2.0(5)	13.0(5)	105(2)	150(20)
7	3.0(5)	2.0(5)	13.0(5)	106(2)	250(60)
9	3.0(5)	2.0(5)	13.0(5)	107(2)	250(60)
9.5	3.0(5)	2.0(5)	13.0(5)	107(2)	250(60)
10	3.0(5)	2.0(5)	13.0(5)	107(2)	250(60)
10.5	3.0(5)	2.0(5)	13.0(5)	108(2)	250(60)
11	3.0(5)	2.0(5)	13.0(5)	106(2)	250(60)
13	3.0(5)	2.0(5)	13.0(5)	102(2)	230(50)
15	3.0(5)	2.0(5)	13.0(5)	100(2)	220(50)
20	3.0(5)	2.0(5)	13.0(5)	91(2)	180(40)
25	3.0(5)	2.0(5)	13.0(5)	87(2)	170(40)
30	3.0(5)	2.0(5)	13.0(5)	80(2)	140(30)
50	3.0(5)	2.0(5)	13.0(5)	69(2)	100(20)
70	3.0(5)	2.0(5)	13.0(5)	57(2)	70(20)
90	3.0(5)	2.5(5)	13.0(5)	52(2)	60(10)
110	3.0(5)	2.5(5)	13.0(5)	48(2)	50(10)
150	3.0(5)	3.0(5)	13.0(5)	42(2)	40(10)
180	3.0(5)	3.0(5)	13.0(5)	36(2)	30(10)
210	3.0(5)	3.5(5)	13.0(5)	34(2)	23(5)
240	3.0(5)	4.5(5)	13.0(5)	32(2)	20(4)
282	3.0(5)	4.5(5)	13.0(5)	30(2)	17(4)
294	3.0(5)	5.0(5)	13.0(5)	30(2)	17(4)

towards lower temperatures. This indicates faster spin relaxation at lower temperatures which seems to be counter-intuitive. However, the increase of line width originates from inhomogeneous broadening, as DPPH features g-anisotropy at low temperatures [129]. The correct treatment of such a case will be explained in Section 5.3.4.

The temperature dependence of the collective coupling Ω_{eff} is visualized in Figure 5.8 (black dots). Similar to BDPA·Bz, Ω_{eff} increases towards lower temperature. At temperatures below 10 K, however, it starts to decrease. Again, this behavior is attributed to the thermal polarization $\langle \hat{S}_z \rangle_{\text{eq.}}(T)$ of the spins. Therefore, $\langle \hat{S}_z \rangle_{\text{eq.}}(T)$ was numerical calculated with *Easyspin* using the spin Hamiltonian described in eq. 5.2 with $2J/k_{\text{B}} = -17.7(5)$ K which was determined by the SQUID measurements in Section 5.2.2.

Furthermore, 10% uncoupled spins (meaning $J = 0$) as determined from the SQUID measurements have to be considered. The temperature dependent collective coupling can then be calculated with eq. 5.4 using the computed polarization $\langle \hat{S}_{z,1} \rangle_{\text{Dim}}(T)$ of the antiferromagnetic dimers and the one of the uncoupled spins $\langle \hat{S}_{z,1} \rangle_{\text{uncoupled}}(T)$ in conjunction with the numbers of spins $N = 1.46 \cdot 10^{19}$ of the DPPH sample.

$$\Omega_{\text{eff}}(T) = \sqrt{-2N\left(0.9\langle \hat{S}_{z,1} \rangle_{\text{Dim}}(T) + 0.1\langle \hat{S}_{z,1} \rangle_{\text{uncoupled}}(T)\right)}\, g_{\text{s}} \tag{5.4}$$

The single spin coupling constant $g_{\text{s}}/(2\pi) = 0.143(5)$ Hz was obtained by fitting eq. 5.4 to the data (red line in Figure 5.8). The fit is in a very good agreement with the measured collective coupling at temperatures down to 5 K. Below, it starts to deviate a bit most likely because the sample temperature deviates from the cryostat temperature. As DPPH and BDPA·Bz both are $S = 1/2$ radicals with a very similar g-value, g_{s} should be the same for both systems. Indeed, $g_{\text{s,DPPH}}/(2\pi) = 0.143(5)$ Hz and $g_{\text{s,BDPA}}/(2\pi) = 0.145(6)$ Hz are essentially the same and in a very good agreement with the simulated value of $g_{\text{s,sim}}/(2\pi) = 0.14$ Hz.

In summary, the temperature dependence of DPPH can be described very well with the model of antiferromagnetic dimers introduced in Section 5.2.2 and the single spin coupling constant $g_{\text{s,DPPH}}/(2\pi) = 0.143(5)$ Hz is basically identical to the one determined for BPDA·Bz and in a good agreement with the one obtained from the electromagnetic field simulations.

For both radicals, the antiferromagnetic interaction is not directly included in the Jaynes-Cummings Hamiltonian but only considered for thermal occupation. This is valid in the strong exchange limit where the exchange interactions exceeds the Zeeman interaction. Here, the spin ensemble of exchanged coupled $S = 1/2$ systems can be considered as an ensemble of spins with $S = 1/2,\ 1,\ 3/2, \ldots$ where each spin multiplet has

a different energy but does not interact with the other multiplets. In the case of isotropic exchange, there is no interaction of the m_S states inside the multiplet. Combining strong and isotropic exchange, the system can be effectively described by a $S = 1/2$ with a modified thermal occupation as it was demonstrated in this section.

Up to now, it was assumed that the spin systems can be described with a single resonance frequency ω_s leading to the effective coupling Ω_{eff} defined in eq. 2.77. However, at low temperatures, both radicals show inhomogeneous line broadening. The reason for the broadening is g-anisotropy which appears at low temperature [128, 129]. The presence of inhomogeneous broadening leads to spin packets with different ω_s. As a consequence, an effect called cavity protection and the coupling to former dark states emerge which will be covered in the next section.

5.3.4. Inhomogeneous broadening and the cavity protection effect

The presence of inhomogeneous broadening of the BDPA·Bz resonance line can be recognized by a carefully reexamination of the VNA measurement at 7 K shown before in Figure 5.6a. In Figure 5.9a the same measurement but with a slightly different color scale is shown. There, a faint line crossing the anti-crossing can be observed. This line marks states which should have no cavity part and thus are called dark states. However, inhomogeneous broadening of the spins leads to a small coupling to the cavity field and thus making it possible to measure this states by VNA measurements [137–139].

This behavior can be calculated by discretizing the spin ensemble into $\mathcal{N}$ sub ensembles where each sub ensemble contains $N_{id,j}$ identical spins having the same resonance frequency $\omega_{s,j}$ (Equation 2.81).

$N_{id,j}$ has to be calculated with the help of a discrete spectral density $\rho(\omega_{s,j})$ from the total numbers of spins N.

$$N_{id,j} = \frac{N\rho(\omega_{s,j})}{\sum^{\mathcal{N}} \rho(\omega_{s,j})} \tag{5.5}$$

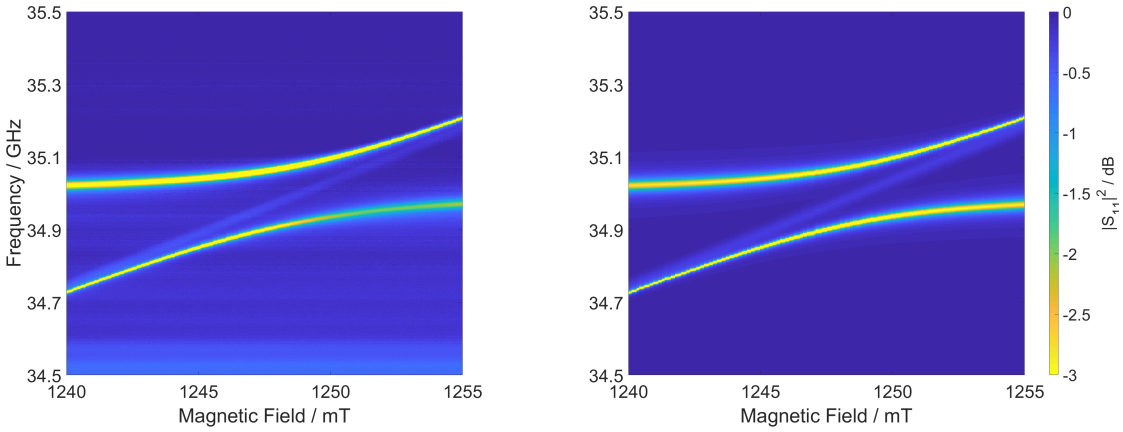

(a) Experiment **(b)** Simulation

Figure 5.9.: Magnitude of the measured reflection parameter S_{11} (left Figure) at 7 K of a 9.4 mg, 5 mm pressed pellet of BDPA·Bz inside the copper Fabry-Pérot (first mode) resonator with respect to the probe frequency and an applied external magnetic field. This Figure shows the same date as presented in Figure 5.6a but with a different color scale. Here, a faint line crossing the anti-crossing is observed. The line originates from a inhomogeneous spectral density of the spin system and can be reproduced (right side) with eq. 2.81.

The measured data shown in Figure 5.9a was simulated using a q-Gaussian spectral density (see eq. 5.6 and 5.7). This spectral density becomes Gaussian for $q \to 1$ and Lorentzian for $q = 2$. It was chosen as the broadening of DPPH and BDPA can not be described by either a Gaussian nor a Lorentzian line [128, 129] and because it was demonstrated that the q-Gaussian distribution can be applied successfully in such cases [54].

$$\rho(\omega_{s,j}) = \left[1 - (1-q)\frac{(\omega_{s,j} - \omega_{s,c})^2}{\Delta^2}\right]^{\frac{1}{1-q}} \tag{5.6}$$

$$\gamma_{inh} = 2\Delta\sqrt{\frac{2^q - 2}{2q - 2}} \tag{5.7}$$

The resulting simulation with a full width at half maximum of $\gamma_{inh} = 11.9(3)$ MHz and the q-parameter $q = 1.1$ is shown in 5.9b, the appearance of the faint line in the simulation can be clearly seen. Slices at certain fields are shown in Figure 5.10, the coupling to dark states can be seen as a side band at the spin resonance in the dispersive region $\omega_c \neq \omega_s$ and as a small hump when the cavity is on resonance with the central spin frequency $\omega_c = \omega_{s,c}$.

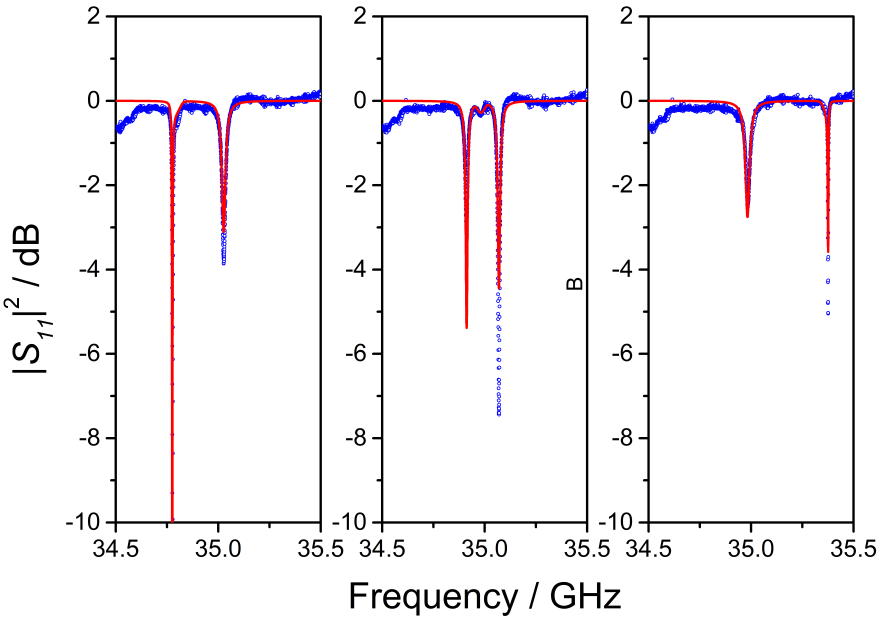

Figure 5.10.: Slices trough the exerimental data (blue dots) and simulation (red line) presented in Figure 5.9 at the fields 12416.9 Gauss(left), 12480.0 Gauss (middel) and 12613.3 Gauss (right)

Interestingly, inhomogeneous broadening does not affect the line width of the polariton modes $\Gamma = (\kappa + \gamma)/2$, where γ is the homogeneous line width. Furthermore, it does not decrease the splitting Ω_{eff} if $\Omega_{\text{eff}} \gg \gamma_{\text{inh}}$. This effect was described first in 1996 [139] where the author suggested to use it in order to measure the homogeneous line width of an inhomogeneous broadened system of interest. In the recent literature [137, 138, 140] the effect is called cavity protection because it effectively removes spin dephasing caused by inhomogeneous broadening similar as the spin echo experiment and hence protects the quantum information.

In summary, the BDPA·Bz sample resonance is inhomogeneously broadened due to g-anisotropy at temperatures below 12 K. This leads to a small coupling to formal dark states, which is visible in the VNA measurements as a faint line crossing the anticrossing. The behaviour can be simulated by discretizing the spin ensemble into sub ensembles using a q-gaussian spectral density. The line width and hence the losses of the polaritons are not affected due to the cavity protection effect.

Up to now, only steady state measurements on the hybrid systems were performed by the means of a VNA. In the next section, time domain measurements performed with a pulsed EPR spectrometer will be discussed.

5.4. Time-domain measurements

The hybrid system of BDPA·Bz in the Fabry-Pérot resonator was probed in time domain using a home built pulsed EPR setup [103]. The BDPA·Bz radical was chosen because of its lower spin losses $\gamma/(2\pi) = 1.5$ MHz compared to DPPH. All measurements in the time domain were simulated using the approach published in [60] and explained in Section 2.4.3 in order to treat the inhomogeneously broadened spin system.

The time domain measurements are organized in three parts. In the first part, vacuum Rabi oscillations under a weak driving pulse and the cavity protection effect are investigated. The second one covers echo measurements and the last part demonstrates how such hybrid systems can work as a quantum memory.

5.4.1. Low-power vacuum Rabi oscillations

Exciting a strongly coupled system with a short microwave pulse can stimulated vacuum Rabi oscillations, where the photons injected into the cavity oscillates back and forth between the cavity and the spin system [58, 137]. As long as the number of photons is small compared to the number of spins, the Rabi frequency does not depend on the microwave pulse power [54]. Furthermore, each photon will be fully absorbed and emitted from the spin system several times, depending on the cooperativity, before it decays.

To demonstrate vacuum Rabi oscillations, the 9.4 mg BDPA·Bz pellet characterized in Section 5.3.2 was mounted in the copper Fabry-Pérot resonator and cooled down to 7 K. The resonator was connected to the pulsed EPR setup via a waveguide. The first mode of the resonator was tuned to $\omega_c = 35.000$ GHz and a magnetic field of 1248.8 mT was applied to tune the spin ensemble to $\omega_s = 35.000$ GHz as well. The hybrid system was stimulated with a 65 ns long pulse with different carrier frequencies and a pulse power of about 5 µW corresponding to a maximum of $2 \cdot 10^9$ photons inside the cavity. The response of the system was measured by down conversion to the baseband.

Figure 5.11 shows the response of a probe pulse with a carrier frequency of $\omega_p/2\pi = 35.00$ GHz. As the pulse is applied, the main part of the signal comes from the reflection of the pulse before it enters the cavity. Still, oscillations with a frequency of $\Omega_{\text{eff}}/2\pi = 78$ MHz are visible on top of the reflected pulse. After switching off the microwave radiation, the system undergoes Rabi oscillations with the same frequency. The measurement is further superimposed by a slow oscillation coming from the detection circuit.

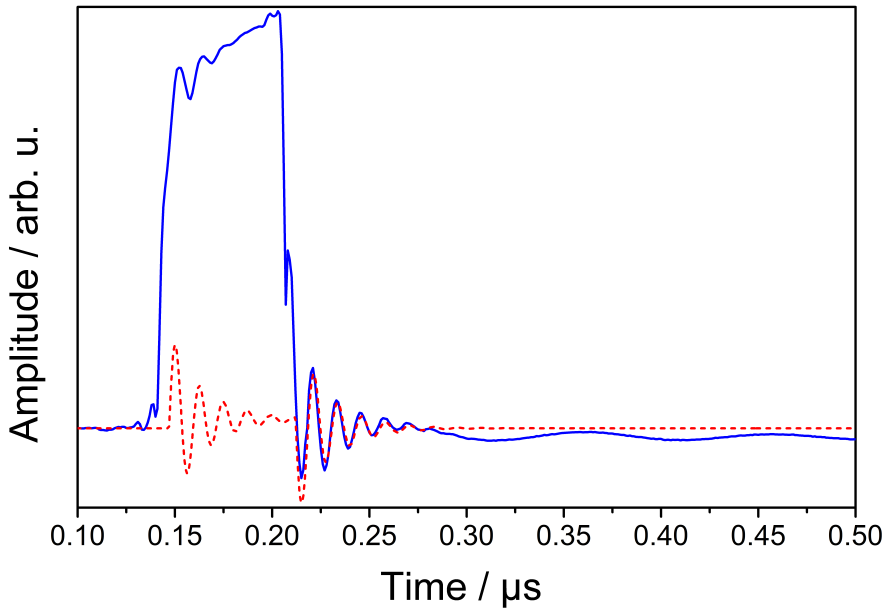

Figure 5.11.: In-Phase signal (blue line) of a reflection measurement on a 9.4 mg BDPA·Bz pellet at 7 Kand 1248.8 mT in time domain. The system was excited by a 65 ns rectangular pulse with a pulse power of 5 µw and a carrier frequency of 35.00 GHz. A simulation (red dotted line, see text for details) based on the method described in 2.4.3 is included as well.

The Rabi oscillations can be qualitatively understand [54] using the eigenstates (polariton modes) of the Jaynes-Cummings Hamiltonian. When the cavity frequency matches the spin frequency $\omega_c = \omega_s$, the polariton modes are given by

$$\langle \pm \rangle = \frac{1}{\sqrt{2}} \left(\langle 1 \downarrow \rangle \pm \langle 0 \uparrow \rangle \right)$$

with the energies $E_\pm/\hbar = \frac{\omega_c+\omega_s}{2} \pm \Omega_{\text{eff}}$. As the system is excited by a rectangular probe pulse with the frequency $\omega_p = \omega_c = \omega_s$ a coherent superposition

$$\frac{1}{\sqrt{2}} \left(\langle + \rangle + \langle - \rangle \right) = \langle 1 \downarrow \rangle$$

can be formed which evolves in time in a frame rotating with ω_p according to

$$\frac{1}{\sqrt{2}} \left(e^{-i\Omega_{\text{eff}}t} \langle + \rangle + e^{i\Omega_{\text{eff}}t} \langle - \rangle \right) = \cos\left(\Omega_{\text{eff}}t\right) \langle 1 \downarrow \rangle - i \sin\left(\Omega_{\text{eff}}t\right) \langle 0 \uparrow \rangle$$

where the excitation bounces back and forth between the cavity and the spin system. A simulation according to the method described in Section 2.4.3 was carried out with the parameters extracted from the VNA measurements in Section 5.3.2. The simulation only considers the intra-cavity field and thus does not capture the reflection of the pulse. The Rabi oscillation decays with $\Gamma = \frac{\kappa+\gamma}{2} \approx \frac{\kappa}{2}$ as the spin loss $\gamma/2\pi = 1.5$ MHz is small compared to cavity loss $\kappa/2\pi = 15$ MHz. Furthermore, this demonstrates the cavity protection effect as the inhomogeneous broadening of $\gamma_{\text{inh.}} = 11.9$ MHz has no effect on the decay rate.

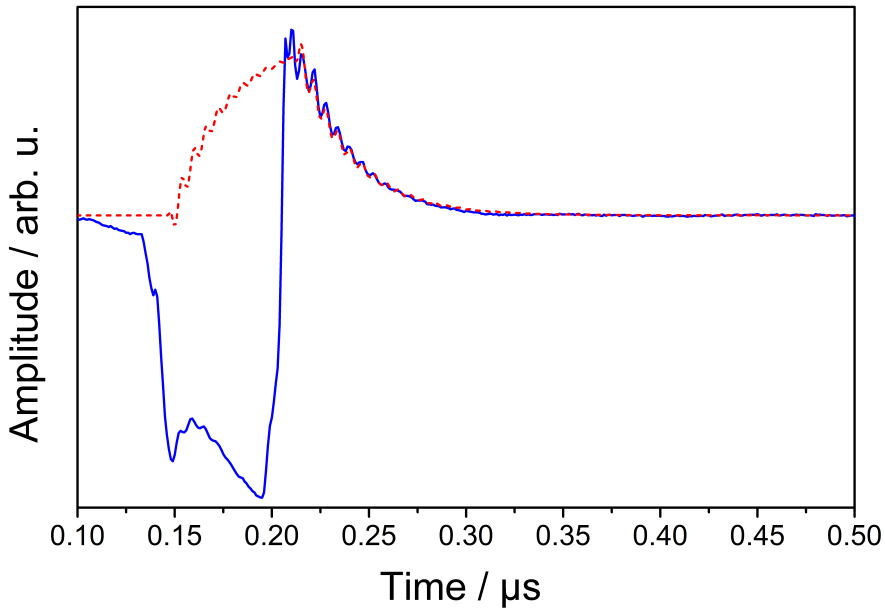

Figure 5.12.: In-Phase signal (blue line) of a reflection measurement on a 9.4 mg BDPA·Bz pellet at 7 K and 1248.8 mT in time domain. The system was excited by a 65 ns rectangular pulse with a pulse power of 5 µw and a carrier frequency of 34.922 GHz. A simulation (red dotted line, see text for details) based on the method described in 2.4.3 is included as well.

Figure 5.12 shows the same measurement except that the carrier frequency was changed to $\omega_p = \frac{\omega_c+\omega_s}{2} - \Omega_{\text{eff}} = 34.922 \cdot 2\pi$ GHz. Again, a large reflection from the incoming pulse is observed. After the radiation is switched off, an exponential decay superimposed by an oscillation with a frequency of $2\Omega_{\text{eff}}/2\pi = 156$ MHz can be observed.

In this case, the lower polariton mode is predominantly excited during the pulse which decays exponentially after the pulse is switched off. The sharp edge of a rectangular pulse has a large bandwidth and excites the other polariton mode as well thus oscillations are visible at the pulse edges. Again, this behavior can be perfectly described with a corresponding simulation.

This preliminary measurements do not yield any new information about the hybrid system but demonstrate that the pulsed EPR setup is suitable to investigate the system in time domain. The system response can be perfectly described by the parameters extracted from the VNA measurements by using the approach described in Section 2.4.3 supporting the treatment of the system so far. From this basis, further pulsed experiments were carried out. In the next section two-pulse sequences will be employed in order to perform echo spectroscopy.

5.4.2. Echo spectroscopy

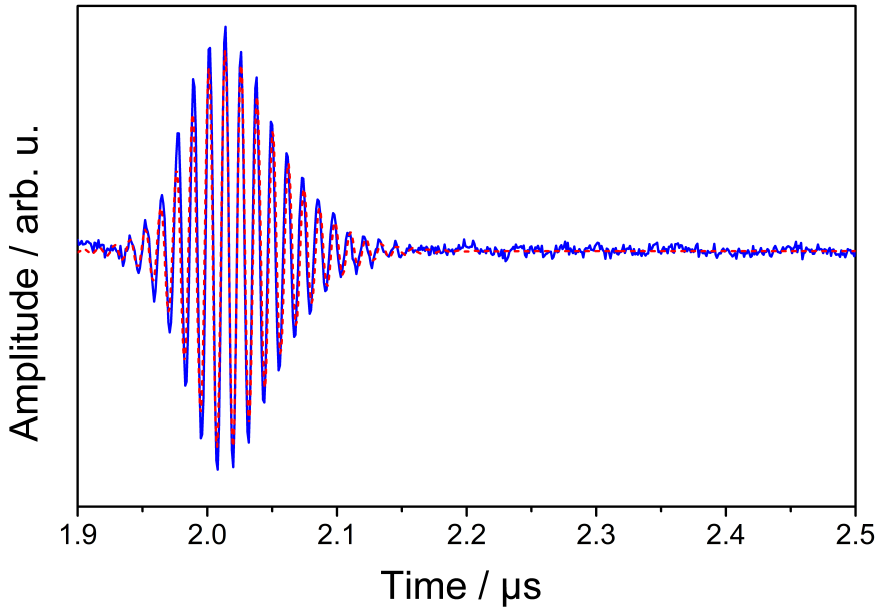

Figure 5.13.: In-Phase signal (blue line) of a modulated recorded on a 9.4 mg BDPA·Bz pellet at 7 K and 1248.8 mT. The modulation frequency corresponds to $\Omega_{\text{eff}}/2\pi = 78$ MHz. The system was excited by two 25 ns rectangular pulse with a pulse power of 5 W and a carrier frequency of 35.00 GHz. The pulses were spaced by $\tau = 1$ µs and the echo emerges after $2\tau = 2$ µs. A simulation (red dotted line, see text for details) based on the method described in 2.4.3 is included as well.

If an inhomogeneously broadened spin system is only weakly coupled to a cavity, there will be no cavity protection effect and the spins dephase due to their different frequencies. This is the usual case when pulsed EPR is applied to investigate spin ensembles. To overcome the dephasing, echo spectroscopy is employed. In the case of the strongly coupled BDPA·Bz sample, echo spectroscopy should not yield a better relax-

ation time because the strong coupling and thus the cavity protection effect effectively removes spin dephasing due to static inhomogeneities. However, in contrast to this expectation, an echo with a much longer relaxation time was observable in this sample which will be investigated in this section.

The 9.4 mg BDPA·Bz characterized in Section 5.3.2 was mounted in the copper Fabry-Pérot resonator and cooled down to 7 K. The resonator was connected to the pulsed EPR setup via a waveguide. The first mode of the resonator was tuned to $\omega_c = 35.000$ GHz and a magnetic field of 1248.8 mT was applied to tune the spin ensemble to $\omega_s = 35.000$ GHz as well. The hybrid system was stimulated with a pulse of variable length and a 25 ns long pulse with a carrier frequency $\omega_p/2\pi = 35.000$ GHz and a pulse power of about 5 W corresponding to a maximum of $2 \cdot 10^{15}$ photons inside the cavity which is less than the number of active spins of $3 \cdot 10^{17}$. The pulses were separated by an inter pulse delay τ between 0.5 µs to 5.5 µs. The response of the system was measured by down conversion to the baseband.

Figure 5.13 shows an echo occurring at 2τ using a pulse sequence of two 25 ns pulses with an inter pulse delay $\tau = 1$ µs. It is modulated with a frequency of $\Omega_{\text{eff}}/2\pi = 78$ MHz.

The emergence of an echo at $2\tau = 2$ µs was surprising and puzzling as the spin relaxation time of BDPA·Bz is $T_2 = \frac{1}{\gamma} = \frac{1}{2\pi \cdot 1.5 \text{ MHz}} \approx 100$ ns (see [141] for reference as well) and thus any coherence should have decayed. Furthermore, the echo is modulated by Ω_{eff} which means that long lasting coherence at the frequency of both polariton modes is required. Therefore, the long lasting coherence has to be stored in an inhomogeneous spin ensemble with a non negligible spin density at the frequencies of both polariton modes. In Section 5.3.4, a q-gaussian shaped spectral density with a FWHM $\gamma_{\text{inh}}/2\pi = 11.9$ MHz was determined for the BDPA·Bz sample. In that case, the spectral density at the polariton modes $\omega_{(s} \pm \Omega_{\text{eff}})/2\pi = 35.000 \pm 0.078$ GHz is about 10^{-7} times smaller compared to the maximum at 35 GHz which can be considered as negligible. In conclusion, the echo can not be explained (and not reproduced by simulation) with the current model of the BDPA·Bz sample.

In order to shed more light on this finding, τ was varied between 0.5 µs and 5.5 µs and the peak to peak amplitude of the modulated echo was recorded in order to extract a relaxation time. The result is shown in Figure 5.14. The amplitude decays exponentially with a decay constant $T_m = 1.4(1)$ µs which correspond to a decay rate of $\gamma_m/2\pi = 0.114(8)$ MHz i. e. much smaller then any line width observed in the system so far.

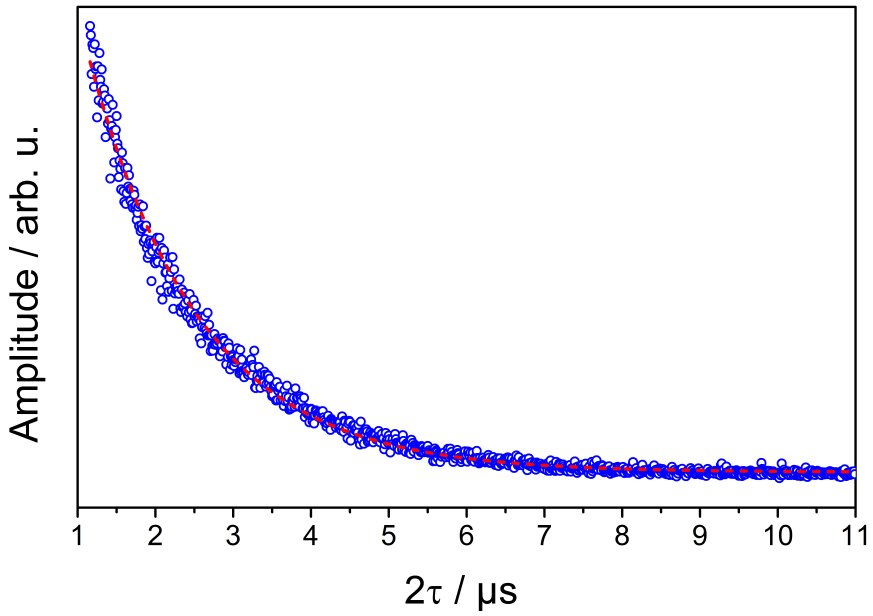

Figure 5.14.: Peak to peak amplitudes (blue dots) of echos of a 9.4 mg BDPA·Bz pellet at 7 K and 1248.8 mT. The echos were generated by two 25 ns rectangular pulse with a pulse power of 5 W and a carrier frequency of 35.00 GHz. The spacing between the pulses was varied between 0.5 µs to 5.5 µs. The decay can be fitted by a monoexponential decay (red dotted line) with an decay constant $T_{\mathrm{m}} = 1.4$ µs which corresponds to a decay rate $\gamma_{\mathrm{m}}/2\pi = 0.114$ MHz

In Section 5.2.1 SQUID measurements revealed that the sample contains about 4% of spins which show no exchange interaction. These spins should be not exchanged narrowed and thus may feature a broad spectral density due to dipolar interactions and strains. Including a second spin ensemble with a gaussian spectral density characterized by the FWMH $\gamma_{\mathrm{inh}}/2\pi = 50(20)$ MHz and a homogeneous linewidth of each spin packet $\gamma_{\mathrm{m}}/2\pi = 0.114$ MHz in the simulation, the echo can be reproduced very well as shown in Figure 5.13. The exact spectral density of this second spin ensemble is unknown, it is only important that it features a non negligible density at the polaritons.

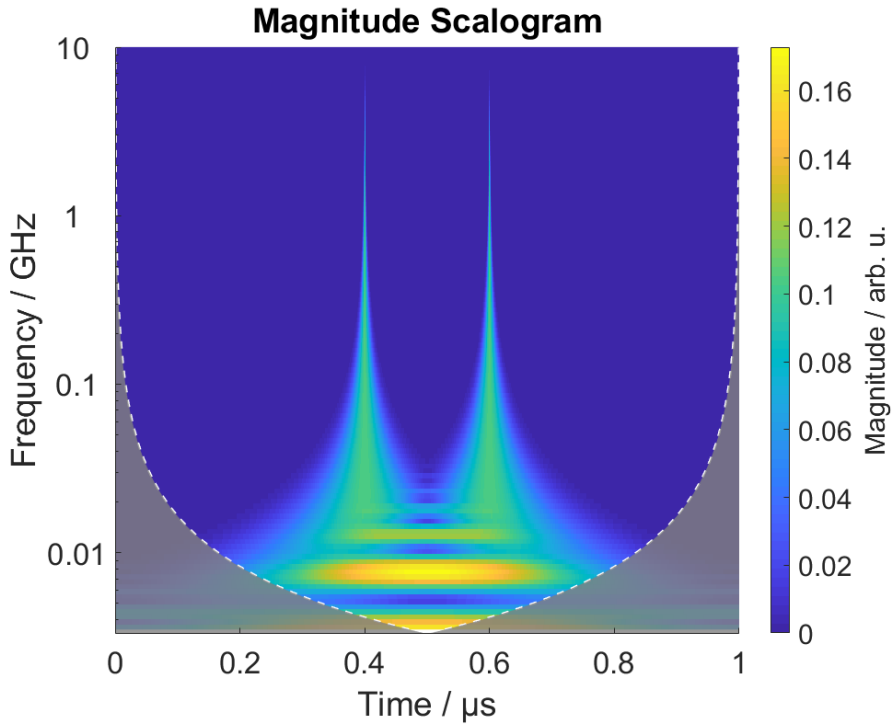

Figure 5.15.: Wavelet transformation of a 200 ns long rectangular pulse showing its time dependent frequency components. The large bandwidth at the pulse edges is clearly visible.

The simulation also helps to understand the echo on a qualitative level. Although the probe frequency is not in resonance with the polaritons, the edges of the first pulse excites them due to the large bandwidth at the pulse edges. The wavelet transform of a rectangular pulse in Figure 5.15 visualizes the time dependent bandwidth of a rectangular pulse. The second spin ensemble has a relatively large spin density at the polariton

modes, thus coherence is transferred from the polaritons to second spin ensemble and dephases there. The second pulse refocuses the coherence which dephased. After 2τ, the coherence is fully refocused on the second spin ensemble and photons are released which excite again both polariton modes.

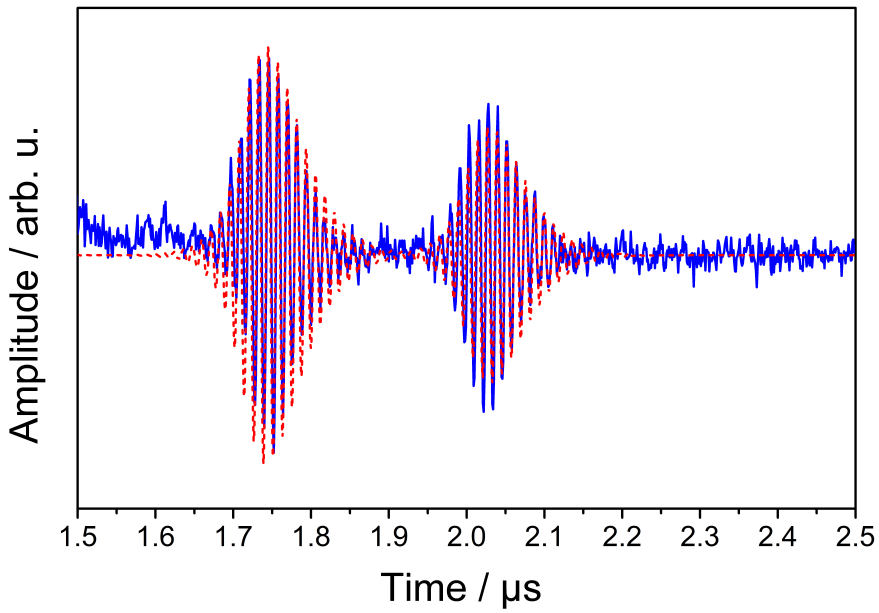

Figure 5.16.: In-Phase signal (blue line) of an modulated double echo of a 9.4 mg BDPA·Bz pellet at 7 K and 1248.8 mT. The modulation frequency corresponds to $\Omega_{\text{eff}}/2\pi = 78$ MHz. The system was excited by one 280 ns followed by an 25 ns rectangular pulse both with a pulse power of 5 W and a carrier frequency of 35.00 GHz. The pulses were spaced by $\tau = 1$ µs and the echo emerges after $2\tau = 2$ µs. A simulation (red dotted line, see text for details) based on the method described in 2.4.3 is included as well.

An interesting effect can be observed, if the length of the first pulse is varied. Figure 5.16 shows the emergence of two echos after $2\tau = 2$ µs utilizing a pulse sequence of one 280 ns followed by an 25 ns pulse. The two echos are modulated with $\Omega_{\text{eff}}/2\pi =$ 78 MHz and spaced by the pulse length of the first pulse. As only the edges of the pulse excite the polaritons, coherence is only generated at the beginning and end of the pulse. Both events will be refocused and create the double echo as shown. This behavior can be reproduced very well by simulation as shown in Figure 5.16 as well.

To my best knowledge, this kind of edge echo measurements in the strong coupling regime have not been demonstrated so far. The really interesting aspect here is that two different spin ensembles are coupled via a cavity. The coupling depends on the spectral overlap between the polaritons of the strongly coupled system with the weakly coupled,

spectrally broad spin ensemble. In further experiments, the coupling could be switched by designing and implementing a system which allows to control the frequency of the polaritons. This has been demonstrated for NV-centers [58], where Ω_{eff} is controlled by changing the spin polarization with laser pulses.

The experiments shown in this section are working with the pulse edge in order to excite the polaritons. For this reason, only a fraction of the pulse energy interacts with the hybrid system. The double echo experiment could be thus seen as a storage of weak excitations in an inhomogeneously broadened spin system, a technique which is recently discussed [47, 60, 142] to allow the storage of quantum information on a single photon level. In the next section, the possibility to use the presented hybrid system as a quantum memory will be explored.

5.4.3. Storage and retrieval of low-power excitations

The idea to store information in an inhomogeneously broadened spin system was already presented in 1955 [143, 144] shortly after the discovery of the spin echo by Erwin Hahn in 1950 [145]. In a nutshell, weak pulses containing the information are used to generate coherence in an inhomogeneously broadened spin system which quickly dephases. A strong refocusing pulse is applied after a time τ and echos containing the stored information will appear after 2τ. It is necessary to use weak pulses for writing in order to prevent that further write pulses will alter the information stored before. However, no commercial device was produced up to now because the capacity of the memory is rather low and the whole device can not be miniaturized very well.

60 years later, after the discovery of cavity QED, this approach has become appealing again. The idea is to use a strongly coupled system with an inhomogeneous spin ensemble, to store quantum information on a single photon level [47, 60, 142]. A cooperativity $C > 1$ ensures that the quantum information of a single photon will be fully transferred to the spin system before it dephases there. The Figure of merit here is the efficiency $\eta = n_{\text{r}}/n_{\text{i}} \approx E_{\text{r}}/E_{\text{i}}$. which is the ration between the number of retrieved n_{r} and input photons n_{i} which can be approximated by the ration between the input E_{i} and retrieved pulse energy E_{r}. In the weak coupling regime [142], $\eta = 1 \cdot 10^{-10}$ has been achieved while the record in the strong coupling regime [47] is $\eta = 2 \cdot 10^{-4}$ at mK temperatures.

With the setup used in this thesis, measuring at a single photon level is not possible. However, the efficiency of a quantum memory could be still approximated by comparing the energy of the input and retrieved pulse.

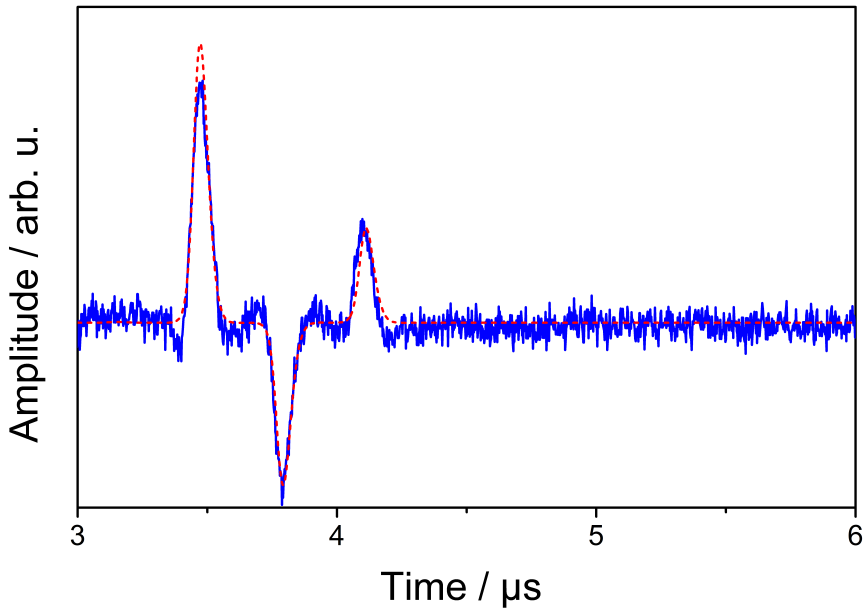

Figure 5.17.: In-Phase signal (blue line) of three echos of a 9.4 mg BDPA·Bz pellet at 7 K and 1248.8 mT. The system was excited by three 30 ns pulses with a pulse power of 5 mW and a carrier frequency of 35.062 GHz. The phase of the second pulse was inverted. After $\tau = 1.4$ µs, the system was excited by a 25 ns pulse with a pulse power of 5 W a carrier frequency of 35.062 GHz. The three echos appear after $2\tau = 2.8$ µs. A simulation (red dotted line, see text for details) based on the method described in 2.4.3 is included as well.

In order to do so, a 5.5 mg BDPA·Bz pellet was mounted in the copper Fabry-Pérot resonator and cooled down to 7 K. The resonator and center spin frequencies were tuned to $\omega_s/2\pi = \omega_c/2\pi = 35.000$ GHz. The collective coupling $\Omega_{\text{eff}} = 62$ MHz was determined with the VNA as described in the previous sections. A pulse sequence with three weak (5 mW) 30 ns long pulses spaced by 290 ns and a strong (5 W) 22.5 ns long pulse after $\tau = 1.4$ µs was employed. The phase of the second pulse was inverted using a 180 degree phase shifter. The carrier frequency was set to $\omega_p/2\pi = 35.062$ GHz to match with the upper polariton mode. The resulting echos emerging after $2\tau = 2.8$ µs are shown in Figure 5.17. The echo emerging from the second pulse is inverted and the amplitudes of the echos decay with $\gamma_m/2\pi = 0.114$ MHz.

By exciting predominantly one polariton mode, the echos are no longer modulated. Furthermore, less microwave power is reflected and thus a better inversion for the refocusing pulse is achieved. The first three pulses are rather weak compared to the refocusing pulse, thus no additional echos from the first three pulses are observable. The phase information of the pulses is stored as well, therefore the second echo is inverted. The experiment can be perfectly reproduced by the model described in the last section. This proof of principle experiment demonstrates the storage of weak excitations quite nicely. Unfortunately, no more pulses can be stored as the pulse amplifier duty cycle is already at its limit. Furthermore, in order to attenuated the first three pulses, a switch coupled with an attenuator has to be used. The switching speed of this assembly is about 1.4 µs, thus no shorter value for τ can be used.

Efficiency

In order to estimate the storage and retrieval efficiency, the experiment was repeated with one 5 mW 300 ns long weak pulse instead of three pulses. The resulting echo appearing after $2\tau = 2.8$ µs is shown in Figure 5.18. A simulation reproduces most of the features observed in the measurement except the top of the echo. The reason of this might be a distorted pulse shape due to the bandwidth of the pulse amplifier.

The integral over the squared amplitude of the signal is proportional to the energy of the signal. Therefore, this quantity was determined for the echo and a fully reflected 5 µW pulse. Because a 5 mW pulse was used in the experiment, the reference value has to be adjusted accordingly. The resulting $\eta = E_r/E_i = 2 \cdot 10^{-6}$ lies somewhere between the state of the art [47] value of $\eta = 2 \cdot 10^{-4}$ at mK temperatures and the efficiency $\eta = 1 \cdot 10^{-10}$ reported in the weakly coupled regime [47, 142].

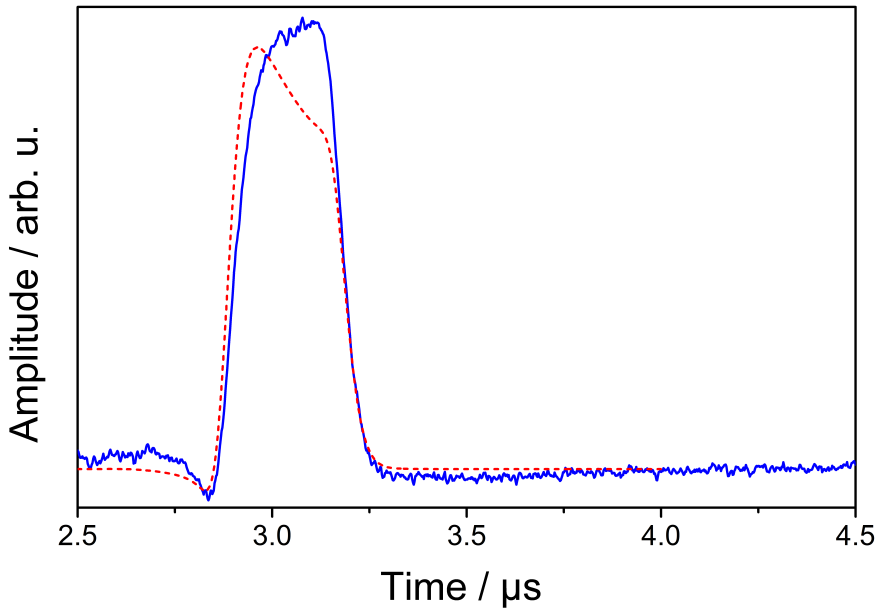

Figure 5.18.: In-Phase signal (blue line) of an echo of a 9.4 mg BDPA·Bz pellet at 7 K and 1248.8 mT. The system was excited by a 300 ns pulse with a pulse power of 5 mW and a carrier frequency of 35.062 GHz. After $\tau = 1.4$ µs, the system was excited by a 25 ns pulse with a pulse power of 5 W a carrier frequency of 35.062 GHz. The echo appears after $2\tau = 2.8$ µs. A simulation (red dotted line, see text for details) based on the method described in 2.4.3 is included as well.

For a high fidelity quantum memory, an efficiency close to one would be required. Therefore, it is important to understand where losses occur. The main loss mechanism should be spin relaxation. The squared amplitude decays with $e^{-2\gamma_m 2\tau} = 0.018$ and thus decreases the efficiency by a factor of 50. However, the total efficiency is still much lower than expected from spin relaxation alone. Thus, the whole storage and retrieval process will be explained in the following in order to understand where the additional losses occur.

Storage process During storage, photons enter the cavity governed by the coupling rate κ_e. Inside the cavity, photons decay with a rate $\kappa_e + \kappa_i$. Furthermore, photons interact with a rate Ω_{eff} with the spin system. Here, the resulting excitations diffuse with a rate γ_{inh} and decay with the spin relaxation rates $\gamma_{m,1}$ of the exchanged coupled system and $\gamma_{m,2}$ of the inhomogeneously broadened system. The diffusing process is the actual storage process, because the involved spins are loosing their phase relation which suppresses the coupling to the cavity.

For an optimum storage process, the collective coupling Ω_{eff} should be $\kappa_e + \kappa_i < \Omega_{eff} < \gamma_{inh}$ in order to minimize cavity losses during the transfer to the spin system and to avoid that the excitation is transferred back to the cavity during the spin diffusion process. Furthermore, the spin relaxation rates should be as small as possible. Last but not least, $\kappa_e + \kappa_i$ determines the bandwidth of the stored signal and should be only as large as needed. Increasing the external coupling κ_e is in principle more useful, as it increase the efficiency of the retrieval process.

Retrieval process In order to retrieve the stored pulse, the spins containing the information need to be inverted in order to bring them back into phase. For a full inversion, one photon for every spin is needed as long as the condition $\kappa_e + \kappa_i < \Omega_{eff}$ is fulfilled. Therefore, pulse duration and power has to be adjusted such that the area of the pulse contains the required amount of photons. After the inversion, the dephasing will be reverted and the spins start to emit photons back to the cavity. Based on the rate κ_e, photons exit the cavity and can be detected.

The main requirement for an efficient retrieval process is that the inversion pulse is strong enough the invert all spins. Generally, the bandwidth of the pulse should match the spectral density of the inhomogenous broadened spin system for an optimum use of the pulse energy. The ideal condition for the collective coupling strength during the readout process would be $\kappa_e > \Omega_{eff} > \gamma_{inh}$ such as the all photons can leave the

cavity before they interact with the spin system again. This contradicts the condition for optimum storage. Thus, either a compromise has to be found or κ_e and γ_{inh} can be controlled during the experiment by an electrical coupling mechanism [60] respectively magnetic field gradients [142].

Analysis of the observed efficiency In order to analyze the observed efficiency, a simulation of the experiment was carried out. The inhomogeneous line width $\gamma_{inh,2}/2\pi =$ 31 MHz of the smaller spin ensemble was fitted to the observed efficiency. The remaining parameters needed for the simulation are shown in Table 5.2. They were all determined from the different experiments presented in the preceding sections. The output

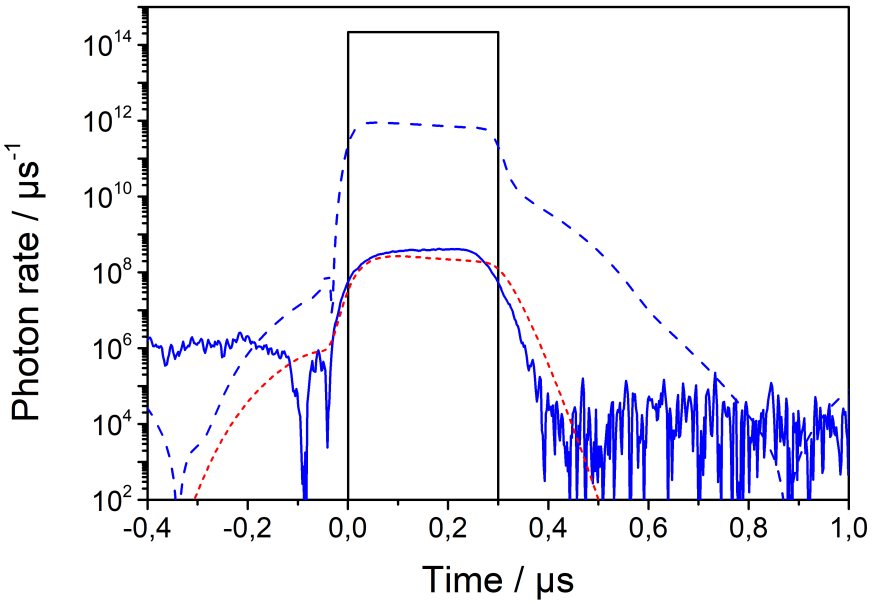

Figure 5.19.: Input pulse (black line) and output echo (blue line) of the experiment presented in Figure 5.18. Included are two quantitative simulations, the first one (red line) is based on the model with two spin ensembles. The second one (red dashed line) is a simulation which excludes the main spin ensemble.

pulse based on the current model is shown in Figure 5.19 (red dotted line), it matches very well with the observed pulse (blue line). Comparing the parameters with the condition for optimum storage and retrieval, the low efficiency is not unexpected. First, the inhomogeneous broadening of the exchanged coupled spin system $\gamma_{inh,1}$ is much lower compared to Ω_{eff} and $\kappa_e + \kappa_i$. Second, $\gamma_{m,1}$ of the main spin system is relatively high. Thus, the main spin system does not contribute to the storage of information. In fact, it just opens up an additional loss channel.

Table 5.4.: Total amount of active spins N_1 and N_2, inhomogeneous line width $\gamma_{\mathrm{inh},1}$ and $\gamma_{\mathrm{inh},2}$ and spin relaxation times $\gamma_{\mathrm{m},1}$ and $\gamma_{\mathrm{m},1}$ for the spin systems used for the simulations in Figure 5.19. Furthermore, Ω_{eff} based on the total number of active spins $N_1 + N_2$ and the single spin coupling constant $g/2\pi = 0.145$ Hz is shown. The cavity loss parameters were determined in Section 5.3.

Parameter	Both Spin System	Main Spin System excluded
N_1	$1.9 \cdot 10^{17}$	-
N_2	$7.8 \cdot 10^{15}$	$7.8 \cdot 10^{15}$
$\gamma_{\mathrm{inh},1}/2\pi$ / MHz	11.9(3)	-
$\gamma_{\mathrm{inh},2}/2\pi$ / MHz	31(3)	31(3)
$\gamma_{\mathrm{m},1}/2\pi$ / MHz	1.5(2)	-
$\gamma_{\mathrm{m},2}/2\pi$ / MHz	0.114(5)	0.114(5)
$g_{\mathrm{s}}/2\pi$ / MHz	1.4(1)	1.4(1)
$\Omega_{\mathrm{eff}}/2\pi$ / MHz	62(2)	12.4(3)
$\kappa_{\mathrm{i}}/2\pi$ / MHz	2.0(5)	2.0(5)
$\kappa_{\mathrm{e}}/2\pi$ / MHz	13.0(5)	13.0(5)

Therefore, a simulation without the main spin system only containing the inhomogenously broadened spin system was performed. The resulting output echo (blue dotted line) can be seen in Figure 5.19 as well. Interestingly, removing the exchanged coupled system increases the efficiency by nearly four orders of magnitude. Compared to the simulation with the main spin system, Ω_{eff} is now smaller compared to γ_{inh}. Furthermore, $\kappa_{\mathrm{e}} + \kappa_{\mathrm{i}}$ is a little bit higher than Ω_{eff} which hurts the storage process a little bit. However, it can be seen as a compromise for the contradicting requirements between the storage and retrieval process. From here, the spin relaxation is the dominant factor on the efficiency which could be further improved by choosing a spin system with longer spin relaxation times.

To sum it up, it is possible to use the hybrid system of BDPA·Bz and the Fabry-Pérot resonator as a quantum memory for weak excitations. At the moment, the efficiency of the storage and retrival process is about two orders of magnitude worse compared to the state of the art at mK temperatures. However, it could be improved by up to four orders of magnitude improving the spin system. Experimentally, a polymer sample highly doped with organic radicals could already improve the quantum memory.

5.5. Conclusion

In the previous sections of this chapter, it was demonstrated that the strong coupling regime can be reached with the organic radicals BDPA·Bz and DPPH and a Fabry-Pérot resonator operating at 35 GHz up to room temperature. An outstanding collective coupling strength of 110 MHz and a cooperativity of 290 were achieved at 7 K. The strong exchange coupling occurring in both spin ensembles was identified to have an strong impact on the temperature dependence of the system because it determines the spin polarization in thermal equilibrium. In further experiments, the cavity protection effect, protecting quantum information from dephasing caused by inhomogeneous broadening, was demonstrated for BDPA·Bz in the time and frequency domain. Echo spectroscopy on the BDPA·Bz revealed a second type of spin ensemble in the sample with a long coherence time of 1.4 µs. The strongly coupled first spin ensemble couples to this second spin ensemble via the cavity. In additional pulses experiments it was demonstrated, how quantum information can be stored in this second spin ensemble. An efficiency of $2 \cdot 10^{-6}$ was reached for the storage and retrieval of quantum information at 7 K which is only two orders of magnitude worse than in recent state of the art experiments at mK temperatures. By improving the spin system, the efficiency is expected to increase by four orders of magnitude. It has to be stressed out that all experiments have been performed in a temperature range between 3 K to 293 K and without any superconducting material. Thus, this hybrid system is a excellent platform for further experiments in the strong coupling regime as it is much more flexible and easier to use then the current devices.

6. Experimental Section

6.1. Chemicals

The chemicals listed in table 6.1 were used for measurements and sample preparation

Table 6.1.: Purity and supplier of the used chemicals

Chemical	Purity	Supplier
α,γ-Bisdiphenylene-β-phenylallyl complex with benzene	pure	Sigma Aldrich
Polystyrene Mw 350k	>95%	Sigma Aldrich
Poly(methyl methacrylate) Mw 350 000		Sigma Aldrich
Toluene	99.9%	Sigma Aldrich
2,2-Diphenyl-1-picrylhydrazyl		Sigma Aldrich
Glycerol-D_8	>98% atom % D	Sigma Aldrich
Water-D_2	>98% atom % D	Eurisotope
Glycerol	>99.8%	Alfa Aesar

6.2. Luminescence spectroscopy

Luminescence measurements were carried out on a AMINCO-Bowman Series 2 Spectrofluorometer by Thermo Fisher Scientific. The sample was ground and placed inside an Oxford Instruments Spectromag 10 T optical cryomagnet. Excitation of the sample was performed with an 450 nm, 5 mW laser. The luminescence coming from the sample was collected by collimating the light using a plano-convex lens and filtered by a 550 nm longpass filter. The light was directed through the emission monochromator of the spectrometer and detected with the built-in photomultiplier detector.

6.3. MCD spectroscopy

Magnetic Circular Dichroism (MCD) spectra were recorded on an Aviv 42 CD spectrometer equipped with an Oxford Instruments Spectromag 10 T optical cryomagnet using a photomultiplier detector. The sample was dissolved in the corresponding solvent, filled into the sample compartment, shock frozen in liquid nitrogen and the put into the cryostat.

6.4. Q-Band pulsed EPR-spectroscopy

All measurements were carried out on a home built pulsed [103] EPR spectrometer operating at 35 GHz. The duration of the π-pulse was usually set to 40 ns. The pulse angles were adjusted by tuning the microwave power to get the maximum signal for a Hahn-echo sequence. The repetition time of a sequence was usually set to $5 \cdot T_1$. The baseline of the signal was corrected and the echoes were fully integrated. Solution samples where degassed by three "Freeze-Pump-Thaw" cycles. .

6.4.1. ESE-detected Spectrum

ESE-Detected EPR spectra were recorded by performing a spin echo experiment at different magnetic fields. The magnetic field range was usually 1000-1300 mT and the simulation was performed with *Easyspin* [43]

6.4.2. Phase memory time T_m

The phase memory time T_m was determined with a simple spin echo sequence with varying τ. The data was fitted with either a monoexponential or biexponential fit.

6.4.3. Longitudinal relaxation time T_1

The longitudinal relaxation time T_1 was determined with either the inversion recovery sequence described in section 2.2.3 or the saturation by fast repetition experiment (spin echo with varying repetition time). In any case, the data with either a monoexponential or biexponential fit.

6.5. High-field EPR Spectroscopy

High Field EPR Spectroscopy measurements were carried out on a home built [146] spectrometer. The powder samples were ground and pressed into a 5 mm pellet. For detection, the magnetic field was modulated with an amplitude of approximately 10 G and frequency of about 1000 kHz.

6.6. Thin Films of BDPA in PMMA

Thin films of the BDPA radical in PMMA with thicknesses ranging from 10 nm to 100 nm were prepared by spin coating solutions of 2 $\frac{g}{l}$ to 20 $\frac{g}{l}$ PMMA in toluene at 1500 RPM under ambient conditions. The solutions contained 5 w.% BDPA based on the PMMA mass. The films were coated on quadratic (1.5 x 1.5 x 0.05 cm) silicon wafers doped with boron (doping concentration about 10^{13} cm^{-3}). Directly before the spin coating process, the wafers were rinsed with acetone, cleaned with a CO_2 snow jet and treated with oxygen plasma for ten minutes.

6.7. Vector Network Analyzer Measurements

Vector network analyzer measurements were performed on a Anritsu MS46322B VNA. The VNA was connected with a WR28-2.92mm coax transition to the Fabry-Pérot resonator. The VNA was calibrated between 34.5 GHz and 35.5 GHz up to the coax connection with a SOLT calibration kit. Residual errors were corrected by recording a baseline with the resonator tuned far away from the observed frequency range. The measurements of the reflection parameter S_{11} were divided by the this baseline measurement.

6.7.1. Strong coupling

For CW-measurements on strongly coupled spin ensembles, the samples were loaded in the Fabry-Pérot resonator on the lower, flat mirror. A static magnetic field was applied using a Varian V-3800 electromagnet, equipped with an Elektro-Automatik EA-PS 9200-140 power supply. The VNA and power supply were controlled by an computer running a self written LabView program. The probe power was set to -20 dBm.

Bibliography

[1] H.-J. Werner, P. J. Knowles, G. Knizia, F. R. Manby, M. Schütz, *WIREs Comput. Mol. Sci.* **2012**, *2*, 242–253.

[2] D. Potter, J. Stadel, R. Teyssier, *Comput. Astrophys.* **2017**, *4*, 16.

[3] Sony, Playstation 4 Pro Specification, **Last checked 14.08.2020**, `https://www.playstation.com/de-de/explore/ps4/tech-specs/`.

[4] *Guinness World Records 2015*, Hoffmann und Campe, s.l., **2015**.

[5] P. W. Shor, *SIAM J. Comput.* **1997**, *26*, 1484–1509.

[6] L. K. Grover in Proceedings of the twenty-eighth annual ACM symposium on Theory of computing - STOC '96, (Ed.: G. L. Miller), ACM Press, New York, New York, USA, **1996**, pp. 212–219.

[7] A. W. Harrow, A. Hassidim, S. Lloyd, *Phys. Rev. Lett.* **2009**, *103*, 150502.

[8] D. P. DiVincenzo, *Fortschr. Phys.* **2000**, *48*, 771–783.

[9] J. Majer, J. M. Chow, J. M. Gambetta, J. Koch, B. R. Johnson, J. A. Schreier, L. Frunzio, D. I. Schuster, A. A. Houck, A. Wallraff, A. Blais, M. H. Devoret, S. M. Girvin, R. J. Schoelkopf, *Nature* **2007**, *449*, 443–447.

[10] C. Neill, P. Roushan, K. Kechedzhi, S. Boixo, S. V. Isakov, V. Smelyanskiy, A. Megrant, B. Chiaro, A. Dunsworth, K. Arya, R. Barends, B. Burkett, Y. Chen, Z. Chen, A. Fowler, B. Foxen, M. Giustina, R. Graff, E. Jeffrey, T. Huang, J. Kelly, P. Klimov, E. Lucero, J. Mutus, M. Neeley, C. Quintana, D. Sank, A. Vainsencher, J. Wenner, T. C. White, H. Neven, J. M. Martinis, *Science* **2018**, *360*, 195–199.

[11] J. L. O'Brien, *Science* **2007**, *318*, 1567–1570.

[12] R. Prevedel, P. Walther, F. Tiefenbacher, P. Böhi, R. Kaltenbaek, T. Jennewein, A. Zeilinger, *Nature* **2007**, *445*, 65–69.

[13] I. Bloch, *Nature* **2008**, *453*, 1016–1022.

[14] L.-M. Duan, E. Demler, M. D. Lukin, *Phys. Rev. Lett.* **2003**, *91*, 090402.

[15] Gershenfeld, Chuang, *Science* **1997**, *275*, 350–356.

[16] D. Loss, D. P. DiVincenzo, *Phys. Rev. A* **1998**, *57*, 120–126.

[17] K. Bader, D. Dengler, S. Lenz, B. Endeward, S.-D. Jiang, P. Neugebauer, J. van Slageren, *Nat. Commun.* **2014**, *5*, 5304.

[18] C. J. Wedge, G. A. Timco, E. T. Spielberg, R. E. George, F. Tuna, S. Rigby, E. J. L. McInnes, R. E. P. Winpenny, S. J. Blundell, A. Ardavan, *Phys. Rev. Lett.* **2012**, *108*, 107204.

[19] S. Lenz, K. Bader, H. Bamberger, J. van Slageren, *Chem. Commun.* **2017**, *53*, 4477–4480.

[20] A. Urtizberea, E. Natividad, P. J. Alonso, M. A. Andrés, I. Gascón, M. Goldmann, O. Roubeau, *Adv. Funct. Mater.* **2018**, *28*, 1801695.

[21] T. Yamabayashi, M. Atzori, L. Tesi, G. Cosquer, F. Santanni, M.-E. Boulon, E. Morra, S. Benci, R. Torre, M. Chiesa, L. Sorace, R. Sessoli, M. Yamashita, *J. Am. Chem. Soc.* **2018**, *140*, 12090–12101.

[22] P. Tamarat, A. Maali, B. Lounis, M. Orrit, *J. Phys. Chem. A* **2000**, *104*, 1–16.

[23] The ATLAS collaboration, *J. Inst.* **2008**, *3*, S08003–S08003.

[24] M. Uecker, S. Zhang, D. Voit, A. Karaus, K.-D. Merboldt, J. Frahm, *NMR Biomed.* **2010**, *23*, 986–994.

[25] C. Schlegel, J. van Slageren, M. Manoli, E. K. Brechin, M. Dressel, *Phys. Rev. Lett.* **2008**, *101*, 147203.

[26] F. Troiani, M. Affronte, *Chem. Soc. Rev.* **2011**, *40*, 3119–3129.

[27] J. Yang, Y. Wang, Z. Wang, X. Rong, C.-K. Duan, J.-H. Su, J. Du, *Phys. Rev. Lett.* **2012**, *108*, 230501.

[28] A. Ardavan, O. Rival, J. J. L. Morton, S. J. Blundell, A. M. Tyryshkin, G. A. Timco, R. E. P. Winpenny, *Phys. Rev. Lett.* **2007**, *98*, 057201.

[29] S. Takahashi, J. van Tol, C. C. Beedle, D. N. Hendrickson, L.-C. Brunel, M. S. Sherwin, *Phys. Rev. Lett.* **2009**, *102*, 087603.

[30] K. Bader, M. Winkler, J. van Slageren, *Chem. Commun.* **2016**, *52*, 3623–3626.

[31] J. M. Zadrozny, J. Niklas, O. G. Poluektov, D. E. Freedman, *ACS. Cent. Sci.* **2015**, *1*, 488–492.

[32] A. M. Tyryshkin, S. Tojo, J. J. L. Morton, H. Riemann, N. V. Abrosimov, P. Becker, H.-J. Pohl, T. Schenkel, M. L. W. Thewalt, K. M. Itoh, S. A. Lyon, **2011**, *11*, 143–147.

[33] N. Bar-Gill, L. M. Pham, A. Jarmola, D. Budker, R. L. Walsworth, *Nat. Commun.* **2013**, *4*, 1743.

[34] A. Gruber, *Science* **1997**, *276*, 2012–2014.

[35] A. Morello, J. J. Pla, F. A. Zwanenburg, K. W. Chan, K. Y. Tan, H. Huebl, M. Möttönen, C. D. Nugroho, C. Yang, J. A. van Donkelaar, A. D. C. Alves, D. N. Jamieson, C. C. Escott, L. C. L. Hollenberg, R. G. Clark, A. S. Dzurak, *Nature* **2010**, *467*, 687–691.

[36] H. Büch, S. Mahapatra, R. Rahman, A. Morello, M. Y. Simmons, *Nat. Commun.* **2013**, *4*, 2017.

[37] Wrachtrup, C. von Borczyskowski, Bernard, Orrit, Brown, *Phys. Rev. Lett.* **1993**, *71*, 3565–3568.

[38] M. S. Fataftah, D. E. Freedman, *Chem. Commun.* **2018**, *54*, 13773–13781.

[39] S. L. Bayliss, D. W. Laorenza, P. J. Mintun, B. D. Kovos, D. E. Freedman, D. D. Awschalom, *Science* **2020**, *370*, 1309–1312.

[40] C. Godfrin, A. Ferhat, R. Ballou, S. Klyatskaya, M. Ruben, W. Wernsdorfer, F. Balestro, *Phys. Rev. Lett.* **2017**, *119*, 187702.

[41] M. Kern, L. Tesi, D. Neusser, N. Rußegger, M. Winkler, A. Allgaier, Y. M. Gross, S. Bechler, H. S. Funk, L.-T. Chang, J. Schulze, S. Ludwigs, J. van Slageren, *Adv. Funct. Mater.* **2021**, *31*, 2006882.

[42] A. Schweiger, G. Jeschke, *Principles of pulse electron paramagnetic resonance*, Reprinted., Oxford Univ. Press, Oxford, **2005**.

[43] S. Stoll, A. Schweiger, *J. Magn. Reson.* **2006**, *178*, 42–55.

[44] L. E. Ballentine, *Quantum mechanics*, Prentice Hall, Englewood Cliffs, NJ, **1990**.

[45] L. Escalera-Moreno, J. J. Baldoví, A. Gaita-Ariño, E. Coronado, *Chem. Sci* **2018**, *9*, 3265–3275.

[46] A. Lunghi, S. Sanvito, *Sci. Adv.* **2019**, *5*, eaax7163.

[47] C. Grezes, Y. Kubo, B. Julsgaard, T. Umeda, J. Isoya, H. Sumiya, H. Abe, S. Onoda, T. Ohshima, K. Nakamura, I. Diniz, A. Auffeves, V. Jacques, J.-F. Roch, D. Vion, D. Esteve, K. Moelmer, P. Bertet, *CR. Phys.* **2016**, *17*, 693–704.

[48] D. Gonţa, P. van Loock, *Phys. Rev. A* **2013**, *88*.

[49] M. Ghasemi, M. K. Tavassoly, *Quantum Inf. Process.* **2019**, *18*, 5932.

[50] A. Blais, R.-S. Huang, A. Wallraff, S. M. Girvin, R. J. Schoelkopf, *J. Opt. Soc. Am. B* **2004**, *69*, 2059.

[51] C.-H. Su, A. D. Greentree, W. J. Munro, K. Nemoto, L. C. L. Hollenberg, *Phys. Rev. A* **2008**, *78*, 1484.

[52] M. O. Scully, M. S. Zubairy, *Quantum optics*, Cambridge University Press, Cambridge, **1997**.

[53] D. F. Walls, G. J. Milburn, *Quantum optics*, 2nd ed., Springer, Berlin, **2008**, `https://ebookcentral.proquest.com/lib/subhh/detail.action?docID=1103742`.

[54] S. Putz, *Circuit Cavity QED with Macroscopic Solid-State Spin Ensembles*, Springer International Publishing, Cham, **2017**.

[55] C. W. Zollitsch, Dissertation, Universitätsbibliothek der TU München, München, **2016**.

[56] C. Grèzes, *Towards a Spin-Ensemble Quantum Memory for Superconducting Qubits*, Springer International Publishing, Cham, **2016**.

[57] D. O. Krimer, S. Putz, J. Majer, S. Rotter, *Phys. Rev. A* **2014**, *90*, 681.

[58] B. C. Rose, A. M. Tyryshkin, H. Riemann, N. V. Abrosimov, P. Becker, H.-J. Pohl, M. L. W. Thewalt, K. M. Itoh, S. A. Lyon, *Phys. Rev. X* **2017**, *7*.

[59] A. Angerer, T. Astner, D. Wirtitsch, H. Sumiya, S. Onoda, J. Isoya, S. Putz, J. Majer, *Appl. Phys. Lett.* **2016**, *109*, 033508.

[60] B. Julsgaard, C. Grezes, P. Bertet, K. Mølmer, *Phys. Rev. Lett.* **2013**, *110*, 250503.

[61] E. T. Jaynes, F. W. Cummings, *Proc. IEEE* **1963**, *51*, 89–109.

[62] G. S. Agarwal, *J. Opt. Soc. Am. B* **1985**, *2*, 480.

[63] A. Wallraff, D. I. Schuster, A. Blais, L. Frunzio, R.-S. Huang, J. Majer, S. Kumar, S. M. Girvin, R. J. Schoelkopf, *Nature* **2004**, *431*, 162–167.

[64] C. P. Poole, *Electron spin resonance: A comprehensive treatise on experimental techniques*, Repr. 2nd. ed., Dover Publications, Mineola, N.Y, **1996**.

[65] L. J. Berliner, S. S. Eaton, G. R. Eaton, *Distance Measurements in Biological Systems by EPR*, Springer, New York, **2012**.

[66] T. Holstein, H. Primakoff, *Phys. Rev.* **1940**, *58*, 1098–1113.

[67] F. Luis, A. Repollés, M. J. Martínez-Pérez, D. Aguilà, O. Roubeau, D. Zueco, P. J. Alonso, M. Evangelisti, A. Camón, J. Sesé, L. A. Barrios, G. Aromí, *Phys. Rev. Lett.* **2011**, *107*, 117203.

[68] S. Nakazawa, S. Nishida, T. Ise, T. Yoshino, N. Mori, R. D. Rahimi, K. Sato, Y. Morita, K. Toyota, D. Shiomi, M. Kitagawa, H. Hara, P. Carl, P. Höfer, T. Takui, *Angew. Chem. Int. Ed.* **2012**, *51*, 9860–9864.

[69] M. Shiddiq, D. Komijani, Y. Duan, A. Gaita-Ariño, E. Coronado, S. Hill, *Nature* **2016**, *531*, 348–351.

[70] C.-J. Yu, M. D. Krzyaniak, M. S. Fataftah, M. R. Wasielewski, D. E. Freedman, *Chem. Sci.* **2019**, *10*, 1702–1708.

[71] L. Tesi, E. Lucaccini, I. Cimatti, M. Perfetti, M. Mannini, M. Atzori, E. Morra, M. Chiesa, A. Caneschi, L. Sorace, R. Sessoli, *Chem. Sci.* **2016**, *7*, 2074–2083.

[72] T. J. Pearson, D. W. Laorenza, M. D. Krzyaniak, M. R. Wasielewski, D. E. Freedman, *Dalton Trans.* **2018**, *47*, 11744–11748.

[73] Lenef, Rand, *Phys. Rev. B Condens. Matter* **1996**, *53*, 13441–13455.

[74] M. S. Fataftah, J. M. Zadrozny, S. C. Coste, M. J. Graham, D. M. Rogers, D. E. Freedman, *J. Am. Chem. Soc.* **2016**, *138*, 1344–1348.

[75] M. J. Graham, J. M. Zadrozny, M. Shiddiq, J. S. Anderson, M. S. Fataftah, S. Hill, D. E. Freedman, *J. Am. Chem. Soc.* **2014**, *136*, 7623–7626.

[76] V. K. Sewani, R. J. Stöhr, R. Kolesov, H. H. Vallabhapurapu, T. Simmet, A. Morello, A. Laucht, *Phys. Rev. B* **2020**, *102*, 610.

[77] S. Otto, M. Grabolle, C. Förster, C. Kreitner, U. Resch-Genger, K. Heinze, *Angew. Chem. Int. Ed.* **2015**, *54*, 11572–11576.

[78] A. Abragam, B. Bleaney, *Electron paramagnetic resonance of transition ions*, Dover Publ, New York, N. Y., **1986**.

[79] Z.-Y. Yang, *J. Phys.: Condens. Matter* **2000**, *12*, 4091–4096.

[80] R. Büscher, G. Lehmann, *Chem. Phys. Lett.* **1986**, *124*, 202–205.

[81] P. C. Riedi, G. M. Smith in *Electron paramagnetic resonance*, (Eds.: B. C. Gilbert, D. M. Murphy, M. J. Davies), Electron Paramagnetic Resonance, Royal Society of Chemistry, Cambridge, **2002**, pp. 254–303.

[82] J. A. Clayton, K. Keller, M. Qi, J. Wegner, V. Koch, H. Hintz, A. Godt, S. Han, G. Jeschke, M. S. Sherwin, M. Yulikov, *Phys. Chem. Chem. Phys.* **2018**, *20*, 10470–10492.

[83] M. Azarkh, P. Gast, A. B. Mason, E. J. J. Groenen, G. Mathies, *Phys. Chem. Chem. Phys.* **2019**, *21*, 16937–16948.

[84] E. Moreno-Pineda, C. Godfrin, F. Balestro, W. Wernsdorfer, M. Ruben, *Chem. Soc. Rev.* **2018**, *47*, 501–513.

[85] A. T. Taguchi, P. J. O'Malley, C. A. Wraight, S. A. Dikanov, *J. Phys. Chem. B* **2014**, *118*, 9225–9237.

[86] R. de Sousa, S. Das Sarma, *Phys. Rev. B* **2003**, *68*, 120.

[87] W. M. Witzel, S. Das Sarma, *Phys. Rev. B* **2006**, *74*, 419.

[88] C. E. Jackson, C.-Y. Lin, S. H. Johnson, J. van Tol, J. M. Zadrozny, *Chem. Sci* **2019**, *114*, 4496.

[89] A. Raitsimring, A. Dalaloyan, A. Collauto, A. Feintuch, T. Meade, D. Goldfarb, *J. Magn. Reson.* **2014**, *248*, 71–80.

[90] S. Otto, M. Dorn, C. Förster, M. Bauer, M. Seitz, K. Heinze, *Coord. Chem. Rev* **2018**, *359*, 102–111.

[91] C. P. Barrett, J. Peterson, C. Greenwood, A. J. Thomson, *J. Am. Chem. Soc.* **1986**, *108*, 3170–3177.

[92] S. J. Bingham, D. Suter, A. Schweiger, A. J. Thomson, *Chem. Phys. Lett.* **1997**, *266*, 543–547.

[93] C. A. Moore, R. A. Satten, *Phys. Rev. B* **1973**, *7*, 1753–1772.

[94] J. Köhler, J. A. J. M. Disselhorst, M. C. J. M. Donckers, E. J. J. Groenen, J. Schmidt, W. E. Moerner, *Nature* **1993**, *363*, 242–244.

[95] S. Geschwind, G. E. Devlin, R. L. Cohen, S. R. Chinn, *Phys. Rev.* **1965**, *137*, A1087–A1100.

[96] L. J. Rogers, M. W. Doherty, M. S. J. Barson, S. Onoda, T. Ohshima, N. B. Manson, *New. J. Phys.* **2015**, *17*, 013048.

[97] J. C. Barbour, A. J. I. Kim, E. deVries, S. E. Shaner, B. M. Lovaasen, *Inorg. Chem.* **2017**, *56*, 8212–8222.

[98] M. Veldhorst, H. G. J. Eenink, C. H. Yang, A. S. Dzurak, *Nat. Commun.* **2017**, *8*, 1766.

[99] J. V. Barth, *Annu. Rev. Phys. Chem.* **2007**, *58*, 375–407.

[100] M. Warner, S. Din, I. S. Tupitsyn, G. W. Morley, Am Stoneham, J. A. Gardener, Z. Wu, A. J. Fisher, S. Heutz, C. W. Kay, G. Aeppli, *Nature* **2013**, *503*, 504–508.

[101] H.-J. Kümmerer, Dissertation, Universität Stuttgart, Stuttgart, **2004**.

[102] M. Schulte, Dissertation, Universität Stuttgart, Stuttgart, **2005**.

[103] I. Tkach, A. Baldansuren, E. Kalabukhova, S. Lukin, A. Sitnikov, A. Tsvir, M. Ischenko, Y. Rosentzweig, E. Roduner, *Appl. Magn. Reson.* **2008**, *35*, 95–112.

[104] G. D. Boyd, H. Kogelnik, *Bell Syst. Tech. J.* **1962**, *41*, 1347–1369.

[105] G. D. Boyd, J. P. Gordon, *Bell Syst. Tech. J.* **1961**, *40*, 489–508.

[106] M. L. van Blaricum, *IEEE Trans. Microwave Theory Techn.* **1975**, *23*, 931–934.

[107] D. P. Dunseith, S. Truppe, R. J. Hendricks, B. E. Sauer, E. A. Hinds, M. R. Tarbutt, *Proc. IEEE* **2015**, *48*, 045001.

[108] I. Kasa, *IEEE Trans. Instrum. Meas.* **1976**, *IM-25*, 8–14.

[109] S. Shahid, J. Ball, C. G. Wells, P. Wen, *IET Microw. Antennas Propag.* **2011**, *5*, 426.

[110] G. A. Rinard, R. W. Quine, S. S. Eaton, G. R. Eaton, W. Froncisz, *J. Magn. Reson.* **1994**, *108*, 71–81.

[111] E. O. Hammerstad, F. Bekkadal, *Microstrip Handbook*, Trondheim, **1975**.

[112] G. R. Eaton, S. S. Eaton, D. P. Barr, R. T. Weber, *Quantitative EPR: A Practitioners Guide*, 1. Aufl., Springer Verlag Wien, s.l., **2010**, `http://site.ebrary.com/lib/alltitles/docDetail.action?docID=10382649`.

[113] C. B. Walsh, E. I. Franses, *Thin Solid Films* **2003**, *429*, 71–76.

[114] C. Finazzo, C. Calle, S. Stoll, S. van Doorslaer, A. Schweiger, *Phys. Chem. Chem. Phys.* **2006**, *8*, 1942–1953.

[115] H. Peisert, T. Schwieger, J. M. Auerhammer, M. Knupfer, M. S. Golden, J. Fink, P. R. Bressler, M. Mast, *J. Appl. Phys.* **2001**, *90*, 466–469.

[116] M. Nakamura, *J. Vac. Sci. Technol. B* **1996**, *14*, 1109.

[117] K.-Y. Law, *Polymer* **1982**, *23*, 1627–1635.

[118] R. Amsüss, C. Koller, T. Nöbauer, S. Putz, S. Rotter, K. Sandner, S. Schneider, M. Schramböck, G. Steinhauser, H. Ritsch, J. Schmiedmayer, J. Majer, *Phys. Rev. Lett.* **2011**, *107*, 060502.

[119] M. K. Bhaskar, R. Riedinger, B. Machielse, D. S. Levonian, C. T. Nguyen, E. N. Knall, H. Park, D. Englund, M. Lončar, D. D. Sukachev, M. D. Lukin, *Nature* **2020**, *580*, 60–64.

[120] M. Tavis, F. W. Cummings, *Phys. Rev.* **1968**, *170*, 379–384.

[121] K. Sandner, H. Ritsch, R. Amsüss, C. Koller, T. Nöbauer, S. Putz, J. Schmiedmayer, J. Majer, *Phys. Rev. A* **2012**, *85*, 1.

[122] C. Bonizzoni, A. Ghirri, K. Bader, J. van Slageren, M. Perfetti, L. Sorace, Y. Lan, O. Fuhr, M. Ruben, M. Affronte, *Dalton Trans.* **2016**, *45*, 16596–16603.

[123] E. Abe, H. Wu, A. Ardavan, J. J. L. Morton, *Appl. Phys. Lett.* **2011**, *98*, 251108.

[124] G. Boero, G. Gualco, R. Lisowski, J. Anders, D. Suter, J. Brugger, *J. Magn. Reson.* **2013**, *231*, 133–140.

[125] S. Putz, A. Angerer, D. O. Krimer, R. Glattauer, W. J. Munro, S. Rotter, J. Schmiedmayer, J. Majer, *Nature Photon.* **2017**, *11*, 36–39.

[126] W. Duffy, J. F. Dubach, P. A. Pianetta, J. F. Deck, D. L. Strandburg, A. R. Miedema, *J. Chem. Phys.* **1972**, *56*, 2555–2561.

[127] J. C. Bonner, M. E. Fisher, *Phys. Rev.* **1964**, *135*, A640–A658.

[128] W. O. Hamilton, G. E. Pake, *J. Chem. Phys.* **1963**, *39*, 2694–2697.

[129] D. Zilić, D. Pajić, M. Jurić, K. Molčanov, B. Rakvin, P. Planinić, K. Zadro, *J. Magn. Reson.* **2010**, *207*, 34–41.

[130] W. Boon, W. Magnus, L. van Gerven, *J. Magn. Magn. Mater.* **1984**, *46*, 95–101.

[131] I. Chiorescu, N. Groll, S. Bertaina, T. Mori, S. Miyashita, *Phys. Rev. B* **2010**, *82*.

[132] D. I. Schuster, A. P. Sears, E. Ginossar, L. DiCarlo, L. Frunzio, J. J. L. Morton, H. Wu, G. A. D. Briggs, B. B. Buckley, D. D. Awschalom, R. J. Schoelkopf, *Phys. Rev. Lett.* **2010**, *105*, 140501.

[133] Y. Kubo, F. R. Ong, P. Bertet, D. Vion, V. Jacques, D. Zheng, A. Dréau, J.-F. Roch, A. Auffeves, F. Jelezko, J. Wrachtrup, M. F. Barthe, P. Bergonzo, D. Esteve, *Phys. Rev. Lett.* **2010**, *105*, 140502.

[134] N. Azuma, T. Ozawa, J. Yamauchi, *BCSJ* **1994**, *67*, 31–38.

[135] P. W. Anderson, P. R. Weiss, *Rev. Mod. Phys.* **1953**, *25*, 269–276.

[136] N. J. Simon, E. S. Drexler, R. P. Reed, *Properties of copper and copper alloys at cryogenic temperatures*, For sale by the Supt. of Docs. U.S. G.P.O and U.S. Dept. of Commerce National Institute of Standards and Technology, Washington, D.C and Gaithersburg, Md, **1992**.

[137] S. Putz, D. O. Krimer, R. Amsüss, A. Valookaran, T. Nöbauer, J. Schmiedmayer, S. Rotter, J. Majer, *Nature Phys.* **2014**, *10*, 720–724.

[138] Z. Kurucz, J. H. Wesenberg, K. Mølmer, *Phys. Rev. A* **2011**, *83*.

[139] R. Houdré, R. P. Stanley, M. Ilegems, *Phys. Rev. A* **1996**, *53*, 2711–2715.

[140] I. Diniz, S. Portolan, R. Ferreira, J. M. Gérard, P. Bertet, A. Auffèves, *Phys. Rev. A* **2011**, *84*.

[141] D. G. Mitchell, R. W. Quine, M. Tseitlin, R. T. Weber, V. Meyer, A. Avery, S. S. Eaton, G. R. Eaton, *J. Phys. Chem. B* **2011**, *115*, 7986–7990.

[142] H. Wu, R. E. George, J. H. Wesenberg, K. Mølmer, D. I. Schuster, R. J. Schoelkopf, K. M. Itoh, A. Ardavan, J. J. L. Morton, G. A. D. Briggs, *Phys. Rev. Lett.* **2010**, *105*, 140503.

[143] S. Fernbach, W. G. Proctor, *J. Appl. Phys.* **1955**, *26*, 170–181.

[144] A. G. Anderson, R. L. Garwin, E. L. Hahn, J. W. Horton, G. L. Tucker, R. M. Walker, *J. Appl. Phys.* **1955**, *26*, 1324–1338.

[145] E. L. Hahn, *Phys. Rev.* **1950**, *80*, 580–594.

[146] P. Neugebauer, D. Bloos, R. Marx, P. Lutz, M. Kern, D. Aguilà, J. Vaverka, O. Laguta, C. Dietrich, R. Clérac, J. van Slageren, *Phys. Chem. Chem. Phys.* **2018**, *20*, 15528–15534.

[147] S. Lenz, H. Bamberger, P. P. Hallmen, Y. Thiebes, S. Otto, K. Heinze, J. van Slageren, *Phys. Chem. Chem. Phys.* **2019**, *21*, 6976–6983.

[148] R. Boča, *Coord. Chem. Rev* **2004**, *248*, 757–815.

[149] S. B. Piepho, P. N. Schatz, *Group theory in spectroscopy: With applications to magnetic circular dichroism*, Wiley, New York, **1983**.

[150] P. H. Butler, *Point Group Symmetry Applications: Methods and Tables*, Springer US, Boston, MA, **1981**, `http://dx.doi.org/10.1007/978-1-4613-3141-4`.

A. Appendix

A.1. $[Cr(ddpd)_2][BF_4]_3$ a photoactive molecular quantum bit

A.1.1. Pulsed EPR

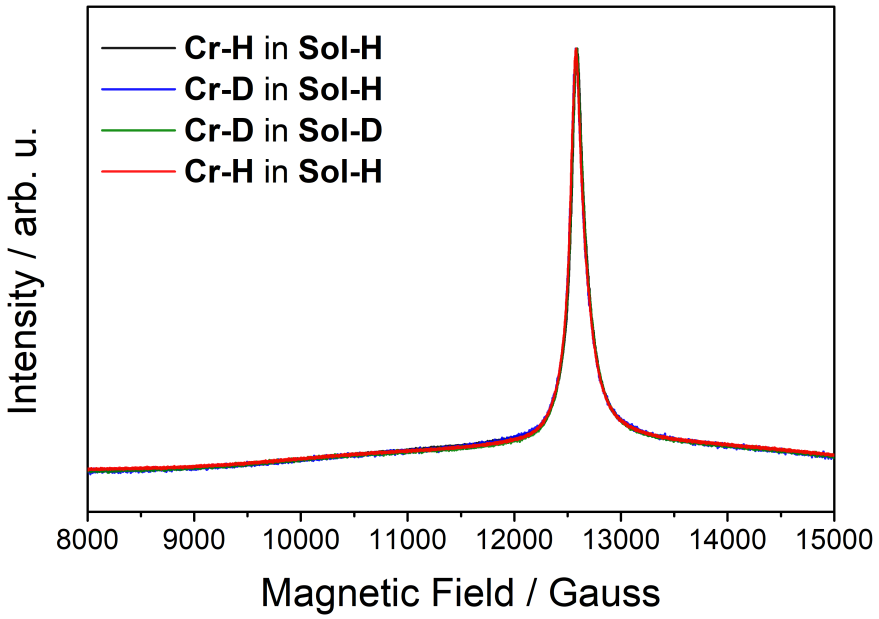

Figure A.1.: ESE-detected EPR spectra (colored line) of the different compound and solvent combinations (1 mM) at 7 K and 35 GHz.

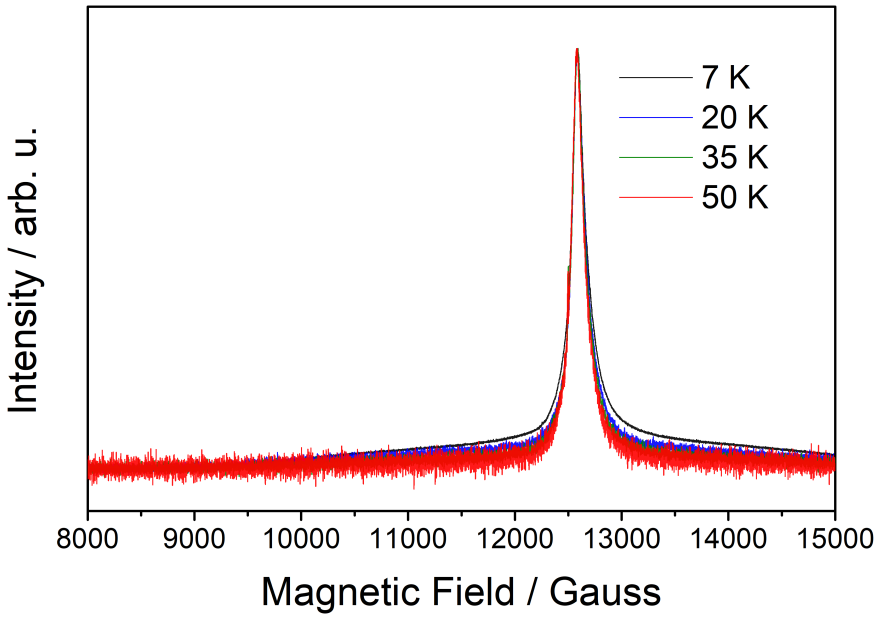

Figure A.2.: ESE-detected EPR spectra of 1 mM **Cr-H** in **Sol-H** at different temperatures and 35 GHz.

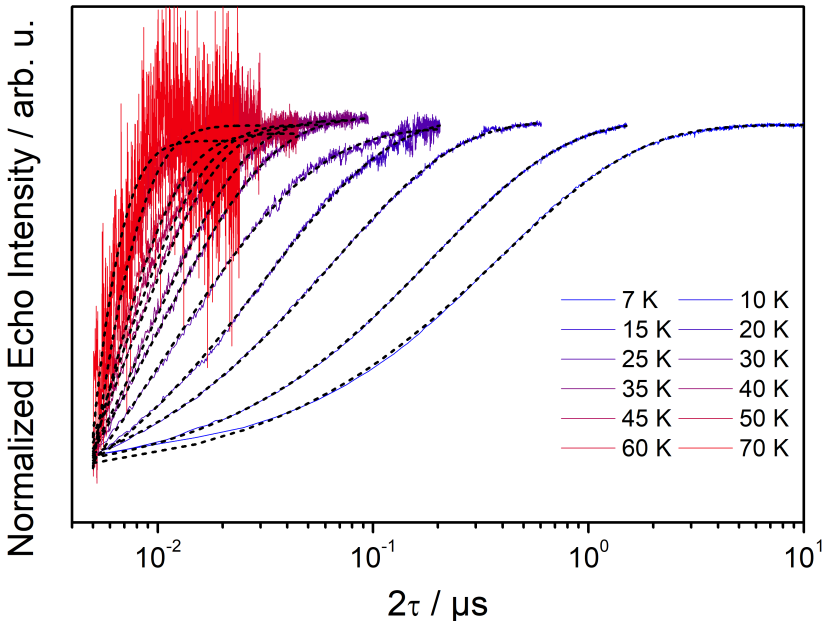

Figure A.3.: Inversion recovery experiments of 1 mM **Cr-H** in **Sol-H** at different temperatures and 35 GHz.

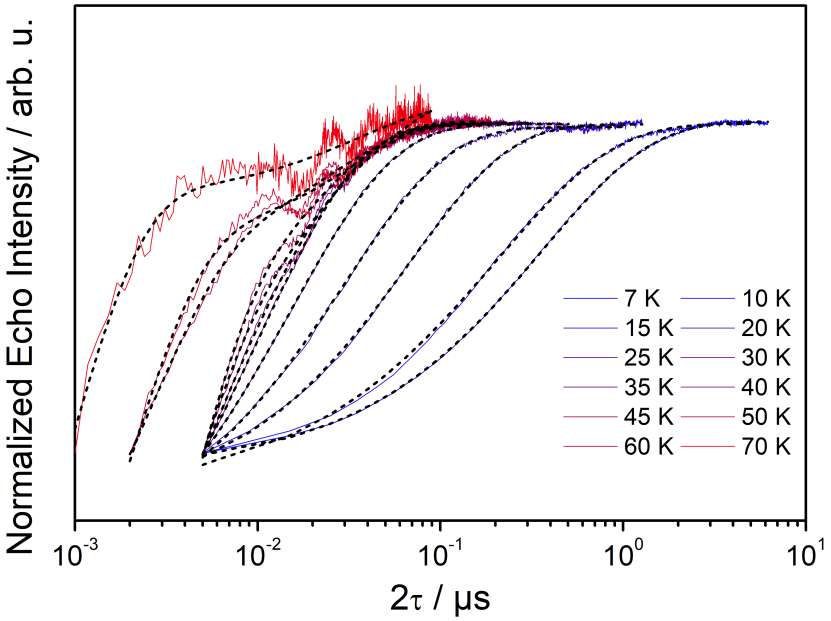

Figure A.4.: Inversion recovery experiments of 1 mM **Cr-H** in **Sol-D** at different temperatures and 35 GHz.

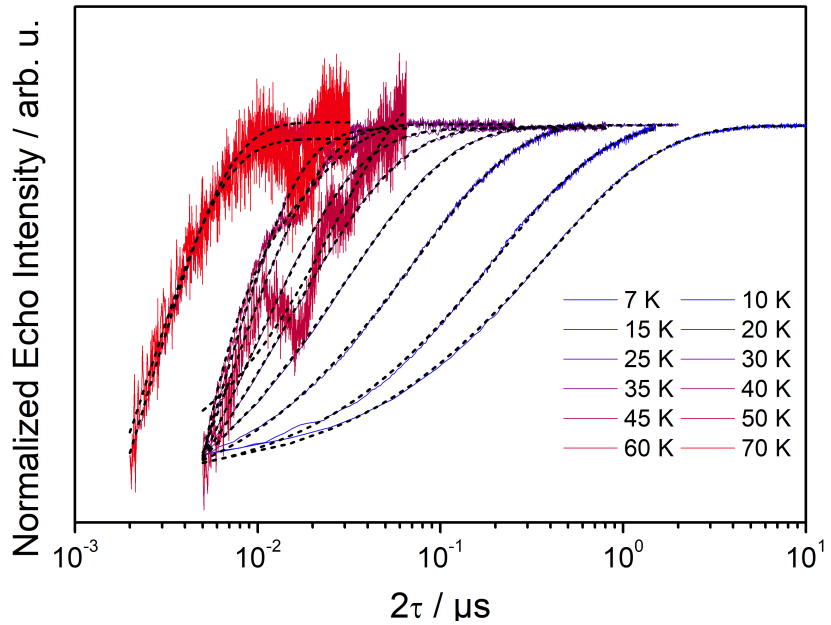

Figure A.5.: Inversion recovery experiments of 1 mM **Cr-D** in **Sol-H** at different temperatures and 35 GHz.

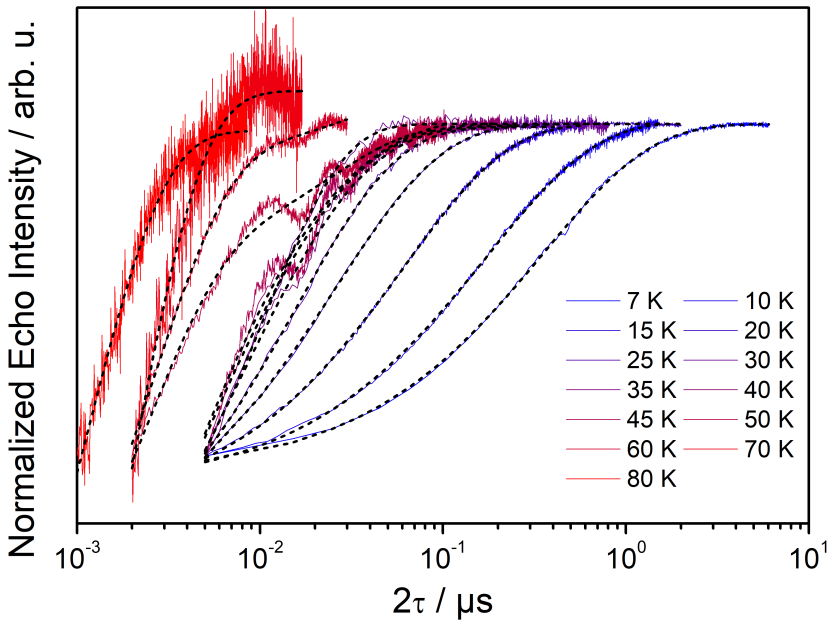

Figure A.6.: Inversion recovery experiments of 1 mM **Cr-D** in **Sol-D** at different temperatures and 35 GHz.

A.1.2. Derivation of the Λ-Tensor

The derivation of the Λ-Tensor was performed by the author of this thesis (S. Lenz) and was published in [147]. The following paragraph is a literal citation.

In case of the lighter transition metal ions, magnetic properties are mainly dominated by the spin momentum due to the quenching of angular momentum. However, in the most cases there is still some residual angular momentum left which can be described by second order perturbation using a crystal field basis. The properties of interest can then be calculated by evaluating the Λ-tensor [148] which connects the crystal field states with the same multiplicity via the angular momentum operator $\hat{L}$.

$$\Lambda_{ab} = \sum_{k \neq 0} \frac{\langle 0|\hat{L}_a|k\rangle \langle k|\hat{L}_b|0\rangle}{E_k - E_0} \tag{A.1}$$

For example, the ZFS parameters D and E can be calculated from the Λ-tensor:

$$D = -\frac{1}{2}\zeta^2 (2\Lambda_{zz} - \Lambda_{xx} - \Lambda_{yy}) \tag{A.2}$$

$$E = -\frac{1}{2}\zeta^2 (\Lambda_{xx} - \Lambda_{yy}) \tag{A.3}$$

The Λ-tensor for **Cr-H** is calculated by evaluating the matrix elements $\langle 0|\hat{L}_a|k\rangle$ in octahedral symmetry O for a d^3 electron configuration and account for the real symmetry D_2 of the molecule by applying the chain of groups $O \supset D_4 \supset D_2$. In octahedral symmetry, the ground state of our system transform as A_2 while the excited states transform

either as E, T_1 or T_2. As the angular momentum operator transform as T_1 and states with different spin-multiplicity are orthogonal only the $^4T_2$ excited state has to be taken into account. Furthermore, only the diagonal elements of the Λ-tensor are non-zero. The remaining matrix elements $\langle {}^4A_2|\hat{L}_a|{}^4T_2\rangle^{O\supset D_4\supset D_2}$ can be decomposed into a reduced matrix element $\langle {}^4A_2||L^{T_1}||{}^4T_2\rangle^{O}$, a 2jm and a 3jm using the Wigner-Eckhart theorem (see Table A.1 for the irrep. branching table):

$$\langle {}^4A_2|\hat{L}_x|{}^4T_2\rangle^{O\supset D_4\supset D_2} = \begin{pmatrix} A_2 \\ B_1 \end{pmatrix} \begin{matrix} O \\ D_4 \end{matrix} \cdot \begin{pmatrix} B_1 \\ A_1 \end{pmatrix} \begin{matrix} D_4 \\ D_2 \end{matrix} \cdot \begin{pmatrix} A_2 & T_1 & T_2 \\ B_1 & E & E \end{pmatrix} \begin{matrix} O \\ D_4 \end{matrix} \cdot \begin{pmatrix} B_1 & E & E \\ A_1 & B_3 & B_3 \end{pmatrix} \begin{matrix} D_4 \\ D_2 \end{matrix} \cdot \langle {}^4A_2||L^{T_1}||{}^4T_2\rangle^{O} \tag{A.4}$$

$$\langle {}^4A_2|\hat{L}_y|{}^4T_2\rangle^{O\supset D_4\supset D_2} = \begin{pmatrix} A_2 \\ B_1 \end{pmatrix} \begin{matrix} O \\ D_4 \end{matrix} \cdot \begin{pmatrix} B_1 \\ A_1 \end{pmatrix} \begin{matrix} D_4 \\ D_2 \end{matrix} \cdot \begin{pmatrix} A_2 & T_1 & T_2 \\ B_1 & E & E \end{pmatrix} \begin{matrix} O \\ D_4 \end{matrix} \cdot \begin{pmatrix} B_1 & E & E \\ A_1 & B_2 & B_2 \end{pmatrix} \begin{matrix} D_4 \\ D_2 \end{matrix} \cdot \langle {}^4A_2||L^{T_1}||{}^4T_2\rangle^{O} \tag{A.5}$$

$$\langle {}^4A_2|\hat{L}_z|{}^4T_2\rangle^{O\supset D_4\supset D_2} = \begin{pmatrix} A_2 \\ B_1 \end{pmatrix} \begin{matrix} O \\ D_4 \end{matrix} \cdot \begin{pmatrix} B_1 \\ A_1 \end{pmatrix} \begin{matrix} D_4 \\ D_2 \end{matrix} \cdot \begin{pmatrix} A_2 & T_1 & T_2 \\ B_1 & E & E \end{pmatrix} \begin{matrix} O \\ D_4 \end{matrix} \cdot \begin{pmatrix} B_1 & E & E \\ A_1 & B_1 & B_1 \end{pmatrix} \begin{matrix} D_4 \\ D_2 \end{matrix} \cdot \langle {}^4A_2||L^{T_1}||{}^4T_2\rangle^{O} \tag{A.6}$$

$$\langle {}^4T_2|\hat{L}_x|{}^4A_2\rangle^{O\supset D_4\supset D_2} = \begin{pmatrix} T_2 \\ E \end{pmatrix} \begin{matrix} O \\ D_4 \end{matrix} \cdot \begin{pmatrix} E \\ B_3 \end{pmatrix} \begin{matrix} D_4 \\ D_2 \end{matrix} \cdot \begin{pmatrix} T_2 & T_1 & A_2 \\ E & E & B_1 \end{pmatrix} \begin{matrix} O \\ D_4 \end{matrix} \cdot \begin{pmatrix} E & E & B_1 \\ B_3 & B_3 & A_1 \end{pmatrix} \begin{matrix} D_4 \\ D_2 \end{matrix} \cdot \langle {}^4T_2||L^{T_1}||{}^4A_2\rangle^{O} \tag{A.7}$$

$$\langle {}^4T_2|\hat{L}_y|{}^4A_2\rangle^{O\supset D_4\supset D_2} = \begin{pmatrix} T_2 \\ E \end{pmatrix} \begin{matrix} O \\ D_4 \end{matrix} \cdot \begin{pmatrix} E \\ B_2 \end{pmatrix} \begin{matrix} D_4 \\ D_2 \end{matrix} \cdot \begin{pmatrix} T_2 & T_1 & A_2 \\ E & E & B_1 \end{pmatrix} \begin{matrix} O \\ D_4 \end{matrix} \cdot \begin{pmatrix} E & E & B_1 \\ B_2 & B_2 & A_1 \end{pmatrix} \begin{matrix} D_4 \\ D_2 \end{matrix} \cdot \langle {}^4T_2||L^{T_1}||{}^4A_2\rangle^{O} \tag{A.8}$$

$$\langle {}^4T_2|\hat{L}_z|{}^4A_2\rangle^{O\supset D_4\supset D_2} = \begin{pmatrix} T_2 \\ E \end{pmatrix} \begin{matrix} O \\ D_4 \end{matrix} \cdot \begin{pmatrix} E \\ B_1 \end{pmatrix} \begin{matrix} D_4 \\ D_2 \end{matrix} \cdot \begin{pmatrix} T_2 & T_1 & A_2 \\ E & E & B_1 \end{pmatrix} \begin{matrix} O \\ D_4 \end{matrix} \cdot \begin{pmatrix} E & E & B_1 \\ B_1 & B_1 & A_1 \end{pmatrix} \begin{matrix} D_4 \\ D_2 \end{matrix} \cdot \langle {}^4T_2||L^{T_1}||{}^4A_2\rangle^{O} \tag{A.9}$$

The reduced multielectron matrix element $\langle {}^4A_2||L^{T_1}||{}^4T_2\rangle^{O}$ can be related to the reduced single electron matrix element $\langle t_2||l^{T_1}||e\rangle^{O}$ using the concept of fractional coefficents described in [149]. $\langle t_2||l^{T_1}||e\rangle^{O}$ can be directly calculated from SO_3:

$$\begin{aligned} \langle {}^4A_2||L^{T_1}||{}^4T_2\rangle^{O} &= \langle {}^4T_2||L^{T_1}||{}^4A_2\rangle^{O} \\ &= \langle t_2||l^{T_1}||e\rangle^{O} \\ &= \begin{pmatrix} 2 & 1_1 & 2 \\ T_2 & T_1 & E \end{pmatrix} \begin{matrix} SO_3 \\ O \end{matrix} \sqrt{l\,(l+1)\,(2l+1)} \\ &= \left(-\frac{\sqrt{2}}{\sqrt{5}}\right)\sqrt{30} = -2\sqrt{3} \end{aligned} \tag{A.10}$$

The remaining 2jm and 3jm factors can be looked up in the tables of Butler [150], for example:

$$\begin{aligned}
&\left(\begin{array}{c} A_2 \\ \hline B_1 \end{array}\right)^{O}_{D_4} \cdot \left(\begin{array}{c} B_1 \\ \hline A_1 \end{array}\right)^{D_4}_{D_2} \cdot \begin{pmatrix} A_2 & T_1 & T_2 \\ B_1 & E & E \end{pmatrix}^{O}_{D_4} \cdot \begin{pmatrix} B_1 & E & E \\ A_1 & B_3 & B_3 \end{pmatrix}^{D_4}_{D_2} \\
&= \left(\begin{array}{c} \widetilde{0} \\ \hline 2 \end{array}\right)^{O}_{D_4} \cdot \left(\begin{array}{c} 2 \\ \hline 0 \end{array}\right)^{D_4}_{D_2} \cdot \begin{pmatrix} \widetilde{0} & 1 & \widetilde{1} \\ 2 & 1 & 1 \end{pmatrix}^{O}_{D_4} \cdot \begin{pmatrix} 2 & 1 & 1 \\ 0 & \widetilde{1} & \widetilde{1} \end{pmatrix}^{D_4}_{D_2} \\
&= 1 \cdot 1 \cdot \frac{\sqrt{2}}{\sqrt{3}} \cdot \frac{-1}{\sqrt{2}}
\end{aligned} \tag{A.11}$$

Finally, we arrive at:

$$\left\langle {}^4A_2 \middle| \hat{L}_x \middle| {}^4T_2 \right\rangle^{O \supset D_4 \supset D_2} = \left\langle {}^4T_2 \middle| \hat{L}_x \middle| {}^4A_2 \right\rangle^{O \supset D_4 \supset D_2} = +2 \tag{A.12}$$

$$\left\langle {}^4A_2 \middle| \hat{L}_y \middle| {}^4T_2 \right\rangle^{O \supset D_4 \supset D_2} = \left\langle {}^4T_2 \middle| \hat{L}_y \middle| {}^4A_2 \right\rangle^{O \supset D_4 \supset D_2} = -2 \tag{A.13}$$

$$\left\langle {}^4A_2 \middle| \hat{L}_y \middle| {}^4T_2 \right\rangle^{O \supset D_4 \supset D_2} = \left\langle {}^4T_2 \middle| \hat{L}_y \middle| {}^4A_2 \right\rangle^{O \supset D_4 \supset D_2} = +2 \tag{A.14}$$

The elements of the Λ-tensor are then:

$$\Lambda_{xx} = \frac{\left\langle {}^4A_2 \middle| \hat{L}_x \middle| {}^4T_2 \right\rangle^{O \supset D_4 \supset D_2} \left\langle {}^4T_2 \middle| \hat{L}_x \middle| {}^4A_2 \right\rangle^{O \supset D_4 \supset D_2}}{E_1 - E_0} = \frac{4}{E_1} \tag{A.15}$$

$$\Lambda_{yy} = \frac{\left\langle {}^4A_2 \middle| \hat{L}_x \middle| {}^4T_2 \right\rangle^{O \supset D_4 \supset D_2} \left\langle {}^4T_2 \middle| \hat{L}_x \middle| {}^4A_2 \right\rangle^{O \supset D_4 \supset D_2}}{E_2 - E_0} = \frac{4}{E_2} \tag{A.16}$$

$$\Lambda_{zz} = \frac{\left\langle {}^4A_2 \middle| \hat{L}_x \middle| {}^4T_2 \right\rangle^{O \supset D_4 \supset D_2} \left\langle {}^4T_2 \middle| \hat{L}_x \middle| {}^4A_2 \right\rangle^{O \supset D_4 \supset D_2}}{E_3 - E_0} = \frac{4}{E_3} \tag{A.17}$$

Table A.1.: Branching table for the important irreducible representations for the chain $O \supset D_4 \supset D_2$. The symbol in round brackets corresponds to the Butler notation

O	D_4	D_2
$A_2\left(\widetilde{0}\right)$	$B_1\,(2)$	$A_1\,(0)$
$T_1\,(1)$	$A_2\left(\widetilde{0}\right) + E\,(1)$	$B_1\left(\widetilde{0}\right) + B_2\,(1) + B_3\left(\widetilde{1}\right)$
$T_2\left(\widetilde{1}\right)$	$B_2\left(\widetilde{2}\right) + E\,(1)$	$B_1\left(\widetilde{0}\right) + B_2\,(1) + B_3\left(\widetilde{1}\right)$

A.2. Pulsed EPR on thin film samples

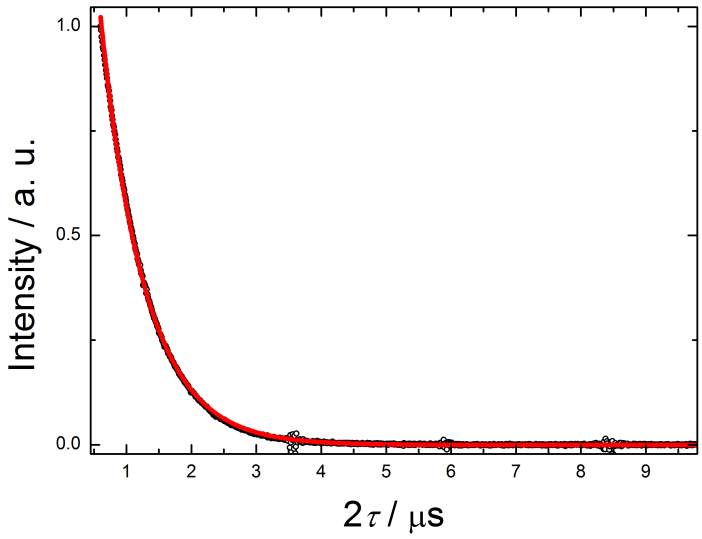

Figure A.7.: Hahn-echo decay (black dots) of a 2.1 mg 5 w.% BDPA in polystyrene sample measured at 1249.2 mT, 35 GHz and room temperature. A monoexponential fit with $T_{\mathrm{m}} = 680(10)$ ns (red line) is included as well.

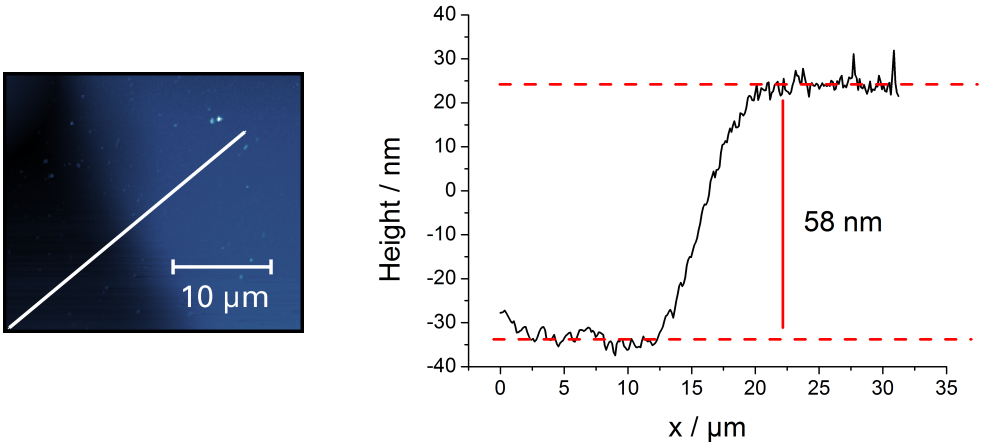

Figure A.8.: AFM image of the edge of the CuPc and H_2Pc film (left hand side). A white line indicates a slice through the AFM measurement (right hand side) which was used to determine the film thickness of 58 nm.

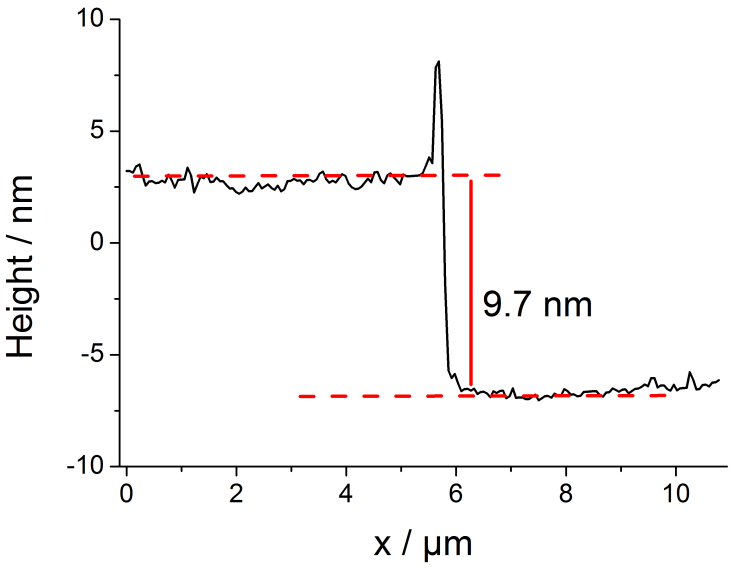

Figure A.9.: AFM measurement of a 5% BDPA in PMMA thin film spin coated from a 2 g/l solution in toluene. A scratch was induced by the means of a wooden needle, the thickness was measured across that scratch.

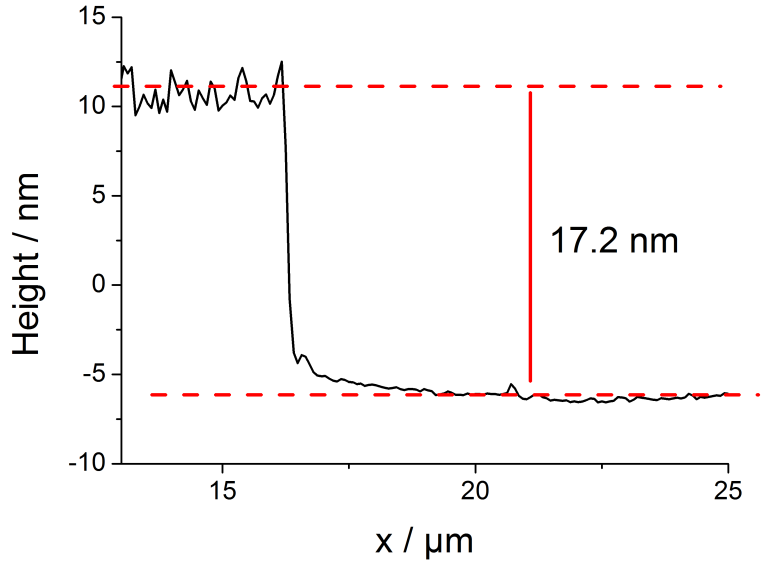

Figure A.10.: AFM measurement of a 5% BDPA in PMMA thin film spin coated from a 4 g/l solution in toluene. A scratch was induced by the means of a wooden needle, the thickness was measured across that scratch.

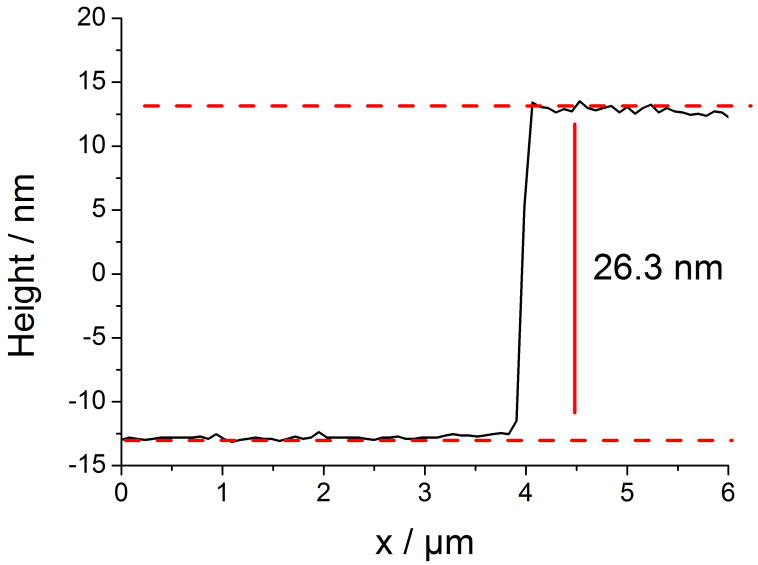

Figure A.11.: AFM measurement of a 5% BDPA in PMMA thin film spin coated from a 6 g/l solution in toluene. A scratch was induced by the means of a wooden needle, the thickness was measured across that scratch.

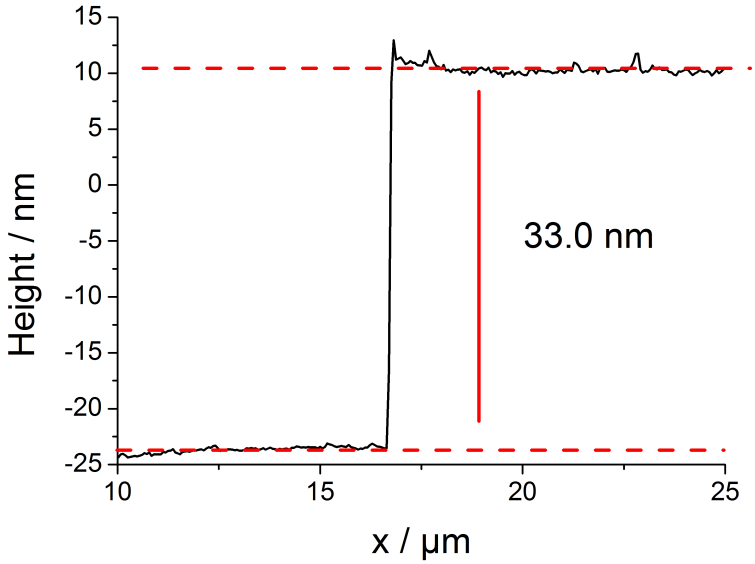

Figure A.12.: AFM measurement of a 5% BDPA in PMMA thin film spin coated from a 8 g/l solution in toluene. A scratch was induced by the means of a wooden needle, the thickness was measured across that scratch.

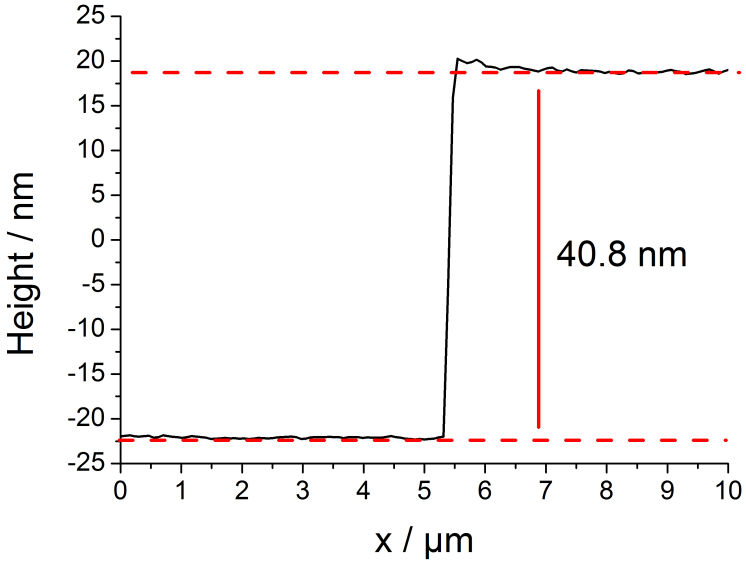

Figure A.13.: AFM measurement of a 5% BDPA in PMMA thin film spin coated from a 10 g/l solution in toluene. A scratch was induced by the means of a wooden needle, the thickness was measured across that scratch.

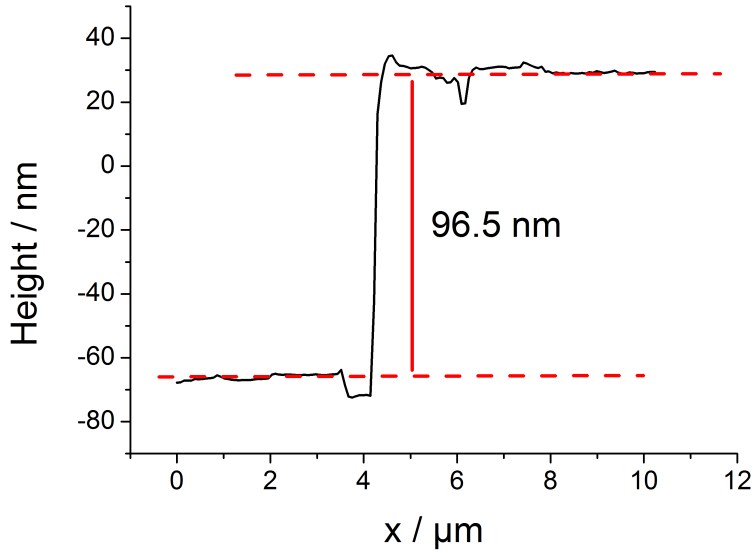

Figure A.14.: AFM measurement of a 5% BDPA in PMMA thin film spin coated from a 20 g/l solution in toluene. A scratch was induced by the means of a wooden needle, the thickness was measured across that scratch.

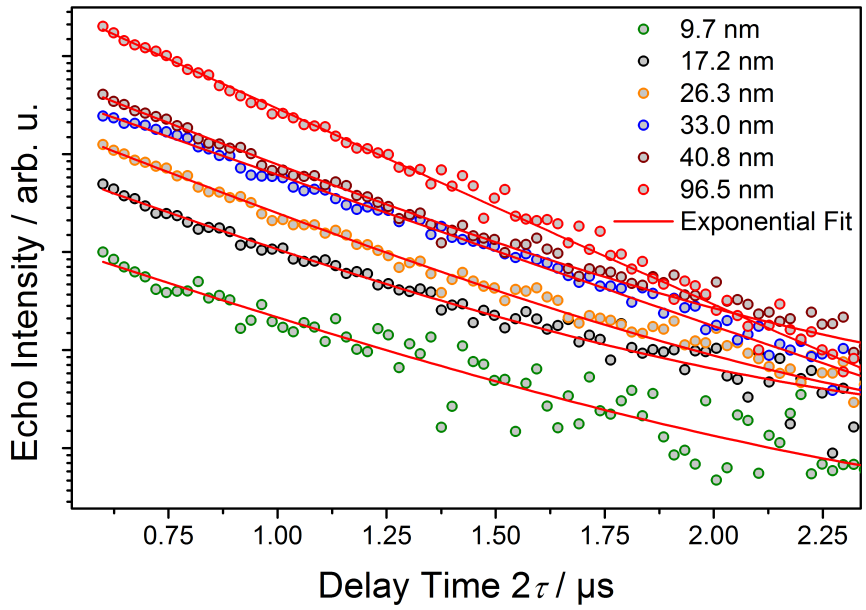

Figure A.15.: Hahn-echo decays (colored dots) of the 5% BDPA in PMMA thin films with a thickness between 9.7 nm and 96.5 nm at 7 K and 35 GHz. Exponential fits (red lines) used to extract the corresponding T_m are shown as well.

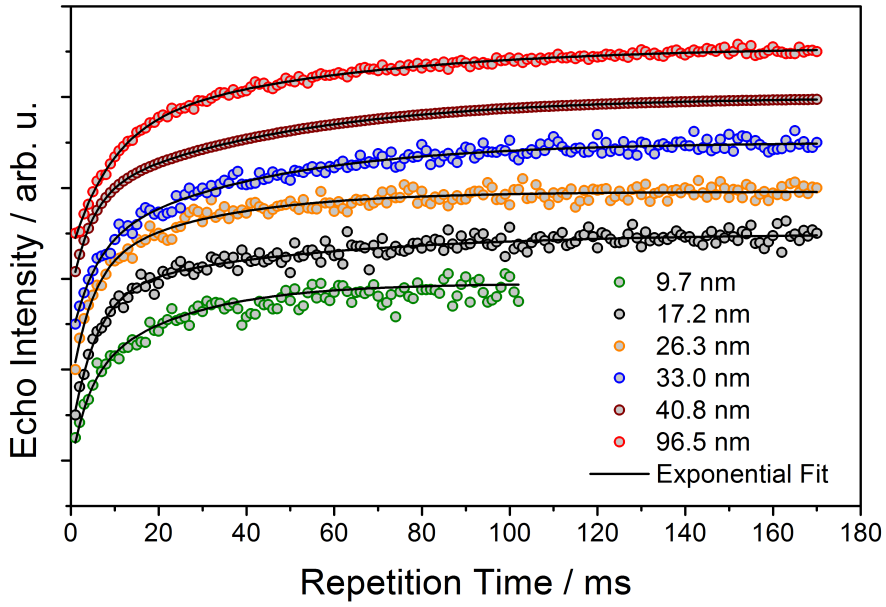

Figure A.16.: Saturation recovery experiments (colored dots) of the 5% BDPA in PMMA thin films with a thickness between 9.7 nm and 96.5 nm at 7 K and 35 GHz. Exponential fits (red lines) used to extract the corresponding T_1 are shown as well.

A.3. Strong coupling of photons with molecular quantum bits

The following *Matlab* scripts can be used to solve the differential equations presented in Section 2.4.3. Main.m is the file where the initial conditions are defined which starts the simulation. cQEDODEsKappas.m contains the differential equations and pulseTrain.m can be used to model the driving field using rectangular pulses.

```
clear,close all
omega=78*pi*2;
Nges=omega.^2/((1.4e-7*2*pi).^2)*0.2;
%Nges=10
%Nges=2e16;
res=0.5*2
bw=200*2*pi
bw2=100*2*pi
res2=50*2*pi;

%sPData=dlmread('BDPA_9.4mg_7K_35.000
    ↪ GHz_12488Gauss_SinglePulse_LowPower.dat','',1,0);



kappaE=13*1*2*pi;
kappaI=13*1*2*pi;
w=0%1500
deltaCS=0*2*pi;
FWHM=11.9*2*pi

freq1=-bw/2:res:bw/2;

freq2=-bw2/2:res2:bw2/2;


gamma1=[0.5;0.01]*2;
gamma1=repmat(gamma1,1,length(freq1));
gamma2=[1.5;0.0000]*pi*2;
gamma2=repmat(gamma2,1,length(freq2));
gamma=[gamma1 gamma2];



a=0
b=1-a
```

```
FWHM=70*2*pi
q=1.001
sigma=FWHM/2/sqrt((2^q-2)/(2*q-2));

rho1=(1+(1-q)*-(1/(2*sigma.^2))*(freq1).^2).^(1/(1-q));

q=1.11
FWHM=11.9*2*pi*1
sigma=FWHM/2/sqrt((2^q-2)/(2*q-2));
rho2=(1+(1-q)*-(1/(2*sigma.^2))*(freq2).^2).^(1/(1-q));

Nm1=b*1*Nges*1*rho1./sum(rho1);
Nm2=a*Nges*1*rho2./sum(rho2)*1;
freq=[freq1 freq2];

Nm=[Nm1 Nm2];


y0=zeros(length(freq)+2,1);
gm=ones(size(freq))*1.4e-7*2*pi;

cov=zeros(2+3*length(freq));
for j=1:length(gm)
    y0(2+3*j)=-Nm(j)/2;
end

options = odeset('RelTol',1e-5,'AbsTol',1e-4,'InitialStep',0.005);




 pl=[0.065 0.065];
phase=[0 0];
tw=0.29
pStart=[0.037 0.3];
pwrA=[1e13 2e14];
tspan=0:0.0025:0.8;

beta=@(t) pulseTrain(t,pl,phase,pStart,pwrA,w);


odes2solve=@(t,y) cQEDODEsKappas(t,y,gm,kappaE,kappaI,beta,deltaCS
    ↪ ,freq,gamma,Nm,cov);
[t,y]=ode45(odes2solve,tspan,y0,options);
```

```
tg=t;
yg=y;

H=yg(:,1);
E=yg(:,2);


EM=H+1i*E;
alpha=0
%EM=EM.*exp(1i*(-w*2*pi*tg+alpha/180*pi));




clf

figure(1)

hold on
plot(tg,real(EM)*sqrt(kappaE)-real(beta(tg)))
%plot(sPData(:,1)*1e6-0.097,(sPData(:,2)*-1e6)*-0.4)
hold off
```

```
function dydt=cQEDODEsKappas(t,y,gm,kappaE,kappaI,b,deltaCS,deltam,
    ↪ gamma,Nm,cov)
    dydt=zeros(length(y),1);
    dydt(1)=-1*(kappaI+kappaE*1)*y(1)+deltaCS*y(2)-sum(gm.*sqrt(2)
        ↪ .*y(4:3:end-1)')+2*sqrt(kappaE)*real(b(t));
    dydt(2)=-1*(kappaI+kappaE*1)*y(2)-deltaCS*y(1)-sum(gm.*sqrt(2)
        ↪ .*y(3:3:end-2)')+2*sqrt(kappaE)*imag(b(t));
        for j=1:length(gm)
            dydt(j*3)=-gamma(1,j)*y(j*3)-deltam(j)*y(1+j*3)-sqrt(2)*
                ↪ gm(j)*(y(2+3*j)*y(2)+cov(2+3*j,2));
            dydt(1+j*3)=-gamma(1,j)*y(1+j*3)+deltam(j)*y(j*3)-sqrt
                ↪ (2)*gm(j)*(y(2+3*j)*y(1)+cov(2+3*j,1));
            dydt(2+j*3)=sqrt(2)*gm(j)*(y(j*3)*y(2)+cov(j*3,2)+y(1+j
                ↪ *3)*y(1)+cov(1+j*3,1))-gamma(2,j)*(y(2+j*3)+Nm(j))
                ↪ ;
        end
end
```

```
function beta=pulseTrain(t,pl,phase,pStart,pwrA,w)
    if isrow(t)
        t=t';
    end
```

```
    beta=zeros(length(t),1);
    tspanP1=zeros(2,1);
    for i=1:length(pl)
        pulseL=pl(i);
        tspanP1(1)=pStart(i)-1.5*pl(i);
        tspanP1(2)=pStart(i)+2.5*pl(i);
        pwr1=pwrA(i);
        beta=beta+imag((sqrt(pwr1)./pi.*log(((t-(tspanP1(2)+tspanP1
            ↪ (1))*0.5)/pulseL+0.5)./((t-(tspanP1(2)+tspanP1(1))
            ↪ *0.5)/pulseL-0.5)))).*exp(1i*(w*2*pi*t+phase(i)/180*pi
            ↪ ));
    end
end
```